Dissertation

submitted to the

Combined Faculty of Natural Sciences and Mathematics

of the Ruperto Carola University Heidelberg, Germany

for the degree of

Doctor of Natural Sciences

Presented by

Elisa Gallo, M.Sc.

born in Cantu', Italy

Oral examination: 5th February 2021

FGF signaling and cell state transitions during organogenesis

Referees: Dr. Martin Jechlinger

Prof. Dr. Joachim Wittbrodt

Summary

Organogenesis is a complex choreography of morphogenetic processes, patterns and dynamic shape changes as well as the specification of cell fates. Although several molecular actors and context-specific mechanisms have already been identified, our general understanding of the fundamental principles that govern the formation of organs is far from comprehensive.

The application of the concept of 'rebuild it to understand it' from synthetic biology represents a promising alternative to the classical approach of 'break it to understand it' in order to distill biological understanding from complex developmental processes. According to this 'rebuilding' concept, in this study we sought to develop an experimental approach to induce the formation of organs from progenitor cells 'on demand' and to investigate the minimum requirements for such a process.

The zebrafish lateral line chain cells are a powerful *in vivo* model for our study because they are a group of naïve multipotent progenitor cells that display mesenchyme-like features. In order to bring these cells to form organs, we used the well-known role of the FGF signaling pathway as a driver of organogenesis in the lateral line and developed an inducible and constitutively active form of the fibroblast growth factor receptor 1a (chemoFGFR). The cell-autonomous induction of this chemoFGFR in chain cells effectively triggered the formation of fully mature organs and thus enabled spatial and temporal control of the organogenesis process.
Next, we asked what it takes to form an organ *de novo*. We used a combination of real-time microscopy, single cell tracking, polarity quantification, and mosaic analysis to study the cell behaviors that result from chemoFGFR induction. The picture that emerges from these analyses is that *de novo* organs form through a genetically encoded self-assembly process that is based on the pattern of chemoFGFR induction. In this scenario, cells expressing chemoFGFR aggregate into clusters and epithelialize as they sort out of non-expressing cells. We found that this sorting process occurs through cell rearrangement and slithering, which involves an extensive remodeling of the cell-cell contacts. Chain cells that do not express chemoFGFR can envelop these chemoFGFR expressing cell clusters and form a rim at the cluster periphery. This multi-stage process leads to the establishment of the inside-outside pattern of *de novo* organs, which is used as a blueprint for cell differentiation. In summary, in this study we provide insights into the mechanisms involved in the self-assembly of organs from a naïve population of progenitor cells.

Zusammenfassung

Organogenese ist eine komplexe Choreografie aus morphogenetischen Prozessen, Mustern und dynamischen Formänderungen sowie der Spezifizierung von Zellschicksalen. Obwohl bereits einige molekulare Akteure und kontextspezifische Mechanismen identifiziert wurden, ist unser generelles Verständnis von grundlegenden Prinzipien, die die Entstehung von Organen steuern, alles andere als umfassend. Die Anwendung des Konzepts „Nachbauen, um zu verstehen“ aus der synthetischen Biologie stellt eine vielversprechende Alternative zum klassischen Ansatz „Zerstören, um zu verstehen“ dar, um biologisches Verständnis aus komplexen Entwicklungsprozessen zu destillieren. Gemäß dieses „Nachbau“-Konzepts, haben wir in dieser Studie versucht, einen experimentellen Ansatz zu entwickeln, um die Bildung von Organen aus Vorläuferzellen ‘auf Abruf’ zu induzieren und so die Mindestanforderungen für einen solchen Prozess zu untersuchen. Die Kettenzellen der Zebrafisch-Laterallinie sind ein geeignetes *in vivo* Modell für unsere Studie, da sie eine Gruppe von naiven multipotenten Vorläuferzellen sind, die Mesenchym-artigen Merkmale aufweisen. Um diese Zellen dazu zu bringen, Organe zu bilden, nutzten wir die bekannte Rolle der FGF-Signalpfads als Treiber von Organogenese in der Laterallinie und entwickelten eine induzierbare und konstitutiv aktive Form des Fibroblasten-Wachstumsfaktor-Rezeptors 1a (chemoFGFR). Die zellautonome Induktion dieses chemoFGFRs in Kettenzellen löste effektiv die Bildung von Organen aus, die sich normal weiterentwickelten und ermöglichte somit die räumliche und zeitliche Kontrolle des Organogenese Prozesses. Als nächstes fragten wir, was notwendig ist, um ein Organ *de novo* zu bilden. Wir nutzten eine Kombination aus Echtzeit-Mikroskopie, Einzelzell-Verfolgung, Polaritätsquantifizierung und Mosaikanalyse, um das Zellverhalten zu untersuchen, das sich aus einer chemoFGFR-Induktion ergibt. Das Bild, das sich aus diesen Analysen ergibt, ist, dass *de novo* Organe durch einen genetisch codierten Selbstorganisationsprozess entstehen, der auf dem Muster der chemoFGFR-Induktion aufbaut. In diesem Szenario aggregieren Zellen, die chemoFGFR exprimieren, zu Clustern und epithelisieren, während sie sich aus nicht exprimierenden Zellen aussortieren. Wir fanden heraus, dass dieser Sortierprozess durch das Gleiten und Umordnen von Zellen geschieht, was durch eine umfassende Umgestaltung der Zell-Zell-Kontakte vermittelt wird. Kettenzellen, die kein chemoFGFR exprimieren, können diese chemoFGFR exprimierenden Zellcluster umhüllen und einen Ring an der Clusterperipherie bilden. Dieser mehrstufige Prozess führt zur Etablierung des Innen-Außen-Musters von *de novo* Organen, das als Blaupause für die Zelldifferenzierung genutzt wird. Zusammenfassend geben wir in dieser Arbeit Einblicke in die Mechanismen, die bei der Selbstorganisation von Organen aus einer naiven Population von Vorläuferzellen beteiligt sind.

Table of Contents

1 Introduction

1.1 Mesenchymal-to-epithelial and epithelial-to-mesenchymal transitions

During development and the entire lifespan of multicellular organisms, cells undergo state transitions to generate different phenotypes and functions. The Epithelial to Mesenchymal Transition (EMT) and the Mesenchymal to Epithelial Transition (MET) provide classical examples that are involved in a plethora of physiological and pathological contexts, ranging from developmental processes, body plan formation and tissue homeostasis, to regeneration, wound healing, tissue fibrosis and cancer metastasis. EMT drives cells from an epithelial to a mesenchymal phenotype, which involves the loss of apical-basal polarity and of cell-cell junctions and generates singles cells that often display migratory behaviors. MET refers to the reverse process, that converts mesenchymal cells into apical-basal polarized cells, that become integrated into epithelia through stable adherens and tight junctions [Kim et al., 2016]. As such, MET appears to represent a fundamental program for the assembly and organization of multicellular structures during organogenesis.
We start in section 1.2 with a description of the steps involved in the induction of the MET program, while in section 1.3 we focus instead on how MET is integrated with other processes during development and how dynamically the MET program can be tuned in different contexts.

1.2 The regulation and execution of MET transitions

MET has been suggested to be a multistep process that requires an initiation phase where the MET program is triggered, a second step where apical-basal polarity is established, and a final step where stabilization of the epithelial phenotype in the new architectural setup occurs (Figure 1.1 a) [Kim et al., 2016].

1.2.1 Induction of the MET program

While the core set of inducers and transcription factors involved in EMT has been extensively characterized [Stemmler et al., 2019; Yang et al., 2020], our knowledge of the inducers of the reverse process MET is far less comprehensive. A diverse set of inducers have been shown to activate the cascades promoting MET, most of which are cell non-autonomous signals of chemical or mechanical nature. Within the class of chemical cues, Wnt and FGF signaling pathways have been implicated in the onset of MET. During kidney development, Wnt9b released from the ureteric bud was shown to induce MET of the adiacent metanephric ‘cap’ mesenchyme, engaging cells into rosette-shaped cell clusters that give rise to the renal vesicle [Carroll et al., 2005]. Additionally, during somitogenesis in chick and mouse, Wnt6 secreted by the ectoderm was found to promote MET in the presomitic mesoderm by

activating the transcription factor Paraxis [Rowton et al., 2013; Schmidt et al., 2004; Šošić et al., 1997]. FGF signaling has also been identified as a trigger of MET in several developmental contexts, for instance during formation of the chick hindgut, the mouse primitive endoderm and the Kupffer's vesicle (described in section 1.4 and 1.3.3.4). Furthermore, studies on early stages of somatic cell reprogramming and on cancer cell cultures provided evidences that several transcription factors involved in the stabilization of the epithelial phenotype can trigger MET [Pei et al., 2019]. GRHL2, BMP and KLF4 induce MET by expressing epithelial-related genes during differentiation of pluripotent stem cells [G. Chen et al., 2011; Li et al., 2010; Samavarchi-Tehrani et al., 2010], GATA3 triggers MET in breast cancer cells [Takaku et al., 2016] while members of the Ovol family in various cancer cells and in dermal fibroblasts [Roca et al., 2013; Watanabe et al., 2019].

A growing body of evidence suggests that mechanical cues also contribute to the initiation of MET. During heart development in *Xenopus*, endoderm tissue stiffness and contraction appear to play important roles in MET induction of the overlaying hearth precursor cells, that assemble polarized epithelia [Trinh & Stainier, 2004] while migrating toward the ventral midline [Kim et al., 2016; Shi et al., 2015; Varner & Taber, 2012]. Similarly, mechanical properties of traversed microenvironments were proposed to contribute to MET and 'homing' of metastasizing cells into secondary sites [Gunasinghe et al., 2012; Jolly et al., 2017; Shibue & Weinberg, 2011]. Furthermore, recent work in *Xenopus* embryonic aggregates suggested that an increase of tissue stiffness drives epithelialization of mesenchymal cells at the surface of the aggregate and regeneration of Goblet cell precursors. Notably, perturbation of actomyosin contractility with pharmacological and genetic tools was shown to control the extent of surface epithelialization [Kim et al., 2020]. Other mechanical cues associated with the induction of MET are compaction of cell aggregates and fluid hydrostatic pressure [Fleming & Johnson, 1988; Kim et al., 2016]. During mouse blastocyst development, indeed, the luminal fluid drives stretching of trophectoderm cells at the tissue-fluid interface, that leads to tight junction maturation [Chan et al., 2019].

Remarkably, MET can be triggered in macrophages as part of the immune response to pathogens [Cronan et al., 2016]. It was found that, in presence of a persistent *Mycobacterial* infection, macrophages undergo MET to encapsulate the pathogenic source into granulomas. To do so, macrophages activate modules of the canonical epithelial program such as adherens, tight junctions and desmosome, while converting both their morphology and protein expression profile to a more epithelial phenotype [Cronan et al., 2016].

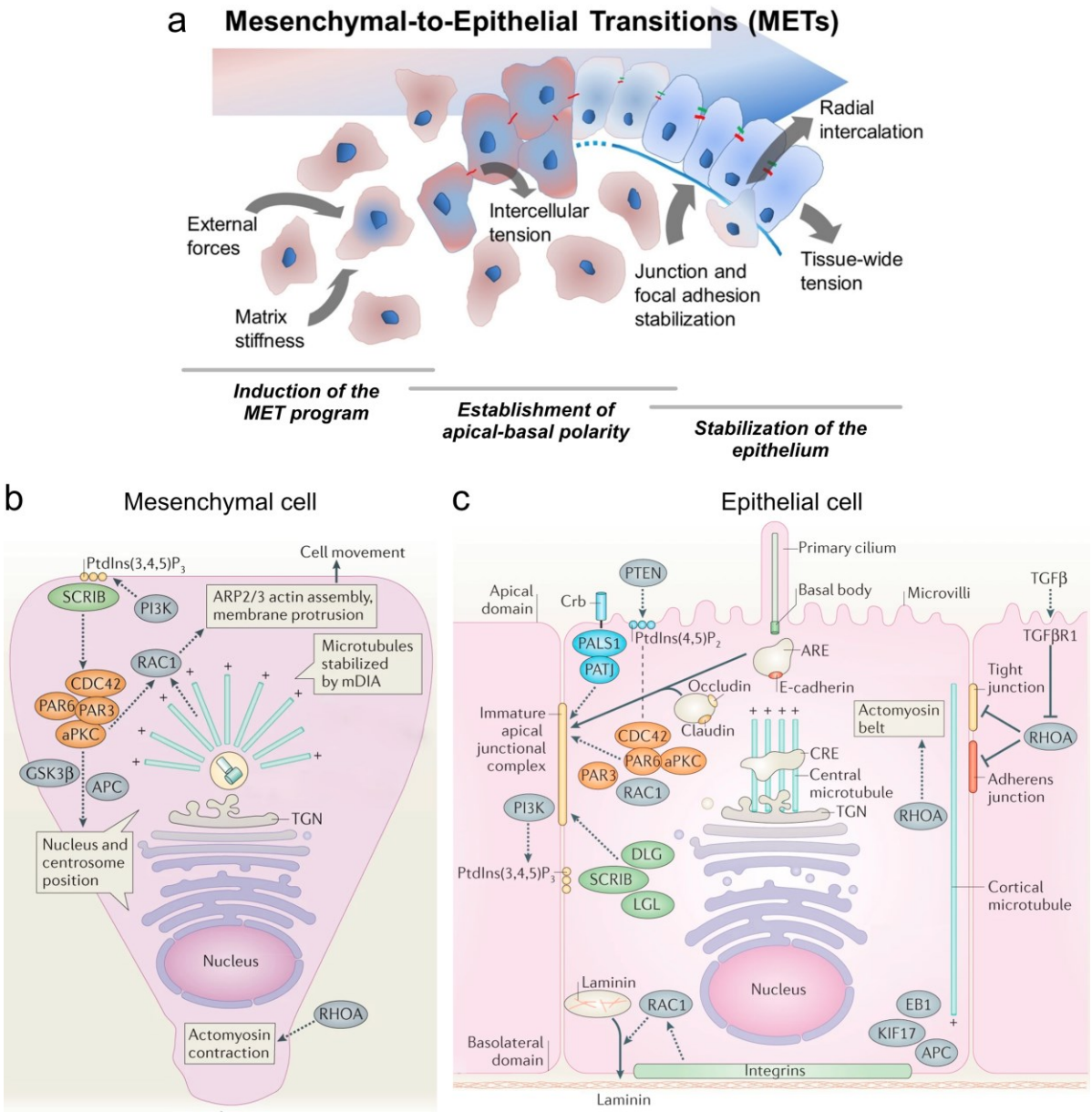

Figure 1.1: The mesenchymal-to-epithelial transition

(a) Mesenchymal-to-epithelial transition (MET) is a multistep process that leads a mesenchymal cell to adopt an epithelial phenotype. The process, that can be triggered by various chemical and mechanical cues, involves the conversion of the cell polarity axis to an apical-basal polarity, the formation of stable junctions between cells and a profound remodeling of cellular architecture, organelles positioning and of intracellular trafficking. Finally, the epithelial phenotype is stabilized by epigenetic, metabolic and cell fate changes (adapted from [Kim et al., 2016]). (b) A typical migratory mesenchymal cell presents a front-back polarity and lacks junctional complexes. At the migration front, RAC1 and CDC42 promote actin polymerization and lamellipodium formation while, in the back, RHOA drives the actomyosin-mediated retraction of the cell rear following the front movement. The Scribble complex is located at the cell front (modified from [Rodriguez-Boulan & Macara, 2014]). (c) In a typical epithelial cell, the polarity complex Crumbs (Crb in blue) and PAR are located in the apical domain, while Scribble (Scrib in green) at the basolateral membranes. Phosphoinosides, proteins regulating their conversion and regulators of the actomyosin cytoskeleton are also asymmetrically polarized along the apical basal axis. Additionally, formation of various junctional complexes (such as tight junctions and adherens junctions) and a polarized intracellular

trafficking are crucial for the maintenance of the compartmentalization of cellular domains (modified from [Rodriguez-Boulan & Macara, 2014]).

1.2.2 Apical-basal polarity establishment

MET transition involves a switch of the polarity axis of the cell, from a front-rear polarity typical of mesenchymal cells to an apical-basal polarity typical of epithelial cells (Figure 1.1 b). In mesenchymal cells, the axis of front-rear polarity is aligned with the direction of migration and the cell front is characterized by high activity of the Rho GTPases RAC1 and CDC42 that triggers actin polymerization, promoting formation of lamellipodia or filopodia. The cell rear is instead enriched in RHOA, which ensures contraction and detachment of the cell rear during migration (Figure 1.1 b). Polarized reorganization of integrins, lipids and of organelles across the cell axis ensures the robustness of the migration. Transition from this configuration to an apical-basal polarity requires a profound remodeling of intracellular organization.

1.2.2.1 The players of the Epithelial Polarity Program

The establishment of apical-basal polarity lies at the very core of epithelial cell functionality and, as such, it is a crucial step during MET. Apical-basal polarity provides cells with specialized membranes that adopt distinct molecular profiles and functionalities: apical membranes, lateral and basal membranes (Figure 1.1 c). Apical membrane faces circumscribed microenvironment such as lumina, lateral membranes are surfaces of cell-cell contact while basal membrane face the extracellular matrix. The generation and maintenance of functionally distinct membranes relies on an epithelial polarity program (EPP). Execution of this program requires asymmetric segregation and local activity of polarity complex proteins, phosphoinositides and Rho GTPases (Figure 1.1 c) [Rodriguez-Boulan & Macara, 2014].

Polarity complex proteins assemble into three main polarity complexes: CRB (Crumbs) PAR and SCRIB (Scribble) complex [Rodriguez-Boulan & Macara, 2014]. The Crumbs complex locates at the apical domain and it is composed of Crumbs, PALS1 and PATJ. The Par complex localizes at tight junctions and includes Par-1, Par-2, Par-3, Par-5, Par-6 and aPKC [Kemphues et al., 1988]. The Scribble complex is instead restricted at basolateral membranes and consist of DLG, LGL and Scribble. In *Drosophila*, another basolateral complex has been identified, the Coracle group, constituted of ezrin, radixin, moesin, Coracle, Neurexin IV and Na+, K+-ATPase [Laprise et al., 2009].

The second class of players contributing to apical-basal polarity establishment are the phosphoinositides, which are known to function as docking sites for cytoplasmic effectors [Gassama-Diagne & Payrastre, 2009]. Localization of distinct phosphoinositide species at specific membrane subdomains, which results from polarized segregation of metabolizing enzymes such as the kinase PI3K and the phosphatase PTEN, leads to asymmetric recruitment of polarity complex proteins. For example restricted production of PtdIns(4,5)P2 by PTEN at the apical membrane contributes to the recruitment of Par6 and aPKC in this location [Martin-Belmonte & Mostov, 2007; Shewan et al., 2011], while

PtdIns(3,4)P2, acts an anchor point for DLG1 at the basolateral membrane [Gassama-Diagne et al., 2006; Peng et al., 2015].

The third class of molecular players involved in the EPP is the family of Rho GTPases, which include RhoA, Rac and CDC42 [Jaffe & Hall, 2005]. Rho GTPases are GTP-binding monomeric signaling proteins that functions as molecular switches, whose local recruitment and activity is regulated by several GEFs (guanine nucleotide exchange factors) and GAPs (GTPase-activating proteins). They represent the key regulators of actomyosin cytoskeleton and, as such, they are implicated in a plethora of functions during establishment of the apical-basal polarity, such as the formation and anchoring of polarity protein complex and junctions, the directional orientation of the axis of polarity, the generation of contractile forces and of specialized apical membranes [Rodriguez-Boulan & Macara, 2014].

A complex reciprocal crosstalk between these core sets of polarity components, which are dynamically recruited or excluded from certain membrane subdomains depending on reciprocal interactions, establishes partitioning of the distinct specialized membranes of apical-basal polarized cells [Bilder et al., 2003].

1.2.2.2 Orientation of the new axis of polarity

Although the restricted recruitment of the epithelial polarity players across the cell axis is the very core of the emerging functional asymmetry in the cell, many aspects of the mechanisms underpinning the establishment of the correct orientation of the axis remain to be elucidated. Specific interactions with the extracellular matrix appear to be important to correctly orient the apical-basal axis of the cell. Cell-extracellular matrix interactions are mainly mediated by integrins, transmembrane receptors that connect the actin cytoskeleton with the extracellular basement membrane [Humphries et al., 2006; B. Lee et al., 2014; Manninen, 2015]. The functional relevance of the interaction with extracellular membrane in this context has been demonstrated for example by the observation that MDCK cysts reorient their apical side from outwards to inwards (toward the cyst lumen) when cultured on a collagen matrix, through a β1-integrin/Rac1/laminin-mediated response [D. M. Bryant et al., 2010; O'Brien et al., 2001; Yu et al., 2005, 2008].

1.2.2.3 Cellular rearrangements associated with the epithelial polarity program

Once an initial asymmetric distribution of polarity components is established, the three players of the EPP act together to amplify it by driving a profound intracellular rearrangement, which involves polarized assembly of junctions and an elaborated cytoskeletal reorganization (Figure 1.1 c). Assembly of junctional complexes such as tight junctions, adherens junctions and desmosomal junctions is important to maintain the compartmentalization of distinct membrane domains and to ensure cell-cell adhesion and communication during assembly of multicellular structures. Tight junctions are sealing junctions located at apical-lateral contact points. Composed of occludins and claudins, they form a physical barrier between apical and basolateral membranes and restrict the paracellular movement of molecules across the epithelium. Adherens junctions are specialized adhesion complexes that consist of E-cadherin, cytoskeleton components and a network of intracellular associated proteins and linkers.

These junctions allow adhesive interactions between adjacent cells by engaging in homophilic interactions and are involved in dynamic changes of cell-cell contacts in stress condition. Desmosomal junctions instead decorate the lateral membrane of the cells where they are linked to the intermediate filament cytokeratins, providing resistance to mechanical stress [Rodriguez-Boulan & Macara, 2014].

The EPP program also guides an elaborate remodeling of the microtubule network and of the actomyosin cytoskeleton. During apical-basal polarity establishment, cells rearrange their microtubule network in a more stable and apical-basal oriented cortical network. Centrosome shifts apically, close to the apical membrane, from where in vertebrate cells the primary cilium assembles, while Golgi re-localizes above the nucleus in a microtubule-dependent process [Bacallao et al., 1989; Gilbert et al., 1991]. Remodeling of actomyosin cytoskeleton during EPP is crucial for shaping of functional apical membranes. Apical constriction and apical emergence are examples of process that relies on a polarized actomyosin activity. During rosette neuromast formation in the lateral line primordium, FGF signaling induces apical recruitment and activation of Rho-associated kinase Rock2a, leading to actomyosin-mediated constriction of the cell apex [Harding & Nechiporuk, 2012]. In *Xenopus* mucociliary epithelia instead, radial intercalation of progenitor cells from the basal layer into the pre-formed tissue, relies on an actin-based pushing force exerted by the apical surface of the integrating cell [Sedzinski et al., 2016]. Moreover, establishment of specialized structures such as microvilli also requires assembly of bundles of actin filaments and actin-mediated motility is involved in brush border maturation [Meenderink et al., 2019].

Finally, to maintain the correct segregation of polarity components, polarization of the intracellular trafficking is required. Targeted delivery of apical and basolateral components is achieved by intracellular sorting mechanisms, that act directly after biosynthesis or during recycling and transcytotic routes. Both actomyosin cytoskeleton and microtubule network are crucially involved in the establishment of this vectorial transport [Rodriguez-Boulan & Macara, 2014].

1.2.3 Stabilization of epithelia phenotype

Although multiple cycles of EMT-MET are often required during morphogenetic processes in development (see section 1.3.2), ensuring stabilization of the newly acquired epithelial features is also crucial for epithelial functions. As such, mechanisms acting as gatekeeper to protect the epithelial phenotype are redundant and tightly regulated at different levels [Pei et al., 2019]. Stabilization of epithelial phenotype involves a complex integration of epigenetic modifications [Bedi et al., 2014], expression and regulation of transcription factors (TF), post-transcriptional and post-translational regulation [Pei et al., 2019; Tam & Weinberg, 2013]. These mechanisms can act as stabilizer of the epithelial phenotype or as repressor of mesenchymal phenotypes. The epithelial-specific protein 1 and 2 (ESRP1, 2) for example promote an alternative splicing program that reinforce epithelial features of the cells [Warzecha & Carstens, 2012]. The transcription factors Ovol1 and 2 protect epithelial phenotype by repressing expression of several EMT-TF and other mesenchymal-associated genes in

mammary gland [Watanabe et al., 2014], in human corneal epithelium [Kitazawa et al., 2016] and in mouse embryonic epidermal cells of the skin [B. Lee et al., 2014]. Some transcription factors drive both an active suppression of mesenchymal-related genes and an activation of transcription of epithelial-related genes. For instance, Grainyhead-like 2 (GRHL2) enhances transcription of ectoderm-specific proteins E-cadherin and Claudin4 during neural tube closure [Ray & Niswander, 2016]. Moreover, together with Ovol2, GRHL2 is involved in repression of ZEB1, one of the EMT-TF [Frisch et al., 2017] and in activation of expression of epithelial junctional complex proteins during kidney development [Aue et al., 2015]. Other factors involved in the protection of the epithelial phenotype are the proteins ELF5, p53, EZH2, ubiquitin ligases [Chakrabarti et al., 2012; Chang et al., 2011; S. S. Wang et al., 2015; H. Yang et al., 2015] and components of the miRNA family miR-200 [Chung et al., 2016; Lamouille et al., 2013; Nieto et al., 2016].

At the tissue level, the establishment of apical-basal polarity functions as a key checkpoint to protect the epithelial phenotype [Jung et al., 2019]. A recent study in 3D epithelial organoids indeed demonstrated that, in fully apical-basal polarized cells within the epithelium, apical Par3/aPKC complex induces SNAI1 degradation, preventing induction of EMT and metastatic dissemination of cells [Jung et al., 2019]. Furthermore, epithelial stability might be strengthened by stress-induced reinforcement of cell-cell junctions and assembly of supra-cellular actomyosin cables, that enhance mechanical stability of the epithelium [Hoffman & Yap, 2015; Kim et al., 2016; Leckband & de Rooij, 2014; Röper, 2013]. For instance, tensile stress in epithelial monolayers stimulates Myosin V-dependent RhoA activity and recruitment of the formin mDia1 at adherens junctions, leading to junctional reinforcement [Acharya et al., 2018].

Finally, MET is often associated to profound cellular changes leading to metabolic, epigenetic and cell fate switches [Pei et al., 2019]. Cell fate specification in particular might represent a strategy to ensure ‘lockdown’ of cells in the newly established epithelial phenotype [Wong & Gilmour, 2020].

1.3 How is MET integrated in developmental programs?

1.3.1 A spectrum of phenotypes

EMT and MET were classically thought to operate as binary switches from a stationary epithelial cell to a motile mesenchymal cell or vice versa. However, a large body of evidence in the last decade have unveiled that the transition between these two cellular states is often incomplete, leading to the emergence of several intermediate cellular phenotypes, called ‘partial’ or ‘hybrid’ EMT states [Campbell & Casanova, 2016; Yang et al., 2020]. These hybrid states can be arrayed along a continuum spectrum of cell phenotypes, depending on the combination of epithelial and mesenchymal features they present. Fully mesenchymal and fully epithelial phenotypes represent only the extreme ends of this spectrum and, as a norm, cells display hybrid phenotypes. Likewise, full transitions from one to

the other extreme of the spectrum are rare, while commonly losses and gains of epithelial features determine the degree of progression along the spectrum. The ability of cells to move fluidly between phenotypes is termed 'epithelial-mesenchymal plasticity' [Yang et al., 2020].

Previous emphasis was placed on defining EMT and MET according to the loss and gain of a limited set of epithelial and mesenchymal markers. Examples of molecular and cellular descriptors used as markers for mesenchymal cells are N-cadherin, vimentin and expression of transcription factors such as SNAIL, TWIST and ZEB, while for epithelial cells E-cadherin, keratins, adherens and tight junctions [Nieto et al., 2016]. However, these markers alone often do not accurately reflect the complex orchestration of EMT and MET programs. It has been observed that crucial steps of EMT, such as the loss of apical-basal polarity and the dissolution of junctions can be implemented using a wide range of strategies, strictly dependent on the biological context. Examples of this are the various mechanisms leading to cell dissociation from the original tissue during EMT. While in many systems the transcriptional repression of adherens junction proteins is a key step of cellular dissociation, it was observed that neural crest cells occasionally lose their junctional complexes by shedding their apical membranes and leaving the apical fragments behind while retracting from the original neuroepithelium and migrating away [Ahlstrom & Erickson, 2009]. Furthermore, not only transcriptional downregulation but also post-translational modifications of key proteins such as E-cadherin can affect the adhesive properties of cells and lead to dissociation [Yang et al., 2020].

Concurrently, in different biological contexts, changes in the same molecular marker can lead to different functional consequences. For example, the transcriptional repression of E-Cadherin has been considered for long a critical step in EMT because of the conserved role of E-cadherin in maintaining adherens junction. However, several recent findings suggest that the relationship between E-Cadherin and the mesenchymal state is more complex. It was indeed found that E-cadherin is required for migration of mesenchymal endodermal cells during gut formation [Campbell & Casanova, 2016] and for border cell migration through nurse cells during oogenesis in *Drosophila* [Cai et al., 2014]. Moreover, cells can adopt migratory mesenchymal features while actively transcribing E-Cadherin [Campbell et al., 2011; Campbell & Casanova, 2015]. Another classical landmark of EMT is the switch in cadherin expression from E to N. More recent studies on *Xenopus* neural crest cells showed that the switch to N-cadherin is not required for the EMT or for dissociation from the original tissue but is instead essential for repulsion between contacting cells (through so-called 'contact inhibition of locomotion') that drives neural crest migration [Scarpa et al., 2015].

The challenge in identifying a reliable set of universal markers reflects the fact that EMT and MET are functional transitions. The steps and the mechanisms involved in the transition thus depend on the features of the tissue of origin and from the degree of transition required to fulfill a certain biological function. In some cases, cells undergoing EMT migrate as single entities to disseminate far away from the original epithelium (for instance neural crest cells). In other cases, cells undergo EMT without losing cell-cell adhesion and tissue cohesion and migrate as collectively migrating tissues (for instance lateral line primordium and sprouting angiogenesis). This collective migrating configuration enables cells to tightly coordinate the elongation of the tissue with the assembly of functional structures. Similarly, some MET transitions involve single progenitor cells integrating into an overlaying epithelium, while,

in other contexts, large cohorts of cells aggregating into an epithelium and establishing apical-basal polarity *de novo*.

A more integrative approach that combine analysis of molecular, morphological, functional and behavioral features appears thus crucial to assign cells along the phenotypic spectrum and to better explore the emergent properties of hybrid states, which appears to be relevant in several contexts. The acquisition of hybrid phenotypes can indeed provide important advantages to cells, such as circulating tumor cells [Lorentzen et al., 2018]. By retaining their apical poles while displaying migratory behavior, circulating tumor cells can adhere and 'home' more efficiently into other tissues. The hybrid state in this context seems to enhance the metastatic potential of the cells. Another recent study showed that in human mammary epithelial cell culture, cells induced to a hybrid EMT state though expression of the transcription factor ZEB1 are less contractile and migrate faster than both fully epithelial or mesenchymal counterparts [Margaron et al., 2019], indicating that hybrid 'intermediate' phenotypes do not necessarily display intermediate properties.

However, several aspects of hybrid EMT states remain to be elucidated, such as whether the phenotypic spectrum is a true continuum or instead a sequences of discrete entities and how stable and important these phenotypic states are in different tissue contexts [Yang et al., 2020].

1.3.2 EMT-MET cycles

One of the key features of epithelial-mesenchymal plasticity is its reversibility with cells often undergo through cycles of sequential EMT and MET transitions [Yang et al., 2020]. A classical process that involves sequential EMT-MET is heart development. The heart develops from mesodermal heart precursors that undergo EMT, ingress through the primitive streak during gastrulation and migrate in the lateral plate mesoderm, where they undergo MET and assemble two bilateral heart fields. Following the coalescence of these two territories into a single heart tube at the ventral midline, a second and third cycle of EMT-MET drive respectively the establishment of endocardium and epicardium layer [Abu-Issa & Kirby, 2007; Lim & Thiery, 2012; Sugi & Markwald, 1996]. Therefore, EMT-MET cycles enable cells to migrate for long distances to their target location and to contribute to several tissues and cell types.

Work on *in vitro* somatic cell reprogramming and differentiation shed a new light on the relevance of EMT-MET cycles, suggesting that the transition through a mesenchymal state is important for cell decision-making. During somatic cell reprogramming, application of a cocktail of transcription factor known as Yamanaka factors [Takahashi & Yamanaka, 2006], leads to reprogramming of mesenchymal somatic cells into epithelial pluripotent stem cells [Hansson & Chien, 2012; Li et al., 2010]. MET was found to be a prerequisite for reprogramming of several somatic cell types, such as mouse embryonic fibroblasts, human adult fibroblasts, cultured B cells, hematopoietic and spermatogonial stem cells [An et al., 2017; Di Stefano et al., 2014; Gao et al., 2016; X. Liu et al., 2013; Subramanyam et al., 2011]. However, it was shown that induction of EMT at early stages of reprogramming, prior to MET, further

enhances reprogramming efficiency compared to exclusive induction of MET in some cell types [Di Stefano et al., 2014; X. Liu et al., 2013].

There is growing evidence that an EMT-MET sequence is also important for *in vitro* differentiation [Li et al., 2017]. The transition of human embryonic stem cells through an intermediate mesenchymal state before MET is required for hepatic lineage commitment [Li et al., 2017], reflecting the EMT-MET sequence observed during liver development *in vivo* [Choi & Diehl, 2009]. Therefore, the transit through a mesenchymal phase appears to be a crucial crossroad for cell fate choice at early phases of both pluripotency reprogramming and differentiation, although the molecular mechanisms at the basis of it are still unknown. It has been speculated that an initial pulse of EMT might promote cell synchronization or ensure that cells are in an 'optimal mesenchymal state' more permissive to reprogramming [Pei et al., 2019; Shu & Pei, 2014] by affecting the epigenetic landscape of cells [Li et al., 2017]. Exploring whether a transient EMT step plays a similar role in cell fate decisions *in vivo* remains an important future challenge.

1.3.3 Propagation of MET across tissues

A fundamental question raising from the study of MET in multicellular systems is how MET transition propagates across tissues. More precisely, what are the components and the regulatory networks involved in driving the spreading of epithelial polarity? Is epithelialization executed entirely cell-autonomously or a coordinated collective behavior? How do cells that undergo MET affect the organization of surrounding cells? Currently, the mechanisms underpinning the spreading of epithelialization *in vivo* are poorly understood, mainly due to the limited *in vivo* accessibility to the process in real-time. Based on observations from the available systems, a set of hypothetical modes of MET propagation have been suggested. They can be loosely classified as single-cell MET and collective MET (Figure 1.2) [Kim et al., 2016].

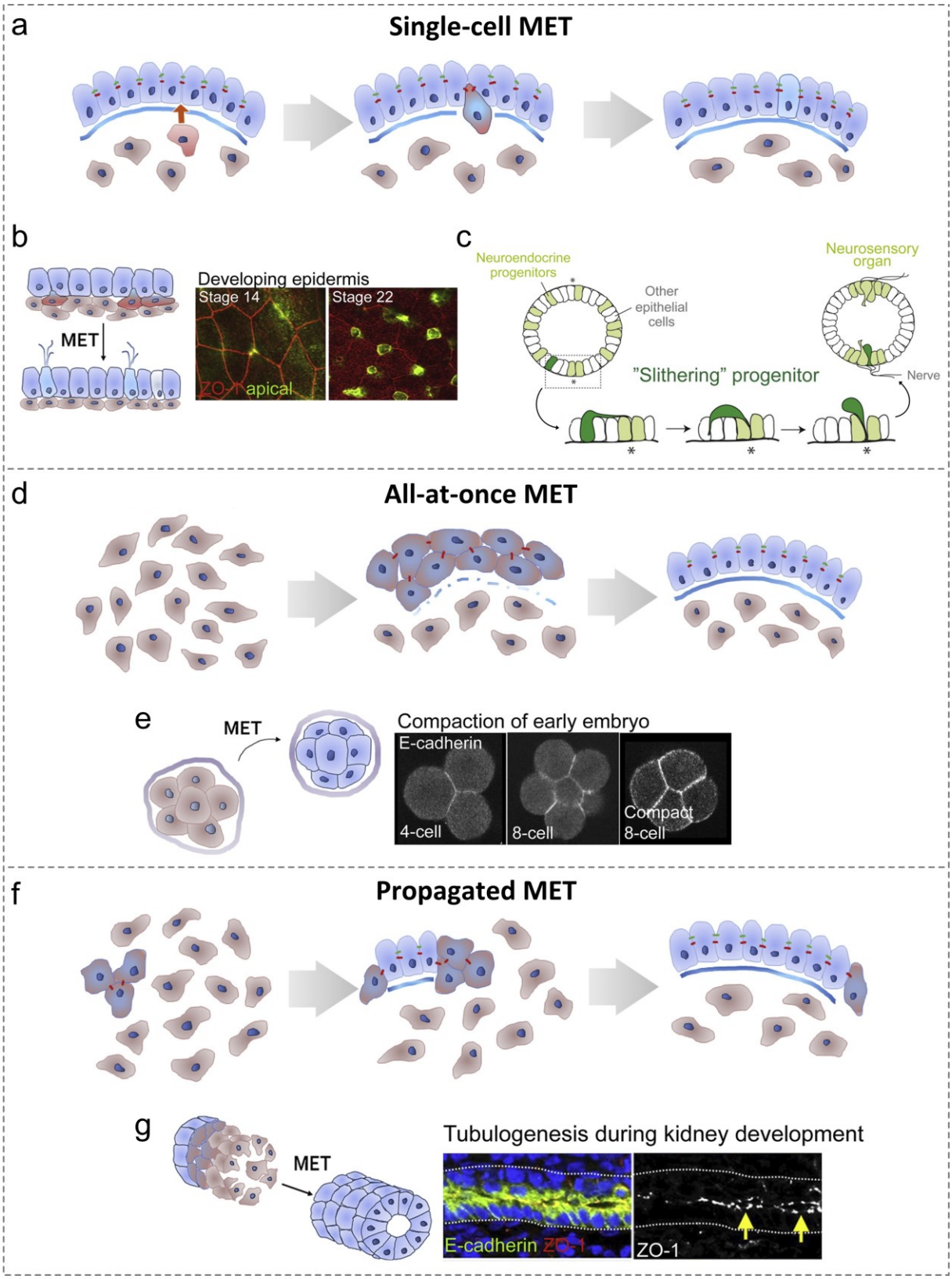

Figure 1.2: Hypothetical modes of MET propagation

(a) In the single-cell MET, individual mesenchymal progenitors undergo MET transition by inserting into a pre-existing epithelium, giving rise, for example, (b) to multiciliated cells in the Xenopus developing epidermis (adapted from [Kim et al., 2016; Stubbs et al., 2006]) (c) A particular case of single-cell MET occurs during the cell

slithering process that drives the formation of neurosensory organs in the mouse lung. Here, individual neuroendocrine progenitors adopt a mesenchymal state, which enables them to delaminate from the epithelium of origin and migrate on top of the neighboring cells. The cells would then reintegrate into the epithelium of origin and re-epithelialize several cell diameters away where other neuroendocrine progenitors are located, forming a new neurosensory organs [Kuo & Krasnow, 2015; Noguchi et al., 2015] (adapted from [Kim et al., 2016; Kuo & Krasnow, 2015]). (d) The all-at-once MET is a modality of collective MET where cells undergo MET transition simultaneously, (e) for example during compaction of the 8-cell stage mouse embryo (adapted from [Kim et al., 2016; Thomas et al., 2004]). (f) The propagated MET is a modality of collective MET where epithelialization progressively spreads across the mesenchymal pool from a 'seed' of few initiator cells, (g) such as during formation of the kidney tube in the chicken embryo. The yellow arrows indicate the assembled lumen (adapted from [Atsuta & Takahashi, 2015; Kim et al., 2016]). In the schematics, the blue color indicates an epithelial phenotype, the brown color a mesenchymal phenotype and shades in between represent a 'hybrid' phenotypic state.

1.3.3.1 Single-cell METs

Single-cell MET occurs when a single independent cell intercalates into a pre-formed epithelium and adopt the epithelial features of the neighboring cells (Figure 1.2 a). MET, in this case, is exploited to either maintain or expand an epithelium or to populate it with specialized cells. This strategy is employed during homeostatic replenishment of multilayered epithelia such as airway, tracheal, corneal and olfactory epithelia [Evans et al., 2001; Y. F. Leung et al., 2007; Rock et al., 2009], which rely on a basal pool of a mesenchymal progenitor cells for epithelial renewal. In other contexts, single-cell MET is at the basis of the radial intercalation of specialized cell subtypes into the epithelium (Figure 1.2 b), such as multiciliated cells and other accessory cells forming the epidermis of the *Xenopus* embryo [Dubaissi et al., 2014]. Multiciliated cells are derived from a basally located mesenchymal pool and insert into the overlaying epithelial sheet through a cell autonomous process of apical emergence [Sedzinski et al., 2016]. Similarly, during renal tubulogenesis in *Drosophila*, mesenchymal cells from the caudal visceral mesoderm basally integrate within the pre-formed tubule by undergoing MET and differentiate into stellate cells [Campbell et al., 2010].

1.3.3.2 Single-cell EMT-MET during 'slithering'

A form of single-cell MET is involved in the regular pattern of assembly of sensory organs, for example the neuroendocrine mini-organs in the mouse lung (NEB) [Kuo & Krasnow, 2015; Noguchi et al., 2015] and the taste buds in zebrafish [Kapsimali, 2017; Soulika et al., 2016]. Formation of NEBs is a multistep process that engages cells in a single-cell EMT-MET cycle and involves a modality of cell migration called 'slithering' (Figure 1.2 c). First, neuroendocrine cells (NE) transiently adopt a mesenchymal phenotype to dissociate from the bronchial epithelium and slither on the apical sides of neighboring cells. Second, migrating NE cells reintegrate into the bronchial epithelium at airway branch junctions and re-epithelialize forming clusters of NE cells [Kuo & Krasnow, 2015; Noguchi et al., 2015]. Progressive addition of NE cells gives rise to mature NEB clusters. The process is accompanied by changes in expression of transcription factors, polarity and adhesion proteins consistent with a transient EMT transition followed by a MET [Kuo & Krasnow, 2015].

1.3.3.3 Collective METs

In collective METs, multiple cells are engaged in the MET transition in a coordinate manner. Depending on the modality of cellular engagement, collective MET can be described as 'all-at-once MET' or as 'propagated MET'. In the all-at-once MET, a group of cells aggregate and undergo a simultaneous MET (Figure 1.2 d). Coordination of the onset of MET might rely on cell non-autonomous cues, such as a homogeneous tension exerted from a fluid [Chan et al., 2019], from compaction or from extraembryonic membranes [de Vries et al., 2004; Münster et al., 2019]. Compaction is the developmental process by which cells participating in a 'grape-like' cluster tighten into a more packed structure [Turlier & Maître, 2015]. In the 8-cell stage mammalian embryo, an E-cadherin-dependent compaction drives homogeneous MET of the loosely adhesive blastomeres by spreading cell-cell contacts area, flattening the outer surface of the cells and establishing apical basal polarity (Figure 1.2 e) [Fleming & Johnson, 1988; Kim et al., 2016; Maître et al., 2015].

In a propagated MET, a few initiator cells undergo MET at first and the transition subsequently spreads from them across a mesenchymal pool by progressive recruitment of neighboring cells (Figure 1.2 f). Some initiatory 'leader' cells are thus sufficient to seed epithelialization and to propagate it to 'follower' cells. It has been proposed that propagated MET is involved in a variety of tubulogenesis processes in development [Kim et al., 2016]. During Wolffian duct morphogenesis in chicken embryo, for example, a progressive epithelialization wave across the collectively migrating kidney progenitors drives assembly of a tubular structure equipped with luminal tight junctions and E-cadherin (Figure 1.2 g) [Atsuta & Takahashi, 2015; Attia et al., 2015].

Mechanisms underpinning the inter-cellular transduction of polarity information are still mostly unexplored. Intriguingly, it has been suggested that mechanical traction and cellular mechanosensing might be involved in MET propagation [Kim et al., 2016]. Recent studies on collectively migrating tissues and on hindgut formation seem to support this idea [Nerurkar et al., 2019; Petridou et al., 2017]. In the chick embryo, elongation of the hindgut tube relies on a directional collective movement of connected endodermal cells, which is coordinated by an FGF8-mediated contraction gradient. By reaching the domain with high level of FGF8, endodermal cells contract and, while doing so, they actively drag connected neighbor cells into the 'contractile' FGF region and the contraction wave propagates progressively. Therefore, the interplay of inter-cellular coupling together with an FGF gradient drives recruitment of new cells in the forming hindgut and progressive cell tightening and packing [Nerurkar et al., 2019].

1.3.3.4 Lumen formation and MET

Establishment of apical-basal polarity and MET are often coupled with lumen formation, for example during formation of tubular networks (such as the ureteric bud or tracheal intercellular tubes) or hollow structures (such as the Kupffer's vesicle). Two main mechanisms underlying *de novo* lumen formation associate with MET [Marciano, 2017]: 'hollowing' and 'cavitation'. During hollowing, specific apical vesicles are exocytosed directionally at cell-cell contact points and their fusion leads to *de novo* formation of a central lumen. In cavitation, selective apoptosis of the innermost cells in a solid cellular

mass determines formation of a hollow lumen and apical-basal polarization of cells surrounding it. The first mechanism is observed in early kidney tubulogenesis [Marciano, 2017], while the second one in mammary acini and salivary gland development [Debnath & Brugge, 2005].

An important model system for lumenogenesis are MDCK cells, a 3D epithelial culture model assembling monoclonal cysts from single plated cells. Interestingly, studies on MDKC cells showed that cells employ cavitation and hollowing complementarily depending on the contexts. While plating cells in matrigel leads to hollowing, the use of a loosely polarizing matrix such as collagen leads instead to cavitation, suggesting that cavitation is a corrective mechanism if the rate of cell polarization is too slow [Marciano, 2017].

In the process of hollowing of MDCK cysts, axis of cell division plays a pivotal role in orienting apical polarity. Following a first round of mitosis, MDCK cells display an inverted polarity with apical proteins such as Crumbs and Podocalyxin facing the ECM. At 2-cell stage, the axis of polarity reorients to the site of cytokinesis and apposition between the two daughter cells, the so called midbody region [D. M. Bryant et al., 2010, 2014; Ferrari et al., 2008]. This reorientation occurs via transcytosis and recruitment of apical domain proteins to a forming apical patch in the midbody region, followed by opening of a *de novo* lumen at the interface between the two cells and its progressive expansion. Misorientation of the division axis or mislocalization of the midbody lead to abnormal lumen or multiple lumen phenotypes [Jaffe et al., 2008]. Once initiated, the forming lumen can further expand through cell division and accumulation of fluid [D. M. Bryant et al., 2010]. In addition, electrostatic repulsion mediated by exposure of negatively charged molecules at the apical membrane (such as Podocalyxin) might be implicated in induction or maintenance of lumina through their anti-adhesive properties [Shahbazi et al., 2017]. In mouse embryogenesis, MET is accompanied by formation of a lumen through hollowing during the reorganization of the inner cell mass into a rosette-shaped structure [Bedzhov & Zernicka-Goetz, 2014].

1.4 Cell sorting

One of the most prominent features of development is the capability to coordinate the spatial segregation of cells into distinct domains. A classical example of this process is the lineage segregation occurring in early mouse blastocysts (Figure 1.3 b). Here, progenitors of the primitive endoderm are specified stochastically in the inner cell mass, in a 'salt and pepper' pattern [Hermitte & Chazaud, 2014]. At 64-cell stage, these progenitors sort from epiblast cells and migrate at the interface with the blastocoel cavity, where they form the primitive endoderm, an epithelial layer marked by tight junctions and apically localized aPKC [Meilhac et al., 2009; Plusa et al., 2008; Saiz et al., 2013]. What are the mechanisms at the basis of cell segregation? Fundamental advances in the study of cell sorting come from *in vitro* studies of intermixed cell populations. Studies on dissociated amphibian embryonic cells pioneered by Holtfreiter showed that mixtures of cells obtained from different embryonic tissues are able to spontaneously sort into homotypic domains when re-aggregating (Figure 1.3 a), mirroring the relative spatial organization of tissues observed *in vivo* [Townes & Holtfreter, 1955]. Partitioning into homogeneous domains was also observed in aggregates of germ layer progenitors obtained from hydra, zebrafish embryos and *Rana Pipiens* [Davis et al., 1997; Foty et al., 1996; Rieu et al., 1998]. The finding that cells can discriminate the identity of their neighbors and segregate depending on a certain 'cell affinity' [Townes & Holtfreter, 1955] led Steinberg to formulate the idea that cells behave like molecules of immiscible fluids and that differences in tissue surface tension underlie the sorting of cells, predicting that cells with similar surface tension would co-segregate and that lower surface tension-cell regions would encircle higher surface tension-cell regions [Foty & Steinberg, 2005].

Various theoretical models have been proposed to explain differences in tissue surface tension underlying sorting. In the 'Differential Adhesion Hypothesis' (DAH) hypothesis, Steinberg proposed that intercellular adhesion strength was sufficient to explain cell segregation into homotypic domains and their relative positioning [Foty & Steinberg, 2005; Steinberg, 1970]. The DAH model was later expanded by the recognition that cortical tension, generated by the contractile actomyosin cytoskeleton, is a crucial contributor of tissue surface tension [Harris, 1976], resulting in the formulation of the Differential Interfacial Tension hypothesis (DITH) [Brodland, 2002]. According to this integrated model, the interplay of cell-cell adhesion and cortical contractility is at the basis of the tension generated at cell-cell and cell-medium interfaces and the formation and stability of cell contacts depends on the antagonism of these two players [Brodland, 2002; Maître, Salbreux, et al., 2012].

At the molecular level, sorting could result, for example, from differential expression levels of a certain cadherin, as suggested for the segregation of intermixed fibroblast cells presenting different levels of N-cadherin and for the interaction of oocytes with follicle cells in *Drosophila* [Foty & Steinberg, 2005; Godt & Tepass, 1998]. In other cases, sorting might result from the expression of different sets of adhesion molecules at the surfaces of different cell types [Miyatani et al., 1989; Nose et al., 1988]. Based on the assumption that homophilic bindings are preferred to heterophilic ones, the expression of distinct cadherin subtypes has been suggested to mediate the segregation of neuronal populations in the mouse telencephalon, of motoneurons in the chick spinal cord and, more recently, of neural

progenitors in the zebrafish spinal cord [Inoue et al., 2001; Price et al., 2002; Tsai et al., 2020]. Differences in cortical tension, however, have been proposed as the major contributors to interfacial tension in several contexts, such as the segregation of zebrafish germ-layer progenitors *in vitro* and in mammalian trophectoderm segregation (Figure 1.3 c) [Krieg et al., 2008; Maître et al., 2012; Maître et al., 2016]. Indeed, during the 8 to 16 cell-stage transition of the mammalian blastocyst, blastomeres segregate in an outer position or in an inner position depending on differences in their actomyosin contractility, generated by asymmetric inheritance of a non-adhesive apical domain during division [Maître et al., 2016]. While highly contractile cells are internalized as precursors of the inner cells mass, the lower contractile outer cells (that inherited the apical domain) give rise to the trophectoderm layer, the first epithelium formed in the embryo, which establishes tight and adherens junctions that seal the embryo [H. Wang et al., 2008; Zenker et al., 2018].
Various other cell properties and mechanisms have been suggested to contribute to cell sorting, such as differential cell motility [B. M. Jones et al., 1989], directed migration [Krens et al., 2017; Townes & Holtfreter, 1955], cell repulsion at heterotypic cell contact interfaces [Fagotto et al., 2013]. This latter modality in particular seems to be important to sharpen boundaries forming between tissues, via a process mediated by Ephrin/Eph signaling-dependent increase in interfacial tension at heterotypic interfaces [Canty et al., 2017; Rohani et al., 2011]. In addition, a recent preprint investigating primitive endoderm sorting in mouse blastocyst suggested that differences in surface fluctuations between prospective endoderm cell and epiblast cells, namely an increased blebbing behavior of the former, could be implicated in the sorting of the two lineages [Yanagida et al., 2020].

The technological advances in genetic perturbation and measurement techniques developed in the last decade have enabled the access to intact organisms for the investigation of sorting mechanisms. However, some discrepancies observed between *in vivo* and *in vitro* assays raised the important question of whether and when the sorting potential of cells is relevant for developmental processes [Krens & Heisenberg, 2011]. To what extent are the modalities of sorting identified *in vitro* actually employed *in vivo*? For instance, differences in tissue surface tension were shown to drive segregation of zebrafish germ layer progenitors in an *in vitro* re-aggregation assay, but not *in vivo*, where directed migration appeared instead to be the major contributor of the sorting process and no difference in tissue surface tension could be detected [Krens et al., 2017]. The authors suggested that the incongruence in term of tension between the *in vitro* and *in vivo* systems could be explained by the different osmolarity of the culture medium compared to the interstitial fluid present in the embryonal physiological context [Krens et al., 2017]. This and other studies highlights the importance of assessing differential tissue surface tension *in vivo* and investigating the influence of sorting during development of intact organisms [Krens & Heisenberg, 2011; Ninomiya et al., 2012].
Another fundamental question with respect to cell sorting *in vivo* is how is sorting reliably controlled during development, to give rise to reproducible patterns. Cell sorting is indeed often accompanied by cell fate changes, state transition, boundary formation and other morphogenetic processes. It has been suggested that, in the mouse inner cell mass, the sorting of the prospective primitive endoderm cells might be driven by their progressive polarization and epithelialization, occurring as cells acquire

an endodermal identity through a FGF-dependent increase of ERK signaling [Hermitte & Chazaud, 2014; Moore et al., 2009]. In addition, a recent study demonstrated that, in the zebrafish spinal cord, cell type-specific cadherin expression is regulated, together with cell fate specification, by the Sonic hedgehog morphogen gradient, suggesting that an interplay between the classical morphogen-based model and the tuning of cell adhesive properties might enhance robustness in patterning [Tsai et al., 2020].

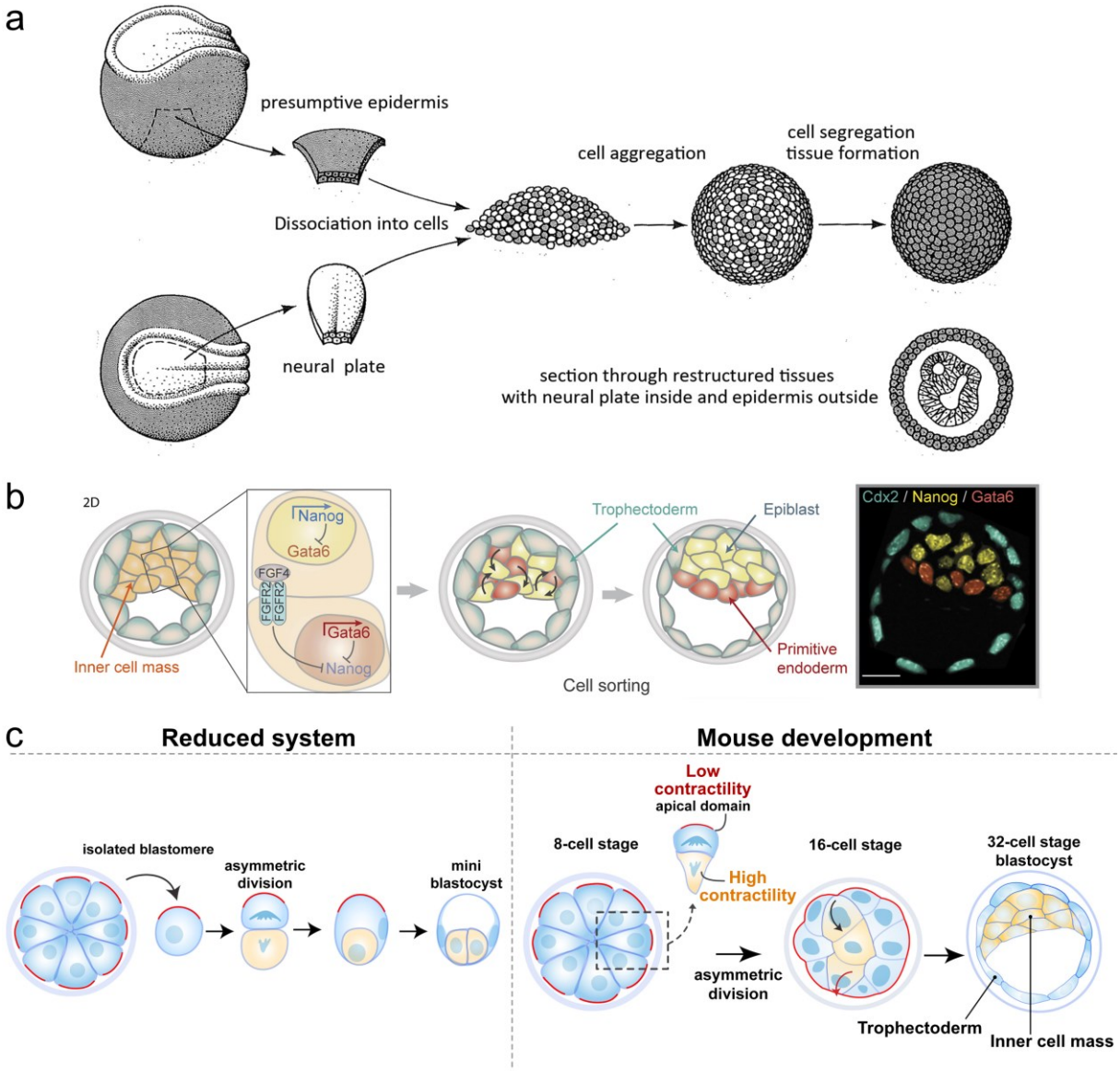

Figure 1.3: Cell sorting

(a) In their pioneering experiments, Townes and Holtfreter observed that dissociated cells derived from different amphibian tissues spontaneously re-segregate into homotypic domains after mixing (adapted from [Heisenberg, 2017; Townes & Holtfreter, 1955]). (b) In the inner cell mass of the mouse blastocyst, precursors of primitive endoderm and of epiblast initially specify in a salt and pepper pattern in an FGF signaling-dependent mechanism and later sort into homotypic cell domains, forming the primitive endoderm and the epiblast (modified from [White et al., 2018]). (c) Schematic representing the first lineage segregation event during mouse pre-implantation development. The process is recapitulated during the formation of mini-blastocysts, a simplified

experimental system obtained by the isolation of individual blastomeres from 8-cell stage embryos. Apical domains form at contact-free surfaces of blastomeres and their asymmetric inheritance during cell division impacts cell contractility and sorting. Low contractile cells inheriting the apical domain tend to segregate to outer position within the blastocyst, while highly contractile apolar cells move to inner positions, becoming respectively trophectoderm and inner cell mass (modified from [Srinivas & Rodriguez, 2017]and referred to [Korotkevich et al., 2017; Maître et al., 2016]). Scale bar (b) 10 µm.

1.5 FGF signaling

1.5.1 The FGF signaling axis

Fibroblast growth factor receptor (FGFR) and its ligand fibroblast growth factor (FGF) play pivotal roles for cell-cell communications in a plethora of biological contexts, from development to homeostasis, regeneration and disease. Belonging to the group of tyrosine kinase receptors, FGFRs are a family of single-pass plasma membrane proteins that is highly conserved across phyla, from metazoans to humans. FGFR is activated upon binding secreted fibroblast growth factor (FGF) ligands. In humans, 4 FGFR and 22 FGFs are encoded. The human FGFR has an extracellular domain, which is composed of three immunoglobulin-like subunits (Ig from I to III), a transmembrane domain and two intracellular kinase domains (Figure 1.4 a). FGF ligand binds Ig-II and Ig-III domains. The FGFR kinase domain presents a typical bi-lobed structure with a binding site for ATP at the lobe interface, which toggle the kinase between an open and closed configuration [Dai et al., 2019] during catalytic cycles. Upon binding of FGF ligand, FGFR dimerizes and juxtaposition of tyrosine kinase domains enables trans-phosphorylation of tyrosine residues at the C-terminal tails, which constitute multiple docking sites for several adaptor and effector cytoplasmic proteins, that in turns trigger intracellular signaling pathways [Hubbard & Miller, 2007]. Four main intracellular signaling cascades are activated by FGFR phosphorylation: Ras/MAPK, PLCγ/Ca^{2+}, the PI3K/AKT and STAT pathway. FRS2alfa phosphorylation and binding of GRB2 are the first steps of Ras/MAPK and PI3K/AKT cascade triggering (Figure 1.4 a) [Kouhara et al., 1997]. The Ras/MAPK pathway activates transcription factors that induce expression of FGF-specific target genes such as pea3, while PI3K/AKT promotes cell proliferation by inactivating FOXO1 transcription factors and activating mTOR complex [Manning & Cantley, 2007]. PLCγ activation induces an increase in calcium concentration and activates PKC [Dudka et al., 2010; Peters et al., 1992]. Activation of proteins of the STAT family, finally, also results in expression of FGF-specific target genes [Su et al., 1997].

1.5.2 Regulation of FGF signaling in tissues

Several regulators and mechanisms tightly tune FGF signaling at different levels. A first level of control is the accessibility of the FGF ligand. FGF is one of the main morphogens during development and thus its distribution and levels need to be tightly regulated, as they encode crucial information involved in cellular decision-making [Makarenkova et al., 2009; Shimokawa et al., 2011]. Diffusion of secreted FGF in the extracellular matrix is limited by high affinity binding to heparin sulfate (HS) [Matsuo & Kimura-Yoshida, 2013; Ornitz, 2000; Yayon et al., 1991]. HS are long polysaccharidic chains of the ECM that can be bound to core proteins (proteoglycans, HSPG), associated to cell surfaces or secreted in the ECM. HSPG intrinsic regulation (expression, secretion and cleavage) and differential affinity with different FGFs are thus crucial for establishment of extracellular FGF gradients and together tune the range of action of FGF ligands [Makarenkova et al., 2009; Shimokawa et al., 2011]. Indeed, canonical FGFs mostly have a paracrine or autocrine range of action, while only the subfamily of FGFs that displays a very low affinity for HSPG presents an endocrine range [Goetz et al., 2007]. Reduced

diffusion of FGF by HSPG-dependent retention might be crucial to generate local spikes in FGF concentration required in some biological contexts, for example during joint formation. Indeed, expression of a mutated version of FGF9, whose affinity with HSPG is reduced, results in defective joint formation [Harada et al., 2009; X. lin Wu et al., 2009]. Assembly of enclosed extracellular spaces wherein FGF ligands are trapped, such as microlumina in the zebrafish lateral line primordium [Durdu et al., 2014] or the fluid-filled cavity of the mouse blastocyst [Ryan et al., 2019] represents another strategy to restrict the access of the FGF ligand to a specific subset of cells. In addition, FGF can be sequestered by binding decoy receptors lacking the intracellular kinase domain, such as FGFRL1 [Trueb, 2011] or secreted forms composed exclusively of the extracellular domains of the receptor Ig-II and III [Duan et al., 1992; Tomlinson et al., 2005]. Binding with other secreted proteins such as FGFBP1 contributes instead to the mobilization of the HS-trapped FGF pool [Czubayko et al., 1997]. Other strategies to regulate FGF, particularly important for gradient formation, are the control over FGF secretion, its endocytosis and intracellular trafficking [Peterson & Krasnow, 2015; Yu et al., 2009].

A second level of control is FGFR. While the extracellular domain Ig-II and III of the receptor are responsible for the binding of FGF, an auto-inhibition mechanism relies on Ig-I and a conserved acidic box (located between Ig-I and Ig-II), which suppress FGF and HSPG binding [Kalinina et al., 2012]. Ligand-binding specificity can be tuned through alternative splicing of the Ig-III domain of FGFR1-3, increasing even more the combinatorial possibilities of the system [Chellaiah et al., 1994; Werner et al., 1992]. Interaction with HSPG also regulates FGF-FGFR complex formation by increasing affinity between FGF and FGFR [Matsuo & Kimura-Yoshida, 2013] and by regulating the binding specificity [Matsuo & Kimura-Yoshida, 2013; Ornitz, 2000; Yayon et al., 1991].
Regulation of FGFR synthesis, exposure at the plasma membrane, degradation and subcellular trafficking is also important for modulation of FGF signaling and depends on interactions with specific intracellular adaptors, kinases and phosphatases [Francavilla et al., 2013]. Classically, upon FGF ligand binding, FGFR undergo endocytosis, ubiquitination and degradation in the lysosome [Wong et al., 2002]. Different proteins can functionally interact with FGFR and affect its stability, including NCAM and N-cadherin (NCAD) [Cavallaro & Christofori, 2004]. NCAM is a surface glycoprotein of the Ig superfamily composed of five Ig-like domains and two Fibronectin type II modules [Hinsby et al., 2004] that drives cell-cell adhesion through homophilic and heterophilic binding in cis and trans. Its functional interaction with FGFR has been reported in neural cells during neurite projection outgrowth [Williams et al., 1994]and in several other cell types [Francavilla et al., 2007; Sanchez-Heras et al., 2006]. NCAM behaves as non-conventional ligand of FGFR and differentially regulates intracellular trafficking of the receptor [Francavilla et al., 2009]. Binding with NCAM promotes RAB11-mediated FGFR recycling at the plasma membrane, while NCAM activation itself is also enhanced [Francavilla et al., 2009]. NCAD also interacts with FGFR and prevents its degradation by inhibiting its endocytosis [Kon et al., 2019]. In turn, FGFR stabilizes NCAD at cell-cell contacts by stimulating its anchoring to actin and adhesion strengthening [Nguyen et al., 2019].

A third level of control is the intracellular signaling. To precisely modulate cell responses and to ensure a tight control over signaling, activation of FGF pathway triggers not only the expression of positive regulators of the pathway, such as pea3 and ERM [Raible & Brand, 2001], but also of its own negative regulators Sprouty [Kim & Bar-Sagi, 2004], Sef [Fürthauer et al., 2002; Tsang et al., 2002], Dusp6 [Camps et al., 1998]. They can constitute regulatory positive and negative feedback loops in the same intracellular route that lead to their activation or in other FGF signaling-dependent routes.

1.5.3 FGF signaling and epithelial mesenchymal interactions and transitions in development

At cellular level, FGF signaling has diverse biological functions and promotes a plethora of distinct programs, from cell survival, migration, proliferation and differentiation. These contributions are integrated into fundamental tissue-wide processes during development and organogenesis, in a context-specific manner. Here we focus on the role of FGF signaling in epithelial-mesenchymal interactions and in EMT/MET transitions (Figure 1.4).

1.5.3.1 FGF and epithelial-mesenchymal interactions

FGF signaling is crucial for epithelial-mesenchymal interactions. Interestingly, it has been observed that FGF subfamilies and alternative splicing isoforms of FGFR can be tissue specific. In many contexts, FGFR1 and 2 isoforms with Ig-IIIc are detected consistently in mesenchymal cells and are responsive to epithelial FGFs, while the Ig-IIIb isoform is often expressed in epithelial cells and it bounds mesenchymal-produced FGFs [Bellusci et al., 1997; MacArthur et al., 1995]. This reciprocal signaling code, given by the tissue-specific expression of distinct sets of FGFRs and FGFs in epithelial and adjacent mesenchymal cells, is crucial to select the responder counterpart.

In the context of epithelial-mesenchymal interactions, FGFs have been shown to act as classical chemoattractant cues, as chemorepellent cues or as coordinators of patterning.

An example of FGF used as chemoattractant is during formation of branched tubular organs, such as branching morphogenesis of tracheal network in *Drosophila* (Figure 1.4 b) [Sutherland et al., 1996]. During *Drosophila* trachea formation, the FGF ligand branchless is secreted from mesenchymal cells and drives a directional migration of adjacent epithelial tracheal cells. Tip 'leader' tracheal cells having high level of FGFR breathless are required to lead the sprouting of the tracheal branches toward FGF sources, while 'follower' cells collectively migrate with them [Gabay et al., 1997; A. S. Ghabrial & Krasnow, 2006]. Similarly, expression of FGF10 from mesoderm adjacent to the site of lung bud formation appears to regulate epithelial branching during lung formation in mouse [Min et al., 1998; Sekine et al., 1999].

Distinct FGFs can also serve as chemoattractant and chemorepellent in the same system, during chick gastrulation and axonal growth in the midline [Chuai & Weijer, 2009; Dos Santos et al., 2019; Shirasaki et al., 2006]. For instance in chick, during the migration of mesoderm cells that follows ingression, FGF8 expressed in the streak behaves as a repellant cue, while FGF4 expressed in the forming notochord

acts as an attractor cue, driving migrating cells back to the midline (Figure 1.4 c) [Oates et al., 2012; Serrano Nájera & Weijer, 2020].

Furthermore, FGF can function as coordinator of patterning of adjacent tissues, for example during generation of the periodic pattern of hair follicles and feather buds. The periodic pattern of hair follicles arises from two associated patterning events: condensation of mesenchymal cells in discrete multicellular aggregates in the dermal layer and the formation of epidermal hair placodes in the epidermis (Figure 1.4 d). Interactions between BMP, FGF and WNT pathways in the epidermis drive formation of an epidermal periodic pattern, which in turn serves as a guiding template for dermal condensation by establishing local foci of FGF secretion [Glover et al., 2017]. FGF in fact promotes local recruitment and aggregation of mesenchymal cells at FGF foci, at the dermal-epidermal interface, acting as a chemoattractant. Importantly, dermal mesenchymal cells are able to aggregate into discrete condensates in absence of epidermal instructions, showing a latent self-organizing potential. Thus, focused sources of FGF are not required for the periodic pattern of mesenchymal condensates. Rather, the establishment of foci of FGF production in the epidermis during hair follicle formation ensures a tight coupling between dermal and epidermal patterning, that robustly and efficiently organizes the global pattern of hair follicles [Glover et al., 2017]. FGF fulfils a similar role in coupling epidermal and dermal patterning in feather bud formation. In the avian skin, that also consists of a dermal and an epidermal layer, patterning of epidermal is initiated by mechanical forces within the dermis. Indeed, formation of mesenchymal condensates in the dermis drives compression and bucking of the overlying epidermal layer [Shyer et al., 2017]. This compression in turn triggers differentiation of the epithelial placode via β-catenin-mediated activation of Wnt signaling and leads to activation of FGF production [Ho et al., 2019; Shyer et al., 2017]. FGF20 foci in the epithelial placode then guide condensation of dermal mesenchymal cells (like in hair bud formation), that, in a positive feedback loop, further reinforces the epidermal patterning and amplify FGF20 epithelial production [Ho et al., 2019]. The coordination between the dermal and epidermal patterning systems thus relies on FGF.

1.5.3.2 FGF and EMT/MET transition

Another key function of FGF is to induce epithelia-mesenchymal state transitions (EMT and MET) in a multitude of morphogenetic contexts. A classical example of FGF-dependent EMT dependent is mesoderm formation during mouse gastrulation. Here, FGF8 signaling drives EMT of epiblast cells that is required for cells to migrate away from the primitive streak and, though ingression, to form the mesoderm layer [Ciruna & Rossant, 2001; Sun et al., 1999]. Similarly, FGF signaling is also involved in *Drosophila* mesoderm formation during ventral furrow invagination. In this context, FGF not only act as chemoattractant but activation of FGFR Heartless also promotes loss of epithelial polarity by remodeling of E-Cadherin-dependent adhesions [Clark et al., 2011].

FGFs are implicated in several aspect of the emergence of the limb bud, such as regulation of proliferation and patterning. Furthermore, it has been found that, at early stages of limb bud induction, FGF10 expressed by the lateral plate mesoderm drives localized EMT of cells of coelomic epithelium and elicits in this way their recruitment to the limb bud, where they later on proliferate and differentiate [Gros & Tabin, 2014; Jin et al., 2019]. FGF signaling orchestrates MET during lateral line

neuromast assembly, chick hindgut (Figure 1.4 e) and Kupffer's vesicle formation (Figure 1.4 f) [Matsui et al., 2015; Nerurkar et al., 2019; Revenu et al., 2014]. The Kupffer's vesicle, the left-right organizer of the body plan of zebrafish, is a fluid-filled sphere derived from collectively migrating clusters of dorsal forerunner cells. Dorsal forerunner cell clusters rely on autocrine FGF8 signaling and on activation of a FGF positive feedback loop for expression of Cdh1, Canopy1 and Tbx16, which are involved in compaction and epithelialization of the clusters [Amack et al., 2007; Matsui et al., 2011, 2015; Oteíza et al., 2008].

In some contexts, FGF signaling is instead required to prevent epithelialization, such as during somite formation (Figure 1.4 g) from presomitic mesoderm cells (PSM) [Naoki & Matsui, 2020]. Somites assemble from PSM through the interaction of antagonistic signaling gradients, travelling rostro-caudally across the embryo, and molecular oscillators (Notch and Wnt), according to the so called 'clock and wavefront' model [Aulehla & Pourquié, 2010; Cooke & Zeeman, 1976]. The process results in a progressive MET transition that leads to periodic assembly of discrete epithelial condensates. In this context, FGF, Wnt and retinoic acid establish spatial gradients throughout the PSM, regulating the wavefront. High level of FGF in the tail bud prevents MET transition by inducing Snail2 expression, while cells exposed to level of FGF below a certain threshold are in a state permissive to MET [Dale et al., 2006; Sawada et al., 2001]. FGF-dependent increase of random cell motility, in addition, ensures that cells move away from the precursor zone and from high levels of FGF [Bénazéraf et al., 2010; Oginuma et al., 2017]. It has been recently suggested that, in zebrafish, the spatial fold-change in FGF signaling levels detected by adjacent PMS cells encodes the positioning of somite borders (and thus segment size) [Simsek & Özbudak, 2018]. During formation of the Wolffian duct in chick embryos, similarly, FGF8 prevents epithelialization while promoting tubule elongation and cellular migration [Atsuta & Takahashi, 2015].

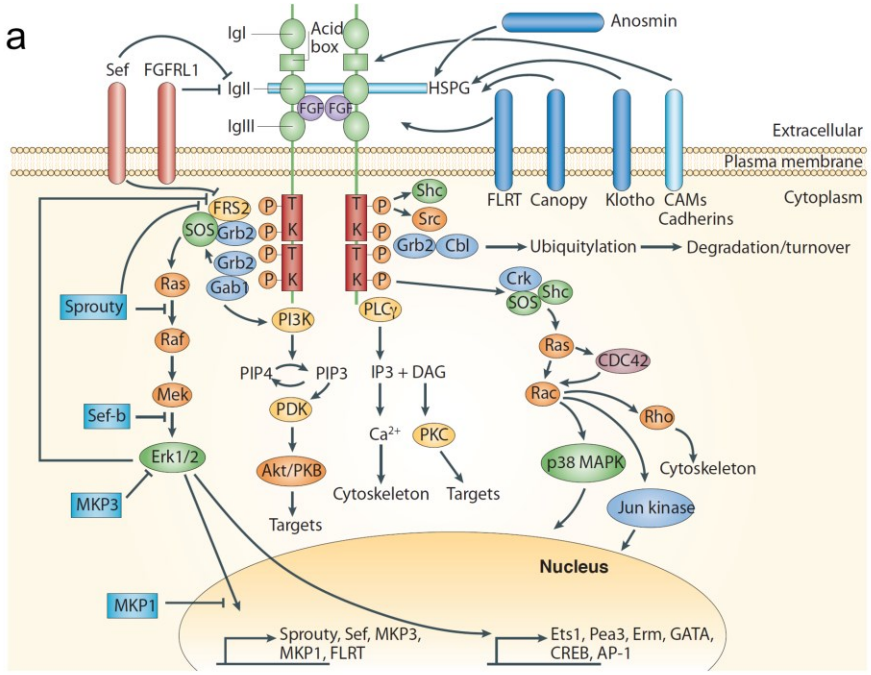

FGF and epithelial-mesenchymal interactions

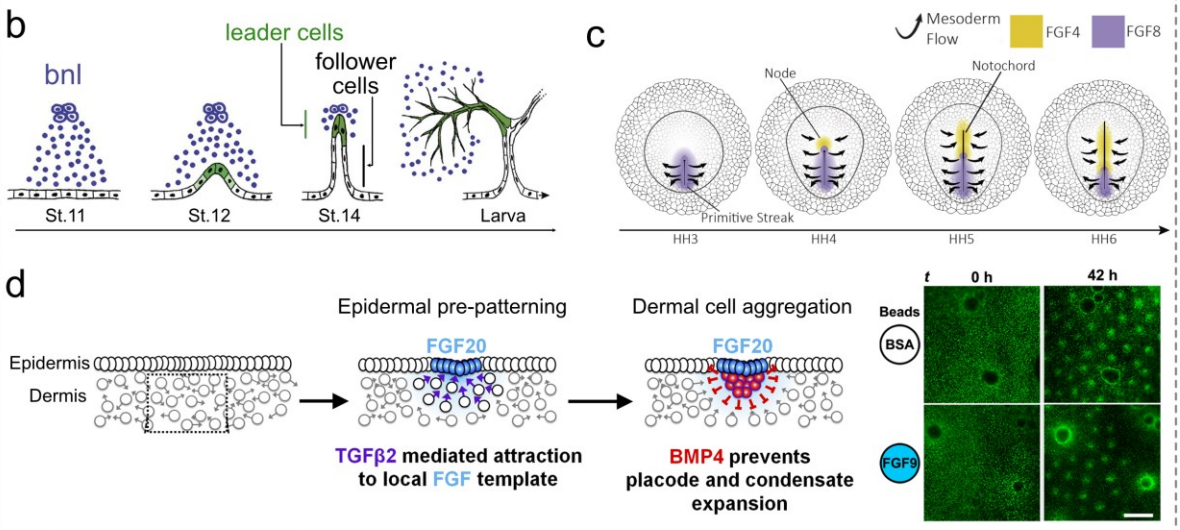

FGF and MET/EMT transition

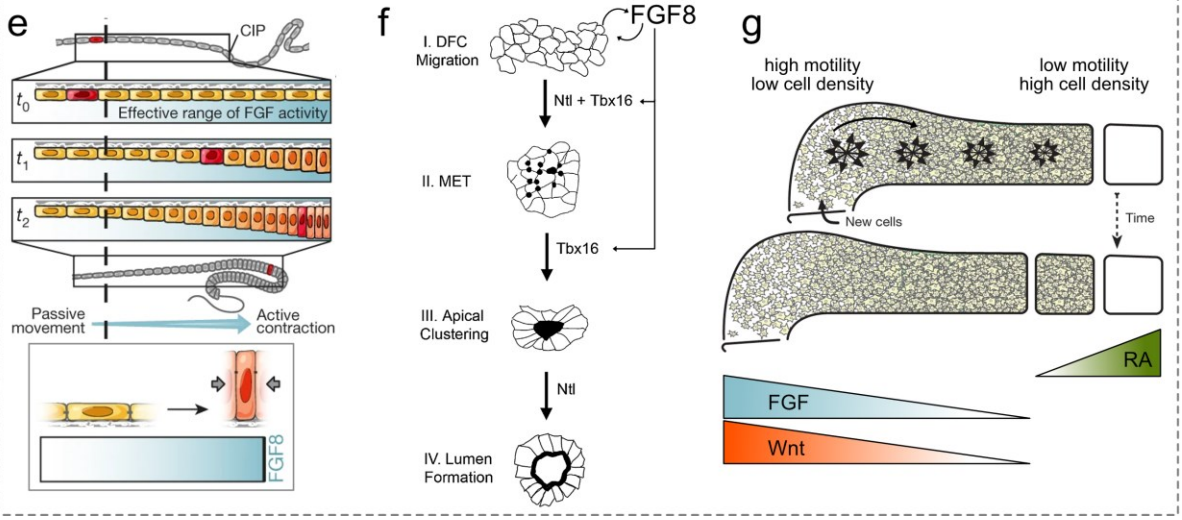

Figure 1.4: FGF signaling pathway and biological functions in development

(a) FGF signal transduction pathway (adapted from [Mason, 2007]). FGFR is a tyrosine kinase receptor that, upon binding with FGF ligand and heparin sulfate proteoglycan (HSPG), dimerizes and activates the tyrosine kinase activity. Transphosphorylated tyrosines in the kinase domains provide docking sites for the activation of cytoplasmic proteins that trigger downstream signaling cascades, such as the Ras/MAPK, PLCγ/Ca2+, STAT and PI3K/AKT [Mason, 2007]. (b) During the developing *Drosophila* trachea, branchless FGF ligand (bnl) secreted by clusters of mesenchymal cells serves as chemoattractant for guiding the sprouting and the migration of tracheal cells via FGFR (btl) signaling. Secondary and terminal branch formation also relies on Bnl/Btl signaling (adapted from [A. Ghabrial et al., 2003]). (c) During chick gastrulation, streak cells migration is coordinated by a FGF8-mediated chemorepulsion and a FGF4-mediated chemoattraction (adapted from [Oates et al., 2012; Serrano Nájera & Weijer, 2020]). (d) During hair follicle patterning, FGF-secreting foci in the epidermis promote local recruitment and aggregation of dermal cells in regularly spaced dermal condensates, ensuring coordination between epidermal and dermal patterning. FGF9-soaked beads consistently attract dermal cells in skin explants (on the left). In the process, TGFβ2 potentiates cell aggregation to FGF foci while BMP4 prevents condensate expansion (adapted from [Glover et al., 2017]). (e) During chick hindgut formation, FGF signaling coordinates a gradient of contraction in endodermal cells, driving progressive cell packing and tissue elongation (adapted from [Nerurkar et al., 2019]). (f) Kupffer's vesicle epithelialization relies on the cooperative activity of the transcription factors Ntl and Tbx16. FGF8-dependent expression of Tbx16, in particular, triggers Cdh1 expression and leads to apical clustering (adapted from [Amack et al., 2007; Matsui et al., 2011]). (g) During mouse and chick somitogenesis, somites sequentially assemble via the interplay of molecular oscillators and signaling gradients. Gradients of FGF and Wnt signaling activity establish across the paraxial mesoderm, with highest signaling activity in the tail bud and a progressive decrease toward the anterior portion, opposing the retinoic acid (RA) gradient. This sets up a cell motility gradient and a progressive anterior-to-posterior MET transition (adapted from [Bénazéraf et al., 2010]). Scale bar in (d) 250 µm.

1.6 The zebrafish posterior lateral line system

The lateral line is the mechano-sensory system that allows the detection of water flow in amphibians and fish. Sensing of local vibrations in water is important for a wide range of behaviors such as schooling, pray detection, predator avoidance and courtship [Ghysen & Dambly-Chaudiere, 2007; Schlosser, 2006]. The lateral line system consists of multiple arrays of discrete sensory organs lying on the body surface underneath the skin, organized into two main branches, the anterior lateral line in the head region of the animal and the posterior lateral line in the trunk and tail region. The latter will be the object of description from now on.

The posterior lateral line primordium (pLLP) originates from the lateral line placode, positioned at both sides of the head behind the otic vesicle [Kimmel et al., 1995]. At 18 hours post fertilization (hpf) the lateral line placode delaminates and splits into two clusters, the pLLP and a smaller cluster that gives rise to the lateral line sensory ganglion [Ghysen & Dambly-Chaudière, 2007]. pLLP is a collectively migrating tissue constituted of around 100 cells that migrate along both flanks of the zebrafish embryo, along the horizontal myoseptum, from ear to tail between 20hpf and 48hpf (Figure 1.5 a). While migrating, the primordium deposits from its rear five radially organized clusters of around 20-30 cells with a stereotyped periodicity and, by approaching the tail, fragments into two or three terminal clusters. These clusters, referred to as rosettes or neuromasts, mature into a set of mechano-sensory organs. Projections from the lateral line ganglion co-migrate with the pLLP and ensure innervation of the sensory organs. In between consecutive neuromasts, the pLLP deposits a connected chain of interneuromast cells, also referred to as 'chain cells' (Figure 1.5 a). After this first wave of neuromast deposition, in fish and amphibians, the lateral line pattern is further modified and refined during development and adult life with addition of supplementary sets of sensory organs according to a specie-specific pattern, to account for body growth. Additional sources of sensory organs are the second primordium, the anterior primordium and chain cells from the first and second primordium [Ghysen & Dambly-Chaudière, 2007].

1.6.1 Lateral line primordium and MET transition

Collectively migrating tissues such as the pLLP of the zebrafish are model systems particularly suited for the study of MET-EMT transition *in vivo*. pLLP displays a tissue-scale polarity along the leading-trailing axis of migration, which gives a gradient of cells in different states. The iterative process of neuromast formation and deposition requires cells of the pLLP to progressively transition from the mesenchymal-like 'leader' state to the 'follower' epithelial state, establishing a continuous progression of MET across the tissue. Cells at the leading edge of the primordium, the 'leader' cells, exhibit a mesenchymal-like morphology, spreading on the extracellular substrate and displaying front-rear polarity and motile protrusions (Figure 1.5 a) [Lecaudey et al., 2008]. Despite their mesenchymal state, they are endowed of apical-basal polarity and N-Cadherin based cell-cell adhesions [Revenu et al., 2014]. Follower cells are located behind leader cells at the trailing edge of the tissue. They exhibit an epithelial morphology with a typical columnar shape, a pronounced apical-basal polarity and a higher height/width ratio compared to leader cells [Lecaudey et al., 2008]. Moreover, Golgi and centrosome

in follower cells are polarized at the apical side of the cell, while nuclei are basally located [Durdu et al., 2014; Harding & Nechiporuk, 2012; Revenu et al., 2014]. While displaced toward the rear of the primordium, follower cells progressively organize into highly packed rosette structures called pro-neuromasts, which are sequentially deposited from the pLLP during migration. Cells in pro-neuromasts and neuromasts are apically constricted and radially organized, exhibiting adherens junctions, tight junctions and desmosomes [Durdu et al., 2014; Lecaudey et al., 2008]. During pro-neuromast formation, N-cadherin redistributes to the apical sides of the cells in a microtubule-dependent process and, as the neuromast ages, this apical N-Cadherin pool stabilizes [Revenu et al., 2014].

1.6.2 Signaling networks in the pLLP

Primordium polarity in a leading and trailing zone reflects the presence of two spatially distinct signaling poles, established by the antagonism of the Wnt/β-catenin signaling and the FGF signaling (Figure 1.5 b). At the leading edge of the pLLP, the Wnt/β-catenin signaling dominates and represses FGF signaling. Wnt signaling induces expression of its own positive regulators, such as Lef1, and of FGF3 and FGF10 ligands. However, it inhibits FGF signaling through expression of Sef and Dusp6, thus preventing responsivity of the leading edge to the produced ligands [Aman & Piotrowski, 2008; Matsuda et al., 2012; Tsang et al., 2002]. In addition, FGFR1a expression is downregulated in the leading edge [Lecaudey et al., 2008]. In the trailing zone of the pLLP, FGF signaling dominates and represses Wnt/β-catenin signaling. FGF signaling downregulates Wnt/β-catenin signaling by expressing Dkk1 and induces expression of its own positive mediators, such as FGFR1a [Aman & Piotrowski, 2008]. The trailing zone is thus responsive to FGF ligands secreted by the leading zone, as probed by increased expression of the transcriptional target of FGF signaling, pea3 [Lecaudey et al., 2008]. FGFR1a is expressed throughout the trailing zone apart few cells in the center of pro-neuromasts that instead express FGF10, the prospective hair cells [Lecaudey et al., 2008]. FGF signaling also induces the expression of DeltaD and Atonal (Atoh1a), implicated in the specification of hair cells within neuromasts [Matsuda & Chitnis, 2010; Nechiporuk & Raible, 2008]. The reciprocal regulation of the Wnt/β-catenin signaling and the FGF signaling keeps the balance between the leading and trailing zones during the progressive conversion from leader to follower cells (Figure 1.5 c).

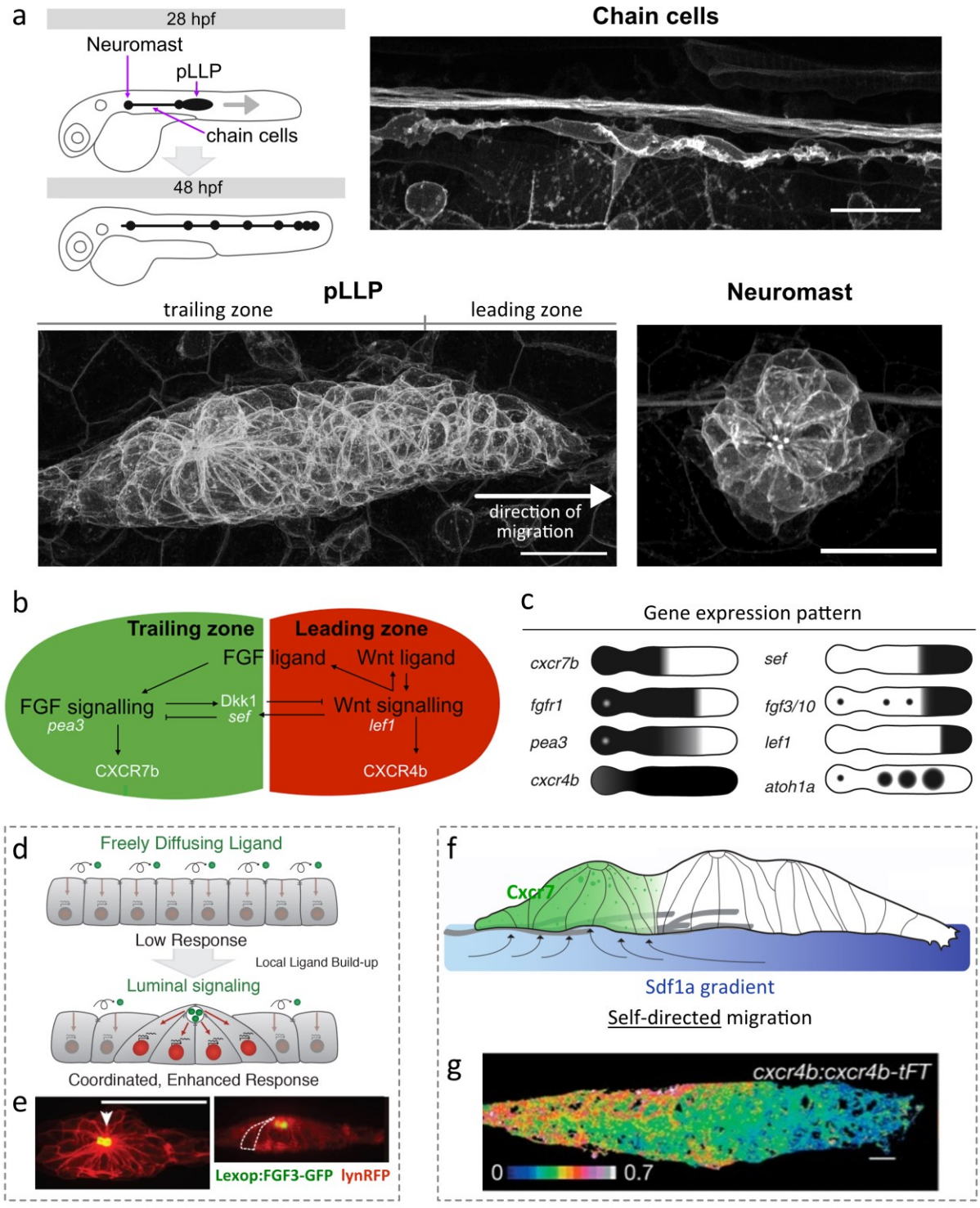

Figure 1.5: Morphogenesis of the posterior lateral line primordium

(a) During the migration of the posterior lateral line primordium (pLLP), rosette-shaped neuromasts and a string of chain cells in between consecutive neuromasts are deposited. The posterior lateral line primordium (pLLP) presents a front-rear polarity. The leading zone at the front is populated of 'leader' cells with mesenchymal-like features, while in the trailing zone 'follower' cells display an epithelial phenotype and organize in rosette-shaped pro-neuromasts. Z-projected view of a 28hpf posterior lateral line primordium, chain cells and neuromast (apical view) labelled with a membrane label (cldnb:lyn-GFP). (b) The leading and trailing zone identities are regulated by the interplay of the FGF and Wnt/β-catenin signaling pathways (adapted from [Knutsdottir et al., 2017]). (c) Gene expression profiles of genes involved in the lateral line primordium patterning (adapted from [Ma & Raible,

2009]). (d) Illustration of the luminal signaling model, where FGF ligand is trapped in a multicellular shared lumen and FGF signaling is amplified only in cells accessing it (adapted from [Durdu et al., 2014]). (e) Apical and z-view of a neuromast showing a luminal accumulation of FGF3 expressed using the LexPR/LexOP transactivation system (adapted from [Durdu et al., 2014]). (f) Illustration of the self-generated gradient model, where Cxcr7 in the trailing zone of the pLLP internalizes Sdf1a and establish in this way the local Sdf1a gradient along which the pLLP directionally migrate (adapted from [Donà et al., 2013]). (g) Ratiometric image of a pLLP obtained with the Cxcr4b tandem fluorescent timer approach, allowing the detection of a Sdf1a gradient. The Cxcr4b protein pool is older in the trailing zone (more red), where less chemokine is present, while newly synthetized in the leading zone (more blue), where more chemokine is available for binding (adapted from [Donà et al., 2013]). Scale bar (a) 20 µm; (e) 50 µm; (g) 10 µm.

1.6.3 FGF and MET transition in the pLLP

FGF signaling at the rear of the pLLP enhances epithelialization of follower cells and is required for the morphogenesis of rosette-shaped neuromasts [Durdu et al., 2014; Harding & Nechiporuk, 2012; Lecaudey et al., 2008; Revenu et al., 2014]. Manipulation of FGF signaling rapidly controls cell state and behavior over a wide dynamic range [Durdu et al., 2014; Lecaudey et al., 2008]. Inhibition of FGF signaling with pharmacological methods (like SU5402) or genetic methods (like a dominant negative form of FGFR or FGF ligand morpholinos) results in defective neuromast formation and deposition. Conversely, over-activation of FGF signaling via FGF3 and FGF10 misexpression accelerates neuromast deposition in a dose-dependent manner and leads to epithelialization of the entire mesenchymal-like leading zone of the pLLP [Durdu et al., 2014; Lecaudey et al., 2008]. FGF signaling ensures epithelialization of the pLLP by driving two processes, apical constriction and microlumen formation in assembling neuromasts**.** Apical constriction of follower cells requires polarized activation of actomyosin contractility through Rock2a-dependent phosphorylation of Myosin-II, which apically localizes shortly before constriction [Ernst et al., 2012; Harding & Nechiporuk, 2012]. FGF signaling drives Ras/ MAPK pathway activation, that is cell-autonomously required for Rock2a localization at the apical membrane [Harding & Nechiporuk, 2012]. In addition, FGF induces expression of Shroom3, a regulator of non-muscle myosin that also displays apical accumulation in follower cells and that mediates apical recruitment of Rock in MDCK cells [Ernst et al., 2012; Nishimura & Takeichi, 2008]. Downregulation of Shroom3 phenocopies inhibition of FGF signaling, causing a loss of apical constriction and neuromast formation [Durdu et al., 2014; Harding & Nechiporuk, 2012]. These studies suggest that the FGFR/Ras/MAPK axis controls apical constriction by driving Shroom3 expression, which in turn mediates accumulation of Rock2a at the apical side where actomyosin contraction is induced [Ernst et al., 2012; Harding & Nechiporuk, 2012]. Interestingly, inhibiting the components of the apical constriction process does not prevent adoption of apical-basal polarity in cells of the pLLP, indicating that other mechanisms are involved.

In addition to apical constriction, during neuromast morphogenesis a self-feeding amplification between FGF signaling and multicellular architecture occurs (Figure 1.5 d, e) [Durdu et al., 2014]. As follower cells assemble into a radially organized pro-neuromast, they arrange their apical sides to form a shared central cavity sealed with tight junctions. Secreted FGF is trapped within this enclosed extracellular pocket, known as microlumen. The microlumen acts as a signaling hub that, on one side,

restricts the range of FGF activity exclusively to connected cells, and, on the other side, locally boosts FGF ligand concentration, enhancing FGF signaling activity and further reinforcing the epithelial character of the exposed cells. Perturbation of individual FGF luminal pools affects the deposition timing of the perturbed neuromast, indicating that the luminal pool acts as a local coordinator of cell response within each rosette unit. The feedback between the FGF signaling and the microlumen might serve as checkpoint that ensures that only properly assembled cells are deposited from the primordium and further differentiate [Durdu et al., 2014]. Furthermore, it has been suggested that the FGF ligands secreted from the leading edge of the pLLP function as chemoattractant for follower cells, coordinating the collective migration of leaders and followers [Nogare et al., 2014]. Heparan sulfate proteoglycans, whose expression in the pLLP is regulated by the Wnt-FGF signaling axis, appear to control the diffusion of the FGF ligands secreted form the leading edge of the primordium and the activation of FGF signaling [Galanternik et al., 2015; Venero Galanternik et al., 2016].

1.6.4 pLLP migration

In the pLLP, organogenesis is tightly coupled with migration. Migration of the pLLP is directed by the chemokine Cxcl12a/Sdf1a, which is produced by cells of the horizontal myoseptum as a homogeneous stripe [David et al., 2002; Valentin et al., 2007]. Two receptors expressed in the pLLP, Cxcr7b and Cxcr4b, bind to Sdf1a and serve distinct functional roles: Cxcr7b generates a Sdf1a gradient while Cxcr4b senses it. Cxcr7b is a non-signaling chemokine receptor whose expression is induced by FGF signaling in the trailing zone of the pLLP and in chain cells. The binding of Cxcr7b with Sdf1a drives internalization of the ligand-receptor complex, determining 'clearing' of Sdf1a at the trailing edge of the primordium while the tissue migrates toward the tail [Donà et al., 2013; Venkiteswaran et al., 2013]. This mechanism leads to the generation of a Sdf1a gradient. Because of its 'sink' activity, Cxcr7 is defined 'scavenger' receptor. Perturbations affecting either Cxcr7 expression or internalization impairs Sdf1a gradient formation and primordium migration. However, re-introduction into Cxcr7 mutant of a sinking activity external to the lateral line, such as a cxcr7 expressing lateral line nerve (that co-migrate with pLLP), is sufficient to rescue both [Donà et al., 2013; Venkiteswaran et al., 2013]. Therefore, the primordium self-generates the gradient required for its own directional migration through the scavenger activity of Cxcr7b (Figure 1.5 f, g). In addition, a recent study showed that Cxcr7b is crucial for adaptation of the pLLP to abruptly changing chemokine levels. By switching from a degradative route to a recycling route upon internalization, Cxcr7 scavenger activity is upregulated in presence of elevated Sdf1a levels, ensuring robust migration of the pLLP [Lau et al., 2020; Wong et al., 2020]. Cxcr4b is the gradient-sensing receptor of the pLLP, which is required to lead the directional migration of the tissue. Cxcr4b is a canonical G-coupled chemokine receptor. Importantly, its activity is graded across the leading-trailing axis of the pLLP, reflecting the Sdf1a gradient [Donà et al., 2013; Venkiteswaran et al., 2013]. The half-life of Cxcr4b in the leading edge of the tissue is shorter than in the trailing edge, because of the high rate of binding with Sdf1a of leader cells, that in turn drives receptor internalization and degradation [Donà et al., 2013]. Recover of plasma membrane levels of Cxcr4b occurs through new biosynthesis. Remarkably, directional migration of the pLLP does not

require that all the cells in the tissue express Cxcr4b. Transplantation experiments generating chimeras of Cxcr4 mutant and wild type cells demonstrated that few Cxcr4b positive cells are enough to drive directional migration of the whole collective [Haas & Gilmour, 2006].

1.6.5 Cell types in the lateral line neuromasts

Once deposited, lateral line neuromasts differentiate into fully functional sensory organs, constituted of three main cell types concentrically arranged: hair cells, supporting cells and mantle cells (Figure 1.6 a, b). Hair cells are terminally differentiated cells located centrally in the neuromast representing the mechano-sensory component of the organ (Figure 1.6 b). To fulfill this function, the hair cell projects into the external environment two types of cilia: a kinocilium composed of microtubules and several actin-rich stereocilia. Deflexion of the stereocilia toward the kinocilium induces depolarization of the cell, leading to activation of the connected terminal nerve responsible for the transduction of the signal to the brain [Shotwell et al., 1981]. To be able to respond to stimuli coming from different directions, hair cells within each neuromast adopt a specific planar polarity orientation, controlled by planar polarity proteins such as Vangl2. Oppositely oriented hair cells organize in an organ-scale mirror symmetry within each neuromast [Lopez-Schier & Hudspeth, 2005; Wibowo et al., 2011]. FGF signaling drives specification of hair precursors through activation of Atoh1a and Notch ligand Delta [Millimaki et al., 2007]. Lateral inhibition mediated by Notch/Delta signaling progressively restricts the hair cell fate to few cells per neuromasts. Inhibition of Notch indeed leads to the overproduction of hair cells, at the expenses of supporting cells [Romero-Carvajal et al., 2015]. Supporting cells are non-sensory cells constituting the vast majority of cells within the neuromast (Figure 1.6 b). They display an intimate interaction with hair cells as they surround them and interdigitate membrane processes in between them [Balak et al., 1990; Williams & Holder, 2000]. They constitute the progenitor population from which hair cells regenerate in homeostatic and injury conditions (described in the next paragraph). Moreover, it has been suggested that supporting cells serve as adhesive linker between hair cells and outer non-sensory cells [Chitnis et al., 2012]. Mantle cells constitute the most external ring of cells of the neuromast, surrounding the supporting and hair cell pool (Figure 1.6 b). They secrete the mucous cupola that encapsulate the ciliary bundles of hair cells [Ghysen & Dambly-Chaudière, 2007]. Mantle cells might be involved in controlling neuromast size. Indeed, they express high levels of Fat1a and 1b [Steiner et al., 2014], that have been shown to contribute to the control of cell division and organ size in *Drosophila* [Bryant et al., 1988; Katoh, 2012; Mahoney et al., 1991]. A new cell type has been recently identified in the lateral line neuromasts of both zebrafish and medaka, known as neuromast border cells (nBC) (Figure 1.6 b) [Seleit et al., 2017]. nBC surround mantle cells in neuromasts deposited by the pLLP, forming an outer ring that might function as stem cell niche for mantle cells. Remarkably, the border cell population does not originate from the pLLP but derives from the suprabasal skin epithelium through a process of conversion. Proliferation of nBC also contributes to the expansion of the nBC ring [Seleit et al., 2017].

1.6.6 Regeneration of the lateral line neuromasts

Hair cells in non-mammalian vertebrates are physiologically replaced throughout life and rapidly regenerate upon severe damages, while this regenerative potential is lost in mammals [Kniss et al., 2016]. Because of its extensive regenerative potential and its experimental accessibility, zebrafish posterior lateral line system has been widely used as a model system for regeneration in the last decades. Studies of the regeneration capability of the lateral line system mostly rely on three perturbation approaches, which cause different degrees of damage: drug-induced depletion of hair cells (using for example heavy metals, copper or neomycin at low concentration), laser-mediated ablation of neuromast sub-regions and whole neuromast electro-ablation. These techniques, together with live cell-lineage tracing and, transcriptomic analysis, have contributed to the understanding of important aspects of hair and neuromast regeneration. In the lateral line system, there are three cell populations that possess multipotent regenerative potential: supporting cells, mantle cells and chain cells. However, these populations are differentially responsive to various degrees of damage and contribute to regeneration in distinct contexts (Figure 1.6 c).

Supporting cells are the main contributors of hair cell regeneration during homeostatic growth and upon mild injuries such as hair cell depletion. Between 24 and 36 hours post injury, hair cells robustly regenerate from them through mitotic regeneration [Hernández et al., 2007]: a non-sensory supporting cell symmetrically divides into two daughter hair cells [Cruz et al., 2015; Lopez-Schier & Hudspeth, 2005; Mackenzie & Raible, 2012; Pinto-Teixeira et al., 2015; Romero-Carvajal et al., 2015; Viader-Llargués et al., 2018; Wibowo et al., 2011]. Trans-differentiation of one cell type into another, observed for supporting and hair cells in several sensory organs (for example the avian basilar papilla) does not appear to contribute to regeneration in the posterior lateral line system [Jacques et al., 2012; Romero-Carvajal et al., 2015; Viader-Llargués et al., 2018]. Importantly, supporting cells also undergo self-renewing symmetric divisions to amplify the supporting cell pool and thus ensure maintenance of the regenerative potential of the neuromast. Recent studies indicate that whether a supporting cell generates hair or supporting daughter cells depends on the position of the dividing support cell within the neuromast, suggesting the existence of several functional supporting cell subtypes located in distinct domains [Cruz et al., 2015; Lush et al., 2019; Thomas & Raible, 2019]. These subtypes contribute differently to hair regeneration [Thomas & Raible, 2019]. For example, supporting cells in the dorsal-ventral pole preferentially divide into supporting cells, while supporting cell located close to the center of the organ divide into hair precursors [Cruz et al., 2015; Lush et al., 2019; Thomas & Raible, 2019]. Furthermore, supporting cells are also involved in regenerative responses to severe injuries. In zebrafish larvae, as little as four supporting cells are sufficient to restore an entire neuromast, regenerating hair, mantle and supporting cells and reestablishing the correct relative ratio and concentric organization of cell types [Viader-Llargués et al., 2018]. The interplay between Delta/Notch, FGF and Wnt/ β-catenin signaling controls supporting cell proliferation and differentiation within homeostatic neuromasts and during neuromast regeneration in the zebrafish

lateral line [Lush et al., 2019; Ma et al., 2008; Romero-Carvajal et al., 2015; Wada et al., 2013; Wibowo et al., 2011].

Mantle cells are a population of multipotent progenitors that do not proliferate in response to hair cell depletion, but they re-enter the cell cycle solely upon severe depletion of the supporting cell pool [Romero-Carvajal et al., 2015]. Thus, they are quiescent unless an extensive injury occurs. Following fin-tail amputation in adult zebrafish, for example, mantle cells have been shown to regenerate a new primordium that reconstitute the entire missing portion of the lateral line in the regenerated tail [Dufourcq et al., 2006], analogous to what has been observed for the amphibian lateral line mantle cells [Jones & Corwin, 1996]. Importantly, mantle cells do not give rise to hair cells directly, but divide into supporting cells, that in turn divide into hair cells [Ghysen & Dambly-Chaudière, 2007]. A recent study showed that mantle cells in medaka not only contribute to neuromast regeneration upon severe damage, but they also serve as progenitors during homeostatic growth and post embryonic organogenesis, indicating that they represent a *bona fide* neural stem cell population in medaka [Seleit et al., 2017].

The third population of multipotent progenitors implicated in neuromast regeneration is the chain cell pool, deposited by the pLLP as a string connecting consecutive neuromasts (Figure 1.6 b). Physiologically, chain cells undergo proliferation and form additional neuromasts (named intercalary neuromasts) during late larval development [Ghysen & Dambly-Chaudière, 2007]. Analogously, upon severe damage leading to complete loss of the neuromast (employing electroablation), chain cells can regenerate the entire organ [Sánchez et al., 2016]. As little as two chain cells are sufficient to regenerate an entire organ, by migrating in the injury side, undergoing Wnt-dependent proliferation and differentiating. However, it was found that the regenerative response of chain cells solely occurs when lateral line glial cells are concurrently damaged, suggesting that the interaction between glia and chain cells is crucial to control chain cell behavior in the zebrafish posterior lateral line [Sánchez et al., 2016]. Indeed, in other studies where glia was removed without damaging the lateral line, a similar proliferative response of chain cells was observed, leading to premature formation of intercalary neuromasts (Figure 1.6 e) [Grant et al., 2005; Lopez-Schier & Hudspeth, 2005]. Moreover, these studies suggest that glia, in homeostatic conditions, prevents the assembly of chain cells-derived intercalary neuromasts through inhibition of Wnt/β-catenin signaling in chain cells (Figure 1.6 d, e) [Lush & Piotrowski, 2014a]. However, both the signal inhibiting Wnt/β-catenin signaling and the mechanism employed to release it in late larval stages (when intercalary neuromasts physiologically assemble) still need to be elucidated. It has been suggested that the ventral displacement of the chains occurring at larval stage and the consequent physical distancing of chains from glial cells might contribute to the attenuation of the inhibitory signal [Lush & Piotrowski, 2014a].

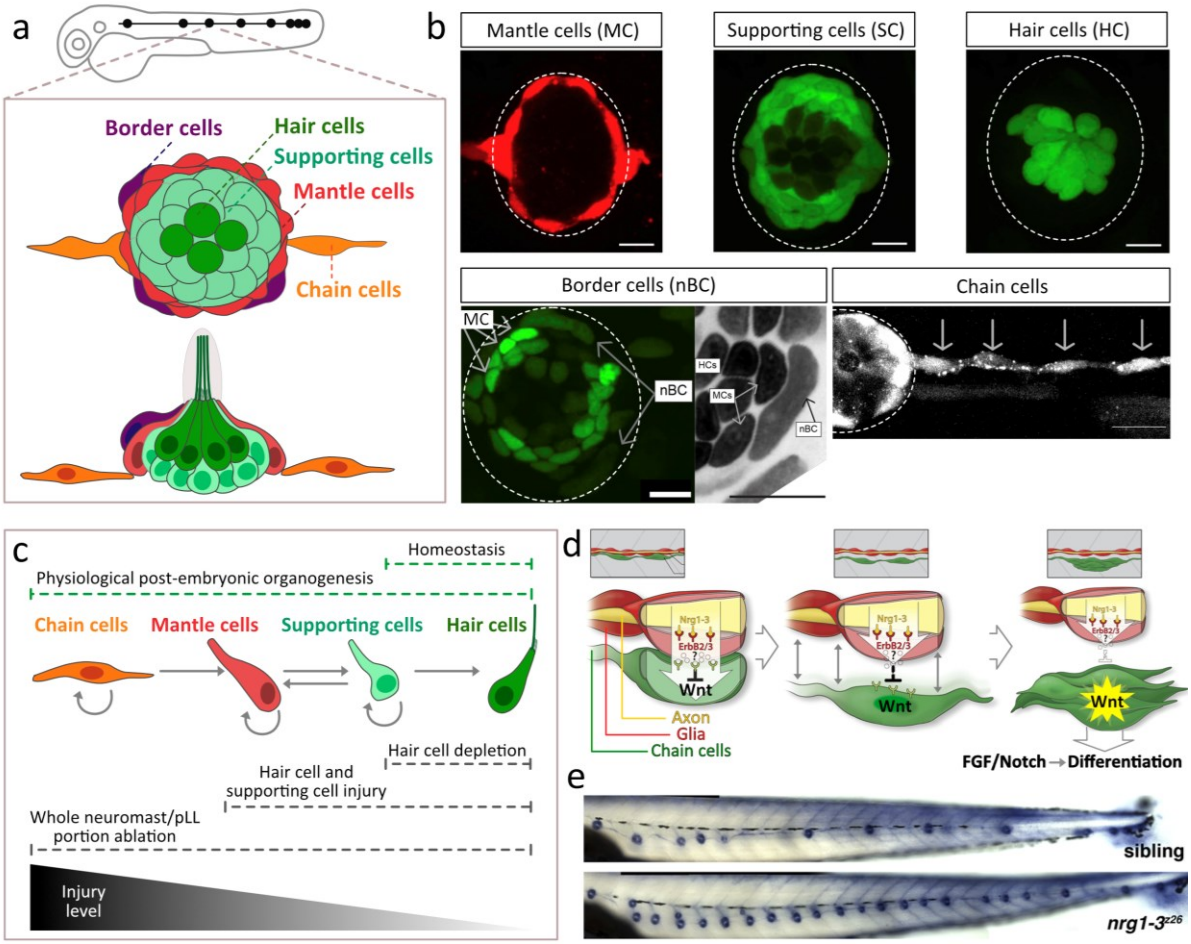

Figure 1.6: Cell types in the lateral line neuromasts and regenerative capability

(a) Overview of the main cell types in lateral line neuromasts, (b) labelled using cell type-specific fish lines: mantle and chain cells visualized with the AlpI:mCherry line; supporting cells with the SqGw57A line ; hair cells with the SqEt4 line; border cells with the krt15:H2B-EGFP line and dapi staining (adapted from [Viader-Llargués et al., 2018], except the border cell images adapted from [Seleit et al., 2017]). Dashed lines approximate the neuromast outline. The lateral line nerve, that is also part of the lateral line system and run parallel to chain cells, is omitted in this overview. (c) Supporting cells, mantle cells and chain cells are multipotent progenitors that are responsible for cell regeneration following damages. These populations differentially respond to injuries depending on the extent of damage. In homeostatic conditions, hair cells are replaced throughout life by proliferating supporting cells in zebrafish and intercalary neuromasts are formed from chain cells during post-embryonic development. (d) In embryonic stages glial cells keep chain cells quiescent by inhibiting Wnt/β-catenin signaling, while, at larval stages, the physical separation between these two populations is thought to attenuate this inhibition, with consequent proliferation and differentiation of chain cells into intercalary neuromasts (modified from [Lush & Piotrowski, 2014a]). (e) Removal of glial cells with various methods, including mutation of the neuregulin protein (nrg), leads to precocious formation of intercalary neuromasts. Nrg1-3 is an ErbB ligand that is expressed in the lateral line ganglion and is involved in glial cell migration. The nrgz26 mutant lacks lateral line-associated glial cells. Neuromasts are labeled with Alkaline phosphatase staining (adapted from [Lush & Piotrowski, 2014a]). In (b), scale bars are 10 µm, except for the chain cell panel where it is 20 µm.

1.7 Aim of the study

The ability of cells to transition from one phenotype to another is a fundamental feature of organogenesis. Mesenchymal-to-epithelial transitions (MET) allows motile and dynamic mesenchymal cells to assemble into epithelia, the key building blocks of organs. A major challenge in the field is to understand how MET is implemented in the developmental programs during organogenesis and how it integrates with other processes such as cell fate choices. However, the scarcity of models providing access to the process in real time and *in vivo* have prevented an in-depth exploration of mechanistic principles governing the establishment and spreading of MET across collectives. In this study, we use the zebrafish lateral line system and, in particular, a subpopulation of mesenchymal-like progenitor cells lined between deposited neuromasts, called chain cells, that provide an easily accessible minimal 1D model to address principle of organogenesis. Since previous studies have demonstrated that the epithelial state of the lateral line primordium is modulated by FGF signaling, we sought to exploit FGF signaling as a tool to induce MET and organogenesis.

In this study, we addressed three main questions:

1) Can we drive MET from 'scratch' in an *in vivo* system? The first aim of the project was to develop an approach to perturb FGF signaling in a cell-autonomous manner and at high spatial and temporal resolution, with the goal of driving MET in the mesenchymal-like population of lateral line chain cells.

2) How does MET emerge from a mesenchymal-like cell population? The second aim of the project was to exploit the developed approach to gain insights into the progression of MET across cell collectives *in vivo*. To achieve this goal, we enforced mosaic FGF signaling activity in chain cells and we resolved how the differently activated cells interact with each other, investigating in this manner both cell-autonomous and non-cell autonomous responses to ectopic FGF signaling activation.

3) How does MET transition relate to cell differentiation? The main aim of the project was to explore whether cells undergoing MET give rise to fully mature organs and, if so, to investigate how the differentiation pattern emerges.

2 Material and Methods

2.1 Zebrafish handling and husbandry

Zebrafish (*Danio rerio*) strains were bred, raised and maintained following standard procedures [Westerfield, 2007]. Embryos were kept in E3 buffer between 26°- 30°C without light cycle and staged as previously described [Kimmel et al., 1995]. All zebrafish experiments were conducted following the guidelines of the European Commission (Directive 2010/63/EU) in accordance with the rules of the European Molecular Biology Laboratory, the veterinary office of the Universität Zürich and the Canton of Zürich. 1-day post-fertilization embryos were bleached with 5% Sodium hypochlorite (Sigma-Aldrich) prior to raising to adulthood to reduce risk of pathogen contamination and kept in E3 medium with 10 µg/ml pronase (Roche) to allow hatching [Nüsslein-Volhard & Dahm, 2002]. Prior manipulations, fixation procedures and during live imaging, embryos were anesthetized with 0.01% Tricaine (Sigma-Aldrich).

2.2 Molecular biology

Plasmids used for this study were generated employing MultiSite Gateway cloning technology (Invitrogen) according to the Tol2Kit system, which relies on a two-step cloning strategy [Kwan et al., 2007]. First, a BP reaction allows the insertion of a PCR-amplified DNA sequence of interest into a donor entry clone. Second, a LR recombination between multiple entry clones enables combinatorial fusion of a DNA sequence of interest with other coding sequences (fluorophores, nuclear or membrane tagging domains) and promoters, generating an expression vector. Several of the entry clones used in this study were taken from the Tol2kit [Kwan et al., 2007] or generated by other current or former lab members. For the generation of new entry clones, KAPA HiFi hot-start polymerase (Kapa Biosystems) was employed for PCR amplification of the insert and for the addition of *att* sites. Primers were designed in SnapGene and purchased from Sigma-Aldrich or Microsynth. Tol2-based destination vectors carry expression cassettes for co-injection markers, driving expression of mKate2 or ECFP in the eye lens (cry:mKate2 named ‘red eye’; cry:ECFP named ‘blue eye’) or expression of EGFP in the heart (clmc2:EGFP named ‘green heart’).
For bacterial transformation, Stellar (Clontech Laboratories) or One Shot Top10 Chemically Competent *E. coli* (Invitrogen) were used following manufacturer’s instructions. BP and LR reaction products were verified by restriction analysis and Sanger sequencing (GATC Biotech or Microsynth). Expression vectors were microinjected directly (as described in section 2.3) or mRNA for injections was synthetized from them using mMessage mMachine kit (Ambion).

2.2.1 Generation of chemoFGFR

We based the design of the chemoFGFR construct on the published optogenetic mFGFR1-VfAU1-LOV named Opto-mFGFR1 [Grusch et al., 2014], which contains a LOV domain derived from *V. Frigida* aureochrome1 (VfAU1-LOV, residue 204–348 of Uniprot entry A8QW55) and the murine intracellular domain of fibroblast growth factor receptor 1 (FGFR1). To generate the zebrafish version of this chimeric construct, the murine FGFR1 portion was substituted with the matching zebrafish counterpart (selected via BLAST [Altschul et al., 1990]) using MultiSite Gateway cloning technology (Invitrogen) and Tol2Kit system [Kwan et al., 2007]. Briefly, the zebrafish intracellular FGFR1a portion (referred to as ziFGFR) and the LOV domain (including a C-terminal HA tag) were at first PCR-amplified separately, using as template respectively zebrafish FGFR1a cDNA and the original Opto-mFGFR1 [Grusch et al., 2014]. Secondly, fusion PCR between the two fragments was performed following a standard protocol, preserving the original linker used for the Opto-mFGFR1. The ziFGFR-LOV fragment was then inserted into a p3E entry vector via BP reaction and recombined in different expression vectors via LR reaction. Given that both the transmembrane and extracellular domains of FGFR1a were omitted, according to the design of the original Opto-mFGFR1 [Grusch et al., 2014], we introduced the membrane tethering palmitoylation sequence lyn to enforce plasma membrane localization [Teruel et al., 1999]. Because of the absence of the extracellular domain, the chimeric construct is unable to bind FGF ligands. Either β-actin, LexOP or SP6 promoters were moreover introduced, to drive respectively ubiquitous expression, chemically inducible transactivation (see section 2.4) or mRNA synthesis. In the result section, we refer to these constructs as lyn-FGFR-LOV and we refer specifically to the LexPR/LexOP-driven version as chemoFGFR.
Three versions of the chemoFGFR were cloned, depending on the fluorophore fused to the N-terminus of the ziFGFR, and transgenic fish lines with a naked-blanc, green and red version of the chimeric receptor were established:

LexOP:lyn-ziFGFR-LOV-HA Entries: (p5'E(LexOP))/pME(lyn no stop)/p3E (ziFGFR-LOV-HA)
LexOP:lyn-mNG-ziFGFR-LOV-HA Entries: (p5'E(LexOP))/pME(lyn-mNG no stop)/p3E (ziFGFR-LOV-HA)
LexOP:lyn-mRFP-ziFGFR-LOV-HA Entries: (p5'E(LexOP))/pME(lyn-mRFP no stop)/p3E (ziFGFR-LOV-HA)

mNG (mNeonGreen) was kindly provided by Prof. Dr. Alex Hajnal, zebrafish FGFR1a cDNA by Prof. Dr. Michael Brand [Nowak et al., 2011] and Opto-mFGFR1 was a gift from Dr. Harald Janovjak (Addgene plasmid # 58745; http://n2t.net/addgene:58745 ; RRID:Addgene_58745 [Grusch et al., 2014]).

2.3 Embryo microinjection and establishment of transgenic lines

To generate transgenic fish lines or misexpressing clones in transient, 1-cell stage embryos were microinjected with the designated expression vector (30-40 μg/μl), together with Tol2 transposase (25ng/μl) [Kwan et al., 2007] and Phenol Red (Sigma). For transient mRNA experiments, embryos were

instead microinjected with 200-300 ng/µl of mRNA and Phenol Red (Sigma), diluted in nuclease-free water (Ambion).

For the establishment of a new transgenic fish line, embryos injected with an expression vector were bleached and raised to adulthood. Germline transmission was detected by outcrossing adult fish and screening their progeny for the expression of the transgenic co-injection marker (present in the backbone of the injected expression vector) and for construct expression. Upon positive expression, F1 embryos were raised to adulthood. The following transgenic lines were generated following this protocol: LexOP:lyn-mIRFP670 (far-red membrane marker), UAS:Centrin-mIRFP670 (far-red centrosomes), CMV:NCAM1b-tagRFPt, UAS:NCAM1b-tagRFPt, LexOP:lyn-mNG-ziFGFR-LOV-HA, LexOP:lyn-mRFP-ziFGFR-LOV-HA and LexOP:lyn-ziFGFR-LOV-HA (see section 2.4.1).

The following published transgenic lines were used in this study: cxcr4b:nls-tdTomato [Donà et al., 2013], cldnb:lyn-GFP [Haas & Gilmour, 2006], gal4 ETLGA346 (GAL4/UAS driver line, described in section 2.4) UAS:mCherry [Distel et al., 2009], cxcr4b:LexPR (driver line described in section 2.4), Cdh2:Cdh2-GFP [Revenu et al., 2014], foxd3:GFP [Gilmour et al., 2002], LexOP:FGF3-GFP [Durdu et al., 2014], LexPR/LexOP:lyn-RFP [Durdu et al., 2014]. Brn3c:mGFP [Xiao et al., 2005] and AlpI:mCherry [Steiner et al., 2014] lines were a kind gift of Dr. Aaron Steiner.

The following transgenic lines were generated by other current of former members of the lab: cxcr7b:lyn-mKate2 was generated by Sabine Görgens and Andreas Kunze, taking advantage of Crispr\Cas9 approach to remove sfGFP from the original Cxcr7b:lyn-mKate2sfGFP made by Alejandra Guzman Herrera; UAS:NCAM1b-GFP and LexOP:nls-GFP were established by Sevi Durdu.

2.4 Inducible gene expression system

To drive the expression of transgenic constructs in the lateral line system, two conditional transactivation methods were used, the LexPR/LexOP system [Emelyanov & Parinov, 2008] or the GAL4/UAS system [Distel et al., 2009]. These systems rely on the generation of an effector fish line, carrying the gene of interest placed under control of a responder element (LexOP or UAS), and a driver fish line, containing the transcriptional activator (LexPR or GAL4). Transactivation of the gene of interest only occurs when the effector line is combined with the driver counterpart in double transgenic animals.

The GAL4/UAS system is comprised of a GAL4/UAS:mCherry enhancer trap element (ETL GA346) that binds a 6xUAS synthetic promoter and transcriptionally activates the gene of interest placed under its control [Distel et al., 2009].

The LexPR/LexOP transactivation involves an additional level of control, provided by the binding of the progesterone analog RU-486 (Sigma) with the hybrid transcription factor LexPR [Emelyanov & Parinov, 2008]. Only upon RU-486-mediated stimulation LexPR can activate the synthetic promoter LexOP, which controls the expression of the transgene. LexPR is in turn expressed under the control of a tissue-specific promoter, which, in our driver line, is the upstream regulatory region of the lateral line chemokine receptor Cxcr4b. This chemically inducible transactivation system allows a stringent spatial

and temporal control of gene expression, with no detectable background expression in absence of the chemical induction. The LexPR driver line was generated by Andreas Kunze via BAC transgenesis [Durdu et al., 2014].

2.4.1 Maintenance of chemoFGFR transgenic lines

Unless otherwise stated, experiments were performed on stable chemoFGFR fish lines. We observed variable levels of chemoFGFR expression among embryos born from different parents, while, within each clutch of siblings, expression levels were consistent. For this reason, at every generation we selected animals whose offspring would give consistently strong chemoFGFR transactivation. To select them, adult chemoFGFR transgenic fish were out-crossed with LexPR driver fish and their progeny was screened after standard RU-486 induction (see section 2.7) for chemoFGFR expression at 48 hour post fertilization (hpf). Only fish giving a high expressing offspring were used for experiments and for propagation of the stable transgenic line. Moreover, to further control for heterogeneity of chemoFGFR expression during experiments, whenever possible we compared experimental embryos with control siblings from the same clutch.

2.5 Gene knockdown using morpholino

For morpholino-mediated knowdown, FGF10 morpholino (start site blocker, 5 ng/nl) [Norton et al., 2005] and FGF3 morpholino (splice site blocker, 5 ng/nl) [Kwon & Riley, 2009] were diluted in nuclease free-water (Ambion) to 1mM, heated to 65°C for 20 minutes and co-injected with Phenol Red (Sigma) in 1-cell stage embryos.

2.6 Gene knockout using Crispr/Cas9

2.6.1 Design and preparation of sgRNA guides

To achieve efficient gene knockout, we took advantage of the Crispr/Cas9 gene editing technology using a multi-guide targeting strategy that had been recently described [R. S. Wu et al., 2018a]. This approach involves redundant targeting of the gene of interest at four independent sites on the coding sequence, to increase the chances of obtaining null phenotypes already in injected G0 embryos (crispant). To generate Cdh2 (ENSDART00000024627.11) knockout, we used four anti-Cdh2 sgRNA guides reported in the zebrafish genome-wide guide table provided by the authors alongside the publication [R. S. Wu et al., 2018a]. Each sgRNA guide targeted a different exon of the gene. For NCAM1b (ENSDARG00000007220) and NCAM1a (ENSDARG00000056181) knockout, we instead employed the CRISPRscan software [Moreno-Mateos et al., 2015] to design and select sgRNA guides targeting the Fibronectin domain I. To favor site-spanning deletion of large fragments, the four sgRNA guides targeted sites within a genomic region of 150 bp [R. S. Wu et al., 2018a]. To generate templates

for sgRNA guides, we performed Overlap PCR (KAPAHiFi hot-start polymerase, Kapa Biosystems) between a scaffold oligo, carrying the standard Cas9-binding sequence, and the designed guide oligo, containing T7 promoter, target-specific sequence and an overlapping sequence [Varshney et al., 2016; R. S. Wu et al., 2018a].

Overlap PCR mix:

Components	Volumes per sample (50 µm reaction)	Final concentration
Nuclease free water	28.5 µl	-
Scaffold Oligo (100 µM)	5 µl	10 µM
Guide Oligo (100 µM)	5 µl	10 µM
KAPAHiFi polymerase (1 U/µl)	0.5 µl	0.5 U
KAPA dNTP Mix (10 mM each)	1 µl	0.2 mM
KAPA HiFi Fidelity Buffer (5X)	10 µl	1X

Cycling conditions:

98°C 30 sec
45 cycles of:
98°C 10 sec
60°C 10 sec
72°C 15 sec
72°C 5 minutes

Oligos used:

Scaffold Oligo sequence:
5'-
AAAAGCACCGACTCGGTGCCACTTTTTCAAGTTGATAACGGACTAGCCTTATTTTAACTTGCTATTTCTAGCTCT
AAAAC-3'

sgRNA set Cdh2:
guide1: 5'-TAATACGACTCACTATAGGAACGATGTACCGTTCCGGGTTTTAGAGCTAGAAATAGC-3'
guide 2: 5'-TAATACGACTCACTATAGGTGTTGGACAGACCATACGGTTTTAGAGCTAGAAATAGC-3'
guide 3: 5'-TAATACGACTCACTATAGGATTCCAGGCTGGAGTCCCGTTTTAGAGCTAGAAATAGC-3'
guide 4: 5'-TAATACGACTCACTATAGGTGCAACGTACCACTGATTGTTTTAGAGCTAGAAATAGC-3'

sgRNA set NCAM1b:
guide 1: 5'-TAATACGACTCACTATAGGGCCCTCGGCGCCGTCCATGTTTTAGAGCTAGAAATAGC-3'
guide 2: 5'-TAATACGACTCACTATAGGAGCCGAGTGGAGAGCCGTGTTTTAGAGCTAGAAATAGC-3'
guide 3: 5'-TAATACGACTCACTATAGGAGAGCCCGAGTCCACTGGGTTTTAGAGCTAGAAATAGC-3'

guide 4: 5’-TAATACGACTCACTATAGGAGGGCACATCTGCACCACGTTTTAGAGCTAGAAATAGC-3’

sgRNA set NCAM1a:
guide 1: 5’-TAATACGACTCACTATAGGGGAGCCTGCTTCCAGTGGGTTTTAGAGCTAGAAATAGC-3’
guide 2: 5’-TAATACGACTCACTATAGGCCCCCTCTATCGAGCGTGGTTTTAGAGCTAGAAATAGC-3’
guide 3: 5’-TAATACGACTCACTATAGGCTCGATAGAGGGGGCCGAGTTTTAGAGCTAGAAATAGC-3’
guide 4: 5’-TAATACGACTCACTATAGGACCGAGAGTATGAACTTGGTTTTAGAGCTAGAAATAGC-3’

PCR products were verified for correct band length by agarose-gel electrophoresis and purified with MinElute PCR Purification Kit (Qiagen). Pooled *in vitro* transcription reactions were carried out for each guide set using MEGAshortscript T7 Kit (Ambion) and mRNA was purified with RNA Clean and Concentrator-5 Kit (Zymo Research) following manufacturer’s instructions. To test the efficiency of cut of sgRNA guides, *in vitro* digestion of template DNA using EnGen Spy Cas9 NLS (New England Biolabs) was performed prior to microinjections into embryos, according to manufacturer’s protocols.

2.6.2 Injections and imaging

To generate knockout animals, an injection mix containing 1 µg/µl sgRNA guides (four guides with a total concentration of 31 µM), 5 µM EnGen Spy Cas9 NLS (New England Biolabs), 4% Phenol Red and 300 mM KCl was microinjected in 1-cell stage embryos, after incubation of the mix at 37°C for 5 minutes and at room temperature (RT) for 30 minutes. Injected embryos were screened for the expression of transgenic markers and, if required, induced at 26hpf with RU-486 (as described in section 2.7). At 48hpf, samples were imaged with Leica MZ16F Fluorescence stereoscope or mounted and imaged with Zeiss LSM880 with AiryScan technology (as described in section 2.9.1).

2.6.3 Genotyping

To associate phenotype with respective genotype, after imaging embryos were individually dislodged from the imaging dish and univocally labeled before proceeding to mutant identification. Genomic DNA was isolated from each labeled embryo using QuickExtract DNA Extraction Solution (Epicentre). Region-specific primers (listed below), designed with NCBI primer-BLAST [Ye et al., 2012] and purchased from Microsynth, were used to PCR-amplify target genomic regions (KAPAHiFi hot-start polymerase, Kapa Biosystems).
For NCAM1b and NCAM1a genotyping, agarose-gel electrophoresis of PCR products was performed to allow detection of extra and smeared bands (2.5% agarose in TBE). To confirm the results, after gel extraction (MinElute Gel Extraction Kit, Qiagen), PCR fragments from individual embryos were sent for sequencing to an external provider (Microsynth). For Cdh2 genotyping, PCR products were gel-extracted after electrophoresis (1.5% agarose gel in TBE) and sent for sequencing (Microsynth).

Primers for genotyping:

sgRNA Cdh2:
Target region 1: product of 322 bp
Forward: 5'-CTTCAGTACCAGACCGAGCG-3'
Reverse: 5'-CGCATAGGGGGAATTGTTCG-3'

Target region 2 and 3: product of 923 bp
Forward: 5'-GTAACTTGCCATAAACCTTTGAAGC-3'
Reverse: 5'-AGGATATGCGAAAAGTGAGAGA-3'

Target region 4: product of 519 bp
Forward: 5'-CTCGCGTCTTCCCACAAGAA-3'
Reverse: 5'-ATCAAATCCACTGCCCGGAA-3'

sgRNA NCAM1a: product of 469 bp
Forward: 5'-GAACCATTCCCCAAGCCCAT-3'
Reverse: 5'-AGCCTCCCAAAAGCCTCATTT-3'

sgRNA NCAM1b: product of 338 bp
Forward: 5'-TTTGAAGTGTCTCCCCTGTGG-3'
Reverse: 5'-GTACGGCCATGGTCTGACT-3'

2.7 Chemical treatments

To prevent skin pigmentation and maintain embryonic transparency during imaging, when required, embryos were treated with 0.002% N-phenylthiourea (PTU) (Sigma-Aldrich) starting at 22hpf.

RU-486 (Sigma) was used to induce LexPR\LexOP-driven gene expression (see section 2.4). For endpoint imaging, expression of LexOP constructs was induced by incubating decorionated embryos with 20 µM RU-486 in E3 from 26hpf to 48hpf, unless otherwise stated. For overnight (ON) time lapse experiment the same concentration of RU-486 was also added to the low melting agarose used for mounting and in the E3 medium (see section 2.9.3). For experiments where image acquisition was performed at 3 or 4 days post fertilization (dpf), RU-486 treatment was still conducted as described and then washed out at 48hpf by transferring the treated embryos in clean E3. Transactivation of the LexPR/LexOP system had been shown to occur relatively fast [Emelyanov & Parinov, 2008] and the delay observed between induction and detection of target gene signal is likely due to the timespan required for synthesis and maturation of the fusion construct (in case of chemoFGFR, it is of around 5-6 hours, see section 2.9.3).

To inhibit FGFR activity, decorionated embryos were incubated with 1 µM SU5402 (Calbiochem) in E3 from 26hpf to 48hpf. Control embryos were treated with 0.1% DMSO. Co-treatments of 1 µM SU5402 and 20 µM RU-486 or RU-486 alone were performed in parallel to evaluate the effect of SU5402 on chemoFGFR-dependent phenotype. These treatments were carried out in 24 Well plates (Nunc), with a density of eight embryos per well in 2 ml of solution.

2.8 Staining of fixed embryos

2.8.1 Fixation and permeabilization

After decorionation, embryos were fixed overnight (ON) with 4% PFA in PBS-T (PBS with 0.1% Tween-20) at 4°C. Following 3 rinsing steps in PBS-T for 5 minutes, embryos were permeabilized with pre-cooled 100% methanol (Sigma-Aldrich) ON at -20°C. Dehydrated embryos could be so stored for several months. Prior to colorimetric in situ hybridization or antibody staining, dehydrated embryos were rehydrated through an inverse methanol series at RT (75%, 50% and 25% Methanol in PBS-T, 5 minutes each step) and 2 washing steps in PBS-T.

2.8.2 Colorimetric in situ hybridization

In situ hybridization (ISH) of pea3 and Krt1c5 was performed according to standard protocols using the NBT/BCIP (Roche) detection method [Lecaudey et al., 2008; C. Thisse & Thisse, 2008; Valentin et al., 2007]. Pea3 and Krt1c5 digoxigenin-labeled probes were generated respectively by Sevi Durdu and Maaike Allers by *in vitro* transcription using the DIG Labeling Kit (Roche) following published protocols [C. Thisse & Thisse, 2008]. DAPI staining and anti-GFP antibody staining (Rabbit-anti-GFP primary antibody with Alexa488-anti-rabbit secondary antibody) were performed to counter-label the lateral line [Valentin et al., 2007].

2.8.3 Antibody staining

After fixation and permeabilization, rehydrated embryos were kept in blocking buffer (1X PBS, 1%DMSO, 2%NCS, 1%BSA, 0,1%Tween) for 1.5 hour and incubated with primary antibody diluted in blocking buffer at 4°C ON. Specifically, mouse-anti-Acetylated Tubulin (Sigma-Aldrich) was diluted 1: 1000, mouse-anti-ZO1 (Zymed) 1:200, while rabbit-anti-GFP antibody (Torrey Pines Biolabs), employed to counterstain the lateral line, 1:500. After being washed 4 times for 30 minutes in blocking buffer, embryos were incubated for 2.5 hours with secondary antibody. Specifically, goat-anti-mouse Alexa 568 Fluor, donkey-anti-mouse Alexa Fluor 647 and goat-anti-rabbit Alexa Fluor 488 secondary antibodies (Molecular Probes) were all diluted 1:500 in blocking buffer. Embryos were then rinsed in PBS-T 3 times for 30 minutes and stained with DAPI (1:1000) (Molecular Probes) in PBS-T for 10 minutes, before mounting in 0.8% low melting agarose (PeqLab) in PBS and imaged.

2.8.4 Single molecule fluorescent in situ hybridization (smFISH)

Single molecule fluorescence in situ hybridization (smFISH) was performed according to standard protocols [Durdu et al., 2014; Raj et al., 2008] using published Quasar 670 conjugated Stellaris RNA FISH probes designed to target pea3 mRNA (Biosearch Technologies), listed below [Durdu et al., 2014]. After treatment with PTU and 20 µM RU-486 (described in section 2.7) and fixation at 38hpf (described in section 2.8.1), embryos were washed 3 times in PBS-T and manually de-yolked. Embryos were then pre-incubated with hybridization buffer (0.1 g/ml dextrane sulfate, 0.02 g/ml RNAase free BSA, 1 mg/ml E.Coli tRNA, 10% formamide, 5x SSC, 0.1% Tween-20 in ddH20) at 30°C for 30 minutes and hybridized with the pea3 probe solution (concentration of 0.1 µM in hybridization buffer) at 30°C ON in the dark. Embryos were finally stained with DAPI (1:1000) in washing buffer (10% formamide, 5x SSC, 0.1% Tween-20 in ddH20) for 15 minutes at 30°C and rinsed with washing buffer 45 minutes at 30°C. To prevent fading of fluorescence due to photobleaching, VECTASHIELD HardSet mounting medium (Vector Laboratories) was used for the mounting of embryos on glass slices and samples were imaged immediately. Z-stacks were acquired using a 100x oil immersion objective (NA 1.4) on a PE Ultraview VOX spinning disk confocal (PerkinElmer), with a voxel size of 0.2 µm in z and of 0.07 µm in xy. smFISH spots were segmented in Imaris 7.6.4 (Bitplane), following a published pipeline established by Sevi Durdu [Durdu et al., 2014]. The number of smFISH spots detected in an organ was divided by the number of nuclei to obtain transcript count per cell.

As a further internal control, for all staining experiments whenever possible, sample embryos and controls were siblings and were pooled together in the same tube, to ensure identical treatment and processing throughout the protocol. Prior mixing, embryos from different conditions were differentially marked to enable identification, for instance with oriented incisions on the tail applied during a post-fixation rinsing step.

Pea3 smFISH probes:
1:aaggaagacggacagaggca, 2:ctgtgttttaatgagctcca, 3:cttaaccgtttgtggtcatt, 4:ccatccatcttataatccat,
5:agtataaggcacttgctggt, 6:atttccttgcgacctattag, 7:tcaacagtctatttaggggc, 8:atgtatttccttttttgtcgc,
9:aagaggtcttcagattcctg, 10:cctgaagttggcttaaatcc, 11:ggaacttgagcttcggtgag, 12:aacaaactgctcatcgctgt,
13:cactgagttctctgagtgaa, 14:ttcttaatcttcacaggcgg, 15:tagctgaagctttgcttgtg, 16:tcataggcactggcgtaaag,
17:ctggacatgagctcttagat, 18:ttgggggaataatgctgcat, 19:tgagggtggattcatatacc, 20:cggaagggaacctggaactg,
21:agagtgttgccgatggaaac, 22:tgctgaggaggataaggcaa, 23:ccatgtactcctgcttaaag, 24:tcctgtttgaccatcatatg,
25:caggttcgtaagtgtagtcg, 26:tgtgatggtacatggatggg, 27:aaacatgtagccttcactgt, 28:tggcacaacacgggaatcat,
29:tcacctcaccttcaaatttc,30:accttcacgaaacacactgc, 31:tagttgaagtgagccacgac, 32:gaagggcaaccaagaactgc,
33:atgcgatgaagtgggcattg, 34:atgagtttgaattccatgcc, 35:ttgtcatagttcatggctgg, 36:gtaacgcaaagagcgactca,
37:ttttgcataattccccttctc, 38:aggttatcaaagcttctggc, 39:cgctgattgtcgggaaaagc, 40:gttgacgtagcgctcaaatt,
41:aagaaactccctcatcgagg,42:tacatgtagcctttggagta,43:aaaggagaatgtcggtggca,44:gtggtaaactgggatgggaa,
45:atacaagaggatggggtggg,46:gaatgcagagtccctaatga,47:agataggcctcagaagtgag,48:gcaatctcttgaaccacagt

2.9 Live imaging

2.9.1 Sample preparation

To perform live imaging, embryos were decorionated manually with forceps or with 10 µg/ml pronase. Embryos were then anaesthetized with tricaine, preselected at the stereoscope based on expression of fluorescent markers of interest and embedded in 0.8% low melting agarose (PeqLab) in E3 containing 0.01% tricaine. Embryos were then mounted on their side on a MatTek glass-bottom dish (with glass thickness of 0.16-0.19 mm or 0.085-0.13 depending on the working distance required) or on a CELLview 4-chamber glass-bottom dish (with 0.17 mm glass thickness) (Greiner bio-one). For live imaging experiments, at most eight embryos were mounted per dish. After solidification of the agarose, 2 ml of E3 containing 0.01% tricaine were added to the dish.

2.9.2 Microscopes

The following microscopes and objectives were employed in this study:
Leica MZ16F fluorescence stereoscope was used for colorimetric in situ imaging and for acquisition of embryo overviews.
Imaging of live or fixed samples was performed using PE Ultraview ERS spinning disk confocal (PerkinElmer) (henceforth ERS), PE Ultraview VOX spinning disk confocal (PerkinElmer) (henceforth VOX), Olympus IXplore SpinSR10 spinning disk confocal (henceforth Olympus), Zeiss LSM880 with AiryScan technology (Zeiss) (henceforth LSM880), Zeiss LSM980 with AiryScan technology (Zeiss) (henceforth LSM980).
SU5402 (section 2.7) and morpholino (section 2.5) imaging was performed on VOX using respectively Zeiss 20x (0.8NA) and Zeiss 10x (0.45NA) air objective. Pea3 smFISH images were acquired on VOX with Zeiss 100x (1.4NA) oil objective. For all the other experiments, Zeiss 40x (1.2NA) water objective with Immersol W immersion fluid (Zeiss) was used on ERS and VOX, Zeiss 40x (1.2NA) objective with silicon oil immersion was used on LSM880 and LSM980, Olympus 60x (1.3NA) objective with silicon oil immersion on the Olympus scope. On LSM880 and LSM980, an optimized acquisition speed was achieved using AiryScan FAST mode [Huff, 2016] together with a piezo stage and bi-directional scanning.

2.9.3 Time lapse experiments

To capture the behaviors of chain cells in real-time, overnight time lapse experiments were performed. Decorionated embryos were pre-treated with 20 µM RU-486 at 26hpf and, after 5 hours of incubation required for chemoFGFR expression to be detectable, embryos showing the desired combination of fluorescent labels were mounted on a 4-chamber imaging dish as described in section 2.9.1. Both the agarose used for embedding and E3 medium added post-solidification were supplemented with 20 µM RU-486. At most, six embryos were mounted per chamber. For time lapse imaging, a multi-position setup was used. This enabled the acquisition of multiple consecutive z-stacks across embryos with z-

step size of 1-2 µm and time resolution of 15 minutes between time points. For each z-stack, both red channel, detecting tdTomato nuclei, and green channel, detecting chemoFGFR mNG, were acquired. Incubation temperature throughout the 14-22 hours of imaging was kept constant at 28°C. 40x objectives were employed for acquisition on ERS, VOX and LSM880 (see section 2.9.2 for the specifics of different objectives). A custom-made feedback microscopy tool implemented by another member of the lab, Jonas Hartmann [Hartmann, 2019] built upon the Microscopy Pipeline Constructor macro (MyPiC)[Politi et al., 2018], was used to ensure autofocus of cells across multiple positions and time points for LSM880 time lapses.

2.9.4 Optogenetic activation

To test activity of the chemoFGFR construct in light and dark conditions in early embryos, embryos microinjected with mRNA and uninjected controls were each split in two batches one hour after injection: one batch was kept in dark conditions to prevent chemoFGFR activation, and the other kept under constant blue light conditions in an ExoTerra incubator equipped with LED lights (ExoTerra Thermoelectric Reptile Egg Incubator) at 30°C. Embryos were then fixed at around 8hpf (protocol described in section 2.8.1). To avoid ambient light exposure, embryos kept in a dark regime were fixed in presence of red lighting. Finally, pea3 in situ hybridization was performed as described in section 2.8.2. To test activity of chemoFGFR constructs in light and dark conditions in stable lines, embryos preselected for the presence of desired labels were chemically induced at 26hpf (section 2.7) and exposed to the dark-light regime described above. Embryos were then fixed at 36hpf and pea3 in situ hybridization was performed. To test light-dependency of the clustering phenotype, the above-mentioned protocol was employed, with the exception that embryos were left in the light-dark regime until imaging at 48hpf. Given that imaging time is negligible in comparison to the time required for the development of a clustering phenotype, embryos overviews were captured live using stereoscope and confocal.

For chemoFGFR experiments, unless otherwise stated, we standardly exposed embryos to constant blue light illumination following induction with 20 µM RU-486 from 26hpf until imaging, since we observed a stronger chemoFGFR-dependent phenotype in light than in dark conditions. However, for time lapse experiments (described in 2.9.3), embryos were kept in dark condition during the 5 hours pre-treatment (with 20 µM RU-486) preceding mounting and imaging.

2.10 Image analysis

2.10.1 Image preprocessing

Prior preprocessing, images acquired with LSM880 or LSM980 were deconvolved with the built-in 3D AiryScan deconvolution tool on ZEN Black or Blue software with default settings (‘auto’ mode). Image preprocessing was performed in Fiji [Schindelin et al., 2012], unless otherwise specified. 16bit z-stacks were linearly rescaled to 8bit TIFF format, setting as minimum and maximum either image-specific

minimum and maximum intensity values (to allow an optimal visualization of the signal for each image) or fixed values kept identical across all images of the dataset (for comparative analysis or where intensities were relevant). To obtain whole lateral line overviews, individual z-stacks acquired with the multi-position setup were flatten by maximum intensity z-projection and stitched using the Grid stitching plugin or the deprecated-3D stitching plugin in Fiji [Preibisch et al., 2009]. When necessary for representative purposes (never before analysis), images were straightened, resliced (from xy-z to yz-x), rotated or cropped [Schindelin et al., 2012]. To process images automatically, Fiji custom-made macros were employed, some of which implemented from templates, while others generated by other members of the lab (Jonas Hartman and Max Brambach) and applied with only minor adaptations. When required, linear unmixing was performed to remove the bleed-through of nls-tdTomato nuclear label into the green channel, using a custom-made script written by another member of the lab, Jonas Hartmann [Hartmann et al., 2020].

2.10.2 Cluster counting and 2D analysis of cluster and cell shape

To quantify the clustering phenotype of chemoFGFR embryos kept in light-dark regime (see section 2.9.4) and of FGF3 overexpressing, chemoFGFR and control embryos, manual counting of neuromasts and clusters was performed on overviews of 48hpf embryos co-labelled with nls-tdTomato marker. To compare the clustering phenotype in FGF3-FGF10 morpholino experiments (see section 2.5), clusters and neuromasts were manually counted on stitched images of 48hpf embryos expressing cldnb:lyn-GFP (a uniform lateral line membrane marker) and chemoFGFR mRFP, acquired with VOX and processed as described (section 2.10.1). We defined as 'cluster' an aggregate of at least three cells with nuclei tightly packed together.

For the analysis of phenotypes in Cdh2 and NCAM1 Crispr experiments (see section 2.6), only clusters formed between first and second neuromast were acquired. The following 2D shape descriptors were calculated on z-projections using Fiji's Analyze options [Schindelin et al., 2012], after manually drawing cluster contours with Fiji's Polygon Selection Tool:

$$Aspect\ Ratio = major\ axis / minor\ axis$$

$$Compactness = \frac{\sqrt{4 * area/\pi}}{Feret\ diameter}$$

$$Circularity = 4\pi * area/perimeter^2$$

where 'axis' represents the axis of an ellipse fitted in the selected surface.

To measure circularity of groups of cells aggregating in clusters across time, z-projections from time lapse experiments were analyzed (see 2.9.3). The area of interest was selected by drawing contours (Fiji's Polygon Selection tool) for every time point.

To compare the aspect ratio of solitary cells expressing chemoFGFR mNG or lyn-mNG control in mosaic experiments, surfaces of cells expressing the construct were automatically retrieved by applying Fiji's

Otsu thresholding [Nobuyuki Otsu, 1979] on the mNG green channel. Shape parameters were extracted from the 2D binary masks using the Analyze Particle tool.

2.10.3 Cell classification based on chemoFGFR expression and cell positioning

Classification of cells as chemoFGFR positive or negative was performed by examining chemoFGFR fluorescence signal at the plasma membrane (in the red channel for chemoFGFR mRFP and in the green channel for chemoFGFR mNG) in z-projections and, when needed, z-stacks. Cells with detectable signal in the appropriate channel were considered chemoFGFR positives while cells that presented no detectable chemoFGFR signal were considered chemoFGFR negatives.

Classification of cells within clusters as part of the inside 'seed' or of the peripheral 'rim' was performed on flat z-projections. Cells were classified depending on the position of their nucleus relatively to a reference point, the cluster apical center (yellow dot). Cell nuclei that were facing directly the reference point, without other nuclei obstructing, were considered part of the cluster seed (red arrows and red marks in Figure 2.1), while cells whose nuclei were 'shielded' for most of their surface from facing directly the reference point, were identified as rim (blue shadows and blue crosses in Figure 2.1). For this analysis, we only considered clusters of at least four cells where an apical center was reliably identifiable.

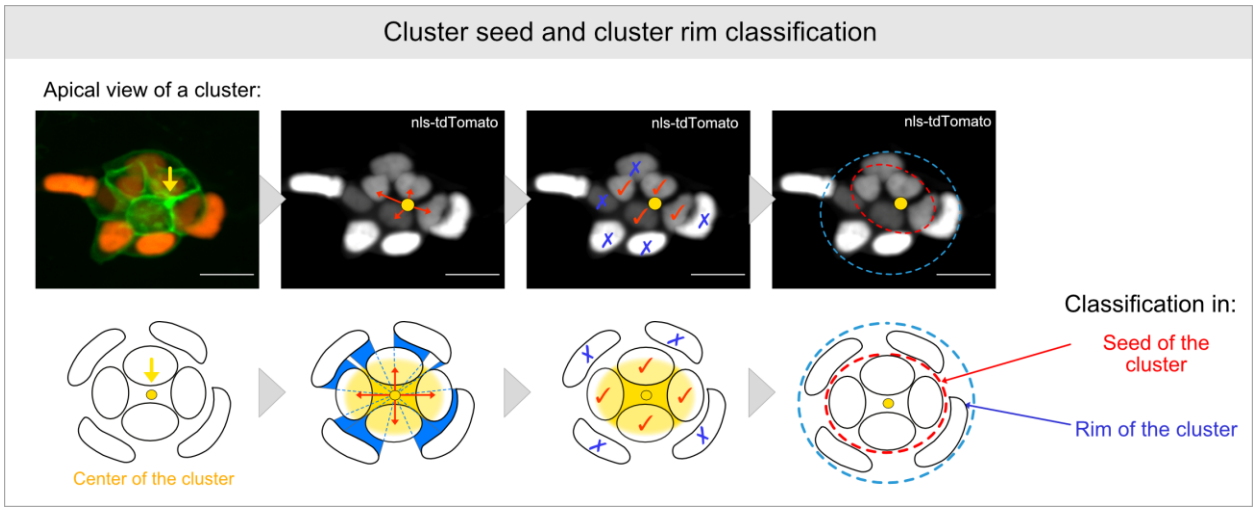

Figure 2.1: Position-based classification of cells within clusters

Schematic displaying the classification of cells within a cluster as belonging to the 'seed' or to the 'rim' of the cluster. The apical center of the cluster, represented as a yellow dot, is the reference point used for the classification. Cells whose nuclei directly face the reference point in 2D z-projections are considered part of the seed (indicated with red marks), while cells whose nuclei are positioned externally are part of the rim (indicated with blue crosses). Scale bar 10 µm.

2.10.4 Quantification of signal intensity and distribution of adhesion proteins

For Cdh2 quantifications, the Cdh2:Cdh2-GFP BAC line [Revenu et al., 2014] was employed. The analysis was performed on preprocessed dual-color z-stacks of 48hpf chain cells expressing Cdh2-GFP

with or without chemoFGFR (drug induction detailed in section 2.7), acquired using LSM880 (40x). 16bit to 8bit conversion was performed using manually selected values for rescaling, chosen with respect to the intensity range of Cdh2-GFP in the dataset and applied identically across all samples and controls. To quantify absolute Cdh2 intensities in chain cells (Figure 2.2 a), 'side' membrane portions (not contacting other membranes) were selected in various z-slices using Fiji's Line tool (line width=1 µm) and signal intensity was measured in the Cdh2 channel. Three measurements per cell were acquired and their mean was background subtracted. ChemoFGFR mRFP channel was used to assign to each cell chemoFGFR positive or negative identity.

To quantify Cdh2 enrichment at cell interfaces, fold increase in signal was measured (Figure 2.2 b). As a control, chain cells co-expressing Cdh2-GFP with uniform membrane label lyn-mKate2 were imaged. To evaluate enrichment, we drawn ROI lines (using Fiji's Line tool, line width=1 µm) along the interface between 2 cells and along 'side' membranes and we acquired, in both locations, signal intensity for both Cdh2 channel and secondary membrane channel, which was lyn-mKate2 for wild types and chemoFGFR mRFP for samples. Interfacial fold increase observed in Cdh2 channel was then normalized by interfacial fold increase retrieved in the secondary membrane channel (Figure 2.2 b).

To generate intensity line profiles for NCAM1b and Cdh2 at cell interfaces (chains, periderm and doublets), preprocessed z-stacks were sum-projected and Fiji's Plot Profile tool was used to extract intensity measures along a manually selected line (line width=1 µm).

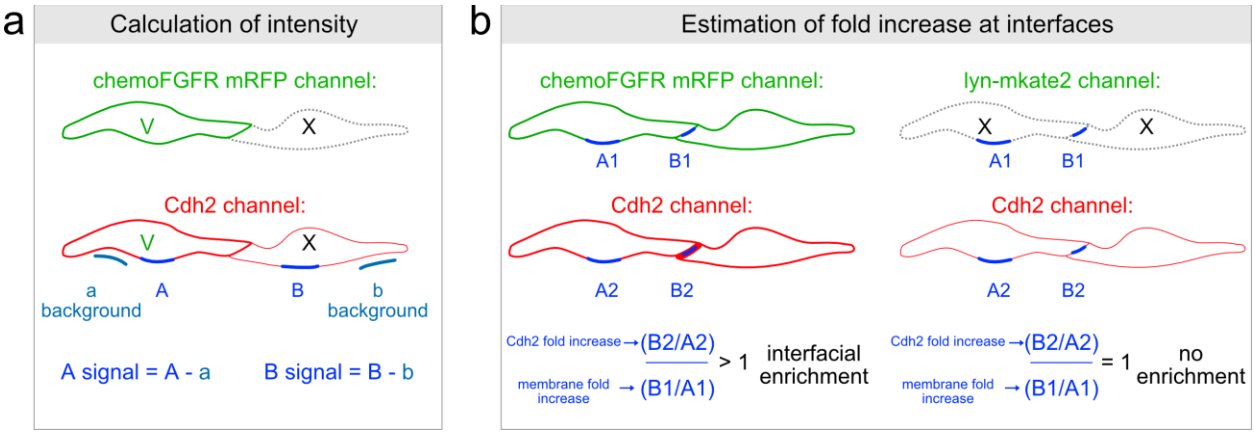

Figure 2.2: Analysis of Cdh2 levels

(a) Schematic representing the analysis of Cdh2 absolute intensities. For simplicity, in the schematic only one A line and B line was drawn, while for the analysis three ROI lines were acquired for each cell. (b) Schematic representing fold increase calculations at cell-cell interfaces. ChemoFGFR mRFP or lyn-mKate2 channels were used as uniform membrane labels to normalize the fold increase of the Cdh2 channel.

2.10.5 Analysis of centrosome orientation

Dual-color z-stacks of 48hpf chemoFGFR mNG expressing embryos and controls, microinjected at 1-cell stage with centrin-tdTomato mRNA (labeling centrosomes), were acquired using ERS scope (40x) with 0.5 µm sectioning. Following preprocessing, the analysis was performed on 2D z-projections of cluster cells and wild type chain cells across the whole lateral line. Single cell polarity angles

represented in the rose plots, were measures of the angle between the centrosome, the 2D centroid of the cell nucleus and a reference point, extracted using the Angle tool in Fiji. As reference point for chain cell analysis we used the y-axis, while, for cluster cell analysis, we used the apical center of each cluster, previously selected manually on the membrane/nuclear channel with Fiji's Multi-point selection. To reliably assign each centrosome to the nucleus of the same cell (labeled with LexOP:nls-GFP), 3D z-stacks were examined alongside the relative 2D z-projections. Cells with multiple centrosomes (likely a consequence of construct misexpression or of the proliferative state of a cell) were excluded from the analysis. This pipeline could not be applied for neuromast cells since the nucleus-centrosome assignation was not reliable.

To analyze centrosome orientation separately for chemoFGFR positive and negative cells within clusters, the above mentioned analysis was applied with two differences: first, to enable 3-color imaging, we generated a fish line containing a far-red version of centrin (LexOP:Centrin-mIRFP670, LexPR) and we combined it with nls-tdTomato nuclei and chemoFGFR mNG; second, images were captured on a LSM880 confocal.

To analyze the nucleus-centrosome configuration of wild type chain cells, we classified chain cell pairs in four categories depending on the positioning of centrosome relative to the nucleus in both cells of each pair and we recorded coordinates of manually selected nuclei with Fiji's Multi-point tool. Distances between consecutive nuclei for each category were calculated in excel and plotted in python.

2.10.6 Hair and mantle cell differentiation analysis

For the analysis of hair cell differentiation, the Brn3c:mGFP fish line was used [Steiner et al., 2014; Xiao et al., 2005]. High-resolution z-stacks of 48hpf embryos fixed and labeled with DAPI with or without chemoFGFR mNG expression were acquired on a LSM980 confocal (40x). Following image preprocessing, the number of *de novo* clusters having at least one Brn3c-labeled cell and the number of Brn3c-labeled and unlabeled cells within each cluster or wild type neuromast were quantified on z-projections. Brn3c-labeled cells were classified as chemoFGFR positive or negative cells as previously described (see section 2.10.3).

For the analysis of mantle cell differentiation, the AlpI:mCherry fish line was used [Steiner et al., 2014]. High-resolution z-stacks of 48hpf or 72hpf live embryos with or without chemoFGFR mNG expression were acquired on a LSM980 confocal (40x) and preprocessed. Two main factors complicated the interpretation of the AlpI:mCherry signal within *de novo* clusters. First the fact that clusters derive from chain cells, that are also strongly labelled with AlpI:mCherry. Following our standard induction protocol (section 2.7), cell clustering normally occurs between 31 and 48hpf. As a consequence, if we image embryos too early after induction, we cannot disentangle whether AlpI:mCherry signal in a certain cell of the cluster is high because the cell has just joined the cluster or because of mantle cell differentiation. Second, being mCherry cytoplasmic, proliferation during cluster formation might cause signal dilution, leading to a reduction of the AlpI:mCherry signal independent of the differentiation state of the cell. To partially circumvent these issues caused by the dynamics of *de novo* cluster

formation, we shifted the endpoint of the AlpI:mCherry analysis within *de novo* clusters from 48hpf to 72hpf. Moreover, given the heterogeneity of the AlpI:mCherry signal levels, in our quantifications we considered '*bona fide*' AlpI:mCherry cells only the ones showing expression levels above a threshold (retrieved from AlpI:mCherry levels observed within wild type neuromasts). AlpI-labeled cells were classified as chemoFGFR positive or negative cells as previously described (see section 2.10.3).

2.10.7 Nuclei detection and kymograph generation

Automatic detection of nuclei and kymograph generation were implemented in a custom python script generated in collaboration with another member of the lab, Jonas Hartmann. The following python modules were used: scikit-image 0.13.0 [Van Der Walt et al., 2014], numpy 1.11.3 [Oliphant & Millma, 2006] and scipy.ndimage 2.0 [E. Jones et al., 2001]. Shortly, time lapse imaging was performed on an ERS spinning disk (40x objective) as previously described (section 2.9.3). After preprocessing in Fiji (section 2.10.1), stitched z-projections of lateral lines co-expressing chemoFGFR mNG and nuclear nls-tdTomato were cropped to remove tdTomato-labelled nuclei not belonging to the lateral line. The nuclear nls-tdTomato channel was processed according to the following pipeline: nuclei were smoothed (gaussian smoothing σ=3 pixels), background subtracted (adaptive background subtraction modality) and binarized with an Otsu Automated Threshold. To split erroneously fused nuclei, a distance transform map was calculated and the maxima retrieved were annotated as nuclei seeds. Seeds were then individually labeled and watershed was applied. To correct for over-split nuclei, we took advantage of the observation that a nucleus boundary displays a decreased fluorescence intensity compared to a nucleus center. By comparing high-intensity pixels (above the 90th percentile) between a nucleus center and its putative nucleus boundary, we could discriminate correct splits from wrong ones. A 2D centroid was then automatically assigned to each nucleus and projected on a 1D spline line. Spatial coordinates of centroids were extracted from each time point, stored as projections on the spline line and plotted on kymographs.

2.10.8 Nuclei segmentation and analysis of orientation

High-resolution z-stacks of 48hpf lateral lines expressing a nuclear label (nls-tdTomato) with or without chemoFGFR mNG, were acquired using a 40x objective on a LSM880 confocal (voxel size: 0.099 µm in xy, 0.225 µm in z). The interactive machine-learning based software Ilastik [Berg et al., 2019; Sommer et al., 2011] was employed to segment lateral line nuclei in 3D. To retrieve nuclei, the nls-tdTomato channel was processed with Ilastik Pixel and Object Classification workflow. Segmented nuclei were then individually labeled using the Fiji plugin 3D object counter [Bolte & Cordelières, 2006] and nuclear shapes were analyzed using the 3D ROI manager plugin [Iannuccelli et al., 2010]. Moreover, single cell nuclear orientations were obtained by calculating Theta angles with the Inertia Ellipsoid module of Morpholib Fiji plugin [Legland et al., 2016]. Finally, segmented nuclei were manually classified depending on the organization the cell was part of (classification in neuromast nuclei, chain cells nuclei, *de novo* cluster nuclei) and on chemoFGFR expression (classification in chemoFGFR positive or negative cells). Nuclear segmentation was manually curated to remove wrongly merged or split nuclei.

The following nuclear features were plotted:

$$Theta\ angle = angulation\ of\ the\ major\ axis\ of\ the\ nucleus\ relative\ to\ XY\ plane\ of\ the\ image$$

$$Nuclear\ elongation = ellipse\ major\ axis / ellipse\ minor\ axis$$

where 'ellipse' is the ellipse inscribed in the segmented nucleus. Imaris 7.6.4 (Bitplane) was used for 3D image rendering.

2.10.9 Single cell segmentation and analysis of chemoFGFR phenotype

High-resolution z-stacks of 48hpf lateral lines expressing a uniform membrane label (cldnb:lyn-GFP) with or without chemoFGFR mRFP were acquired using a 40x objective on a LSM880 confocal (voxel size: 0.099 µm in xy, 0.225 µm in z). After preprocessing (described in section 2.10.1), 3D single cell segmentation and sphericity analysis were performed by another member of the lab, Jonas Hartmann, using a custom-made software detailed elsewhere [Hartmann et al., 2020]. Individual cells, previously labeled as part of wild type neuromasts, small clusters (composed of fewer than 8 cells) or large clusters (composed of 8 cells or more), were automatically classified as chemoFGFR positive cells or negative cells, based on their normalized chemoFGFR signal intensities: a threshold was set at the 50th percentile of fluorescence intensity and cells whose signal was above the threshold were classified as chemoFGFR positives and cell whose signal was below it as chemoFGFR negatives. Sphericity was measured for each cell and compared across categories. Specifically, cell sphericity was calculated as the mean deviation of a sample cell from a sphere centered on the cell centroid and with the radius of the mean sample cell [Hartmann et al., 2020]. The retrieved values were inverted and linearly normalized between 0 and 1, where sphericity of 1 indicates a perfect spherical shape.

2.10.10 Single cell tracking and measurements

After image acquisition (section 2.9.3) and preprocessing (section 2.10.1), time lapse z-projections were corrected for whole-tissue drifting due to embryonic growth using the Correct 3D-drift Fiji plugin [Parslow et al., 2014]. To track individual nuclei in 2D and extract cell speeds, Fiji's Manual Tracking plugin was employed [Cordelires, 2017]. Individual tracks of cells ending up in *de novo* clusters were manually examined to measure the net displacement of each cell (through acquisition of XY coordinates of the cell center in the first and last time frame) and the range of cluster formation (through acquisition of the XY coordinates, in the first time frame, of the most 'external' left and right cells ending up into each cluster). We moreover quantified for individual clusters the number of cells that were acquired via proliferation of cells already present within the cluster and the number of cells that were instead acquired via aggregation.
3D volumes of chain cells, neuromast cells and of cells assembling clusters were rendered with Imaris 7.6.4 (Bitplane), upon manual drawing of the cell contours within the software.

2.10.11 Analysis of compaction angles and cell-cell interfaces in doublets

To analyze doublet compaction, contact angles between the two cells (theta angles) were measured in z-projections across time points using Fiji's Angle tool. For each time point, the value reported on the plot was a mean of the top and bottom interface angles. Cell-cell interface lengths were calculated in z-projections, manually drawing lines using Fiji's Line tool for each time point.

2.11 Plotting and statistical analysis

All statistical analyses were performed in python using statannot [from https://github.com/webermarcolivier/statannot] or scipy.stats [E. Jones et al., 2001] packages. Non-parametric Wilcoxon rank-sum test (two sided) (also referred to as Mann–Whitney U test) was used to estimate statistical significance between two conditions. Plots were generated with python employing matplotlib 1.5.1 [J. D. Hunter, 2007] and seaborn 0.9 libraries [Waskom, 2018] within Jupyter Notebooks (jupyter 4.4.0, notebook 5.7.4) [Kluyver et al., 2016]. All boxplots displayed are standard box and whiskers plots showing median (black line), interquartile range and mean (white line). Individual data points are displayed on top of boxplots. Line plots used to represent circularity of clusters in time, contact angles and cell-cell interface lengths over time display mean (purple line), individual data profiles (dashed lines in different colors) and standard deviation (shaded area). Line plots used to evaluate enrichment of adhesion proteins at cell-cell interfaces were generated in excel. Sample sizes (n) are reported in figure legends. Significance was annotated as follow:

ns: $5e^{-2} < p <= 1$

*: $1e^{-2} < p <= 5e^{-2}$

**: $1e^{-3} < p <= 1e^{-2}$

***: $1e^{-4} < p <= 1e^{-3}$

****: $p <= 1e^{-4}$

For 3D single cell shape analysis (section 2.10.9), we computed effect size using Cohen's d [Cohen, 1988] to estimate the magnitude of the differences.

Effect size was estimated as follow [Cohen, 1988; Sawilowsky, 2009]:

no effect: d≈0.0

small effect: d≈0.2

medium effect: d≈0.5

large effect: d≈0.8

very large effect: d≈1.2

3 Results

3.1 Development and validation of a 'chemoFGFR' approach

3.1.1 Generation of an FGFR with optogenetic and chemically inducible control

We began by developing an approach to manipulate the activity of Fibroblast growth factor receptor 1a (FGFR) in a cell autonomous manner. FGFR, like most tyrosine kinase receptors, requires a ligand-induced homodimerization for activation and triggering of the signaling cascade downstream [B. Thisse & Thisse, 2005] (Figure 3.1 a). To control FGFR activity, we sought to replace the requirement for FGF ligand with chemically induced expression or with light control. We adapted an optogenetic FGFR strategy that had been successfully used in cell cultures [Grusch et al., 2014], which exploited a photosensitive LOV domain for light-mediated dimerization and consequent activation of the chimeric receptor. Following the design of the original chimeric construct, we fused the LOV domain, which dimerizes upon exposure to blue light, with the C-terminal end of the kinase domain of zebrafish FGFR (Figure 3.1 b). To obtain a construct that was responsive exclusively to light and not to endogenous FGF ligands, the extracellular domain of FGFR was omitted and a membrane tag introduced at the N-terminal to allow plasma membrane localization. We generated versions of this receptor coupled to different fluorophores (Figure 3.1 c) to facilitate using it in combination with existing reporter lines.

Tools based on FGFR are notorious for their tendency to spontaneously cluster when overexpressed, leading to constitutive activity [Kirchgeorg et al., 2018]. As FGF signaling is known to play critical roles in early development, from gastrulation onwards, changes in the activity of this key pathway lead to developmental arrest [Kirchgeorg et al., 2018]. Therefore, in order to gain an additional level of control, we placed the construct under the control of the chemically inducible expression system LexPR/LexOP (Figure 3.1 d) [Durdu et al., 2014; Emelyanov & Parinov, 2008]. LexPR/LexOP is a binary expression system that consists of a steroid-regulated variant of the LexA transactivator (LexPR), that can activate genes of interest that are coupled to a LexOP promoter in the presence of the progesterone analog RU-486. This gene expression system enables reliable temporal and spatial control of expression: timing of drug administration allows stringent temporal control of the transactivation, while tissue-specificity given by the promoter driving LexPR expression enables tight spatial restriction. As an extra layer of spatial control, drug concentration and time of administration can tune levels of mosaicism within the domain of expression, which is commonly observed in conditional expression systems [Ryding et al., 2001].

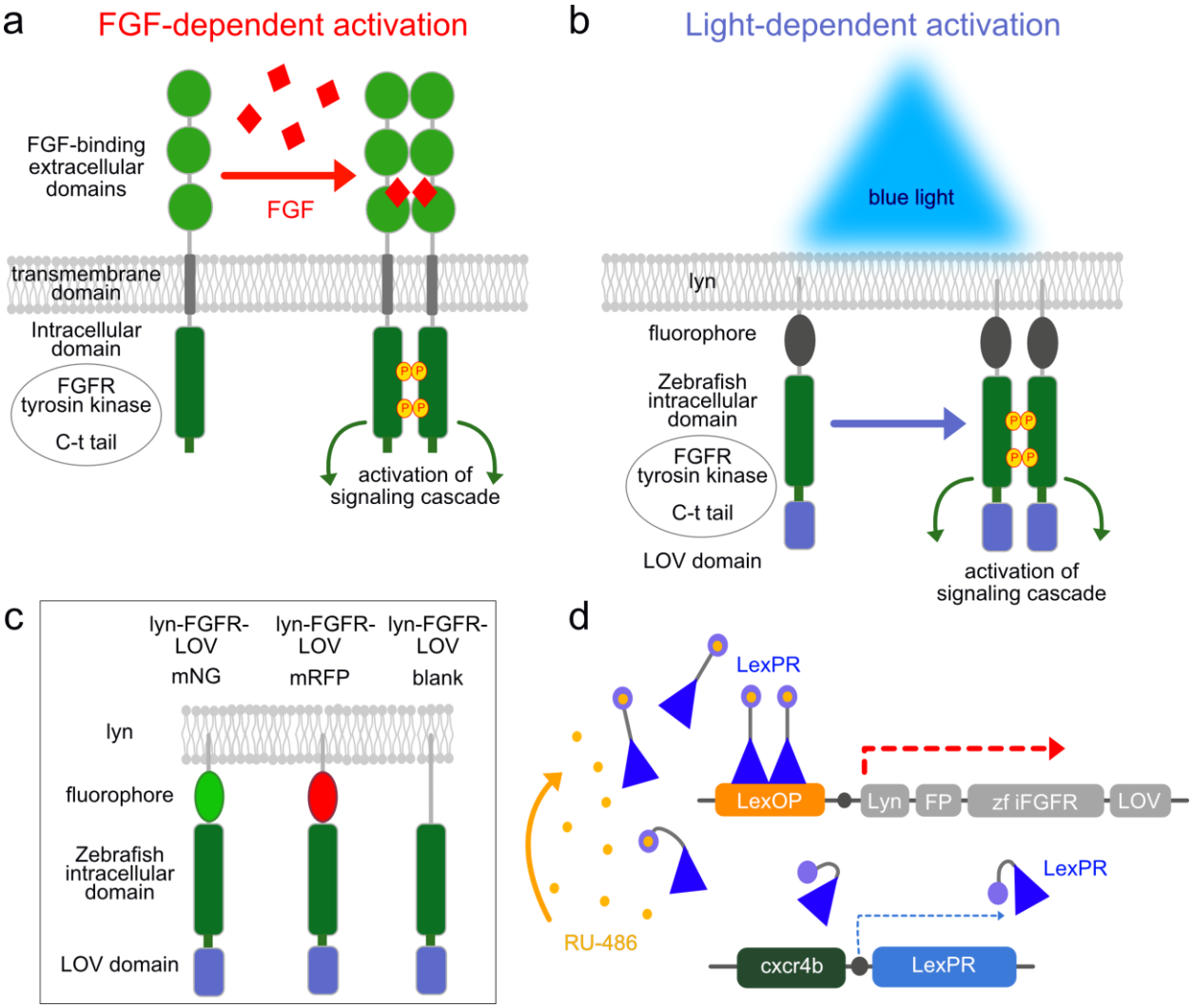

Figure 3.1: Design of optogenetic and chemically inducible lyn-FGFR-LOV constructs

(a) FGF-dependent activation of wild type FGFR. (b) Light-dependent activation of an optogenetic FGFR. Blue light induces dimerization of two chimeric proteins, driving cross-phosphorylation of kinase domains and FGF signaling activation. (c) Different versions of lyn-FGFR-LOV coupled with fluorophores. (d) Schematic representing chemically mediated control of protein expression via LexPR/LexOP transactivation system. The LexPR protein is expressed under the control of a lateral line chemokine receptor promoter (Cxcr4b). Upon binding with the inducer RU-487, LexPR couples with the LexOP promoter, driving expression of the protein of interest.

3.1.2 ChemoFGFR activates FGF signaling and drives cell clustering in the lateral line

We analyzed lyn-FGFR-LOV subcellular localization by plasmid microinjection in 1-cell stage embryos, finding that the chimeric protein was expressed and correctly localized at the plasma membranes of cells in 8 hour post fertilization (hpf) embryos (Figure 3.2 a). We next tested the ability of lyn-FGFR-LOV to activate FGF signaling upon blue light exposure by performing in situ hybridization (ISH) of pea3, a '*bona fide*' FGF signaling target [Durdu et al., 2014], on 8hpf embryos microinjected at 1-cell stage with lyn-FGFR-LOV mRNA and kept in a dark or light exposure regime. Injecting mRNA instead of DNA enabled uniform expression of the construct throughout the embryo. We found that embryos

microinjected with lyn-FGFR-LOV mRNA displayed high levels of pea3 expression throughout the entire embryos, losing the spatially restricted pattern of pea3 expression detectable in uninjected embryos (Figure 3.2 b). However, light-exposed and dark-kept embryos gave very similar results, suggesting that lyn-FGFR-LOV displays constitutive activity also in dark conditions, termed 'dark state activity', when expressed in this manner (Figure 3.2 b).

To test whether lyn-FGFR-LOV could be used to spatiotemporally control activation of FGF signaling within the lateral line system, we generated transgenic fish lines driving tissue-specific chimeric construct expression, exploiting the previously described LexPR/LexOP system. FGFR expression was induced treating 26hpf embryos with 20 µM RU-486 and embryos were either exposed to blue light or kept in the dark until 36hpf, when they were fixed and pea3 in situ was performed. We found that, as for early embryos, lyn-FGFR-LOV was not regulated by light but constitutively active also in the lateral line system (Figure 3.2 c). Nevertheless, the chemically inducible expression system LexPR/LexOP could still enable sufficient spatiotemporal control over FGF signaling, allowing tissue-specificity and cell-autonomous activation. Thus, we decided to exploit the constitutively active construct to activate FGF signaling in the lateral line system. As here expression of the FGFR is chemically inducible, we will use the term 'chemoFGFR' hereafter.

To assess the extent of FGF signaling upregulation upon chemoFGFR activity quantitatively, we compared wild type neuromasts with neuromasts expressing chemoFGFR using single molecule fluorescent in situ hybridization to measure pea3 transcript levels [Durdu et al., 2014; Raj et al., 2008] (Figure 3.2 e). Analysis of pea3 smFISH data showed that FGF signaling was significantly increased in chemoFGFR positive neuromasts when compared to wild type, providing quantitative support for our observations from 'traditional' colorimetric pea3 in situs (Figure 3.2 d, f).

Next, we explored whether in stable transgenic lines chemoFGFR expression could induce a lateral line phenotype consistent with FGFR activation (Figure 3.3). To address that, chemoFGFR expression was induced by treating 26hpf embryos with 20 µM RU-486 until 48hpf and the effects were assayed live. Expressing chemoFGFR in this manner caused alterations in the stereotypic pattern of lateral line organs, with detection of ectopic clusters of cells and, occasionally, reduced spacing between neuromasts (Figure 3.3 a). We found that the total number of cellular aggregates, including *de novo* clusters and neuromasts, was significantly increased in chemoFGFR expressing embryos compared to wild type embryos (Figure 3.3 b). We defined as 'cluster' an aggregate of at least three cells with nuclei tightly packed together. This configuration was easily distinguishable from the typical distribution of control chain cells, whose nuclei appeared aligned as in a chain. The size range of ectopic clusters was highly variable, going from three cells up to twelve cells, with an average of six cells in each cluster (Figure 3.3 c). Strikingly, ectopic *de novo* clusters were found in lateral line regions between neuromasts, where only mesenchymal-like chain cells located in wild type embryos (Figure 3.3 a).

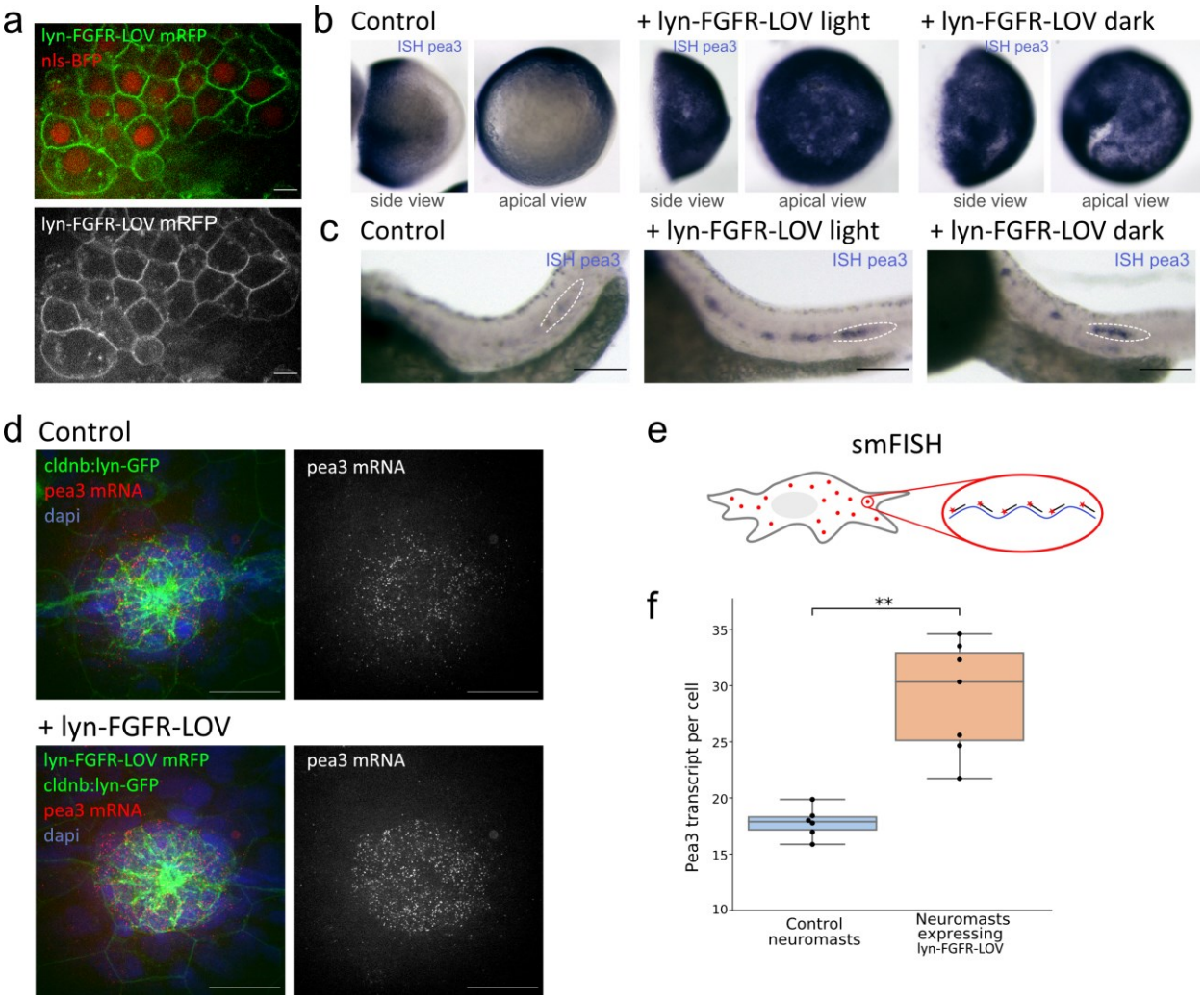

Figure 3.2: Lyn-FGFR-LOV activates FGF signaling

(a) Expression and localization of lyn-FGFR-LOV mRFP (under β-actin promoter) at the plasma membranes in early embryos; the red signal represents a co-injected nuclear marker (β-actin:nls-BFP). (b) Colorimetric in situ of pea3 in early embryos. From left to right: uninjected controls, embryos injected with lyn-FGFR-LOV mRFP mRNA and kept in light conditions, embryos injected with lyn-FGFR-LOV mRFP mRNA and kept in dark conditions. (c) Colorimetric in situ of pea3 in stable transgenic embryos, with expression of lyn-FGFR-LOV mRFP specifically in the lateral line. From left to right: non-expressing control siblings, lyn-FGFR-LOV mRFP expressing embryos kept in light conditions, lyn-FGFR-LOV mRFP expressing embryos kept in dark conditions. Lateral line primordium is outlined with white dashed lines. (d) Representative images of pea3 smFISH in control neuromasts and lyn-FGFR-LOV mRFP positive neuromasts (z-projections). (e) Schematic of the smFISH approach and (f) quantification of pea3 smFISH spots (**: $1e^{-3} < p <= 1e^{-2}$). The number of pea3 transcripts per cell is calculated for each neuromast ($n_{control} = 6$; $n_{lyn\text{-}FGFR\text{-}LOV}=7$), by dividing the number of pea3 mRNA spots by the number of nuclei. Scale bar (a) and (d) 20 µm; (c) 0.5 cm.

The chemoFGFR-dependent phenotype appeared clearly distinct from the phenotype generated by overexpression of one of the FGF ligands involved in neuromast deposition during lateral line migration, FGF3 [Durdu et al., 2014]. Although the identical LexPR driver was employed for FGF3-GFP and chemoFGFR, in embryos overexpressing FGF3-GFP the total number of cellular aggregates was comparable with wild type embryos (Figure 3.3 b). Moreover, as previously described in [Durdu et al.,

2014], in FGF3-overexpressing embryos the spacing between neuromasts was strongly reduced and often no chain cells were detectable in between, while this was not the case in chemoFGFR expressing embryos.

These results suggest that chemoFGFR induction is able to drive profound and unique changes in the lateral line, with a striking impact on organization and patterning of the whole tissue.

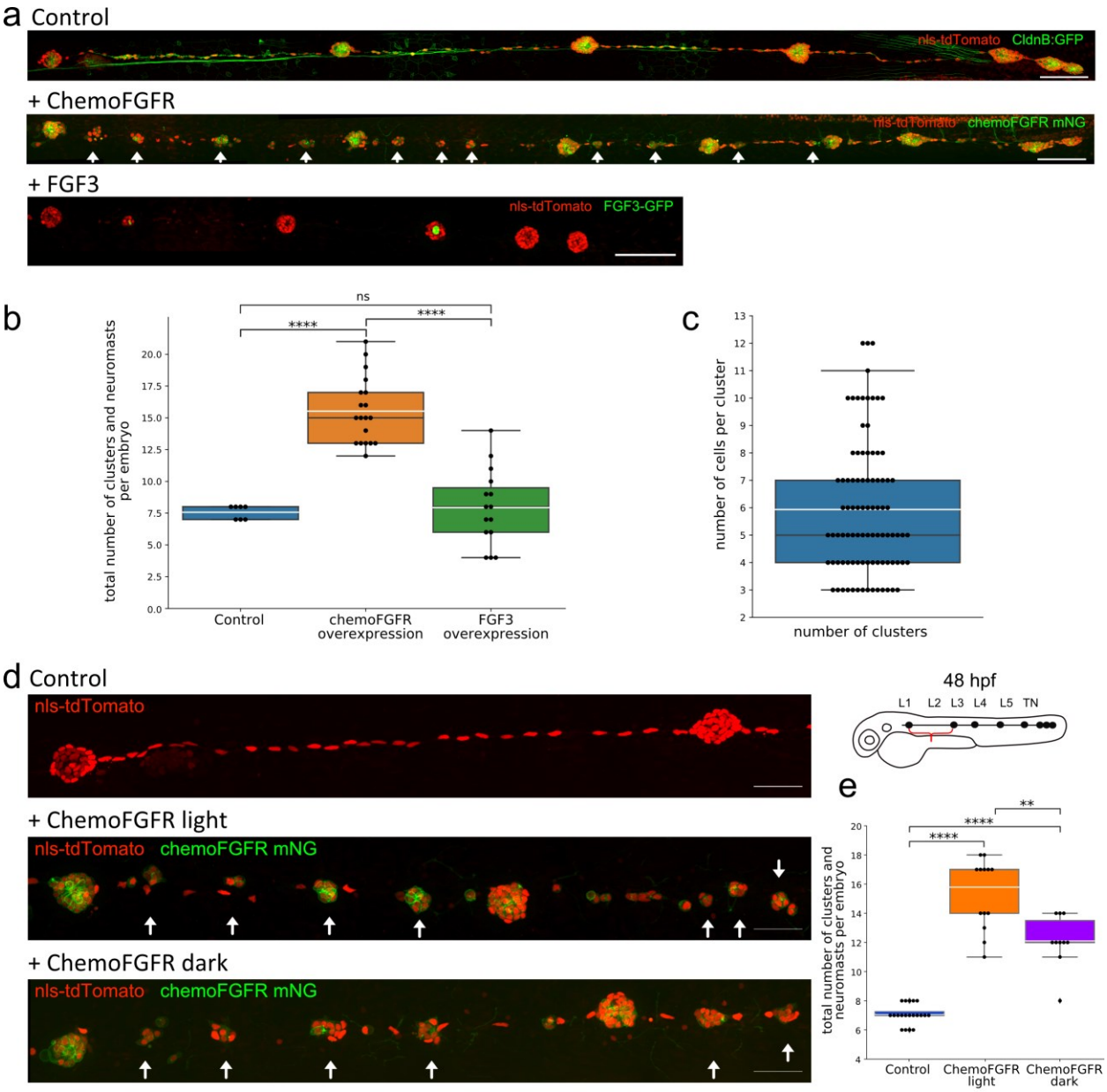

Figure 3.3: ChemoFGFR drives a lateral line phenotype

(a) Overview of a control lateral line, a chemoFGFR expressing lateral line (LexOP:chemoFGFR mNG) and a FGF3-GFP expressing lateral line (LexOP:FGF3-GFP [Durdu et al., 2014]). The images are z-projections with nuclei in red (cxcr4b:nls-tdTomato) and chemoFGFR or FGF3-GFP in green. In FGF3-GFP expressing lateral lines, FGF3-GFP fluorescence signal appears concentrated in central and apical spots in neuromasts, as FGF3 is secreted into microlumina [Durdu et al., 2014]. The integrity of most of the microlumina however is already lost at 48hpf, since they physiologically fuse with the overlying skin, causing the ligand to diffuse out. Write arrows indicate *de novo* clusters. (b) Comparison of total number of *de novo* clusters and neuromasts per embryo at 48hpf in three

conditions ($N_{control}$ = 7; $N_{chemoFGFR}$ =19; N_{FGF3}=15). (c) Quantification of number of cells detected for each *de novo* cluster in 48hpf chemoFGFR expressing lateral lines ($n_{clusters}$=91). (d) Close-up views of the lateral line segment between first and second neuromast of 48hpf control siblings and chemoFGFR expressing embryos kept in light and dark conditions (z-projection). Write arrows indicate *de novo* clusters. (e) Quantification of the total number of neuromasts and clusters per embryo ($N_{control}$ = 20; $N_{chemoFGFR\ light}$=13; $N_{chemoFGFR\ dark}$=10) (****: $p <= 1e^{-4}$; **: $1e^{-3} < p <= 1e^{-2}$; ns: $5\ e^{-2} < p <= 1$). Scale bar (a) 100 µm; (d) 50 µm.

We next tested whether the chemoFGFR-dependent phenotype observed in the lateral line showed light-dependency. Consistently with pea3 ISH results (Figure 3.2 b, c), both light-exposed and dark-kept embryos displayed ectopic *de novo* clusters at 48hpf (Figure 3.3 d, e). Although there was a significant difference in the total number of aggregates for the two conditions, we concluded that chemoFGFR dark state activity was too high to allow the clean on-off switch required for optogenetic experiments. We thus employed the chemoFGFR construct as a constitutively active FGFR. Since the chemoFGFR-dependent phenotype appeared stronger in light conditions, we decided to expose embryos for chemoFGFR experiments to constant blue light illumination before imaging (using a benchtop incubator), unless otherwise stated. All the three variants of chemoFGFR generated gave comparable results in terms of phenotype generation and dark state activity, so we considered them equivalent and we used them interchangeably in different experiments. The chemoFGFR variant labeled with mNG fluorophore was the most frequently used because of the greater brightness of the fluorophore. We established induction of 26hpf embryos with 20 µM RU-486, exposure to blue light and image acquisition at 48hpf as our standard workflow for chemoFGFR-dependent *de novo* cluster generation and detection. We henceforth refer to it as chemoFGFR induction.

3.1.3 ChemoFGFR is a *bona fide* inducible activator of FGF signaling

To confirm that the chemoFGFR-dependent clustering phenotype was specifically mediated by FGF receptor activation, we treated embryos expressing chemoFGFR with a specific FGFR1 kinase domain inhibitor, SU5402. Previous studies showed that SU5402 effectively abrogates FGF signaling in the lateral line, resulting in defective neuromast assembly and deposition, a phenotype equivalent to that of FGF3 and FGF10 morpholino injections [Durdu et al., 2014; Lecaudey et al., 2008; Nechiporuk & Raible, 2008].

Treatment of chemoFGFR expressing embryos with 1 µM SU5402 resulted in abrogation of chemoFGFR-dependent lateral line phenotype, while untreated chemoFGFR expressing siblings displayed a typical chemoFGFR-dependent lateral line phenotype, with expression of the construct at the plasma membrane being comparable in the two conditions (Figure 3.4 a, b, c). We conclude that chemoFGFR-dependent cluster formation requires specific activation of the chemoFGFR kinase domain.

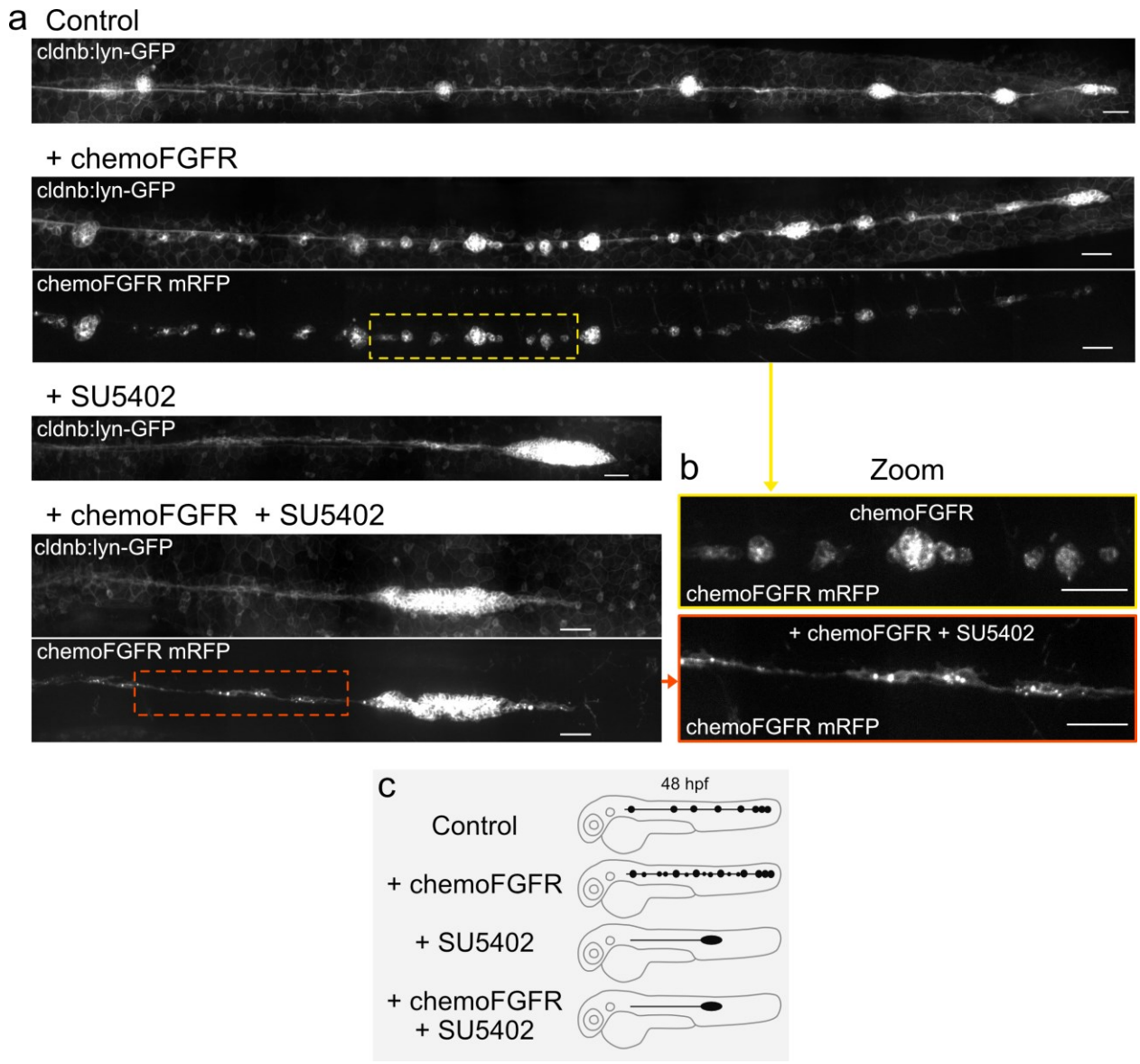

Figure 3.4: SU5402 abrogates the chemoFGFR-dependent lateral line phenotype

(a) Overview of a 48hpf untreated lateral line (wild type control), a chemoFGFR expressing lateral line, a wild type lateral line treated with SU5402 inhibitor, a chemoFGFR expressing lateral line treated with SU5402 inhibitor. The red version of chemoFGFR was used (chemoFGFR mRFP), co-imaged with a lateral line plasma membrane label (cldnb:lyn-GFP). Both channels are displayed for the chemoFGFR expressing lateral lines. (b) Close-up views of the chemoFGFR mRFP channel. (c) Schematic of the outcomes observed for different treatments. Scale bar 50 µm.

3.1.4 *De novo* clusters form through aggregation of chain cells

To address how the unique chemoFGFR-dependent phenotype established, we asked whether *de novo* clusters originated from chain cells or whether they were the result of aberrant deposition from the migrating primordium or primordium fragmentation, a known consequence of a severe loss of Notch signaling [Matsuda & Chitnis, 2010]. Chain cells are a poorly understood population of multipotent progenitors, that display a flat mesenchymal-like morphology and is deposited from the lateral line

primordium in between neuromasts (for this reason also called 'interneuromast cells') [Ghysen & Dambly-Chaudière, 2007].

To explore *de novo* cluster origin, we performed time lapse imaging on chemoFGFR and control embryos co-expressing a lateral line-specific nuclear marker (cxcr4b:nls-tdTomato), from 31hpf to 48hpf (Figure 3.5 a). Prior to imaging, to induce chemoFGFR expression, embryos were pre-treated with 20 µM RU-486 for 5 hours (starting from 26hpf), which is the time delay required for detection of chemoFGFR signal in lateral line cells. During this pre-treatment, embryos were kept in dark conditions to prevent light-dependent signaling activation. RU-486 induction of chemoFGFR was also maintained during imaging by addition of the drug to the mounting agarose and medium. Time lapse experiments were performed on a spinning disk scope, using a multi-position protocol with a time resolution of 15 min for a total of 17-22 hours (Figure 3.5 a). We established this as our standard workflow for time lapse experiments.

To evaluate cell displacement in time, an analysis pipeline was developed in collaboration with another member of the lab (Jonas Hartmann, protocol detailed in Material and Methods 2.10.7). Briefly, nuclear signal (cxcr4b:nls-tdTomato) was employed to automatically segment single nuclei, from which centroid coordinates were retrieved. Centroids detected for each time point were then projected on a spline line and kymographs were obtained, showing how their positions on the spline change over time. Although individual nuclei were retrieved for each time point independently and not linked across frames to obtain single-nuclei time tracks, general trends of cellular displacement could be inferred from the temporal profile of centroid positions (Figure 3.5 b, c). From these data, we identified two distinct modes of cluster formation. Firstly, the well-characterized 'standard' mode where wild type neuromasts are deposited from the migrating primordium, therefore present in both control and chemoFGFR expressing lateral lines (Figure 3.5 b, c). The second mode identified was exclusively detected in chemoFGFR expressing lateral lines forming *de novo* clusters. Strikingly, we observed that *de novo* clusters assembled in the low-density lateral line segments populated by chain cells, which were originally deposited at regular interval and appeared to converge in time. We term this 'aggregation-dependent cluster formation' (Figure 3.5 c). We conclude that the *de novo* clusters originate from the mesenchymal-like population of chain cells. Moreover, our results suggest that aggregation of chain cells is involved in *de novo* clusters formation.

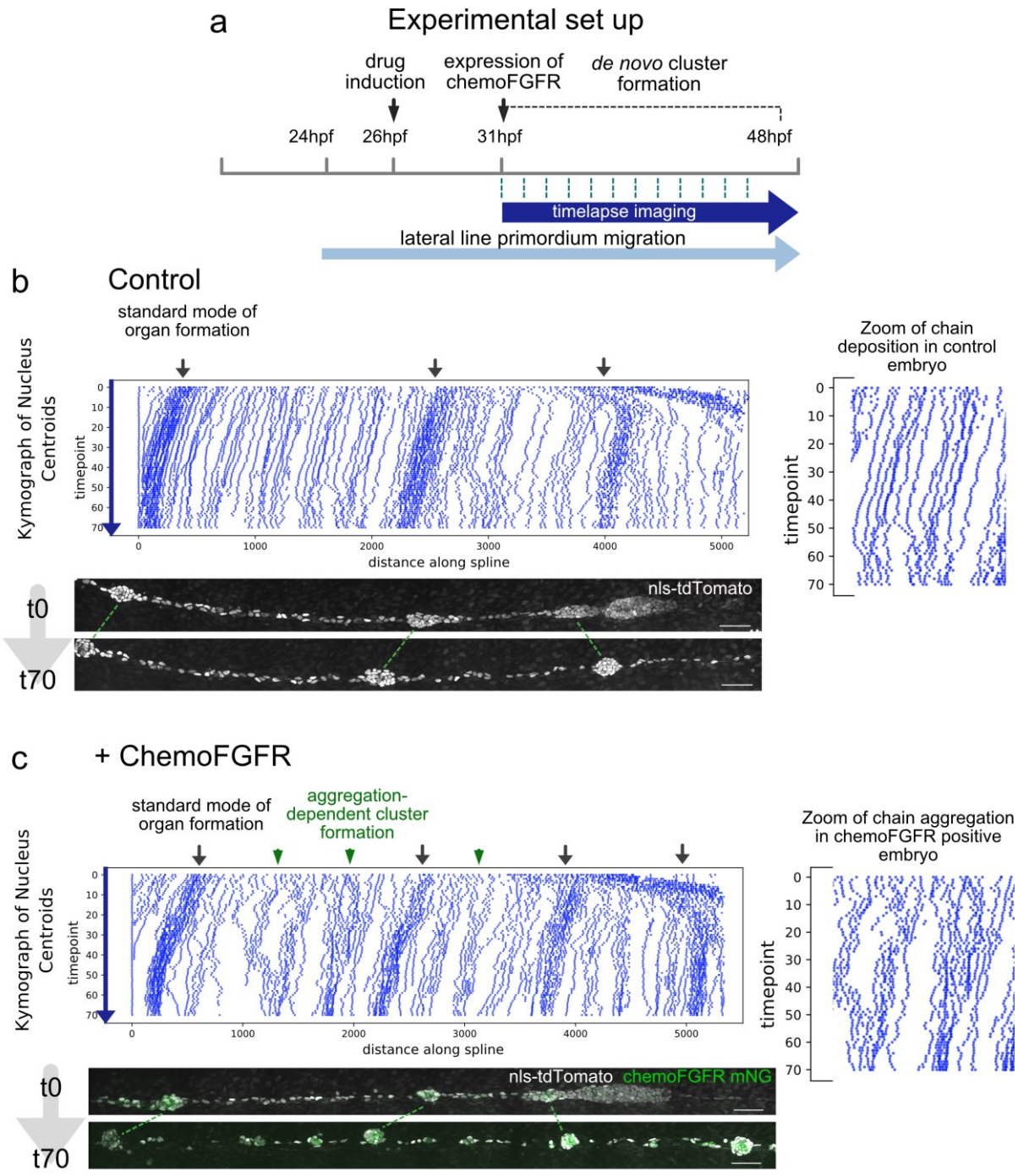

Figure 3.5: De novo clusters form through aggregation of chain cells

(a) Standard experimental set up used for time lapse experiments. (b) Kymograph of a control lateral line, with close-up view of a region between first and second neuromast. Below are reported images of the first and last time point of the corresponding wild type control lateral line. (c) Kymograph of a chemoFGFR expressing lateral lines, with close-up view of a region between first and second neuromast. Below are reported images of the first and last time point of the corresponding chemoFGFR expressing lateral line. Cxcr4b:nls-tdTomato, shown in white, labels cell nuclei; chemoFGFR mNG is shown in green. Black arrows indicate positions where organs are forming via standard primordium deposition, while the green arrowheads indicate positions where aggregation-dependent cluster formation occurs. Scale bars 50 µm.

3.1.5 ChemoFGFR expression in the lateral line does not give an obvious phenotype in associated Schwann cells

During the last decades, the study of organ regeneration upon severe injury, for example appendage regeneration following amputation [Tanaka, 2016; Vogg et al., 2019], has provided insights into epithelial emergence *in vivo*. Analogously, in the zebrafish lateral line, a number of studies employing pharmacological treatments and electro ablation, demonstrated that neuromasts regenerate upon severe damage [Grant et al., 2005; Lopez-Schier & Hudspeth, 2005; Sánchez et al., 2016]. These studies shed light on the regenerative capability of chain cells as multipotent progenitors, and, in addition, on the crucial role of glial cells to regulate this potential. It has been shown that indeed glial cells prevent proliferation and differentiation of chain cells through inhibition of Wnt/β-catenin signaling [Lush & Piotrowski, 2014b] and that the withdrawal of this inhibition during late larval stage enables assembly of chains-derived intercalary neuromasts. Consistently, upon lack or damage of glia, premature formation of intercalary neuromasts occurs [Grant et al., 2005; Lopez-Schier & Hudspeth, 2005; Sánchez et al., 2016].

To confirm that a loss of glial cells did not underlie the chemoFGFR-dependent phenotype observed, we employed the foxd3:GFP fish line to labels Schwann cells [Gilmour et al., 2002], and we combined it with chemoFGFR induction. It had been described [Gilmour et al., 2002] that foxd3:GFP positive cells are organized as two closely proximal chains of cells wrapped around the lateral line nerve. We observed that, at 48hpf, chemoFGFR expressing embryos displayed a continuous uninterrupted chain of foxd3-positive cells, indistinguishable from control embryos (expressing an inert membrane labeling, lyn-RFP) (Figure 3.6). Since we could not detect Schwann cell depletion nor any other obvious difference, we concluded that chemoFGFR-dependent lateral line phenotype is not the result of changes in this Schwann cell population. This result is consistent with our finding that chemoFGFR expression is undetectable in these cells.

We thus found that the multipotent potential of chain cells emerges not only upon damage of the neighboring glial population, but it can be driven cell-autonomously within these cells by chemoFGFR expression. Therefore, the chemoFGFR approach represents a novel strategy to drive formation of ectopic clusters that ensures tighter spatio-temporal control.

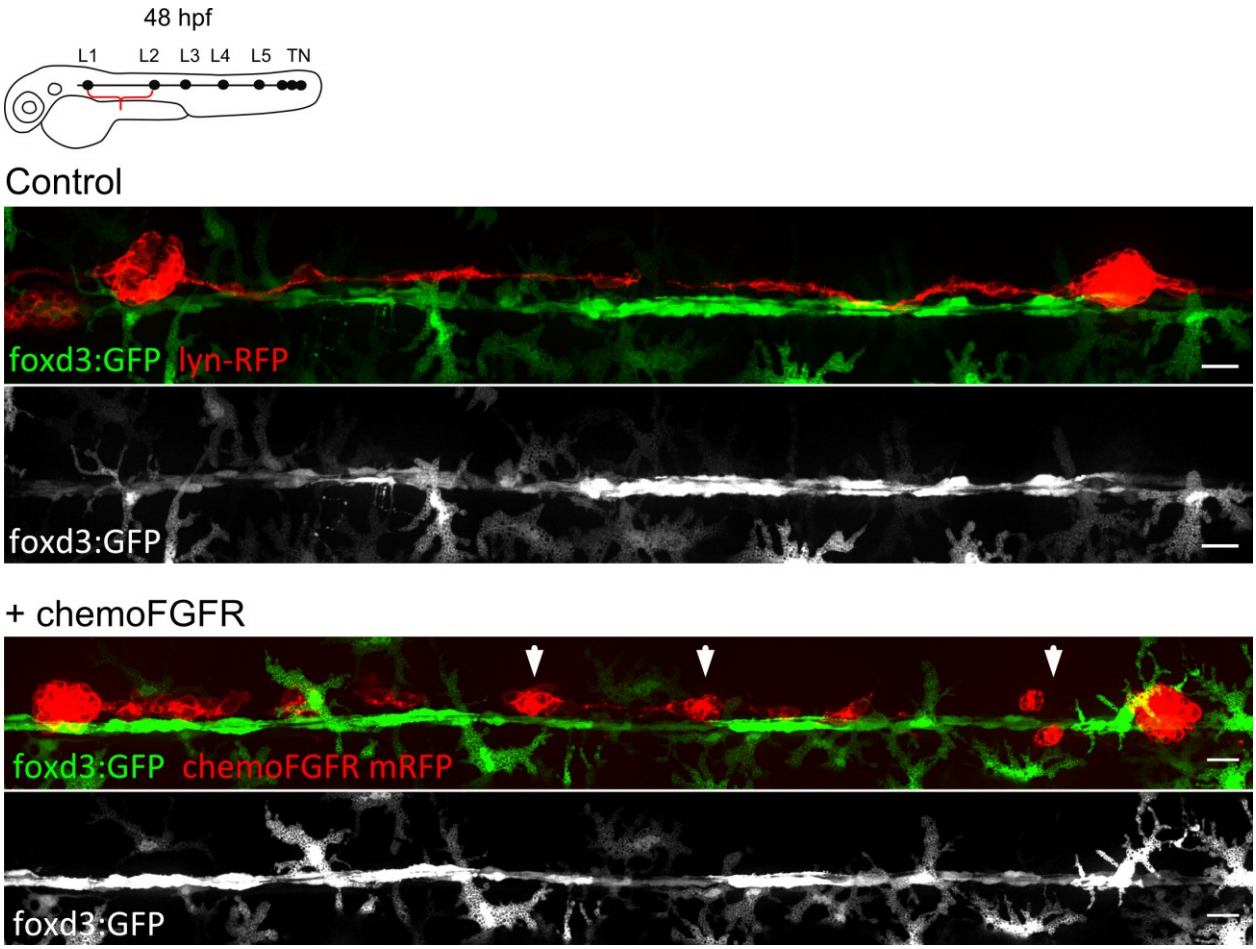

Figure 3.6: ChemoFGFR-dependent organ formation is not the result of a glial phenotype

Close-up view of the lateral line segment between first and second neuromast of 48hpf embryos either expressing a control membrane tag (LexOP:lyn-RFP, top image) or expressing chemoFGFR mRFP (bottom image). Ectopic cell clusters (indicated with white arrowheads) are present in chemoFGFR expressing lateral lines and not in controls, while Schwann cells labelled with foxd3:GFP [Gilmour et al., 2002] appear comparable in the two conditions. Images show the merge of the green (foxd3:GFP) and the red channel (lyn-RFP or chemoFGFR mRFP) and the individual foxd3:GFP channel. Scale bar 20 µm.

3.1.6 ChemoFGFR-dependent cluster formation does not require FGF3 and 10 ligands

A recurrent motif emerging during formation of periodic organs such as tooth primordia [Mammoto et al., 2015] and feathers buds [Ho et al., 2019] is the requirement for attracting cues released from a signaling center, to direct cellular motility toward the site of aggregation or to maintain cells within the assembled organ. For lateral line neuromast assembly, a previous study in the lab [Durdu et al., 2014] demonstrated that neuromast deposition from the migrating lateral line primordium depends on FGF3 and 10 ligands being secreted and trapped in microlumina, extracellular sealed cavities assembled from apical domains of cells composing the neuromast. This signaling 'hub' has the function to locally restrict the ligand and enhance FGF signaling specifically in connected cells [Durdu et al., 2014]. Upon removal of FGF3 and FGF10 ligands using morpholinos (MO), the migrating primordium

turns into a continuous chain of non-constricting mesenchymal-like cells and the assembly of neuromasts is strongly affected [Lecaudey et al., 2008]. Furthermore, another study suggested that FGF ligand released by leader cells could act as a chemoattractive cue guiding follower cells during primordium migration [Nogare et al., 2014].

Therefore, to investigate whether FGF ligands contribute to the observed chemoFGFR phenotype, we depleted these endogenous FGF ligands by injecting FGF3 and FGF10 MO into chemoFGFR transgenic embryos. If FGF ligands contribute to *de novo* cluster formation, their removal should affect or abrogate the chemoFGFR-dependent phenotype. However, chemoFGFR expressing embryos injected with MO displayed a chemoFGFR-dependent phenotype comparable with the one observed in chemoFGFR expressing embryos not injected with MO (Figure 3.7 a, b, c). The observation that depletion of FGF3 and FGF10 did not abrogate the phenotype suggests that the described chemoFGFR phenotype in the lateral line is not dependent on FGF ligands.

This result indicates that FGF signaling is sufficient to drive *de novo* cluster formation in cells not committed to the epithelial fate and that an FGF ligand source is not required to induce cluster assembly.

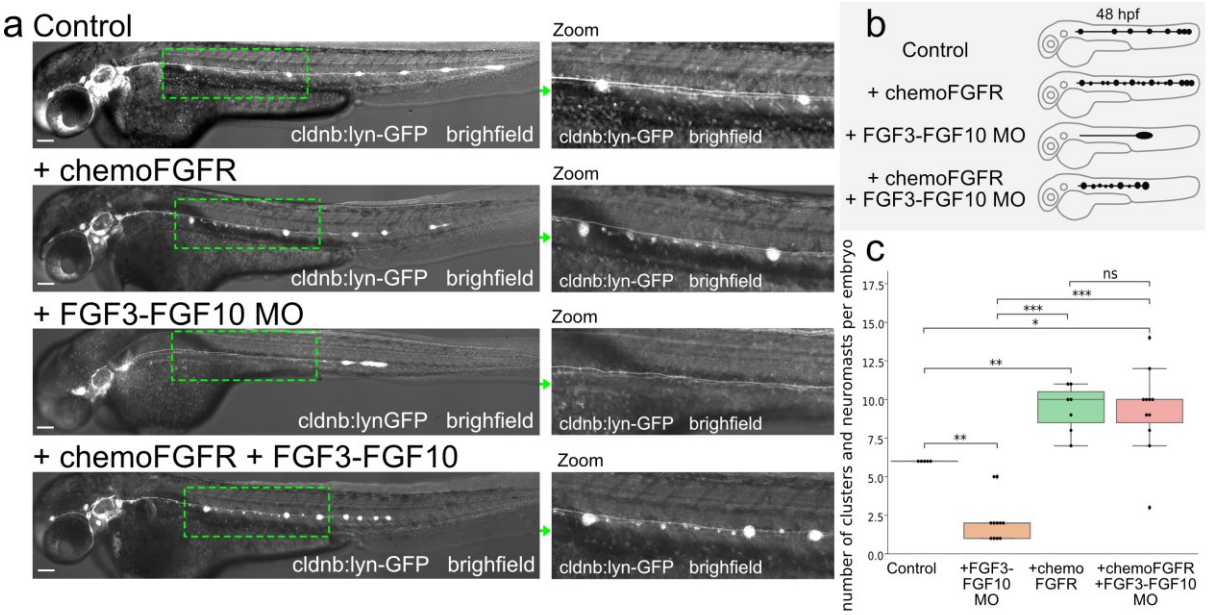

Figure 3.7: Depletion of FGF3 and FGF10 does not abrogate the chemoFGFR phenotype

(a) Overview and close-up of 48hpf representative embryos: a wild type embryo (control), an embryo expressing chemoFGFR, a wild type embryo injected with FGF3 and FGF10 MO, an embryo expressing chemoFGFR and injected with FGF3 and FGF10 MO. (b) Schematic of the outcomes observed and (c) quantification of the number of clusters and neuromasts per embryo in different conditions ($N_{control}$=5; $N_{FGF3\text{-}10\ MO}$=11; $N_{chemoFGFR}$=7; $N_{chemoFGFR+\ FGF3\text{-}10\ MO}$ =11), (***: $1e^{-4} < p <= 1e^{-3}$; **: $1e^{-3} < p <= 1e^{-2}$; *: $1e^{-2} < p <= 5e^{-2}$; ns: $5e^{-2} < p <= 1$). In the images, the lateral line plasma membrane label (cldnb:lyn-GFP) is overlaid to the brightfield channel. Scale bar 100 µm.

3.1.7 *De novo* clusters matures into *bona fide* organs

In the previous sections, we illustrated that FGFR signaling induction in the lateral line, imparted by the chimeric chemoFGFR construct, triggers the formation of *de novo* clusters from chain cells.

Next, we addressed whether *de novo* clusters represented *bona fide* lateral line organs by testing whether they would establish patterns of cell differentiation typical of sensory organs. Lateral line neuromasts are composed of mantle cells, support cells and hair cells (Figure 3.8 b). The mechanosensing properties of lateral line organs rely on apical kinocilia projected from hair cells and composed of tubulin bundles [Ghysen & Dambly-Chaudière, 2007].

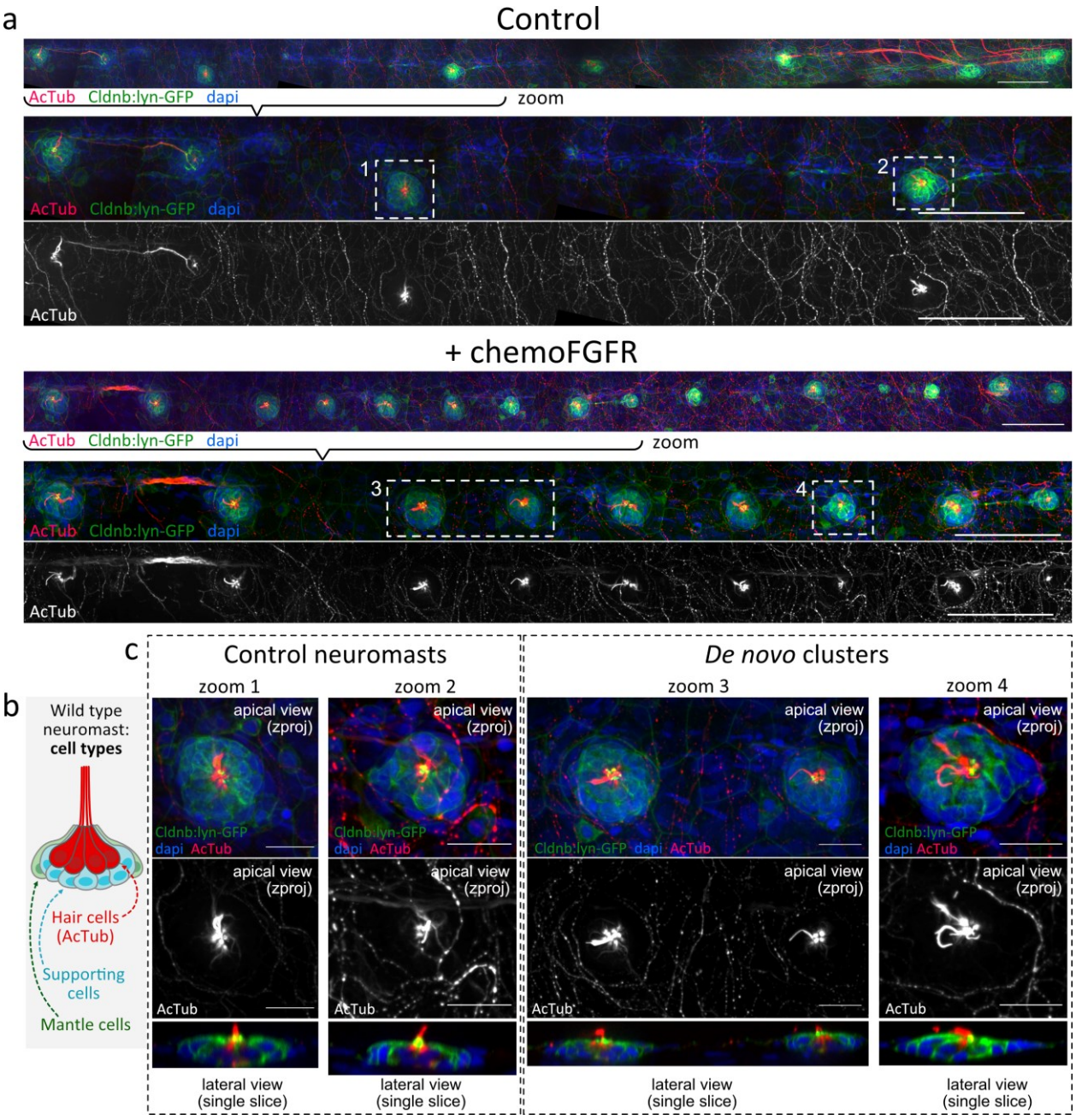

Figure 3.8: ChemoFGFR-dependent de novo clusters display a positive Acetylated tubulin staining

(a) Overview and close-up view of a representative 4dpf control lateral line, displaying Acetylated Tubulin staining (AcTub, in red), co-imaged with a nuclear (dapi, in blue) and a membrane (Cldnb:lyn-GFP, in green) counterstain (z-projections). Below, overview and close-up view of a representative 4dpf chemoFGFR expressing lateral line. Acetylated tubulin is a pan-neuronal marker, meaning that it labels hair cell soma, lateral line nerve and other nerves projecting in the trunk. (b) Schematic showing the cell type composition of a wild type neuromast. (c) Close-up views of organs enclosed in dashed boxes in (a). For each enclosed region, a merge of the Acetylated tubulin, of the membrane and the nuclear channel and the individual AcTub channel are shown as z-projections, while the lateral views are individual mid-section slices obtained through yz-reslicing. ChemoFGFR mRFP, driving *de novo* clustering in this experiment, results undetectable at 4dpf (channel not shown). Scale bar (a) 100 µm, (c) 20 µm.

To check for sensory hair cells specification in *de novo* clusters, we performed at 4dpf antibody staining of Acetylated Tubulin, an established marker of neurons and hair cell kinocilia and soma [Slepecky et al., 1995]. In accordance with previous observations [Lecaudey et al., 2008], wild type neuromasts showed strong labeling of Acetylated Tubulin, whereas immunostaining was undetectable in chain cells (Figure 3.8 a top, c). ChemoFGFR-dependent *de novo* clusters clearly and reproducibly displayed a strong positive Acetylated Tubulin staining in the center of the clusters, consistent with the conclusion that *de novo* clusters can differentiate mechanosensory hair cells (Figure 3.8 a bottom, c). This result suggests that ectopic clusters are fully competent to mature into neuromast-like organs.

Our results suggest that chemoFGFR manipulation allows us to assemble ectopic *de novo* organs on demand *in vivo* from the mesenchymal-like population of chain cells. Chain cells thus constitute a minimal 1D multipotent cell population that is amenable to manipulation. This combination of features indicates that the system has potential to provide mechanistic insights into the principles of organ assembly *in vivo*.

3.2 Mechanisms of cellular rearrangement during *de novo* cluster assembly

3.2.1 *De novo* clusters are polyclonal in origin

The ability to trigger organogenesis on demand at single cell resolution provides an experimental entry-point to many fundamental questions in organ assembly. For example, different cellular mechanisms could lead to the formation of cell clusters. Most obviously, cell proliferation could generate *de novo* clusters from the clonal expansion of individual cells, resulting in organs that are 'monoclonal' in composition (Figure 3.9 c). This mode has been observed, for example during formation of insect sensory bristles [Cubas et al., 1991; Lawrence, 1966] and MDCK cyst formation [Datta et al., 2011]. Alternatively, *de novo* clusters could form through the convergence and aggregation of multiple motile chain cells, resulting in organs that are 'polyclonal' in composition

(Figure 3.9 c). Polyclonal origin has been observed for example during formation of NEB organs in mouse lungs and taste buds in zebrafish [Kuo & Krasnow, 2015; Noguchi et al., 2015; Soulika, 2015].

To address whether chemoFGFR-dependent clusters were monoclonal or polyclonal, we performed manual tracking on time lapse data (obtained as described in in section 3.1.4). The results revealed that 100% of analyzed *de novo* clusters (n=53 clusters) originated from at least two cells (Figure 3.9 a). This finding supports a model where the coalescence of multiple chain cells generates organs of polyclonal origin. It is unlikely that we missed or underestimated proliferation events, since time lapse imaging sessions were initiated shortly after chemoFGFR expression was detectable at the plasma membrane and performed at a time frequency sufficient for proliferation events to be detected efficiently. While monitoring single cell behaviors, we also identified a second cellular configuration that we did not observe in wild type lateral lines, structures composed of two densely packed cells. We reasoned that they that might represent the earliest stage of *de novo* cluster formation and we named them cell doublets. To explore their origin, we tracked cells forming doublets to early time points and we observed that 58% (11/19 doublets) were derived from proliferation of a single clone, while 42% were derived from two cells aggregating (8/19 doublets) (Figure 3.9 b). Therefore, cell doublets can be either polyclonal or monoclonal. Although we cannot exclude that, at later time points, monoclonal doublets could originate monoclonal clusters by proliferation, we could not detect any such events in the time range we monitored. Thus, we conclude that *de novo* clusters detected at 48hpf have polyclonal origin.

Although the results ruled out the possibility that 48hpf clusters could derive from a single proliferating clone, they did not exclude that proliferation could be the main mechanism increasing cell number within nascent clusters from very few progenitor cells. A previous study in the lateral line showed indeed that during organ regeneration upon damage, as few as two chain cells were sufficient to give rise to a whole organ through serial proliferation [Sánchez et al., 2016]. To address this point, we exploited time lapse data and quantified whether most of the cells within forming clusters were acquired through proliferation or through aggregation. We found a linear correlation with a steep slope between the total number of cells in the cluster at the 48hpf endpoint and the number of cells that joined the cluster by aggregation (Figure 3.9 d). Therefore, polyclonal aggregation appears to be the main driver of *de novo* cluster formation, although proliferation takes place during the process.

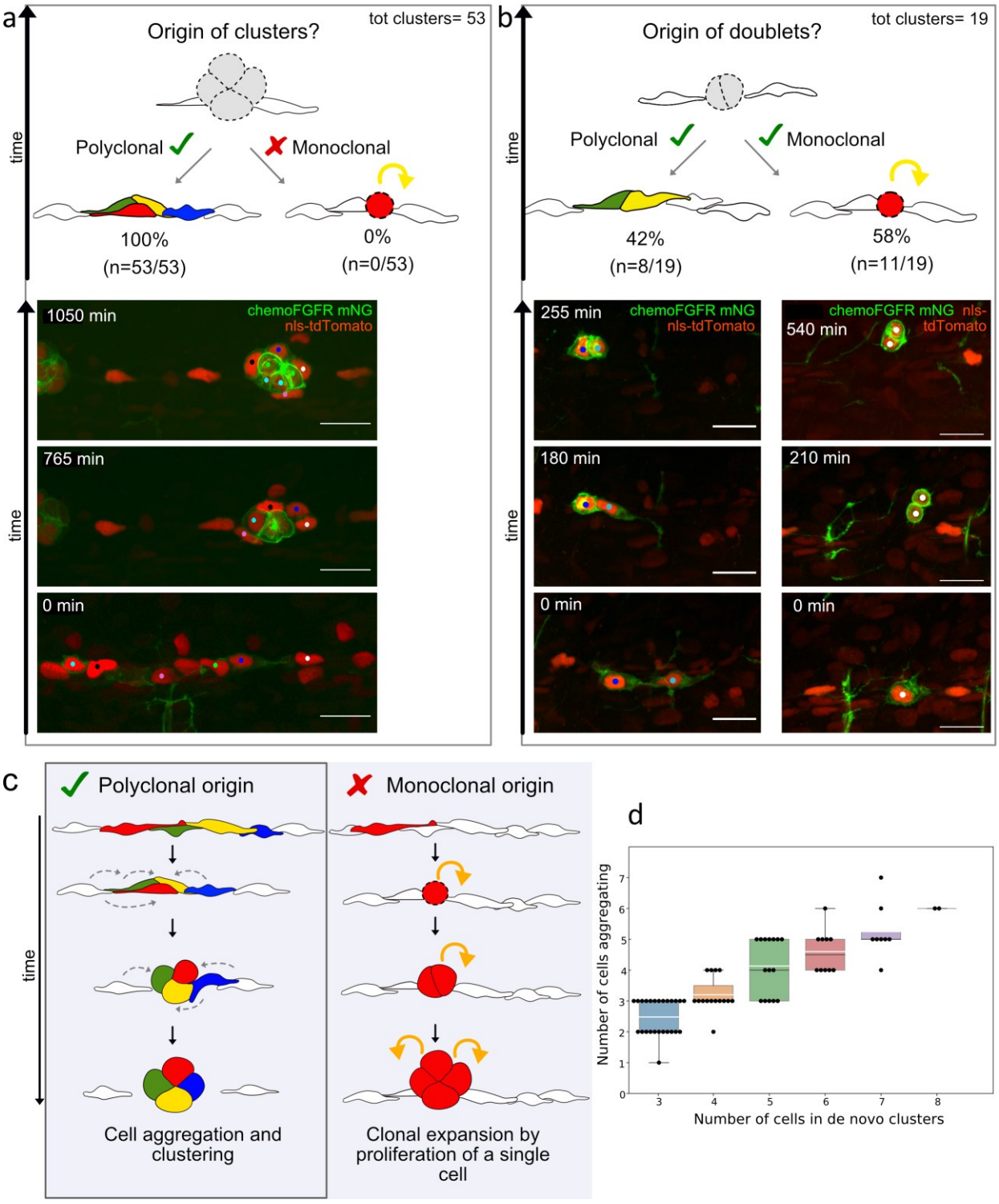

Figure 3.9: De novo clusters are polyclonal in origin

(a) Single cell tracking in time lapses showed that clusters have a polyclonal origin (100% of the 53 clusters analyzed), while (b) doublets can have either polyclonal or monoclonal origin (42% of the 19 doublets analyzed are polyclonal). The images are z-projections with nuclei in red (cxcr4b:nls-tdTomato) and chemoFGFR in green (LexOP:chemoFGFR mNG). (c) Schematic of the two hypothetical models of *de novo* cluster formation in chemoFGFR expressing lateral lines: in a monoclonal model, individual cells would generate monoclonal clusters via serial proliferation, while in a polyclonal model, multiple cells would contribute to cluster assembly via

aggregation. (d) Plot depicting the contribution of cell aggregation in *de novo* cluster formation. Each dot represents a *de novo* cluster. The x axis indicates the total number of cells in a certain cluster at 48hpf, whereas the y axis indicates how many cells joined the corresponding cluster via aggregation. Scale bar 20 µm.

3.2.2 Sorting of chemoFGFR positive cells drives formation of *de novo* clusters

We hypothesized two possible scenarios at the basis of polyclonal cluster formation (Figure 3.10 a). In a chemoFGFR cell autonomous scenario, only 'chemoFGFR positive' cells would aggregate, sorting out from non-expressing 'chemoFGFR negative' cells and resulting in clusters composed of only chemoFGFR positive cells. In a non-cell autonomous scenario, chemoFGFR positive cells would coerce chemoFGFR negative cells to co-aggregate, resulting in epithelial clusters that are comprised of both chemoFGFR positive and negative cells. To distinguish between these two scenarios, we investigated *de novo* clusters in term of chemoFGFR positive and negative cells composition. We induced chemoFGFR expression on embryos co-labeled with nls-tdTomato (nuclei) using our standard chemoFGFR induction protocol (described in section 3.1.2) and performed endpoint imaging at 48hpf. We classified lateral line cells depending on their organization as part of clusters, doublets or remaining as individual chain cells (Figure 3.10 c). Furthermore, we categorized cells as chemoFGFR positive and negative cells, based on whether chemoFGFR signal could be detected or not. Percentages were calculated from counts of cells in a certain category, normalized by total number of cells analyzed for organization or for expression (Figure 3.10 d).

The results revealed that clusters were strongly enriched in chemoFGFR positive cells and doublets were exclusively composed of chemoFGFR positive cells, suggesting that chemoFGFR mediates cluster formation in a chemoFGFR cell autonomous way (Figure 3.10 d). Interestingly, we observed that, while chemoFGFR negative preferentially remained as individual chain cells, 24% of them (out of all the negative cells analyzed) were detected in clusters (Figure 3.10 e). Moreover, 46% of all the clusters analyzed (n=30/65 clusters) had at least one chemoFGFR negative cell associated.

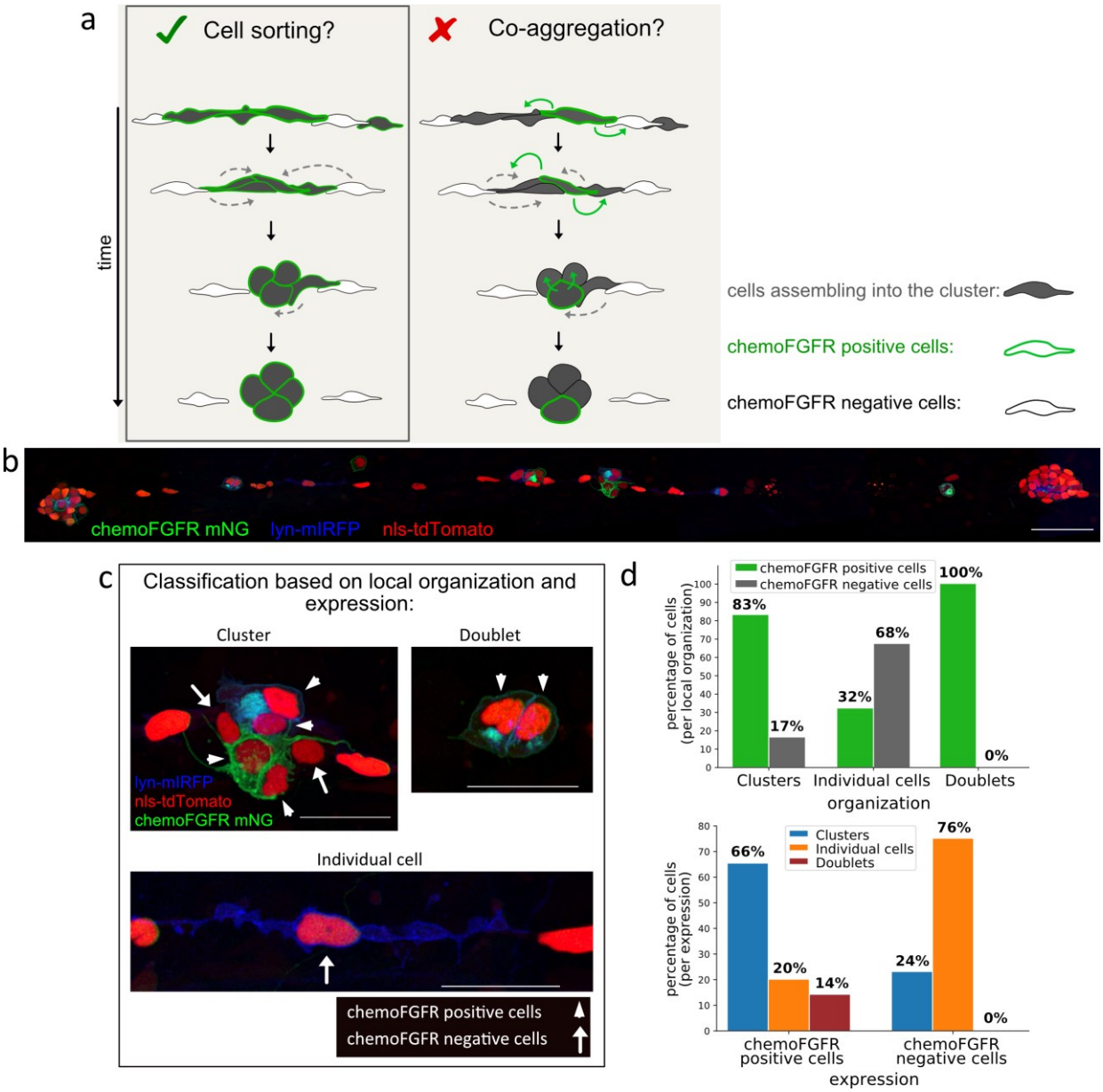

Figure 3.10: De novo clusters are enriched in cells expressing chemoFGFR

(a) Representation of two hypothetical scenarios of *de novo* cluster formation, depending on whether chemoFGFR positive cells co-aggregate with chemoFGFR negative cells or the two populations sort. (b) Representative image of a 48hpf chemoFGFR expressing lateral line used for the single cell classification analysis (z-projection). A far-red lateral line membrane label (using the LexOP:lyn-mIRFP670 line, employed to detect chemoFGFR negative cells, shown in blue), a nuclear label (Cxcr4b:nls-tdTomato, in red) and the chemoFGFR mNG label (in green) were imaged. (c) Cells were classified based on their local organization (in clusters, doublets or individual cells) and based on the presence of a detectable chemoFGFR signal (in chemoFGFR positive or negative cells). The arrowheads indicate chemoFGFR positive cells, the arrows chemoFGFR negative cells. (d) The composition was plotted in function of cell organization (upper barplot) or in function of chemoFGFR expression (lower barplot), reporting the corresponding percentages (For the upper barplot: $N_{embryos}=4$; $n_{cells\ in\ cluster}=175$; $n_{cells\ in\ doublet}=34$; $n_{individual\ cells}=139$) (For the lower barplot: $N_{embryos}=4$; $n_{chemoFGFR\ positive\ cells}= 223$; $n_{chemoFGFR\ negative\ cells}= 125$). Scale bar (b) 50 µm, (c) 20 µm.

To assess whether the detected chemoFGFR negative cells intermingled with positives, or whether they would segregate within clusters, we classified cells within *de novo* clusters based on their organization and expression (Figure 3.11 a, b). Each cluster was subdivided into two concentric regions, with the center of the cluster as reference point: the inner region was defined as 'cluster seed' and the outer 'cluster rim' (Figure 3.11 b). The analysis revealed that chemoFGFR negative cells were exclusively located in the cluster rim, while chemoFGFR positive cells were the only contributors of cluster seed but were also present in cluster rim (Figure 3.11 c).

We concluded that a stereotyped pattern is established in *de novo* clusters, with chemoFGFR positive cells composing the seed of the cluster and negative cells exclusively segregated to the peripheral rim.

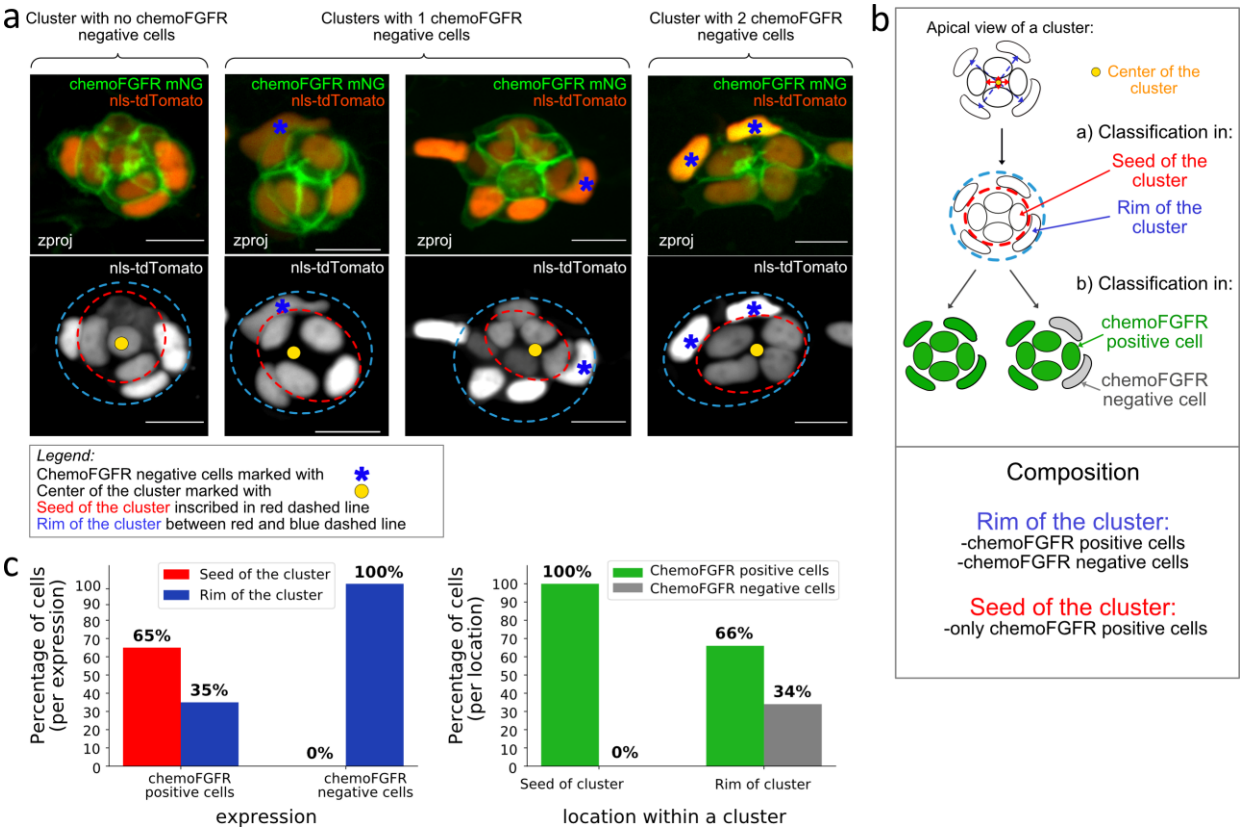

Figure 3.11: ChemoFGFR negative cells located within clusters are peripherally segregated

(a) Representative z-projections of *de novo* clusters, with nuclei in red (cxcr4b:nls-tdTomato) and chemoFGFR mNG in green. ChemoFGFR negative cells are highlighted in the images with blue asterisks. ChemoFGFR positive and negative cells were classified based on the presence of a detectable chemoFGFR signal in individual cells. (b) Pipeline used for the spatial partitioning of clusters in inside 'seed' and outside 'rim' (detailed in Material and Methods 2.10.3). ChemoFGFR negative cells localize in cluster rims ((a) in the annotated nuclear channel images). (c) Quantification of cluster composition in function of cell expression ($n_{\text{chemoFGFR positive cells}}$=207; $n_{\text{chemoFGFR negative cells}}$=37) or in function of cell position within clusters ($n_{\text{cells in seed}}$= 134; $n_{\text{cells in rim}}$= 109). Scale bar 20 µm.

We next addressed how the inside-outside pattern of seed and rim is established. It has been shown that, within the mammalian blastocyst, blastomeres sort based on their surface contractility into an inner core of contractile cells and an outer coat of 'softer' cells [Maître et al., 2016]. To test whether chemoFGFR positive and negative cells would undergo sorting once assembled within clusters, analogously to blastomeres, we investigated single cell behavior dynamically by tracking chemoFGFR positive and negative cells in time lapses. We reasoned that, if that were the case, we would expect aggregation into clusters of both chemoFGFR positive and negative cells to precede sorting and establishment of an inside-outside segregation (Figure 3.12 c). Surprisingly, we observed that, at early steps of cluster formation, exclusively the chemoFGFR positive cell population aggregated into clusters, sorting from negative cells while still in a mesenchymal-like chain configuration (Figure 3.12 a, b). Interestingly, cluster assembly not only engaged chemoFGFR positive cells that were located from the start at adjacent positions, but also positive cells that were initially interspersed with negatives, implicating that cells exchange in the process. Moreover, we observed that upon assembly of a seed of at least two chemoFGFR positive cells, chemoFGFR negative cells in the vicinity arranged around it, forming an outer rim.

These observations suggest that cluster assembly involves two distinct phases. In a first phase, chemoFGFR positive cells sort away from negative cells and aggregate with other chemoFGFR positive cells, assembling a chemoFGFR positive cluster seed, from which negative cells are excluded. In a second phase, chemoFGFR negative cells associate with the chemoFGFR positive seed, without intermingling with cells of the seed but instead segregating at the periphery of it, in a concentric rim. The spatial inside-outside pattern observed in *de novo* clusters is thus the result of cell sorting, which appears to be dependent on FGF activity.

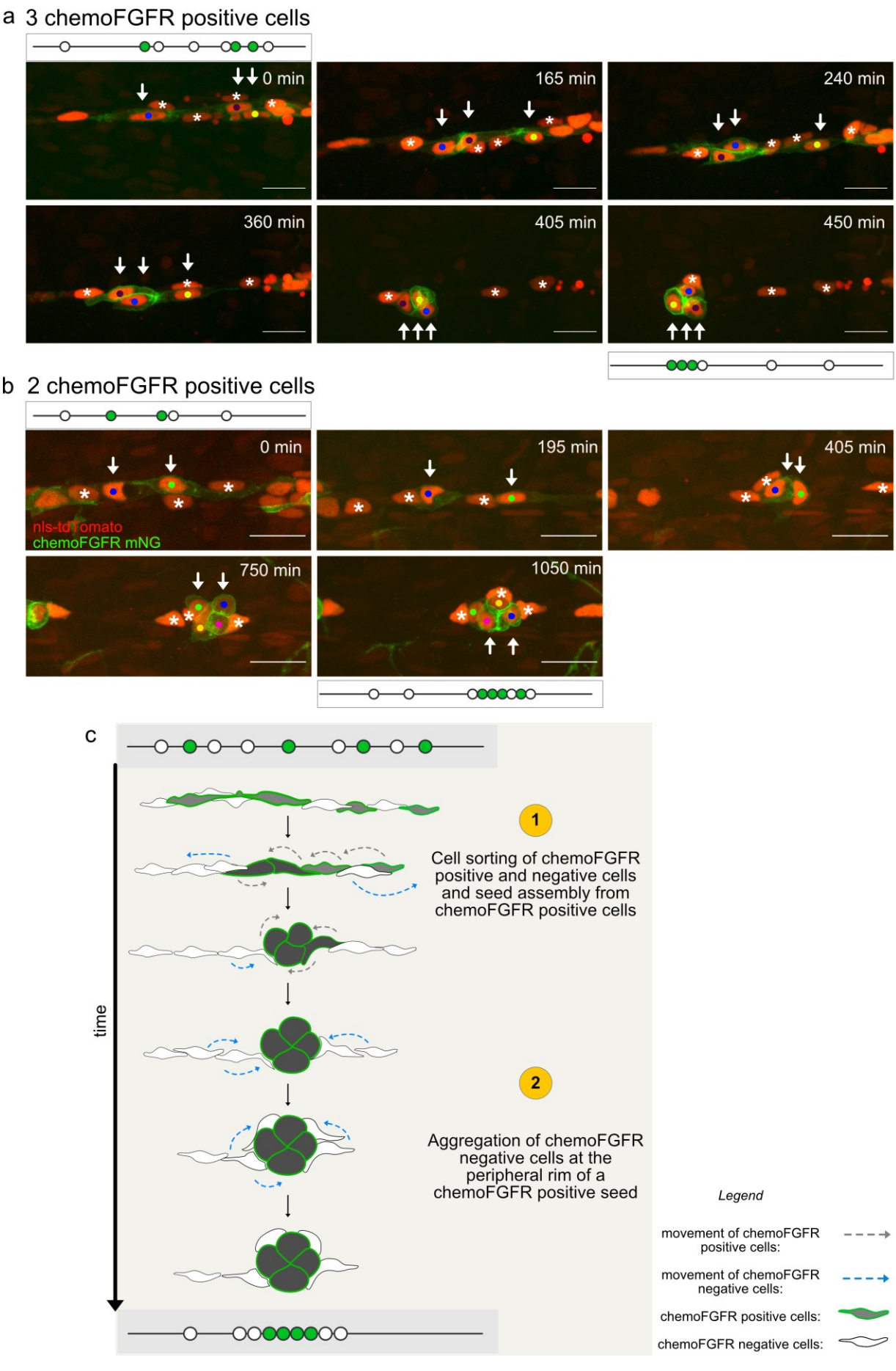
a 3 chemoFGFR positive cells
0 min
165 min
240 min
360 min
405 min
450 min
b 2 chemoFGFR positive cells
0 min
195 min
405 min
nls-tdTomato
chemoFGFR mNG
750 min
1050 min
c
time
1
Cell sorting of chemoFGFR positive and negative cells and seed assembly from chemoFGFR positive cells
2
Aggregation of chemoFGFR negative cells at the peripheral rim of a chemoFGFR positive seed
Legend
movement of chemoFGFR positive cells:
movement of chemoFGFR negative cells:
chemoFGFR positive cells:
chemoFGFR negative cells:

Figure 3.12: De novo clusters are seeded by aggregation of chemoFGFR positive cells

Single cell tracking of chemoFGFR positive and negative cells during cluster formation. Cells were tracked on z-projections using the nuclear channel (cxcr4b:nls-tdTomato) and chemoFGFR positive and negative cells were identified using the green channel (based on the presence of a detectable chemoFGFR mNG signal). ChemoFGFR positive cells are highlighted with colored dots and white arrows, while chemoFGFR negative cells are highlighted with white asterisks. From top to bottom: (a) a case where three chemoFGFR positive cells nucleate a cluster and a chemoFGFR negative cell joins (at time point 450 min); (b) a case where two chemoFGFR cells nucleate a cluster (by aggregating and proliferating) and three chemoFGFR negative cells join (from time point 405 min). Cartoons that approximate the position of cells in 2D for the first and the last time point are associated to the images (green dots represent chemoFGFR positive cells and white dots chemoFGFR negative cells). (c) Schematic representing the proposed model. Scale bar 20 µm.

3.2.3 ChemoFGFR positive cells display a slithering migration during clustering

During embryonic development, cells undergo considerable spatial rearrangement to orchestrate assembly and remodeling of functional organs. We previously mentioned that during *de novo* clusters assembly, chemoFGFR positive cells, even when initially interspersed with negative cells, could sort and join clusters, suggesting that they can dynamically rearrange in the chain (Figure 3.12 a, b). To investigate the extent of rearrangement within chemoFGFR expressing lateral lines, we quantified the motility of chemoFGFR positive and negative cells during cluster formation from 31 to 48hpf and compared it with chain cells of wild type lateral lines. Comparison of cellular mean speed, retrieved from single cells, tracked in time lapse experiments using the nls-tdTomato nuclear label, showed that both chemoFGFR positive and negative cells were more motile in chemoFGFR expressing lateral lines than in wild type lateral lines (Figure 3.13 a), with the highest values of speed detected for chemoFGFR positive cells. To test whether the increased speed was also reflected in an increased net displacement, we calculated distance traveled by chemoFGFR positive cells during cluster formation, by acquiring spatial coordinates of tracked cells in the first and in the last time point. The result demonstrated that not only did chemoFGFR positive cells show an increased speed, they also displaced significantly more than chain cells from wild type embryos (Figure 3.13 b). Remarkably, we detected chemoFGFR positive cells converging into developing clusters from distal sites, up to 130 µm away from their final position, a distance that is almost three times higher than that covered by the most motile chain cells in wild type lateral lines (Figure 3.13 b, c).

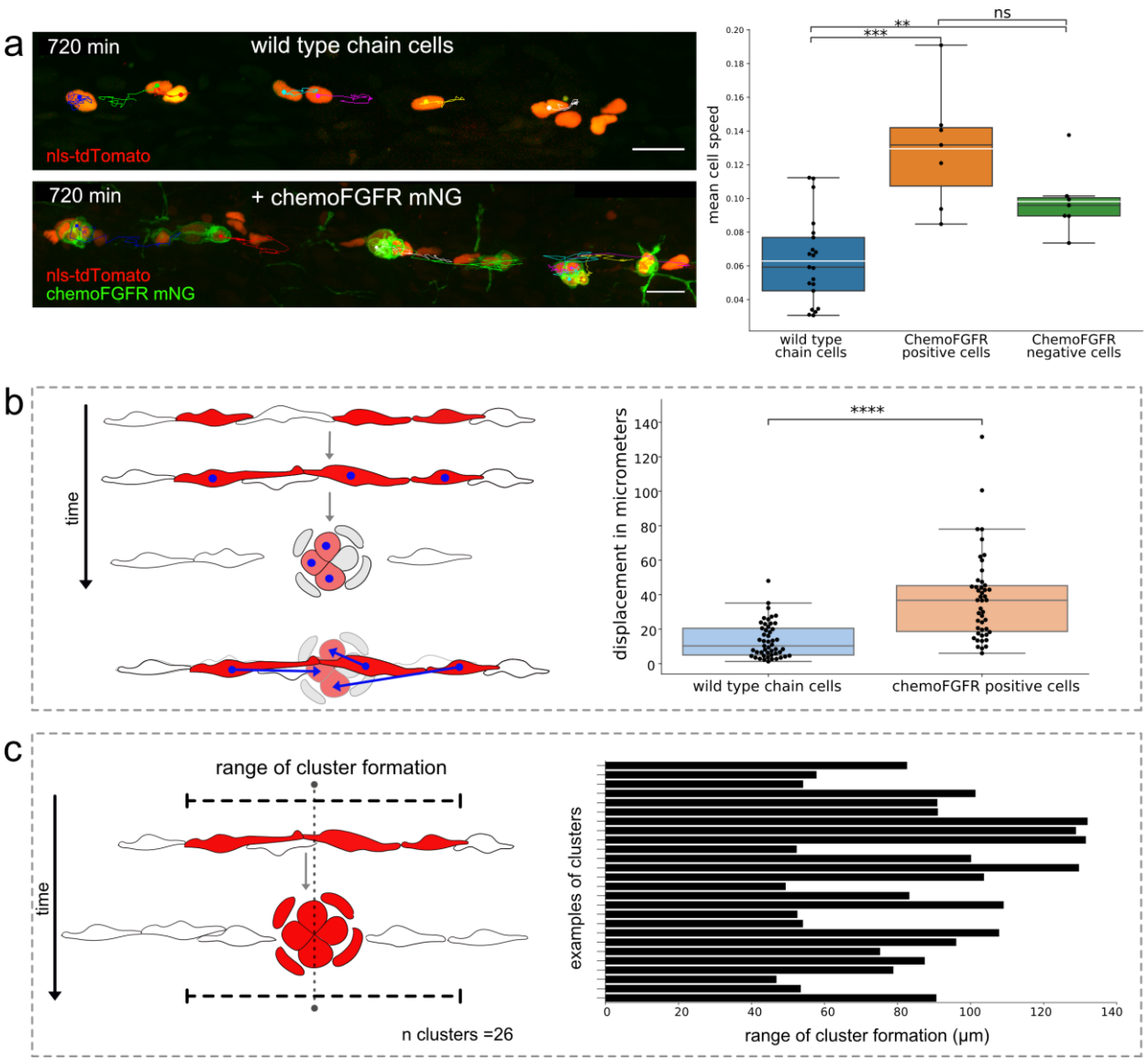

Figure 3.13: ChemoFGFR increases cell motility during clustering

(a) Single cell tracks (shown as colored lines) of chain cells in wild type embryos (top) and of chemoFGFR-induced embryos (bottom), overlapped on z-projections of time lapse frames. Cells were individually tracked on z-projections using the nuclear channel (cxcr4b:nls-tdTomato) and chemoFGFR positive and negative cells were identified using the green channel (based on the presence of a detectable chemoFGFR mNG signal). Each track thus indicates the displacement of a certain cell in time. On the right, comparison of the mean cell speeds of wild type chain cells, chemoFGFR positive and negative cells ($n_{\text{wild type chain cells}}=21$; $n_{\text{chemoFGFR positive cells}}=7$; $n_{\text{chemoFGFR negative cells}}=7$). (b) Comparison of the net displacement of chemoFGFR positive cells during cluster formation and of chain cells in wild type lateral lines, calculated from the spatial coordinates of a cell in the last time frame and in the first time frame ($n_{\text{wild type chain cells}}=49$; $n_{\text{chemoFGFR positive cells}}=46$). (c) Measures of the range of cluster formation in various clustering events (in µm) ($n_{\text{clusters}}=26$).****:$p <= 1e^{-4}$; ***: $1e^{-4} < p <= 1e^{-3}$; **: $1e^{-3} < p <= 1e^{-2}$; ns: $5e^{-2} < p <= 1$. Scale bar 20 µm.

To investigate whether shape changes accompany rearrangements of cells during *de novo* cluster formation, we analyzed the morphology of chemoFGFR positive cells tracked in time lapses, using the chemoFGFR signal at plasma membranes (Figure 3.14 a). Strikingly, we found that, as they assembled

into clusters, chemoFGFR positive cells lost the mesenchymal elongated shape typical of chain cells (Figure 3.14 a, b, c, d) and adopted an epithelial columnar morphology, comparable to cells in wild type rosettes (Figure 3.14 a, b, c, d, e). This observation is consistent with a model where chemoFGFR cells undergo a mesenchymal to epithelial transition (MET) while assembling 3D clusters (Figure 3.14 c). However, during cellular rearrangements preceding epithelialization and cluster assembly, chemoFGFR positive cells displayed features of migratory cells, such as protrusions and dynamic processes, as they were crawling over neighboring cells (Figure 3.14 a, b). The repertoire of dramatic shape changes observed during *de novo* cluster formation presents similarities with a recently described mode of epithelial cell displacement, called 'slithering' migration, which underlies the formation of neuroepithelial bodies (NEB) from pulmonary neuroendocrine cells (NE) [Kuo & Krasnow, 2015; Noguchi et al., 2015]. The term 'slithering' refers to the sliding motion of cells that loosen their interactions with the epithelium of origin and migrate by crawling on top of it. Indeed, analogously to NE cells, chemoFGFR cells were observed to dynamically change direction, to engage in transient contacts with other cells before cluster assembly (for example in Figure 3.14 a, the cell labeled with white dot and the one with light blue dot) and to join the nucleating clusters at different times (for example in Figure 3.14 a, the cells labeled with light blue and purple dots).

It had been observed that solitary NE cells, during NEB formation, extend long protrusions over neighbor epithelial cells and contact other NE cells, even before crawling out from their original position in the tissue and move toward them [Kuo & Krasnow, 2015]. This observation suggested that homotypic contacts might be involved in NE-NE recognition, instructing cells on the direction to move toward to join other NE cells [Kapsimali, 2017; Kuo & Krasnow, 2015]. To address whether homotypic contacts between chemoFGFR positive cells had an impact on cell directionality, we examined cell-cell interactions (by using chemoFGFR signal at plasma membranes) in parallel with single cells tracks (by using nuclear signal). We analyzed specifically the displacement profiles of chemoFGFR positive cells before and after homotypic interactions during assembly of small clusters (Figure 3.15 a, b). We observed that chemoFGFR positive cells moved randomly before contact with another positive cell, while displayed a more persistent directionality toward the homotypic partner after contact (Figure 3.15 b). Consistently, solitary chemoFGFR positive cells only display a random motility profile (Figure 3.15 c, d). This suggests that homotypic interactions might provide directionality in displacement, as in the case of NE cells, and might be involved in rearrangement and sorting of chemoFGFR positive cells.

Altogether, the data revealed that chemoFGFR positive cells transiently display a complex repertoire of cell morphologies and behaviors during cluster formation, which results in slithering-like cell rearrangements and MET.

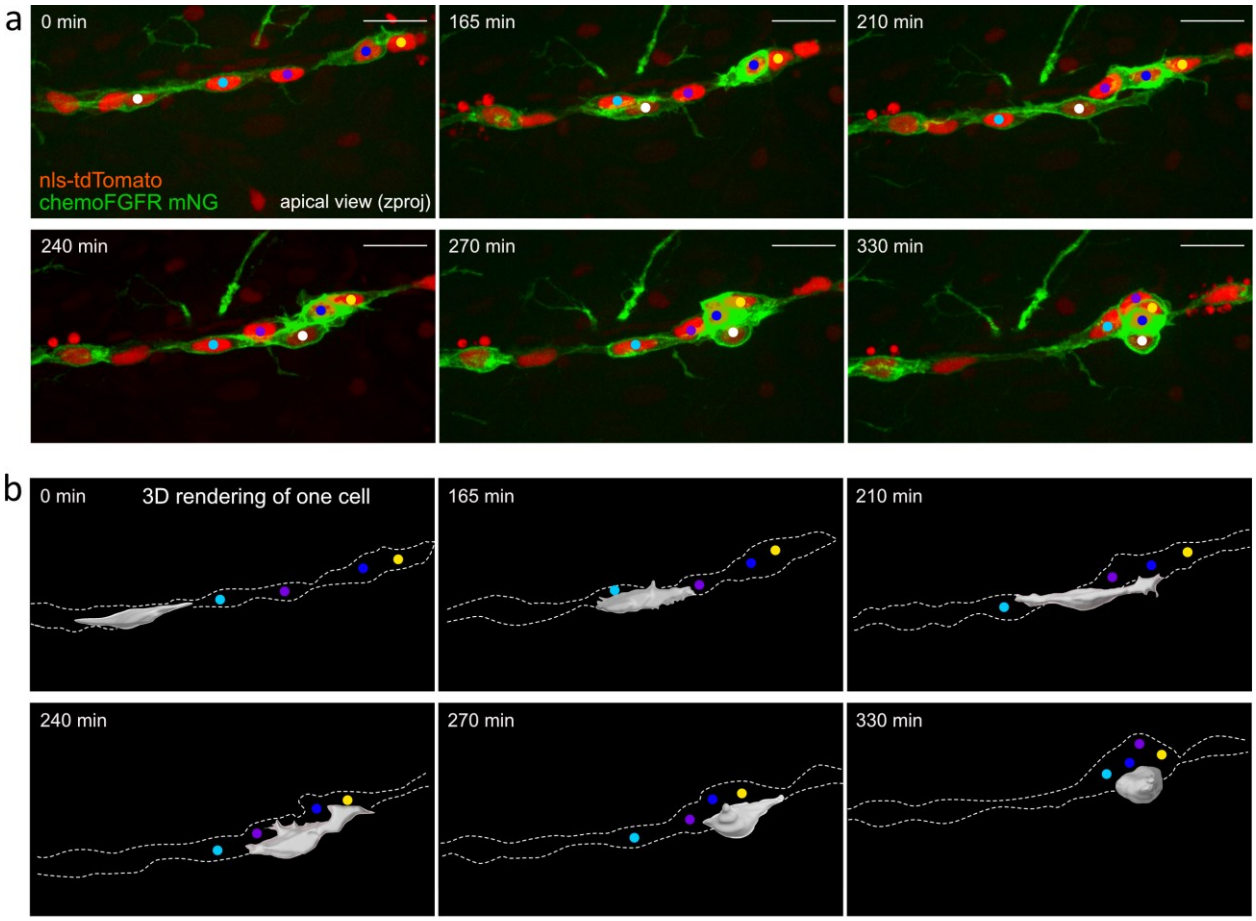
a
0 min
165 min
210 min
nls-tdTomato
chemoFGFR mNG
apical view (zproj)
240 min
270 min
330 min
b
0 min
3D rendering of one cell
165 min
210 min
240 min
270 min
330 min
c
Mesenchymal-like shape
t: 0 min
Epithelial-like shape
t: 330 min
z axis
x axis
d
3D rendering of a
wild type chain cell
apical view
lateral view
e
3D rendering of a
wild type neuromast cell
apical view
lateral view

Figure 3.14: ChemoFGFR positive cells undergo MET and slithering-like rearrangements.

(a) Images from a representative time lapse showing dynamic cell rearrangements during *de novo* cluster formation. Cells were individually tracked on z-projections using the nuclear channel (cxcr4b:nls-tdTomato) and marked with differently colored dots. (b) 3D rendering of the chemoFGFR positive cell marked with a white dot in (a) during clustering. The cell changes its morphology dramatically and slithers over neighboring cells during the process. (c) Lateral view of the 3D volume of the cell followed in (b), in the first and last time point. During clustering, the cell loses the elongated shape typical of chain cells and adopts an epithelial columnar morphology. (d) 3D rendering of a representative wild type chain cell and (e) of a wild type neuromast cell, overlaid on 3D projections. Both apical and lateral projections are displayed. Imaris 7.6.4 was used for manual segmentation and 3D image rendering. Scalebar 20 µm.

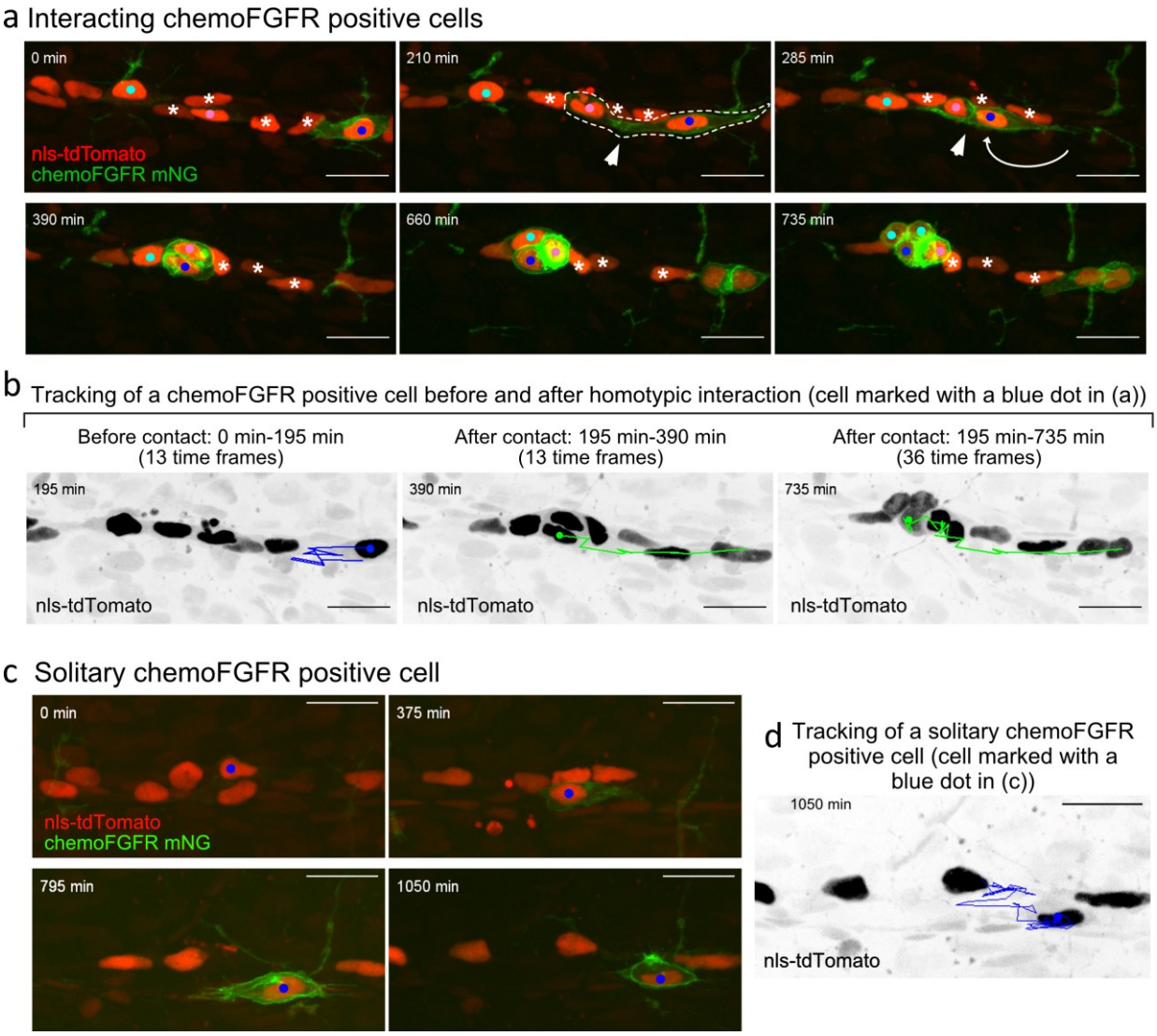

Figure 3.15: Contact-dependent interactions between chemoFGFR positive cells might provide directionality

(a) Images from a representative time lapse showing contact between two non-adjacent chemoFGFR positive cells (at 210 min), followed by aggregation and *de novo* cluster assembly. Cells were individually tracked on z-projections using the nuclear channel (cxcr4b:nls-tdTomato) and cell-cell interactions were detected using the green channel (chemoFGFR mNG). White asterisks mark chemoFGFR negative cells, colored dots mark chemoFGFR positive cells, white arrowhead highlights the contact between the two chemoFGFR positive cells.

(b) Track of the cell highlighted in (a) with the blue dot before and after the homotypic contact: in the 13 time frames before the contact, the cell move randomly (blue track), while in the 13 time frames after the contact, the cell persistently move toward the other positive partner (green track) and they form together a cluster. The track in the last image on the right starts from the time frame when the two cells contact and continues until the end of the time lapse. (c) Representative time lapse of a solitary chemoFGFR positive cell (highlighted with a blue dot), which shows a random displacement (d). Cell tracks are overlaid on z-projections of the inverted nuclear channel. Scalebar 20 µm.

3.2.4 Compaction is involved in *de novo* cluster formation

The track profiles of chemoFGFR positive cells involved in homotypic contacts pointed at the possibility that contact-based interactions might be important for cluster formation. To gain further insights, we investigated what happened in time at these contacts by monitoring more closely cellular membranes of chemoFGFR positive cells in time lapse data. We chose to analyze the formation of the simplest assembled configuration, the polyclonal doublet, formed by aggregation of two chemoFGFR positive cells. We observed that, following a first contact, the chemoFGFR positive cell pair was able to spread dramatically the cell-cell contact interface and to increase contact angle (referred as theta angle) (Figure 3.16 a, b, c). Interestingly, quantification of interface length revealed that the spreading of cell-cell interface was not progressive but multiple cycles of expansions and shrinkages could take place before reaching a maximal plateau (Figure 3.16 c). Contact angles as well as cell-cell interface lengths reflect the adhesive and contractile state of cellular interfaces [Maître et al., 2015], and, consequently, of participating cells. Therefore, the observed maximization of contact could be indicative of a low interfacial tension between the two chemoFGFR positive interacting cells, resulting in an increase in cell-cell cohesion. Our results are therefore consistent with a compaction mechanism contributing to the cohesion of chemoFGFR positive doublets.

We hypothesized that, similarly, compaction might also take place during formation of *de novo* clusters. Indeed, during cluster formation, we observed that cells aggregating from a loose chain-like configuration spread their cell-cell contact interfaces while increasing cohesion and cluster compactness in time (Figure 3.16 d). Consistent with this qualitative observation, circularity of *de novo* clusters, during the process of assembly, increased with time (Figure 3.16 e). As for interface length and angle in doublet formation, we found that fluctuations in the circularity values occurred also during cluster aggregation. This presumably reflects the inherent dynamicity underlying the formation of clusters, where cells are integrating into clusters at different times and cell proliferation might transiently affect total compactness (proliferation for example observed in Figure 3.16 d for the cell marked with red dot at 615 min).

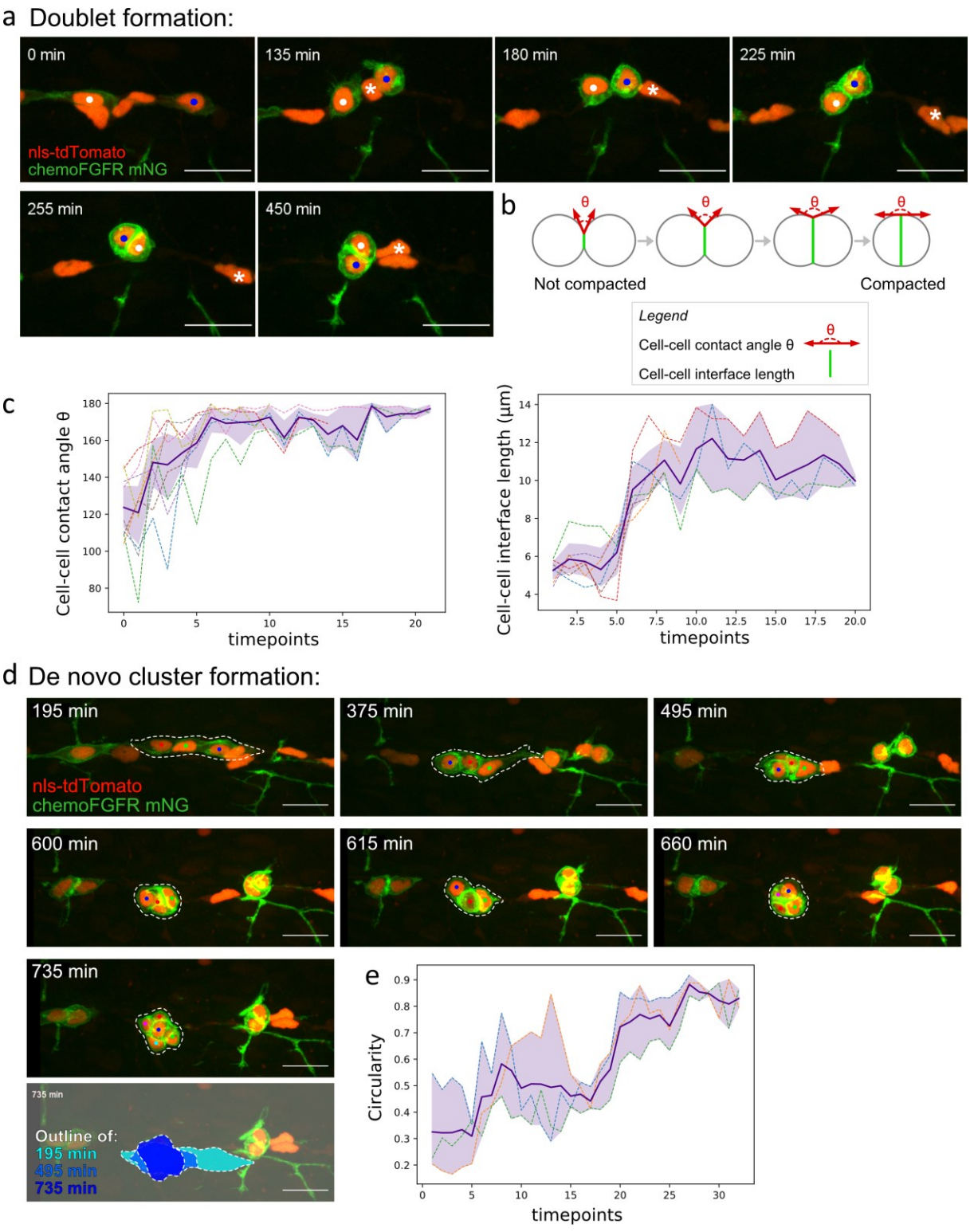

Figure 3.16: Compaction is involved in the formation of doublets and de novo clusters

(a) Z-projections from a representative time series showing doublet formation. Nuclei are shown in red (cxcr4b:nls-tdTomato) and chemoFGFR in green. The white asterisk highlights a chemoFGFR negative cell. Two chemoFGFR positive cells, highlighted with colored dots, interact and spread their cell-cell contact interface while forming a compact doublet. (b) Schematic representing the compaction process and the measured parameters. (c) Quantification of cell-cell contact theta angles ($n_{doublet}$=9) and cell-cell interface lengths ($n_{doublet}$=6) during doublet formation. Each plot displays the mean (purple line), the individual profiles (dashed lines in different

colors) and the standard deviation (shaded area). (d) During *de novo* cluster formation, the circularity of cell clusters increases over time. The bottom image shows the overlap of the areas occupied by the coalescing cells at three time points. (e) Quantification of circularity during *de novo* cluster formation ($n_{cluster}$=3). Scale bar 20 µm.

3.2.5 ChemoFGFR influences cell shapes and cell-cell interactions

The observation that chemoFGFR positive cells maximize contacts with other chemoFGFR positive cells prompted us to probe whether, conversely, they would minimize contacts with chemoFGFR negative neighbors. To address this point, we performed time lapses of chemoFGFR positive or control clones in lateral lines co-expressing a tissue-specific membrane label, to mark also membranes of chemoFGFR negative cells. We focused specifically on the behavior of solitary chain clones (that, as such, were not giving rise to *de novo* clusters) and of their neighboring cells. To achieve sparse mosaic labeling of membranes, we performed DNA injections and generated transiently expressing clones of chemoFGFR mNG or, as a control, of an inert construct sharing the same fluorophore and promoter (LexOP:lyn-mNG).

From control mosaic labeling, we could appreciate the tight connections between cells forming the continuous chain (Figure 3.17 a, e). The complex shape of chain cells makes the detection of physical boundaries between cells very challenging without mosaicism. Time lapses imaging showed that control lyn-mNG clones kept an elongated flat shape and connections with the rest of the chain from the first to the last time point (Figure 3.17 a). By contrast, solitary chemoFGFR positive clones (Figure 3.17 b) exhibited variations in cell shapes that were even more extreme than our previous observations in the transgenic line (section 3.2.3). Cells were extending long processes (Figure 3.17 b, yellow arrowhead at 270 min) and even elongating orthogonally to the plane of neighboring negative cells (Figure 3.17 c, yellow arrowhead at min 90), frequently ending up fully disconnecting from the organization of the original chain (Figure 3.17 c, yellow arrow at min 360). Despite these dramatic cell-autonomous modifications of chemoFGFR positive cell shape and behavior, the integrity of the tightly connected chain tissue was maintained unchanged, likely due to a compensatory rearrangement of chemoFGFR negative chain cells (Figure 3.17 b, c, e). Interestingly, we observed that in the totality of the cases when solitary chemoFGFR positive cells were not proliferating (Figure 3.17 d, representing the 59% of the analyzed cells), they adopted a rounded morphology (Figure 3.17 b at min 630, c white arrow from min 270 to 630).

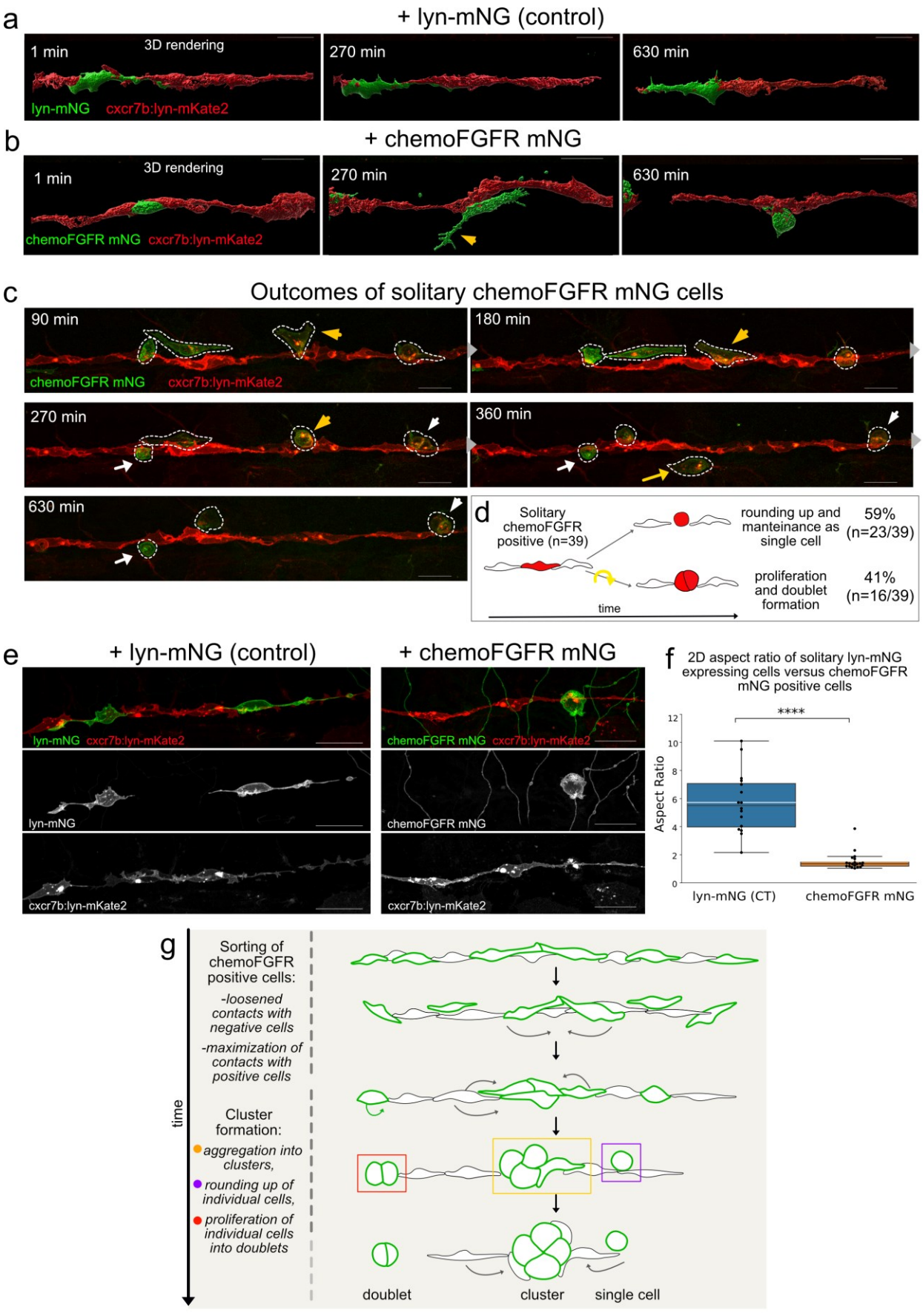
a
+ lyn-mNG (control)
1 min
3D rendering
270 min
630 min
lyn-mNG
cxcr7b:lyn-mKate2
b
+ chemoFGFR mNG
1 min
3D rendering
270 min
630 min
chemoFGFR mNG
cxcr7b:lyn-mKate2
c
Outcomes of solitary chemoFGFR mNG cells
90 min
180 min
chemoFGFR mNG
cxcr7b:lyn-mKate2
270 min
360 min
630 min
d
Solitary chemoFGFR positive (n=39)
rounding up and manteinance as single cell
59% (n=23/39)
proliferation and doublet formation
41% (n=16/39)
time
e
+ lyn-mNG (control)
+ chemoFGFR mNG
lyn-mNG
cxcr7b:lyn-mKate2
chemoFGFR mNG
cxcr7b:lyn-mKate2
f
2D aspect ratio of solitary lyn-mNG expressing cells versus chemoFGFR mNG positive cells
****
Aspect Ratio
0
2
4
6
8
10
12
lyn-mNG (CT)
chemoFGFR mNG
g
time
Sorting of chemoFGFR positive cells:
-loosened contacts with negative cells
-maximization of contacts with positive cells
Cluster formation:
aggregation into clusters,
rounding up of individual cells,
proliferation of individual cells into doublets
doublet
cluster
single cell

Figure 3.17: ChemoFGFR influences cell shapes and cell-cell interactions

(a) 3D volumes of a control cell (in green, labeled with an inert plasma membrane tag, LexOP:lyn-mNG) and (b) of a chemoFGFR positive cell (in green, labeled with chemoFGFR mNG) in time series of sparse mosaics. The cxcr7:lyn-mKate2 label was used to visualize membranes of chemoFGFR negative cells (shown in red). The interaction of the chemoFGFR positive cell with the negative neighbors changed over time (extension of long processes highlighted with the yellow arrowhead). Imaris 7.6.4 was used for segmentation and 3D image rendering. (c) Time series containing solitary chemoFGFR positive cells. Some of them adopt a migratory morphology and extend orthogonally to the chain and subsequently round up (yellow arrowhead), others directly round up (white arrow from 270 to 630 min), others proliferate and form a doublet (white arrowhead from 270 to 630 min). (d) Analysis of behaviors of solitary chemoFGFR positive cells ($n_{\text{chemoFGFR cells}}=39$). (e) Representative images of chemoFGFR positive cells and control cells at 48hpf. The individual green (lyn-mNG or chemoFGFR mNG) and red channels (cxcr7b:lyn-mKate2) and the merge of the two are shown. (f) Comparison of the 2D aspect ratio of chemoFGFR positive cells and control cells ($n_{\text{chemoFGFR cells}}=20$; $n_{\text{lyn-mNG cells}}=16$). ****:p<= $1e^{-4}$. (g) Schematic depicting our hypothetical model. Scale bar 20 µm.

To quantitatively validate this observation, we compared the 2D aspect ratio of individual chemoFGFR positive clones and lyn-mNG control clones at the 48hpf endpoint and confirmed that chemoFGFR positive cells were significantly more rounded than controls (Figure 3.17 f). We excluded that the observed rounded shape was due to cellular proliferation by noticing from time lapses that cells could keep this altered morphology for hours without resulting in cell division (Figure 3.17 c white arrow from min 270 to 630).

Overall, we concluded that dynamic variations in the morphology, acquisition of a rounded shape and disconnection events observed for chemoFGFR positive cells might be indication of a loosened interaction between chemoFGFR positive cells and chemoFGFR negative neighbors.
The results presented are thus consistent with a model where chemoFGFR positive cells maximize contacts with other chemoFGFR positive cells, driving in this way cluster aggregation, while at the same time drastically minimizing interactions with chemoFGFR negative cells (Figure 3.17 g). The selectivity resulting from these interactions might contribute to the cell sorting process in place during *de novo* cluster formation. We reasoned that the observed cellular behaviors might be a consequence of chemoFGFR-dependent cell-autonomous differences in the mechano-adhesive properties of chemoFGFR positive and negative cells.

3.3 Emergence of the 3D organization of *de novo* clusters

We showed in the previous section that mesenchymal-like cells expressing chemoFGFR rearrange into the lateral line chain region by slithering over each other's and assembling the core of 3D *de novo* clusters, that are eventually complemented with a rim of chemoFGFR negative cells. The forming *de novo* clusters develop into fully mature lateral line organs.

In the following section, we explore epithelial modules, expression patterns and architectural rearrangements associated with the emergence of such a remarkable 3D epithelial structure, developed from a simple 1D mesenchymal-like system.

3.3.1 Clusters adopt the radial polarization and tight junction organization typical of neuromasts

As one of the defining features of MET transitions is the adoption of epithelial polarization [Kim et al., 2016], we next explored markers that could be used to monitor dynamic polarity changes in living embryos. Given its central role as organizer of the microtubule network, centrosome positioning reports on epithelial polarization [Tang & Marshall, 2012]. Previous studies showed that cell polarity axis orientation, quantifiable through measurement of angles between centrosome, nucleus and a reference point (henceforth referred as polarity angle), could be used as a proxy of cell directional polarization toward the reference point, such as a lumen, a wound healing site or the interface with another cell [Burute et al., 2017; Margaron et al., 2019]. Moreover, in a previous study performed in our lab [Revenu et al., 2014], 3D nucleus-centrosome vector measurements were exploited to map cell polarity and orientation across the lateral line primordium [Revenu et al., 2014].

To probe centrosome orientation, we microinjected mRNA of a centrosome marker, centrin-tdTomato, and visualized it together with a nuclear label at 48hpf in wild type neuromasts, chain cells and in chemoFGFR-induced *de novo* clusters. The data revealed that in wild type neuromasts, centrosomes were apically localized and organized in a radial pattern (Figure 3.18 a). In wild type chain cells, quantification of polarity angles in 2D, using as reference point the perpendicular axis of the image, showed that chain centrosomes preferentially located at the left-side or right-side with respect to the center of the nucleus (Figure 3.18 b). By contrast, cells in *de novo* clusters displayed an apical and radial centrosome distribution comparable to wild type neuromasts, with polarity angles (obtained using as reference point the center of the cluster) close to 0°, which means that the nucleus-centrosome axis consistently pointed toward the center of the cluster (Figure 3.18 e). Remarkably, this radial centrosome organization was present also in 'small' clusters (composed of only three cells), suggesting that establishment of cluster polarity might be an early event during cluster assembly (Figure 3.18 e).

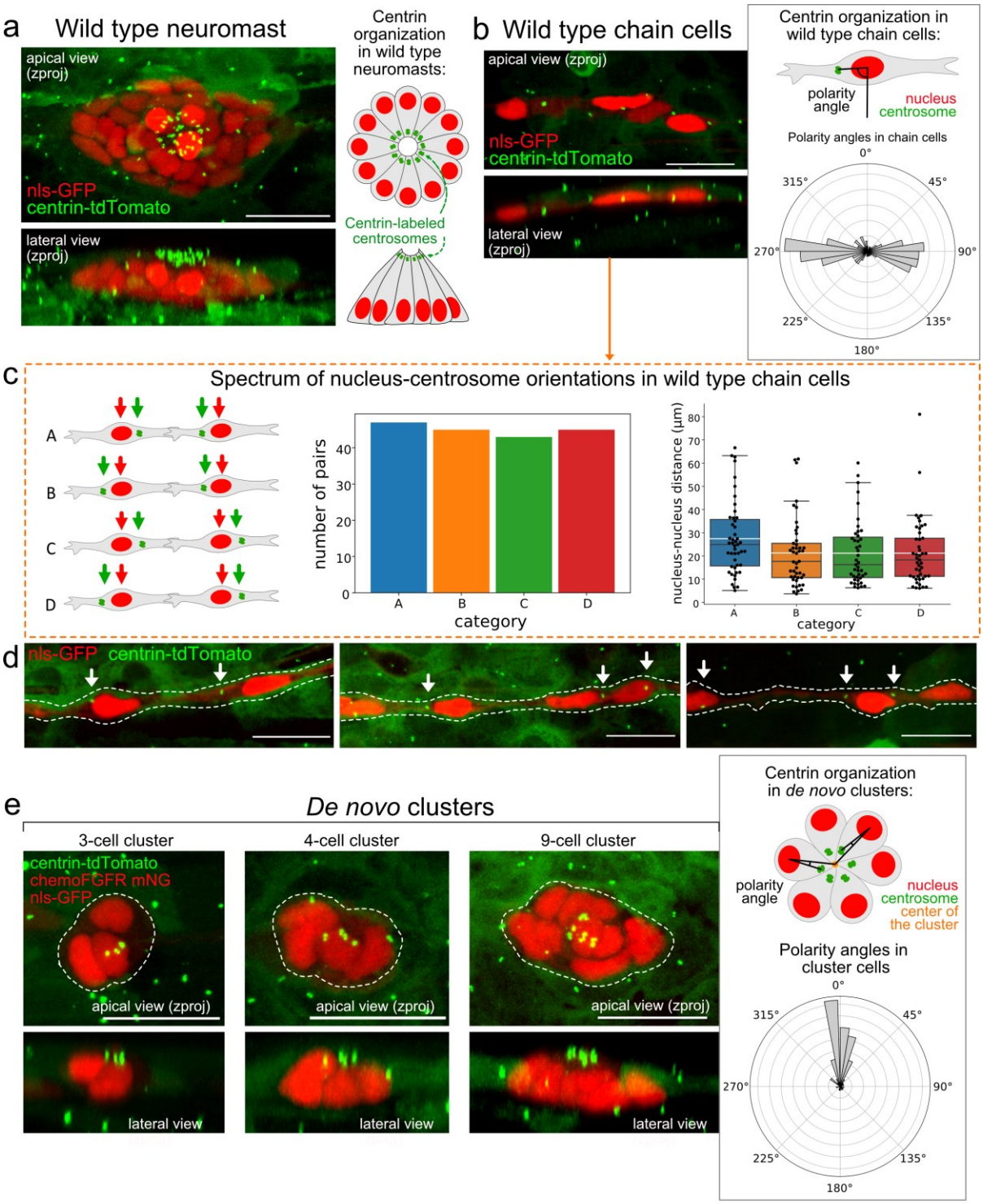
a Wild type neuromast
apical view (zproj)
nls-GFP
centrin-tdTomato
lateral view (zproj)
Centrin organization in wild type neuromasts:
Centrin-labeled centrosomes
b Wild type chain cells
apical view (zproj)
nls-GFP
centrin-tdTomato
lateral view (zproj)
Centrin organization in wild type chain cells:
polarity angle
nucleus
centrosome
Polarity angles in chain cells
0°
45°
90°
135°
180°
225°
270°
315°
c
Spectrum of nucleus-centrosome orientations in wild type chain cells
A
B
C
D
number of pairs
category
nucleus-nucleus distance (µm)
d
nls-GFP centrin-tdTomato
e
De novo clusters
3-cell cluster
4-cell cluster
9-cell cluster
centrin-tdTomato
chemoFGFR mNG
nls-GFP
apical view (zproj)
lateral view
Centrin organization in de novo clusters:
polarity angle
nucleus
centrosome
center of the cluster
Polarity angles in cluster cells
f
ZO1 organization in wild type neuromasts:
ZO1-labeled tight junctions
Wild type neuromast
De novo clusters
apical view (zproj)
ZO1
dapi
cldnb:lyn-GFP
ZO1

Figure 3.18: De novo clusters exhibit neuromast-like radial polarity and tight junctions

(a) Representative z-projection of a 48hpf wild type neuromast showing nuclear (displayed in red, LexOP:nls-GFP) and centrosomal labels (displayed in greed, centrin-tdTomato). Below, the z-projection of the yz-reslice is shown. On the right, a cartoon depicting centrosome organization in neuromasts, that are apically localized and organized in a radial pattern. (b) Representative z-projection of 48hpf wild type chain cells showing nuclear (displayed in red, LexOP:nls-GFP) and centrosomal labels (displayed in greed, centrin-tdTomato). On the right, a cartoon illustrating how polarity angles were collected for chain cells. Y-axis was used as reference point. Polarity angles were represented in a rose plot ($n_{\text{chain cells}}$=133; N_{embryos}=3). For the generation of the rose plot the following parameters were used: distance between lines=3; y max=17; n bins=40. (c) Chain cell pairs from 48hpf wild type lateral lines were classified in four categories, based on the pairwise nucleus-centrosome orientation ($n_{\text{pairs analyzed}}$=181; N_{embryos}=5). From left to right: cartoon displaying the four categories of chain cell pairs, a bar plot illustrating the counts per category, a boxplot comparing cell-to-cell distance for different categories. (d) Three images of 48hpf wild type chain cells: the centrosome tends to be located close to the nucleus (white arrows mark centrosomes). (e) Representative z-projection of 48hpf *de novo* clusters showing chemoFGFR, nuclear (both displayed in red, LexOP:chemoFGFR mNG, LexOP:nls-GFP) and centrosomal labels (displayed in green, centrin-tdTomato). Below, the z-projection of the yz-reslice is shown. On the right, a cartoon illustrating how polarity angles were collected for cluster cells. The center of the cluster was used as reference point. Polarity angles were represented in a rose plot ($n_{\text{cluster cells}}$=82; N_{embryos}=4). For the generation of the rose plot the following parameters were used: distance between lines=3; y max=23; n bins=40. (f) Representative z-projections of a 4dpf wild type neuromast and of *de novo* clusters (highlighted with white arrowheads), displaying immunostaining of the tight junction protein ZO1 (in green). Below, the individual ZO1 channel. On the left, cartoon depicting ZO1 organization in wild type neuromasts. Scalebar 20 µm.

Given that chain cells can be considered the 'ground state' from which *de novo* clusters emerge, we decided to gain further insights into their centrosome organization along the wild type lateral line (Figure 3.18 c). To this aim, we classified adjacent chain cell pairs in four categories (A, B, C, D), based on their pairwise nucleus-centrosome orientation, that is the relative position of centrosome and nucleus of each cell relative to the one in the contiguous cell (Figure 3.18 c, left). We first quantified the frequency of each category along the whole 48hpf lateral line and we found that all the categories had the same frequency (Figure 3.18 c, middle). Secondly, we tested whether cell-cell distance influenced cell pair orientation by measuring nucleus-nucleus distance across distinct categories (Figure 3.18 c, right). The data showed that there was no net difference in cell-cell distance for different categories, suggesting that chain cells display a randomized polarity. In addition, we observed that, in chain cells nuclear-centrosome distance was short (Figure 3.18 d): centrosomes were often located in the immediate proximity of the nucleus. Given that displacement of centrosomes from intercellular junctions to a more central location has been associated with epithelial to mesenchymal transition in different systems [Burute et al., 2017], this observation further strengthens the idea that chain cells are *bona fide* mesenchymal-like cells.

Next, to further address to which extent *de novo* clusters resemble neuromasts in terms of cluster polarity, we probed whether they form tight junctions. Tight junctions are key barriers ensuring the establishment of functionally distinct apical and basolateral membranes in cells and represent another crucial feature of epithelial cells [Rodriguez-Boulan & Macara, 2014]. To investigate tight junction formation, we performed ZO1 immunostaining at 4dpf and compared wild type neuromasts, wild type chain cells and chemoFGFR-induced *de novo* clusters. Consistent with a previous study [Lecaudey et

al., 2008], in wild type neuromasts ZO1 localized apically in the cage-shaped basket forming the microlumina, while resulted undetectable in chain cells (Figure 3.18 f). In *de novo* clusters, ZO1 revealed a distribution comparable with wild type neuromasts (Figure 3.18 f right, white arrows).

Overall, the results demonstrate that, during chemoFGFR-dependent cluster formation, cells rearrange from a ground state where they display a mesenchymal-like randomized polarity into a fully polarized 3D cluster, exhibiting neuromast-like radial polarization and tight junctions.

3.3.2 *De novo* clusters display nuclear orientation characteristic of neuromasts

Previous work in the lab [Revenu et al., 2014] demonstrated that during leader to follower transition in the migrating primordium, cells assume a more pronounced columnar shape and an upright orientation relative to the tissue axis, suggesting a linear correlation between cell 'epithelialness' and cell axis elongation and orientation. We therefore decided to quantitatively investigate cell polarity changes in 3D.

Recent observations in the lab [Hartmann et al., 2020] revealed that, in the migrating primordium, nuclear 3D shape largely recapitulates the overall cell shape, likely due to the large size of the nucleus relative to the entire cell. Given this match, we reasoned that we could use nuclei orientation as an easily accessible readout for cell polarity changes in 3D during *de novo* cluster formation.

We developed a pipeline to extract 3D shape and orientation of single nuclei and applied it to chemoFGF-dependent *de novo* clusters and, for comparison, to wild type neuromasts and wild type chain cells (Figure 3.19 a). First, we performed high-resolution live imaging of 48hpf lateral lines expressing or not expressing chemoFGFR, together with a nuclear label (nls-tdTomato). Second, we implemented an automated 3D segmentation of lateral line nuclei using the machine-learning based Ilastik software and we extracted single nuclei features using Fiji plugins (detailed in Material and Methods, section 2.10.8). Finally, after a manual curation step, we assigned segmented nuclei to three classes (neuromast nuclei, chain cells nuclei, *de novo* cluster nuclei) based on location and organization in the original images. Following feature extraction and assignment, we compared nuclear elongation (described as ratio of major axis and minor axis of the ellipse inscribed in each nucleus) and orientation (described as Theta angle, which is the angle between major axis of the nucleus and XY plane of the image) in wild type neuromasts and chain cells (Figure 3.19 a, b). We observed that chain cells presented more elongated nuclei than neuromast cells and that they robustly oriented their major axis parallel to the plane of the image (that is, parallel to the rostro-caudal axis of the fish), whereas neuromast cell nuclei oriented more perpendicularly to the plane of the image (and so parallel to the dorso-ventral axis of the fish) (Figure 3.19 c). This last observation is consistent with the previously described 'firewood stack' configuration of neuromast cells [Revenu et al., 2014]. ChemoFGFR-dependent *de novo* clusters displayed both a decreased nuclear elongation and a more upright nuclear axis orientation compared to chain cells, similarly to neuromast nuclei (Figure 3.19 d, e). This result confirms that *de novo* clusters adopt a 3D cell orientation typical of wild type neuromasts.

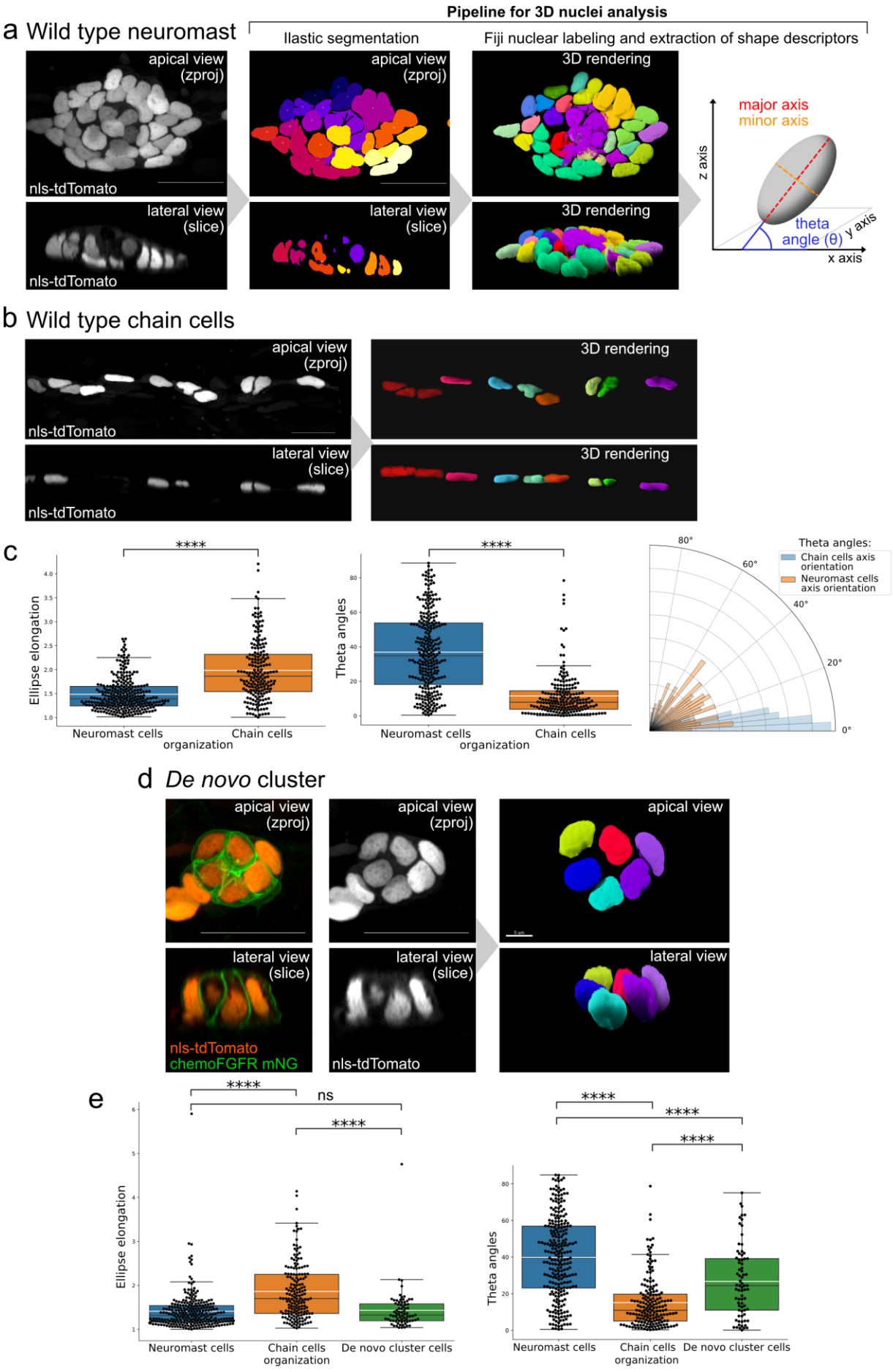
a Wild type neuromast
Pipeline for 3D nuclei analysis
Ilastic segmentation
Fiji nuclear labeling and extraction of shape descriptors
apical view (zproj)
nls-tdTomato
lateral view (slice)
3D rendering
major axis
minor axis
z axis
y axis
x axis
theta angle (θ)
b Wild type chain cells
c
****
Ellipse elongation
Neuromast cells
Chain cells
organization
Theta angles
Theta angles:
Chain cells axis orientation
Neuromast cells axis orientation
d De novo cluster
chemoFGFR mNG
e
ns
De novo cluster cells

Figure 3.19: De novo clusters display nuclear orientation characteristic of neuromasts

(a) Representative z-projection of a 48hpf wild type neuromast with nuclear labeling (cxcr4:nls-tdTomato). Midsection of the yz-reslice is shown below and 3D rendering on the right. On the right, the pipeline used for the 3D nuclear analysis is illustrated: first, an Ilastik-based segmentation is performed, and second, information on shape and orientation of each nucleus are extracted using Fiji plugins, approximating the nuclear shape to an ellipse. (b) Representative z-projection of 48hpf wild type chain cells with nuclear labeling (cxcr4:nls-tdTomato). Midsection of the yz-reslice is shown below and 3D rendering on the right. (c) Nuclei of neuromast cells were compared to nuclei of chain cells in term of elongation (mayor to minor axis ratio) and orientation (theta angle, meaning the angulation of the major axis relative to the XY plane of the image) ($n_{\text{chain cells}}$=196; $n_{\text{neuromast cells}}$=275). For the generation of the rose plot the following parameters were used: distance between lines=5; y max=40; n bins=25. (d) Representative z-projection of 48hpf *de novo* clusters with chemoFGFR mNG and nuclear labeling (cxcr4:nls-tdTomato). Midsection of the yz-reslice is shown below and 3D rendering on the right. Nuclei extracted from *de novo* cluster were processed following the same pipeline described above. (e) Elongation and orientation of cluster nuclei were compared to the ones of chain cells and of neuromast cells from the same embryos ($n_{\text{chain cells}}$=176; $n_{\text{neuromast cells}}$=256; $n_{\text{cluster cells}}$=75). Imaris 7.6.4 was used for 3D image rendering.****:p<= $1e^{-4}$; ns: $5e^{-2}$ < p <= 1. Scale bar 20 µm.

3.3.3 *De novo* clusters show neuromast-specific epithelial marker expression

Classically, MET is associated with shifts in expression from mesenchymal-specific to epithelial-specific genes [Pei et al., 2019]. As a next step, we sought to explore expression patterns of *de novo* clusters and compare them with expression patterns of cells they originate from, chains, and of cells they end up resembling, neuromast cells.

We focused specifically on detection of Krt1c5 expression via Krt1c5 ISH, which we established as a *bona fide* neuromast marker. Indeed, looking at wild type embryos, we observed that Krt1c5 ISH signal was high and specific in neuromasts from early stages (34hpf), immediately after neuromast deposition, to later stages (48hpf) (Figure 3.20 a). The fact that Krt1c5 expression stayed high in neuromasts at 48hpf, when FGF signaling likely decreases because of the physiological opening of FGF-trapping microlumina, is consistent with the hypothesis that Krt1c5 belongs to the class of genes that can be switched on by FGF signaling but do not dynamically fluctuate with its signaling levels [Durdu, 2015]. Even though very little is known about this gene belonging to the intermediate filament family, keratins in general are considered *bona fide* markers of epithelial cells in multiple systems [Hudson, 2002]. To visualize the Krt1c5 expression pattern in *de novo* clusters, we performed chemoFGFR induction and, after fixation at 48hpf, Krt1c5 ISH. *De novo* clusters displayed a strong Krt1c5 signal, comparable with Krt1c5 staining of wild type neuromasts, while Krt1c5 expression was undetectable in chain cells (Figure 3.20 b, c). We next visualized Krt1c5 ISH pattern at earlier stages of *de novo* cluster formation, in 34hpf embryos fixed 8 hours after chemoFGFR induction (Figure 3.20 c). Surprisingly, although clusters were not yet detectable at this early stage of cluster formation, we noticed patchy expression of Krt1c5 in chain regions of chemoFGFR expressing embryos, while no staining was visible in the corresponding regions of wild type lateral lines (Figure 3.20 d, e). We thus showed that during cluster formation, from early stages onwards, chemoFGFR induction drives expression of a neuromast-specific marker. This result further strengthens our hypothesis that expression of chemoFGFR can trigger the entire epithelialization program 'from scratch'.

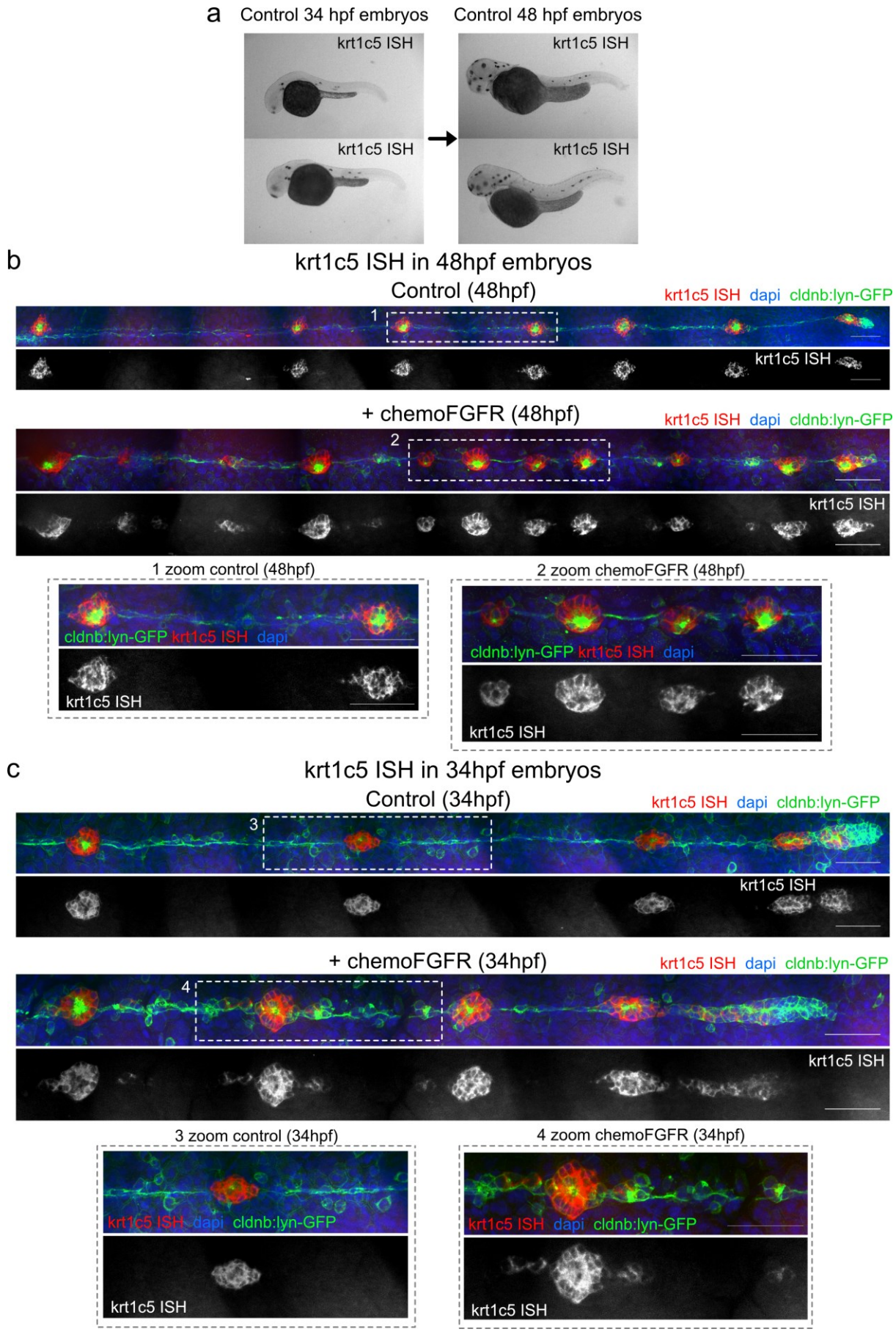
a
Control 34 hpf embryos
Control 48 hpf embryos
krt1c5 ISH
krt1c5 ISH
krt1c5 ISH
krt1c5 ISH
b
krt1c5 ISH in 48hpf embryos
Control (48hpf)
krt1c5 ISH dapi cldnb:lyn-GFP
1
krt1c5 ISH
+ chemoFGFR (48hpf)
krt1c5 ISH dapi cldnb:lyn-GFP
2
krt1c5 ISH
1 zoom control (48hpf)
cldnb:lyn-GFP krt1c5 ISH dapi
krt1c5 ISH
2 zoom chemoFGFR (48hpf)
cldnb:lyn-GFP krt1c5 ISH dapi
krt1c5 ISH
c
krt1c5 ISH in 34hpf embryos
Control (34hpf)
krt1c5 ISH dapi cldnb:lyn-GFP
3
krt1c5 ISH
+ chemoFGFR (34hpf)
krt1c5 ISH dapi cldnb:lyn-GFP
4
krt1c5 ISH
3 zoom control (34hpf)
krt1c5 ISH dapi cldnb:lyn-GFP
krt1c5 ISH
4 zoom chemoFGFR (34hpf)
krt1c5 ISH dapi cldnb:lyn-GFP
krt1c5 ISH

Figure 3.20: ChemoFGFR induction drives expression of the neuromast-specific marker Krt1c5

(a) In situ staining of Krt1c5 in 34hpf and 48hpf wild type embryos (acquired jointly with Maaike Allers). (b) Overviews and close-up views of Krt1c5 in situ staining in 48hpf controls and chemoFGFR-induced embryos, showing positive staining in neuromasts and *de novo* clusters. Both the merge of the red (Krt1c5 ISH), green (cldnb:lyn-GFP) and blue (dapi) channels and the Krt1c5 ISH channel alone are shown. (c) Overviews and close-up views of Krt1c5 in situ staining in 34hpf controls and chemoFGFR-induced embryos. ChemoFGFR-induced embryos show patches of positive staining also in chain regions. Scale bar 50 µm.

3.3.4 Cell adhesion changes during *de novo* cluster formation

De novo cluster formation is a highly dynamic process, where cells undergo transient interactions and crawl over each other while organizing in a radially polarized 3D assembly. Given that lateral line cells are a tightly interconnected system and that contact-based cell interactions appear to be important during chemoFGFR positive cell coalescence (paragraph 3.2.3), we explored the impact of adhesions during *de novo* cluster emergence. Cadherin and CAMs are the two main classes of adhesion molecules described in literature. Intriguingly, previous studies showed that members of the CAM family are involved in cell slithering [Kuo & Krasnow, 2015] and cell intercalation [Bergstralh et al., 2015], but also in other dynamic processes such as cardiac trabeculation, cell segregation [Cirulli et al., 1994; Esni et al., 1999] and epithelial condensation [Y. S. Lee et al., 1998; Widelitz & Chuong, 1999]. Cadherins, on the other side, are crucial components of adherens junction, whose role in a plethora of phenomena such as cell sorting and segregation is well established [Halbleib & Nelson, 2006].

A microarray-based expression profiling study performed by a former student in the lab [Durdu, 2015] provided support to the hypothesis that FGF signaling upregulates cell-cell adhesion. In particular, NCAM1b (a member of the CAM family) was identified as positive FGF target in the lateral line [Durdu, 2015]. Although expression of Cdh1 and Cdh2 (respectively N- and E-Cadherin) were not detectably affected by FGF levels, a second study in our lab demonstrated that their localization within cells of the lateral line could differ [Revenu et al., 2014]. Cdh2 was shown to apically accumulate in neuromast cells and to constitute pools that were more stable in more aged neuromasts than in newly deposited ones [Revenu et al., 2014].

3.3.4.1 Cdh2 during *de novo* cluster formation

To evaluate the impact of chemoFGFR induction on Cdh2 expression and localization, we made use of the Cdh2 BAC fish line (Cdh2:Cdh2-GFP), previously generated in the lab [Revenu et al., 2014]. First, to characterize the 'ground' state of Cdh2 in wild type conditions, we compared the Cdh2 pattern of wild type chain cells, which had never been analyzed in previous studies, with wild type neuromasts at 48hpf (Figure 3.21 a, b). Consistently with published findings, wild type neuromasts displayed Cdh2 signal at plasma membranes, with clear apical enrichment [Revenu et al., 2014] (Figure 3.21 a). By contrast, chain cells exhibited very low levels of Cdh2, barely detectable on top of the strong Cdh2 signal of muscle cells, and no enrichment of Cdh2 could be detected at chain cells interfaces (Figure 3.21 b). The result shows that Cdh2 appears to be differentially expressed in apical-basal polarized neuromast cells and mesenchymal-like chain cells.

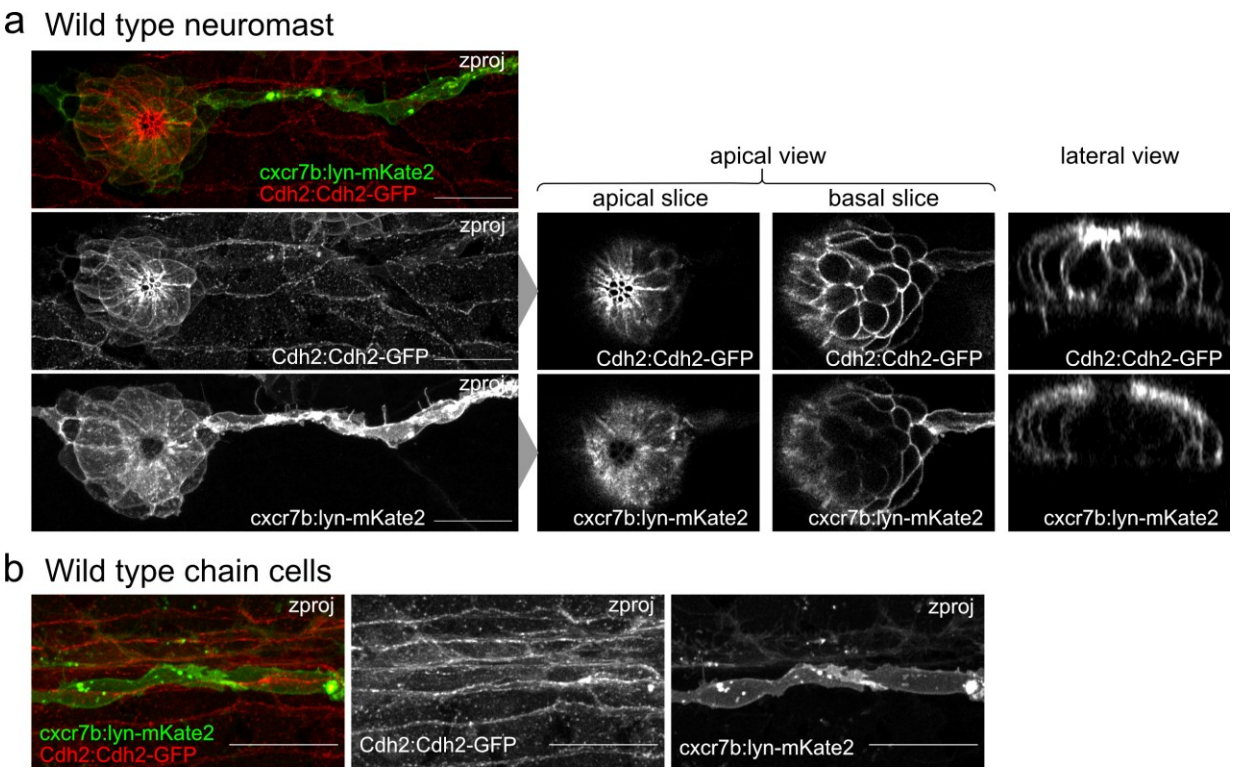

Figure 3.21: Visualization of Cdh2 in wild type neuromast and chain cells

(a) Representative 48hpf wild type neuromast labeled with Cdh2:Cdh2-GFP (in red) and a membrane counterstain (cxcr7b:lyn-mKate2, in green). Above, the merge of green and red channel; below, the individual channels (z-projections). On the right side, an apical and a basal confocal slice from the neuromast z-stack and a mid-section of an yz-reslice (individual channels are displayed), showing apical accumulation of Cdh2. (b) Representative 48hpf wild type chain cells (z-projections). Cdh2 results almost undetectable in this cell population. Merge and individual channels are displayed. Scale bar 20 µm.

We reasoned that these differences might be the consequence of the different extent of exposure to FGF signaling of neuromast cells and chain cells. To test that, we took advantage of chemoFGFR as a tool to cell-autonomously activate FGF signaling in chain cells and we compared Cdh2 levels of chemoFGFR positive and negative cells in 48hpf embryos. Analyzing solitary cells, we found that chemoFGFR positive cells displayed increased Cdh2 expression compared to chemoFGFR negative cells, whose Cdh2 levels were almost undetectable (Figure 3.22 a, b). By contrast, comparison of Cdh2 levels in chemoFGFR positive and negative cells located within deposited neuromasts, where baseline Cdh2 expression is already increased compared to chain cells, did not give detectable differences (Figure 3.22 c). Therefore, it appears that ectopic FGF signaling triggers an increase in Cdh2 expression in naïve chain cells but cannot lead to a further increase of Cdh2 in cells that, as part of neuromasts, did experience high levels of FGF signaling beforehand. We conclude that Cdh2 expression increases cell-autonomously upon chemoFGFR induction but does not scale with signaling level once it is switched on.

Next, we explored Cdh2 expression and localization during *de novo* cluster assembly. To this aim, we acquired images of chemoFGFR positive lateral lines expressing Cdh2:Cdh2-GFP at the 48hpf endpoint, and we analyzed cells in various assembly configurations (as single chain cell, as doublet, as 'small' or 'large' cluster). Based on these endpoint experiments, we reconstructed a conceivable timeline of Cdh2 marker behavior at different stages of the cluster formation process (Figure 3.22 d, g, h). Surprisingly, we found that, when still in a chain configuration, chemoFGFR positive cells displayed Cdh2 enrichment at contact interfaces with other chemoFGFR cells, while no enrichment could be detected at contact interfaces of chemoFGFR negative cells (Figure 3.22 red arrowheads in a, d). This interfacial accumulation persisted also during emergence of a 3D clusters (Figure 3.22 d, g). Interestingly, larger more mature clusters showed an apical shift of Cdh2 accumulation, similarly to wild type neuromasts, while interacting lateral membranes resulted comparably depleted from it (Figure 3.22 h).

These observations suggest that Cdh2 levels and localization are remodeled as apical-basal polarity emerges and cells organize in a 3D organ (Figure 3.22 i). Moreover, increased expression of Cdh2 in chemoFGFR positive compared to negative cells and Cdh2 enrichment observed specifically at the interfaces of chemoFGFR positive cells point at the possibility that Cdh2 might play a role in chemoFGFR-dependent cell sorting and cell-cell 'recognition'.

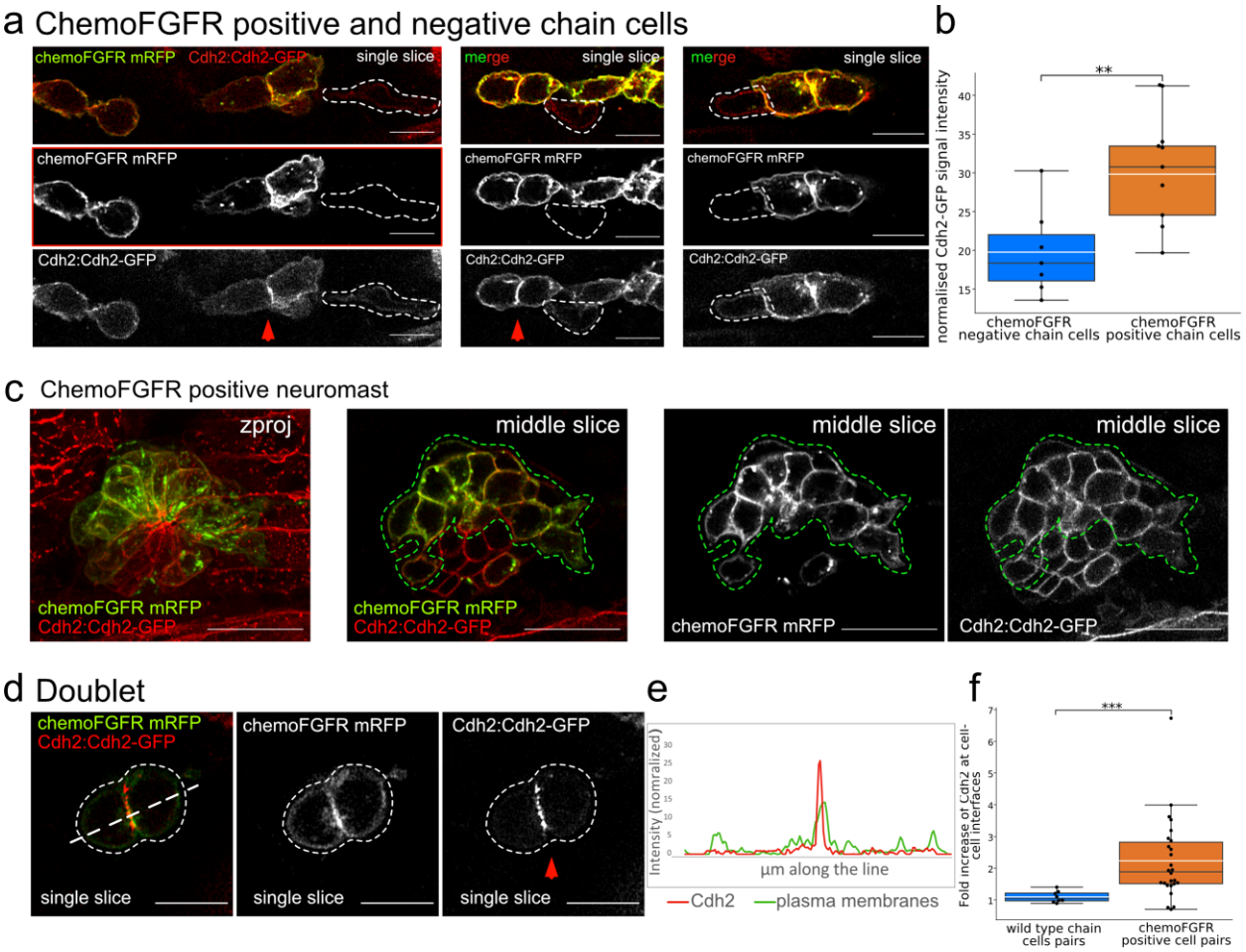
a ChemoFGFR positive and negative chain cells
chemoFGFR mRFP
Cdh2:Cdh2-GFP
single slice
merge
b
normalised Cdh2-GFP signal intensity
**
chemoFGFR negative chain cells
chemoFGFR positive chain cells
c ChemoFGFR positive neuromast
zproj
middle slice
d Doublet
e
Intensity (nomralized)
µm along the line
Cdh2
plasma membranes
f
***
Fold increase of Cdh2 at cell-cell interfaces
wild type chain cells pairs
chemoFGFR positive cell pairs
g De novo cluster 'small'
single apical slice
single basal slice
h De novo cluster 'large'
i
pseudo time
Cdh2
chemoFGFR

Figure 3.22: Visualization of Cdh2 in chemoFGFR expressing lateral lines

(a) Individual z-stack slices show Cdh2:Cdh2-GFP distribution in chemoFGFR positive and negative chain cells in 48hpf chemoFGFR expressing lateral lines. The merge of green (chemoFGFR mRFP) and red channel (Cdh2:Cdh2-GFP) and the individual channels are shown. Contact interfaces between chemoFGFR positive cells display Cdh2 enrichment (highlighted with red arrowheads). Differences in Cdh2-GFP intensity levels of chemoFGFR positive and negative cells (the latter highlighted with dashed white lines) were also observed and quantified in (b). For the boxplot $n_{\text{chemoFGFR positive cells}}=10$; $n_{\text{chemoFGFR negative cells}}=7$. (c) In chemoFGFR positive neuromasts, there is no detectable difference in Cdh2 signal intensity between chemoFGFR positive cells (encircled by a green dotted line) and negative cells. The z-projection and a central z-stack slice (merge and individual channels) are shown. (d) Doublets of chemoFGFR positive cells display interfacial Cdh2 enrichment, quantified in the line profile (e) and in the boxplot (f). For the boxplot $n_{\text{chemoFGFR positive interfaces}}=26$; $n_{\text{wild type chain interfaces}}=8$. (g) Cdh2 enrichment at cell contacts can be observed in 'small' clusters, while (h) in larger clusters, Cdh2 apically accumulates (yellow arrow). Z-projections and individual apical or basal z-stack slices are displayed. White dotted lines were used to outline clusters and doublets. (i) Schematic depicting the behavior of Cdh2:Cdh2-GFP (in red) in a hypothetical pseudo timeline. ChemoFGFR positive cells are indicated with green dots. ***: $1e^{-4} < p <= 1e^{-3}$; **: $1e^{-3} < p <= 1e^{-2}$. Scale bar (a), (d), (g), (h) 10 µm; (c) 20 µm.

3.3.4.2 NCAM1b during *de novo* cluster formation

To evaluate the impact of chemoFGFR induction on NCAM1b localization, we made use of a fish line misexpressing NCAM1b-GFP driven by GAL4/UAS system, previously generated in the lab (by Sevi Durdu, unpublished). We observed that in wild type neuromasts NCAM1b localized at plasma membranes and was specifically enriched on lateral membranes, while no NCAM1b signal was detectable on apical membranes (Figure 3.23 a). Co-expression of NCAM1b and Cdh2, which, as described in the previous paragraph, accumulates apically in neuromasts, confirmed the complementary localization pattern of the two adhesion proteins (Figure 3.23 b). Interestingly, NCAM1b visualization in chain cells and analysis of signal intensity profiles across cell interfaces revealed that NCAM1b enriched at cell-cell contacts between chain cells, similarly to lateral membranes in neuromasts (Figure 3.23 c, d).

NCAM1b appeared however to be enriched at cell-cell interfaces only between UAS:NCAM1b-GFP misexpressing cells. To test this observation, we exploited the architectural simplicity of zebrafish peridermal cells and we generated a 'salt and pepper' pattern of NCAM1b-misexpressing cells by transient injections of CMV-driven NCAM1b-tagRFPt (Figure 3.23 e). By analyzing NCAM1b localization at periderm cells contacts, we found that indeed NCAM1b enriched specifically at interfaces between expressing cells (Figure 3.23 e, g).

These observations suggest that homophilic NCAM1b interactions drive interface enrichment of NCAM1b, as described in other systems [Bloch, 1992]. We conclude that as NCAM1b localization mostly reflects cell-cell contact points, NCAM1b-GFP can be considered a contact-dependent marker.

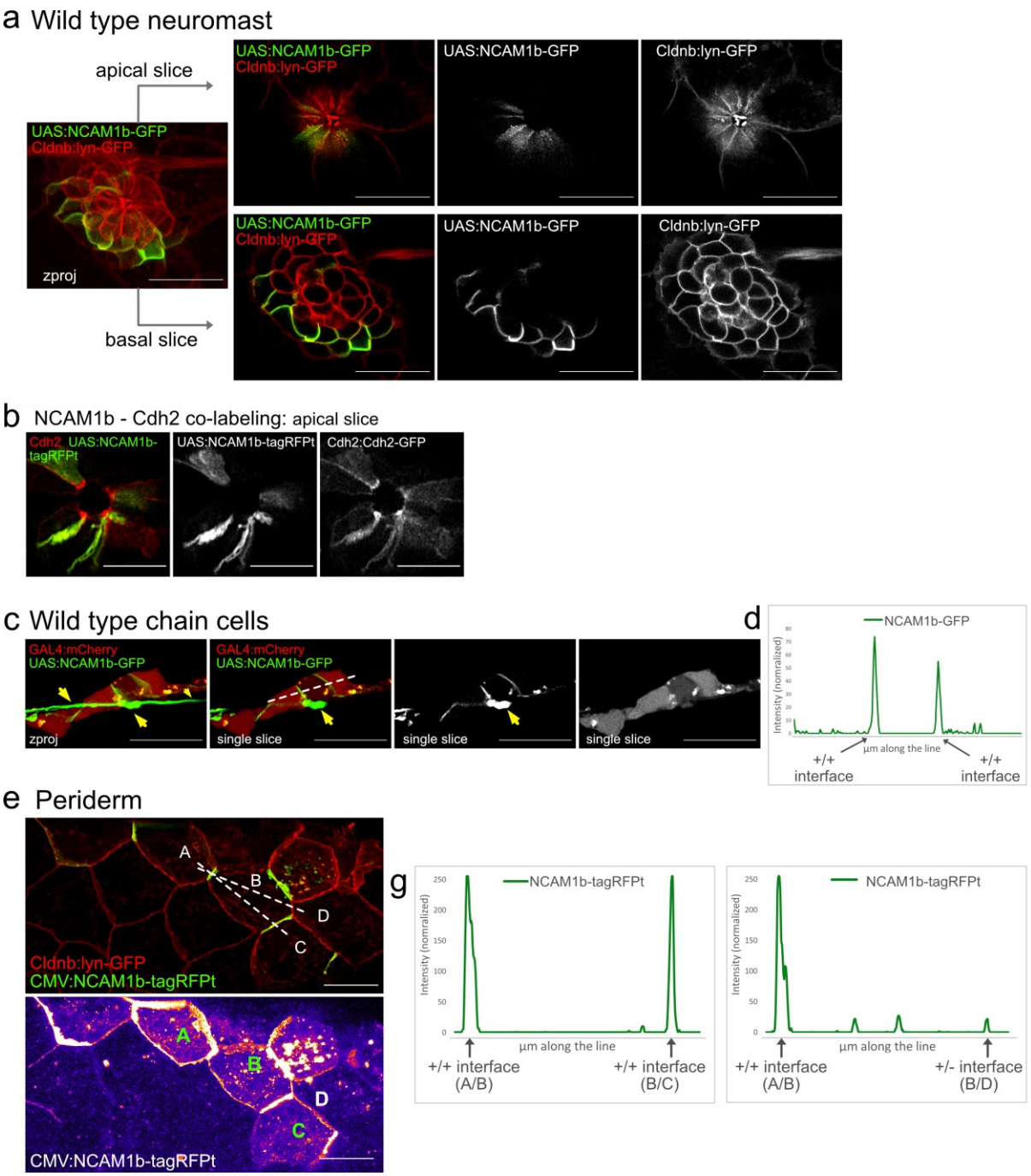

Figure 3.23: Visualization of NCAM1b in wild type neuromasts, chain cells and periderm cells

(a) Representative z-projection of a 48hpf wild type neuromast labeled with NCAM1b-GFP (in green, UAS: NCAM1b-GFP) and a membrane counterstain (in red, cldnb:lyn-GFP), showing NCAM1b-GFP enrichment at lateral membranes. Apical and basal z-stack slices are displayed on the right as individual channels and merge of green and red channels. (b) Apical z-stack slice from a neuromast co-expressing NCAM1b and Cdh2 (UAS:NCAM1b-tagRFPt and Cdh2:Cdh2-GFP). (c) Representative z-projection of 48hpf wild type chain cells. NCAM1b is also expressed in the lateral line nerve (marked with yellow arrowheads) that is one of the GAL4 positive tissues. A central z-stack slice is displayed on the right, as individual channels and a merge of green and red channels. GAL4:mCherry was used as cytoplasmic counterstain. (d) Line plot of the NCAM1b-GFP signal intensity corresponding to the dashed line in (c). (e) Periderm cells showing salt and pepper pattern of NCAM1b misexpression (CMV:NCAM1b-tagRFPt). Below, the NCAM1b-GFP channel is displayed with the fire lookup table and NCAM1b misexpressing cells are marked with green letters and non-misexpressing cells with white letters.

(g) Line plots of the NCAM1b-GFP signal intensity corresponding to the dashed lines in (e), crossing interfaces between misexpressing cells (A/B and B/C) or between a misexpressing and non-misexpressing cell (B/D). Scale bar (b) 10 µm; (a),(c),(e) 20 µm.

Next, we explored localization of NCAM1b-GFP in chemoFGFR expressing lateral lines at the 48hpf endpoint. Analysis of various assembly configurations (single chain cell, as doublet, as 'small' or 'large' cluster) at 48hpf confirmed that NCAM1b behaves as a contact-dependent marker, showing enrichment at cell-cell interfaces of misexpressing cells at every stage of cluster formation, in both chemoFGFR positive and negative cells (Figure 3.24 a, b, c, d, e, f). As for wild type neuromasts, also in *de novo* clusters NCAM1b accumulation was detected on lateral membranes, while no NCAM1b-GFP signal was detectable on clusters apex (Figure 3.24 e, f). Importantly, the fact that NCAM1b-enriched membranes reflects points of cell-cell contact in these transient assembly configurations, confirms that NCAM1b reporters are well-suited for dynamic visualization of cell-cell interactions in time, independently from cellular polarity.

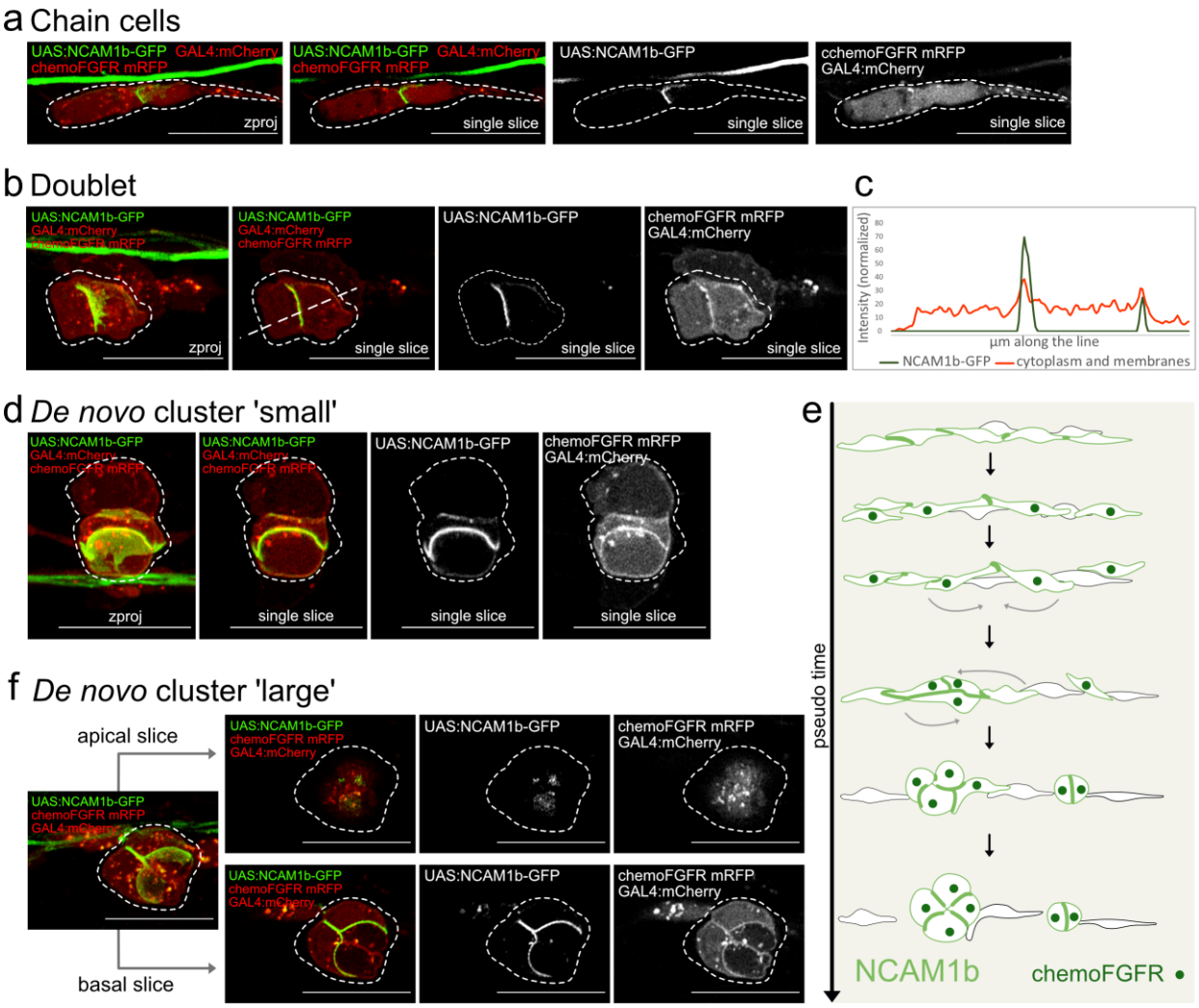

Figure 3.24: Visualization of NCAM1b in chemoFGFR expressing lateral lines

Representative z-projections of 48hpf chemoFGFR positive chain cells (a), doublets (b), 'small' and 'large' *de novo* clusters (d)(f), labeled with NCAM1b-GFP (in green, UAS: NCAM1b-GFP), a cytoplasmic counterstain (in red,

GAL4:mCherry) and the chemoFGFR mRFP at the plasma membrane. Middle or apical and basal z-stack slices are displayed on the right side, as individual channels and merge of green and red channels. (c) Line plot of the NCAM1b-GFP signal intensity corresponding to the dashed line in (b). (e) Schematic representing behavior of NCAM1b-GFP (in light green) in a hypothetical pseudo timeline. ChemoFGFR positive cells are marked with dark green dots. NCAM1b-GFP enriches at the contact interfaces of all misexpressing cells. White dotted lines are used to outline clusters and doublets. Scale bar 20 µm.

3.3.4.3 Cdh2 and NCAM1b and 1a knockouts do not affect cluster formation

Given the interesting patterns of Cdh2 and NCAM1b in the lateral line during *de novo* cluster formation, and, more generally, given the proven contribution of adhesions in processes like slithering, cell reciprocal recognition and sorting, we addressed whether Cdh2 and NCAM1b were required for *de novo* cluster assembly. To this aim, we took advantage of the Crispr-Cas9 technology to perform knockout experiments.

Since a recent publication established injections of four sgRNA guides per gene as the most efficient method to knockout genes directly in F0 embryos (henceforth referred as Crispant), we exploited designed sgRNA guide sets provided from that study to knockout Cdh2 [R. S. Wu et al., 2018b] (Figure 3.25 a, b). As a first control for sgRNA guide efficiency, we microinjected an injection mix containing the four sgRNA guides into homozygous Cdh2:Cdh2-GFP embryos (Figure 3.25 c). We observed that in 87% of the crispant embryos there was no detectable Cdh2-GFP signal, demonstrating the high cut efficiency of the sgRNA guides employed. Moreover, crispant embryos displayed morphological phenotypes, such as an altered tail segment, that were consistent with the published Cdh2 mutant fish line [Revenu et al., 2014] (Figure 3.25 c).

To assess whether Cdh2 knockout affected *de novo* cluster assembly, we compared lateral lines of Cdh2 crispant embryos, expressing or not expressing chemoFGFR with their uninjected counterparts (Figure 3.25 d). First, we confirmed results from previous studies demonstrating that Cdh2 knockout does not affect standard neuromast formation in wild type embryos [Revenu et al., 2014].

Secondly, we observed that in chemoFGFR expressing Cdh2 crispants, *de novo* clusters still assembled, like in uninjected chemoFGFR expressing embryos. We then compared these two latter conditions in term of number of cells per cluster, *de novo* cluster number and cluster shape descriptors. Remarkably, in all our analyses, clusters formed in Cdh2 crispants were indistinguishable from clusters formed in uninjected embryos (Figure 3.25 e). Even the relative location within clusters of chemoFGFR positive and negative cells was comparable in crispants and uninjected embryos, with chemoFGFR negative cells located at the peripheral rim (Figure 3.25 f).

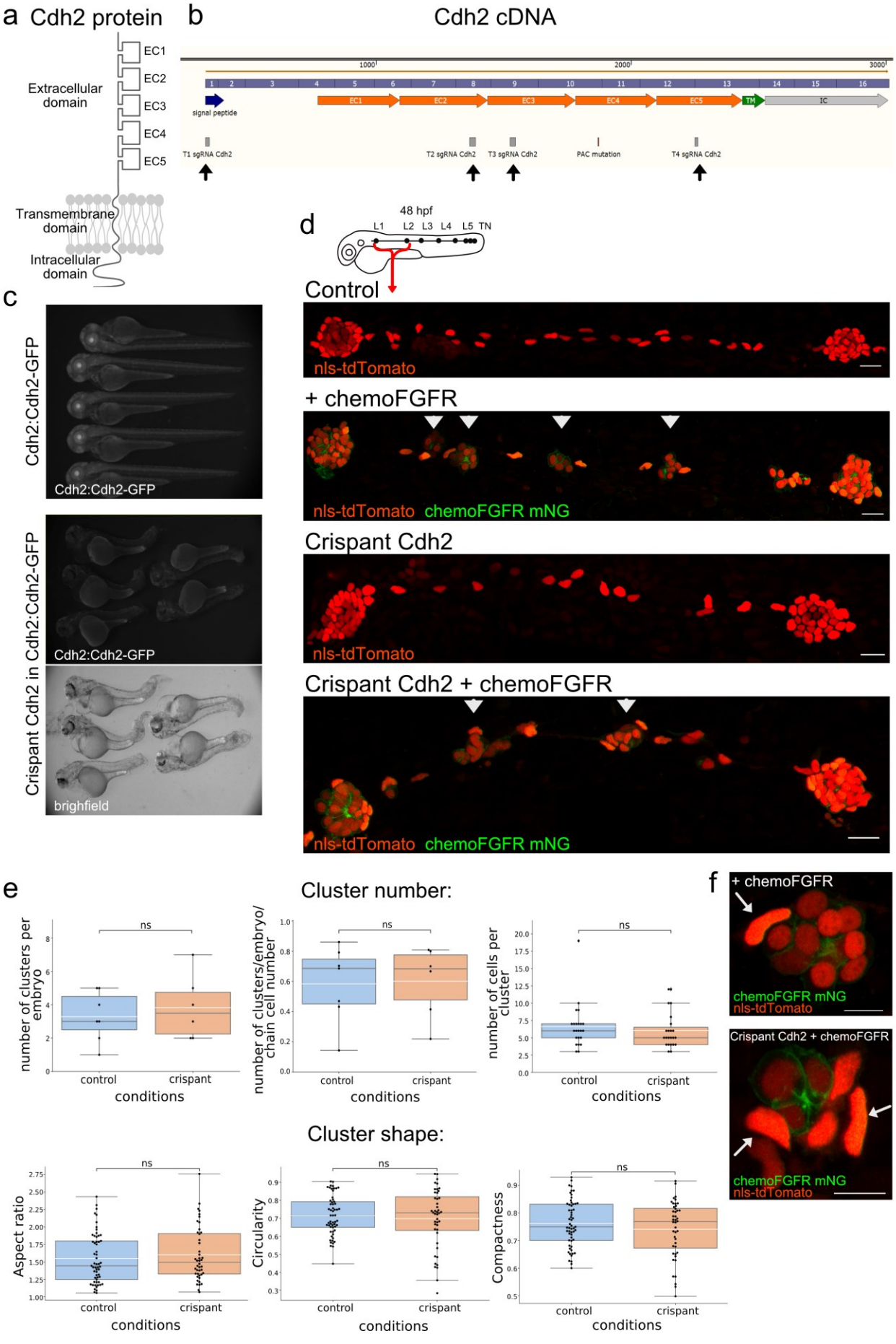
a Cdh2 protein
EC1
EC2
EC3
EC4
EC5
Extracellular domain
Transmembrane domain
Intracellular domain
b
Cdh2 cDNA
signal peptide
T1 sgRNA Cdh2
T2 sgRNA Cdh2
T3 sgRNA Cdh2
PAC mutation
T4 sgRNA Cdh2
c
Cdh2:Cdh2-GFP
Crispant Cdh2 in Cdh2:Cdh2-GFP
brighfield
d
48 hpf
L1 L2 L3 L4 L5 TN
Control
nls-tdTomato
+ chemoFGFR
nls-tdTomato chemoFGFR mNG
Crispant Cdh2
Crispant Cdh2 + chemoFGFR
e
Cluster number:
number of clusters per embryo
number of clusters/embryo/chain cell number
number of cells per cluster
control
crispant
conditions
ns
Cluster shape:
Aspect ratio
Circularity
Compactness
f
+ chemoFGFR
chemoFGFR mNG
nls-tdTomato
Crispant Cdh2 + chemoFGFR

Figure 3.25: Cdh2 knockout does not affect de novo cluster formation

(a) Schematic representing the structure of Cdh2 protein. (b) Annotation of the Cdh2 gene and of the sites targeted by Crispr (marked with black arrows). (c) The efficiency of the sgRNA guide set was verified by knocking-out Cdh2 in Cdh2:Cdh2-GFP expressing embryos. Overview of Cdh2:Cdh2-GFP embryos (above) and of Cdh2:Cdh2-GFP embryos injected with sgRNAs targeting Cdh2 (below, fluorescence channel and brightfield). (d) Comparison of lateral lines (region between first and second neuromast) of control embryos, Cdh2 crispant and chemoFGFR expressing counterparts. The images are z-projections of 48hpf embryos with nuclei in red (cxcr4b:nls-tdTomato) and chemoFGFR in green (LexOP:chemoFGFR mNG). White arrowheads highlight *de novo* clusters. (e) Comparison of cluster of chemoFGFR positive embryos and clusters of crispant chemoFGFR positive embryos. The number of clusters per embryo (normalized or not for chain cell number between neuromast one and two), the number of cells per cluster and cluster shapes were quantified. For cluster number counts: $N_{control\ embryos}=7$; $N_{crispants}=6$. For cluster shape analysis: $n_{control\ clusters}=23$; $n_{crispant\ clusters}=23$. (f) White arrows highlight chemoFGFR negative cells, which are localized in the peripheral rim of the cluster in crispant as well as in uninjected chemoFGFR positive embryos. ns: $5e^{-2} < p <= 1$. Scale bar (d) 20 µm; (f) 10 µm.

Therefore, these results indicate that Cdh2 knockout does not affect *de novo* cluster formation, suggesting that Cdh2 is not required along the process. Alternatively, the lack of effect of Cdh2 knockout on cluster formation might be due to inherent limitations of the system and method. We reasoned that given the redundant expression of adhesion proteins and in particular cadherins in the primordium [Q. Liu et al., 2003], compensation upon loss of Cdh2 could occur. Another possibility is that crispant embryos do not represent *bona fide* null mutants for Cdh2, for example due to chimerism and monoallelic cuts in crispants. Potentially, a resulting sparse expression of Cdh2 might still be sufficient for *de novo* cluster to form. To clarify these points, further work using an established mutant for Cdh2 is currently ongoing.

Next, we employed Crispr-Cas9 technology to perform knockout of both NCAM1b and NCAM1a, to prevent compensatory effects of the 1a paralogue upon 1b loss. For NCAM1a and NCAM1b genes, we designed and *in vitro* tested new sgRNA guide sets, selecting relevant gene regions to target, since the sgRNA guides reported in the previously mentioned study showed low cut efficiency (Figure 3.26 a, b, c). First, we asked whether wild type embryos injected with NCAM1a and 1b sgRNAs developed defects in lateral line patterning (Figure 3.26 d). We observed that both the single NCAM1b knockout (henceforth referred as 'single' crispant) and the double NCAM1a and NCAM1b knockout (henceforth referred as 'double' crispant) did not affect the wild type lateral line pattern (Figure 3.26 d). Next, to assess whether NCAM1a and 1b knockout impaired *de novo* cluster formation, we compared lateral lines of single and double crispants, expressing or not expressing chemoFGFR with their uninjected counterparts. We observed that *de novo* clusters robustly formed in all chemoFGFR expressing conditions, regardless of the embryos being single, double crispant or uninjected (Figure 3.26 e).
Therefore, these results suggest that knockout of NCAM1a and 1b does not affect *de novo* cluster formation. Similar shortcomings of the system and method that had been mentioned for Cdh2 should be considered likewise for NCAMs. Analogously, reproducing the experiments using a stable NCAM1a and 1b mutant fish line will be required to unambiguously address these issues.

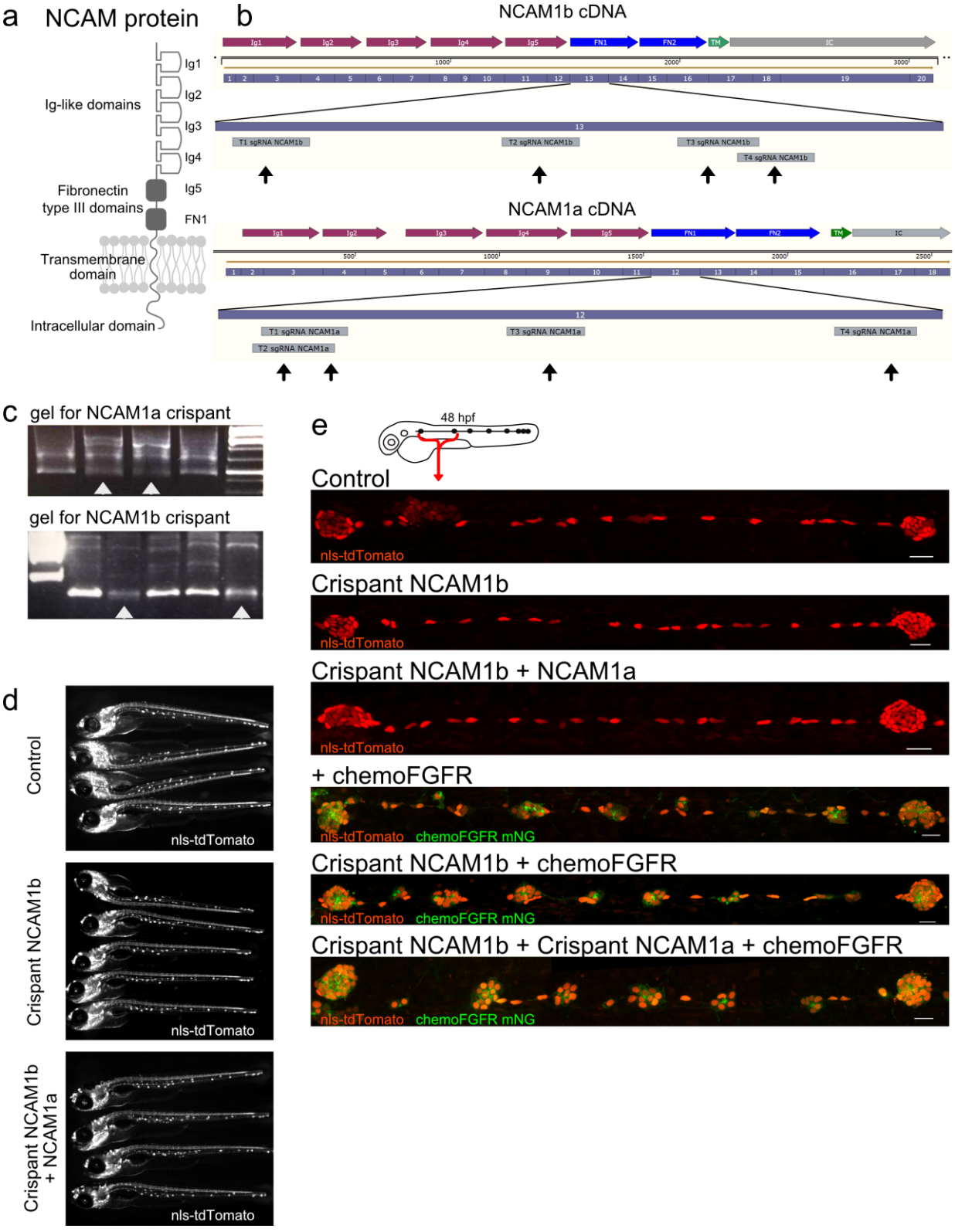

Figure 3.26: NCAM1a and NCAM1b knockout does not affect de novo cluster formation

(a) Schematic representing the protein structure of the NCAM family. (b) Annotation of the NCAM1b and 1a genes and of the sites targeted by Crispr (marked with black arrows). Functional domains are aligned to relative exons. For NCAM1b we targeted exon 13 and for NCAM1a exon 12, both part of the fibronectin domain 1 (FN1). (c) Diagnosis of positive sgRNA cut on agarose gel (deletions highlight with white arrowheads). (d) Overviews of control embryos, NCAM1b crispants and NCAM1b and 1a crispants, showing that the knockout does not affect

lateral line pattern. (e) Comparison of lateral lines (region between first and second neuromast) of control embryos, NCAM1b crispants, NCAM1b and 1a crispants and chemoFGFR expressing counterparts. The images are z-projections of 48hpf embryos with nuclei in red (cxcr4b:nls-tdTomato) and chemoFGFR in green (LexOP:chemoFGFR mNG). Scale bar (e) 20 µm.

3.4 Cell fate specification within *de novo* clusters

In this study, we exploited chemoFGFR and the mosaicism inherent in the LexPR/LexOP transactivation system as a tool to introduce FGF signaling heterogeneity in the naïve population of chain cells. We observed that the two cellular populations emerging in the system from this artificial manipulation, chemoFGFR positive cells and chemoFGFR negative cells, exhibit distinctive behaviors. ChemoFGFR positive cells aggregate with other chemoFGFR positive cells, assembling the seed of the cluster, while chemoFGFR negative cells segregate to the rim. The data thus suggest that heterogeneity of FGF signaling results in cell sorting. We next addressed whether the inside-outside pattern generated by cell sorting would convert into different cell fates as *de novo* clusters mature.

3.4.1 ChemoFGFR negative cells are integrated in *de novo* clusters

We started our investigation by clarifying whether chemoFGFR negative cells encircling chemoFGFR positive cluster seeds show epithelial features. To this aim, we examined whether chemoFGFR negative cells within clusters displayed apical-basal polarization and epithelial organization comparable with chemoFGFR positive cells. First, visualization of 3D cell volumes revealed that chemoFGFR negative cells participating in clusters displayed a columnar morphology and apical-basal polarization, with an apical side directed toward the focal center of the cluster, similar to chemoFGFR positive cells (Figure 3.27 a, Figure 3.14 c for 3D volume of a chemoFGFR positive cell). Second, to quantitatively investigate epithelial polarization, we probed centrosome orientation of cells within 48hpf *de novo* clusters by employing the previously described analysis of 2D polarity angles (paragraph 3.3.1), this time quantifying separately chemoFGFR positive cells and chemoFGFR negative cells (Figure 3.27 b, c, d). To be able to perform three-color imaging of nuclei, centrosomes and chemoFGFR, we generated a fish line where centrin was tagged with a far-red fluorophore (LexOP:Centrin-mIRFP670). We found that the centrosome-nucleus axis of chemoFGFR negative cells pointed toward the center of the cluster (polarity angles close to 0°) to the same extent of chemoFGFR positive cells (Figure 3.27 c, d, e).

These results provide evidence for concluding that chemoFGFR negative cells within clusters are apically polarized and organized in a radial pattern, similarly to chemoFGFR positive cells.

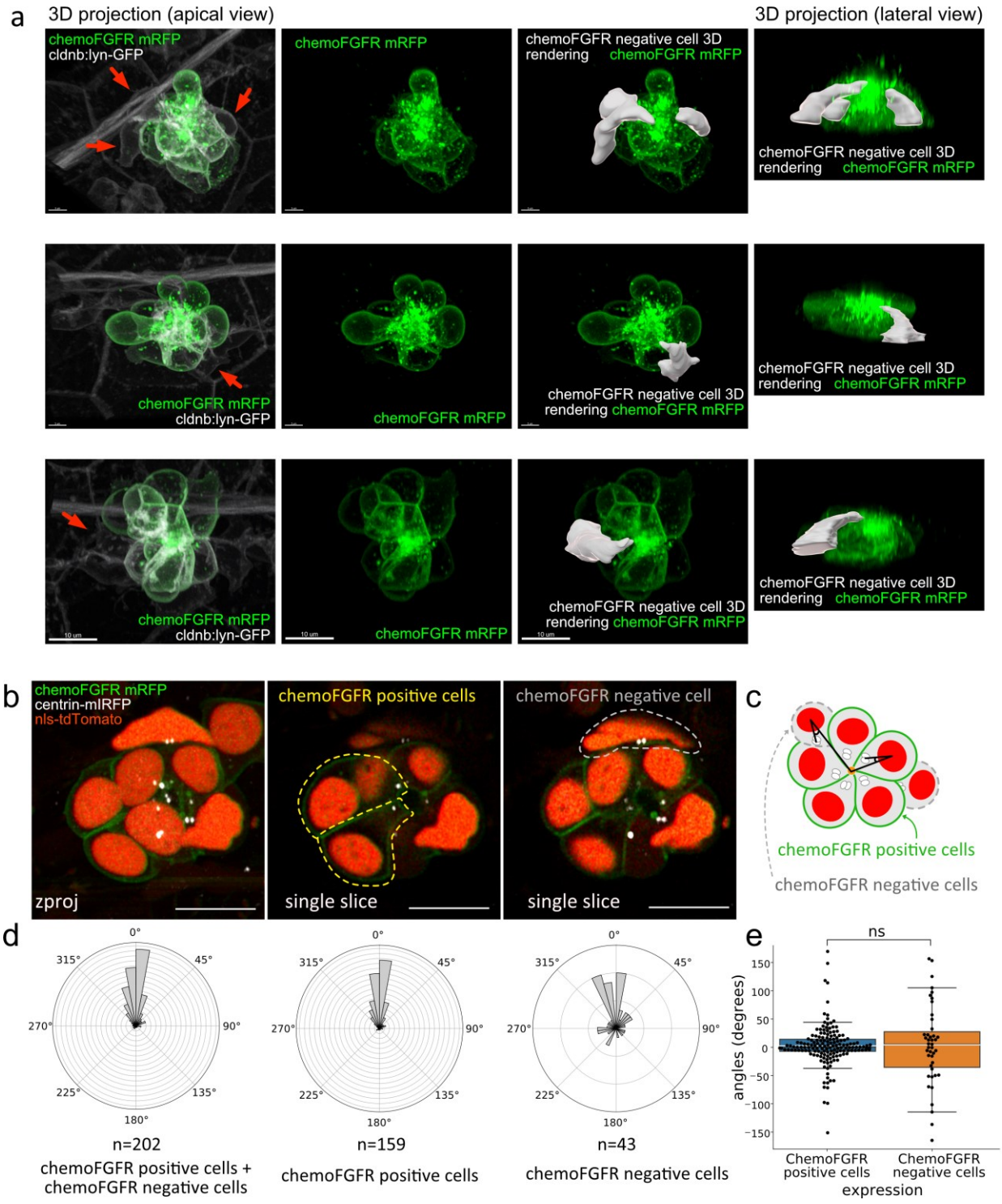

Figure 3.27: ChemoFGFR negative cells are part of clusters and exhibit apical-basal and radial polarization

(a) 3D projections of three examples of *de novo* clusters from 48hpf chemoFGFR expressing embryos. ChemoFGFR positive cells are in green (labeled with LexOP:chemoFGFR mRFP and cldnb:lyn-GFP) and chemoFGFR negative cells in white (labeled with cldnb:lyn-GFP and highlighted with red arrows). On the right, 3D rendering of chemoFGFR negative cells are overlaid on 3D projections and both apical and lateral projections are displayed. Imaris 7.6.4 was used for manual segmentation of chemoFGFR negative cells, 3D projections and 3D rendering. (b) Z-projection and individual slices of a *de novo* cluster from a 48hpf chemoFGFR expressing embryo, labeled with nls-tdTomato (red nuclei), centrin-mIRFP (white centrosomes) and chemoFGFR (green membranes). ChemoFGFR positive and negative cells were classified based on the presence of a detectable

chemoFGFR signal in individual cells. Yellow dashed lines outline chemoFGFR positive cells and a gray dashed line outlines a chemoFGFR negative cell. (c) On the right, a cartoon illustrating how polarity angles were collected for cluster cells. The center of the cluster was used as reference point. Polarity angles of chemoFGFR positive and/or negative cells were represented in rose plots. $n_{\text{chemoFGFR positive cells}}=159$; $n_{\text{chemoFGFR negative cells}}=43$). For the generation of rose plots the following parameters were used: distance between lines=3; y max=9 (for the rose plot on the right), y max=50 (for the first two rose plots); n bins=35. (e) Alternative representation of polarity angles of chemoFGFR positive and negative cells in form of boxplot (angles normalized between -180 to +180). Scale bar (a, top rows) 5 µm; (a, bottom row) and (b) 10 µm.

3.4.2 ChemoFGFR negative cells appear morphologically distinct from chemoFGFR positive cells in *de novo* clusters

As next step, we investigated cellular morphologies of chemoFGFR positive and negative cells within clusters. We compared the 3D shape of chemoFGFR positive and negative cells within 48hpf *de novo* clusters of different sizes (named 'large' when they had at least 8 cells, 'small' for clusters with fewer than 8 cells) and deposited neuromasts, to find out whether chemoFGFR negative cells conformed to the shape of positive ones (Figure 3.28 a). To this aim, we took advantage of a 3D single cell segmentation and analysis pipeline, developed in the lab [Hartmann et al., 2020]. Cells were automatically segmented based on a homogeneous membrane tag (cldnb:lyn-GFP) and classified in chemoFGFR positive and negative cells according to chemoFGFR fluorescence levels. Specifically, cells were classified as chemoFGFR positive when their mean intensity was above a 50^{th} percentile intensity threshold, while cells below were considered chemoFGFR negative. ChemoFGFR positive cells showed consistently higher sphericity values (for all the assembly configurations considered) than negative cells, whose sphericity was instead matching the one of wild type neuromast cells (Figure 3.28 b).

We conclude that, although chemoFGFR negative cells are integrated in clusters and exhibit apical-basal and radial polarization, they appear morphologically distinct from chemoFGFR positive cells.
We reason that the fact that chemoFGFR positive cells acquired a rounded shape might be indicative of a cell-autonomous increase in cortical contractility, as observed in other systems [Zaidel-Bar et al., 2015]. This scenario points at the intriguing possibility that *de novo* clusters constitute structural units composed of 'contractile' chemoFGFR positive cells in the cluster seed, and of softer, more deformable chemoFGFR negative cells in the cluster rim, wrapped around the contractile core.

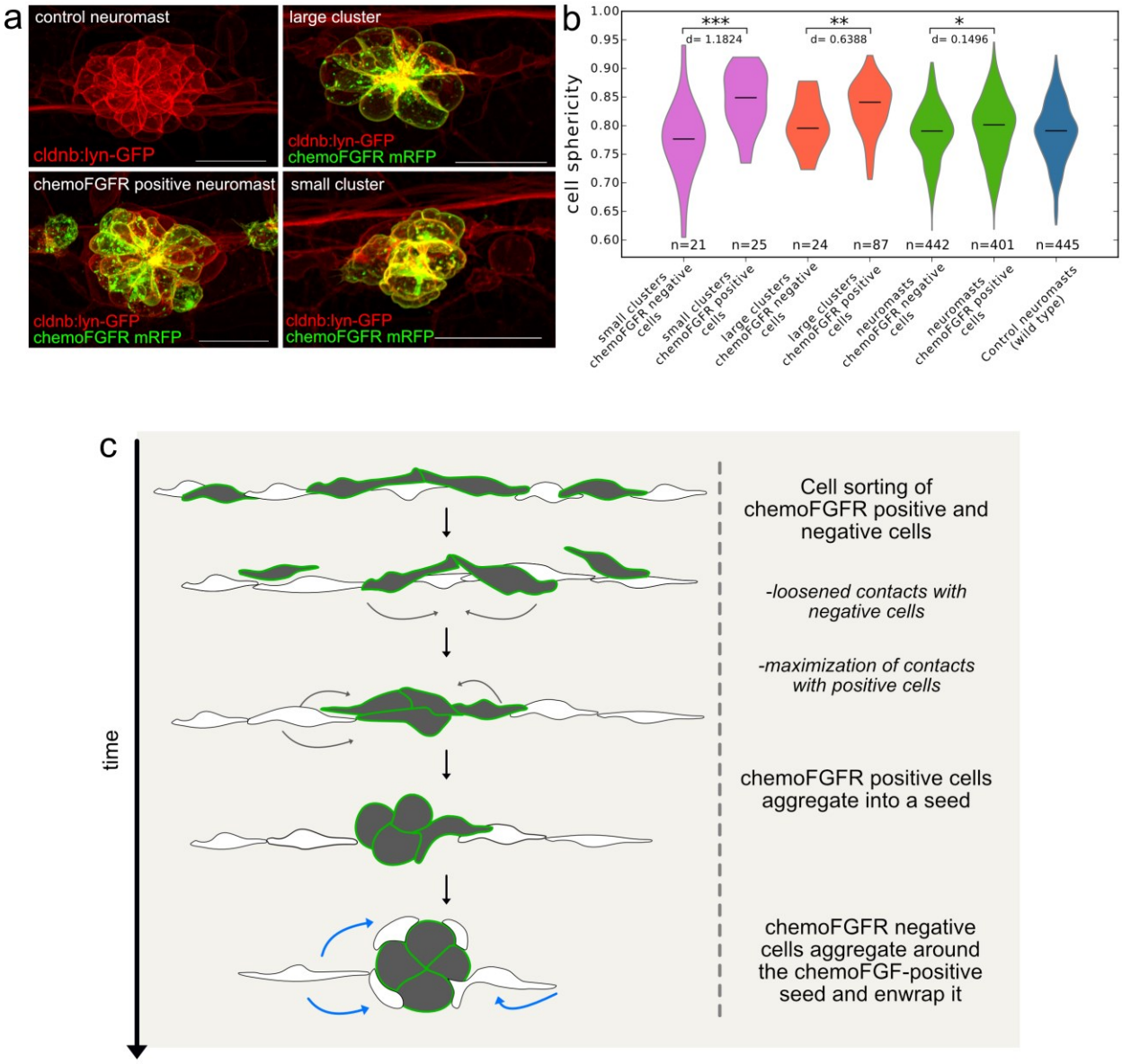

Figure 3.28: ChemoFGFR positive and negative cells appear morphologically distinct

(a) Representative z-projections of a control neuromast, a chemoFGFR positive neuromast, a large and a small *de novo* cluster, from 48hpf embryos. ChemoFGFR positive cells are in green (labeled with LexOP:chemoFGFR mRFP and cldnb:lyn-GFP) and chemoFGFR negative cells in red (labeled with cldnb:lyn-GFP). (b) Quantification of sphericity of single cells belonging to these four categories, additionally classified depending on chemoFGFR expression levels. Sphericity values close to 1 approximate a perfect sphere. The number of cells analyzed for each category is reported in the plot. Effect size is reported in the plot and estimated as follows: small effect: d≈0.2; medium effect: d≈0.5; large effect: d≈0.8; very large effect: d≈1.2. ***: $1e^{-4} < p <= 1e^{-3}$; **: $1e^{-3} < p <= 1e^{-2}$; *: $1e^{-2} < p <= 5e^{-2}$. (c) Proposed model of *de novo* cluster formation. Scalebar 20 µm.

3.4.3 FGF-dependent cell sorting impacts cell fate

The observation that chemoFGFR negative cells keep distinct morphological features from positive ones even when they integrate into clusters, prompted us to address whether differences could go beyond shape. We thus addressed the impact of cell sorting and chemoFGFR expression on cell type differentiation within *de novo* clusters.

3.4.3.1 Hair cells preferentially originate from chemoFGFR positive cells

We started by addressing mechanosensory hair cell fate, taking advantage of the Brn3c:mGFP fish line, that labels hair cells more specifically than Acetylated Tubulin staining [Steiner et al., 2014; Xiao et al., 2005]. We induced chemoFGFR expression according to our standard induction protocol and evaluated 48hpf lateral lines for hair cell labeling. First, we confirmed that wild type neuromasts displayed the stereotyped labeling of Brn3c-labeled cells already at 48hpf, consistent with the observed Acetylated Tubulin immunostaining at 4dpf (Figure 3.29 a, b). We then analyzed chemoFGFR expressing lateral lines and detected Brn3c-labeled cells in 83% of *de novo* clusters. Interestingly, there was no minimum threshold in terms of number of cells per cluster to be reached for Brn3c expression, as we noticed that even doublets occasionally exhibit Brn3c-labeled cells (Figure 3.29 c). Moreover, in *de novo* clusters, the ratio of Brn3c-labeled cell number over total cell number in the cluster was higher than in wild type neuromasts: Brn3c-labeled cells constituted on average 12% of cells in a neuromast, but 29% of cells in a *de novo* cluster (Figure 3.29 d left). To test whether Brn3c expression is cell-autonomously induced by chemoFGFR, we quantified within clusters the frequency of Brn3c-labelled cells that were also chemoFGFR positive, relative to the chemoFGFR negatives. The results showed that Brn3c-labeled cells were preferentially chemoFGFR positive (Figure 3.29 d right). However, not every chemoFGFR positive cell was Brn3c-labeled (Figure 3.29 c). This observation suggests that FGF signaling activation, driven by chemoFGFR, is necessary but not sufficient to induce Brn3c expression. This is consistent with literature evidences that showed that in the lateral line, after drug-mediated hair cell depletion, hair cell regeneration requires FGF signaling and that the new hair cells derive from proliferation of a population of FGFR1a-positive supporting cells [Lee et al., 2016].

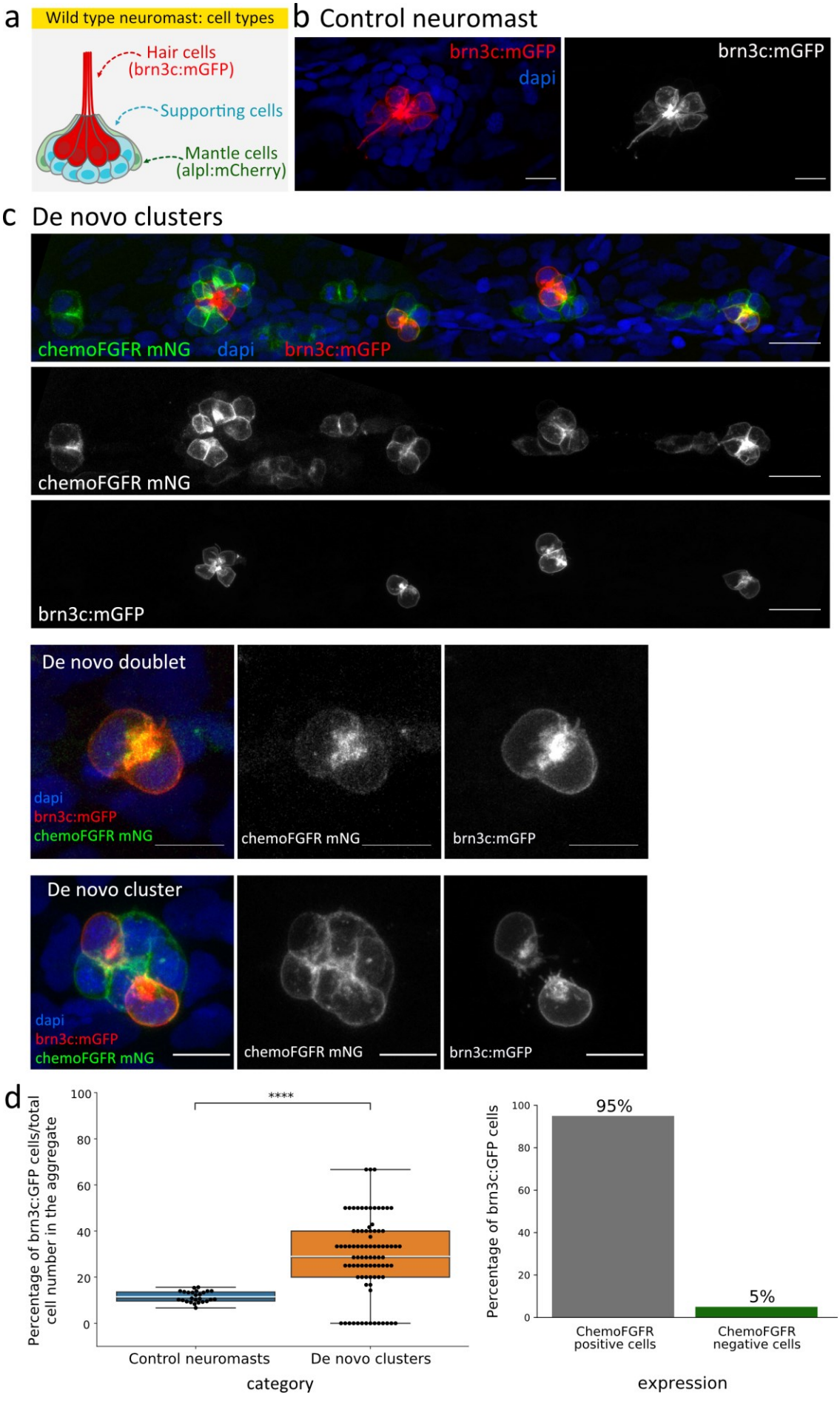
a
Wild type neuromast: cell types
Hair cells (brn3c:mGFP)
Supporting cells
Mantle cells (alpl:mCherry)
b Control neuromast
brn3c:mGFP
dapi
brn3c:mGFP
c De novo clusters
chemoFGFR mNG
dapi
brn3c:mGFP
chemoFGFR mNG
brn3c:mGFP
De novo doublet
dapi
brn3c:mGFP
chemoFGFR mNG
chemoFGFR mNG
brn3c:mGFP
De novo cluster
dapi
brn3c:mGFP
chemoFGFR mNG
chemoFGFR mNG
brn3c:mGFP
d
Percentage of brn3c:GFP cells/total cell number in the aggregate
****
Control neuromasts
De novo clusters
category
Percentage of brn3c:GFP cells
95%
5%
ChemoFGFR positive cells
ChemoFGFR negative cells
expression

Figure 3.29: ChemoFGFR positive cells preferentially form hair cells during* de novo *cluster formation

(a) Schematic showing the cell type composition of a wild type neuromast and the transgenic fish lines used to differentially label them. (b) Representative z-projection of a 48hpf wild type neuromast, with nuclei labeled with dapi (in blue) and hair cells with brn3c:mGFP (in red). (c) Representative z-projection of 48hpf *de novo* clusters and doublets. Merges of the three channels (chemoFGFR mNG in green, dapi nuclei in blue and brn3c:mGFP hair cells in red) and individual channels are shown. (d) On the left, comparison of the percentage of brn3c-labeled cells over the total number of cells in wild type neuromasts and *de novo* clusters. $n_{neuromasts}= 26$, $n_{clusters}= 86$. On the right, quantification of the number of brn3c-labeled cells that are also chemoFGFR positive ($n_{brn3c\ pos+chemoFGFR\ pos\ cells}= 142$; $n_{brn3c\ pos+chemoFGFR\ neg\ cells}=8$). ****:$p<= 1e^{-4}$. Scale bar (c, top overview) 20 µm; (c, bottom panels) and (b) 10 µm.

3.4.3.2 Mantle cells preferentially originate from chemoFGFR negative cells

Next, we analyze mantle cell differentiation in *de novo* clusters. To this end, we took advantage of the published AlpI:mCherry fish line [Steiner et al., 2014], that labels both chain cells and neuromast mantle cells and we combined it with chemoFGFR induction.

First, we explored the pattern of AlpI-labeled cells in 72hpf *de novo* clusters. We observed that *de novo* clusters displayed AlpI-labeled cells in the outer rim of the cluster, resembling the stereotyped pattern of wild type neuromasts, despite the much lower number of cells composing *de novo* clusters (Figure 3.30 a, b). We then asked whether AlpI:mCherry expression in a cell was conditional on presence or absence of chemoFGFR or whether it was a consequence of the cell location in the outside rim of the cluster. To this aim, we quantified within clusters the frequency of AlpI-labeled cells that were also chemoFGFR positive, relative to the ones that were chemoFGFR negatives. We found that 82% of the AlpI-labeled cells were chemoFGFR negative cells (examples in Figure 3.30 e 'mixed clusters') (n=53/65) and 18% of them chemoFGFR positives (12/65) (Figure 3.30 c left, examples in Figure 3.30 b).

To address this point more clearly, we investigated whether AlpI-labeled cells could also originate from chemoFGFR positive cells located at the cluster rim. We classified *de novo* clusters in two categories, one for clusters composed exclusively of chemoFGFR positive cells, including the rim, (named 'chemoFGFR positive clusters') and one for clusters containing both chemoFGFR positive and negative cells (named 'mixed clusters'). We then counted AlpI-labeled cells in each category of clusters and retrieved their relative frequencies. We reasoned that if outside rim positioning was the main determinant of AlpI:mCherry expression, we would expect comparable frequency of AlpI-labeled cells in the two categories. Instead, we observed that mixed clusters were strongly enriched in AlpI-labeled cells (93% of the detected AlpI-labeled cells were found there), while chemoFGFR positive clusters displayed very few of them (7% of the detected AlpI-labeled cells were found there) (Figure 3.30 c right, e). However, although cluster size differences between clusters containing or not containing AlpI-labeled cells were modest (Figure 3.30 d), we observed that chemoFGFR positive clusters frequently did not have a morphologically recognizable cluster rim, while mixed clusters did (Figure 3.30 e). This suggests that chemoFGFR positive clusters might be more immature than mixed clusters and that, as such, the two cluster categories might not be comparable in term of cell fate. We thus conclude that AlpI-labeled cells are mostly, although not exclusively, chemoFGFR negatives and that AlpI-labeled cells are rarely detected in clusters only composed of chemoFGFR positive cells.

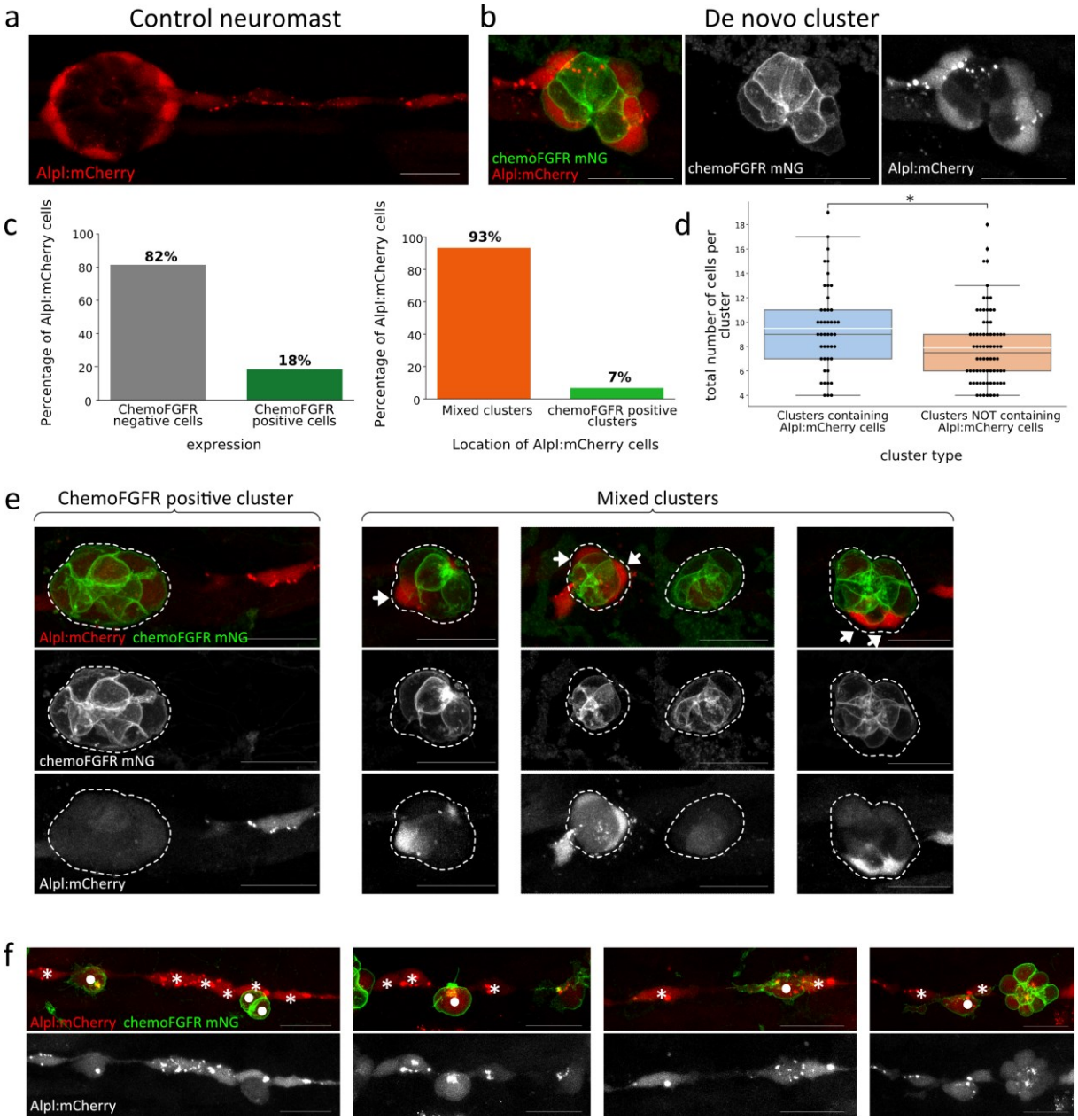

Figure 3.30: ChemoFGFR negative cells preferentially form mantle cells during* de novo *cluster formation

(a) Representative z-projection of a 72hpf wild type neuromast with AlpI:mCherry label (in red). AlpI:mCherry is a cytoplasmic marker expressed in mantle cells and chain cells of the lateral line. (b) Representative z-projection of a 72hpf *de novo* cluster. Merges of the two channels (chemoFGFR mNG in green and AlpI:mCherry in red) and individual channels are shown. (c) From left to right: quantification of the number of AlpI-labeled cells that are also chemoFGFR positive ($n_{AlpI\ pos+chemoFGFR\ poscells}$=12; $n_{AlpI\ pos+chemoFGFR\ neg\ cells}$=53), percentage of AlpI-labeled cells detected in 'mixed clusters' and 'chemoFGFR positive clusters' ($n_{mixed\ clusters}$ =53; $n_{chemoFGFR\ clusters}$ =64), comparison of the size of clusters containing at least one AlpI-positive cell and of cluster without ($n_{AlpI\ clusters}$ =45; $n_{noAlpI\ clusters}$ =75). (e) Representative z-projections of 72hpf chemoFGFR positive and mixed clusters and examples of mantle cells (highlighted with white arrows). White dashed lines outline clusters. Merges of the two channels and individual channels are shown. (f) Representative images of 48hpf lateral lines, containing chemoFGFR negative chain cells (marked with white asterisks) and chemoFGFR chain positive cells (marked with white dots). Corresponding AlpI:mCherry signal is shown as individual channel below. Scale bar 20 µm.

AlpI:mCherry labeling has been extensively characterized as a mantle cell marker in the lateral line [Steiner et al., 2014]. However, given the FGF signaling dependence we observed in our study, we could not exclude that AlpI:mCherry behaved as a negative target of FGF signaling rather than as a reporter of the cellular differentiation state. To rule that possibility out, we monitored fast responses of AlpI:mCherry marker to ectopic perturbation of FGF signaling, by comparing at 48hfp AlpI:mCherry expression in chain cells positive or negative for chemoFGFR. We found that both chemoFGFR positive and negative chain cells had comparable AlpI:mCherry labeling, suggesting that AlpI:mcherry expression is not purely dependent on FGF signaling levels (Figure 3.30 f). This data suggests that AlpI:mCherry can be used as a *bona fide* mantle cell marker also in our context. Nevertheless, complementary work on detecting mantle cells independently from AlpI:mCherry marker or probing levels of AlpI:mCherry marker in FGFR-null conditions is needed for confirmation.

Together, these results are consistent with a model where chemoFGFR expression affects cell fate by driving cell sorting during cluster assembly. Indeed, the spatial segregation of chemoFGFR positive and negative cells within *de novo* clusters (inside-outside pattern) might represent a mechanism to ensure a correct cell fate patterning, with hair cells forming at central locations in the cluster (from few cells of the chemoFGFR positive seed) and mantle cells in the periphery (from the chemoFGFR negative rim).

4 Discussion

4.1 Toward the establishment of a spatiotemporal controlled manipulation of organogenesis: a novel strategy to interrogate tissue dynamics

4.1.1 From cellular behaviors to tissue-scale phenomena

The emergence of developmental patterns and high-order structures relies on the integration of individual cell behaviors. However, understanding how individual cells contribute to tissue-wide responses represents a major challenge, as tissues are not simply collections of cell-autonomous behaviors. Not every cell in a tissue contributes equally to a certain process, neither responds to the same stimuli. Which behaviors are cell-autonomously encoded and which ones result instead from the influence of neighboring cells, of other tissues or of the surrounding microenvironment? In several cases, the activation of a signaling pathway in a few 'activated cells' is sufficient to drive a certain tissue-wide response. For example, in the lateral line primordium of zebrafish, the presence of a few cells expressing the chemokine-binding receptor Cxcr4b at the leading edge of the tissue is sufficient to guide collective migration of the entire primordium [Haas & Gilmour, 2006]. Similarly, leader cells with active FGF signaling are sufficient to drive collective migration of *Drosophila* tracheal branches [Sutherland et al., 1996]. However, neighboring cells surrounding the activated cells are not passive components but often act in concert, contributing to the emergence of tissue-wide responses by coordinating with activated cells. In collectively migrating tissues such as the lateral line primordium or border cell clusters, a tight mechanical coupling between cells in the tissue provide cohesion and spreading of the migratory behavior from leader cells, the chemokine-responsive elements, to follower cells [Haas & Gilmour, 2006], allowing the tissue to migrate as a unit [Rorth, 2012]. It has been suggested that in epithelial monolayers mechanical coupling relies on the relocalization of a transducer from cell-cell junctions to the cytoplasm upon inter-cellular pulling forces, leading to a polarized localization of the Rho GTPase Rac1 in follower cells [Das et al., 2015]. The selective emergence of a certain number of leader cells is also regulated collectively by cell-cell interactions. For example, during angiogenetic sprouting, the number of leader cells is tuned by the contact-based signaling pathway Delta-Notch, while, during wound healing, prospective leader cells emerge from wound margins where follower cells exert higher pulling forces [Vishwakarma et al., 2018]. In other cases, instead, the behavior of activated cells remains cell-autonomously restricted and activated cells and neighboring cells segregate. In the *Drosophila* wing disc, for example, ectopic expression of transcription factors involved in fate specification in a subset of cells leads to cell sorting and extrusion of the misexpressing cells from the tissue as cysts, a process mediated by formation of actomyosin-rich interfaces at heterotypic contacts [Bielmeier et al., 2016]. Cell-cell interactions are such fundamental coordinators of tissue responses that an activated cell can trigger a wide range of different tissue-scale outcomes

depending on its coupling with neighboring cells. An example of this idea can be found looking at possible outcomes of apoptotic cell death. While in several contexts, cells undergoing apoptosis are promptly extruded from the tissue of origin without affecting surrounding cells, during *Drosophila* leg-joint formation, apoptosis induced in cells displaying an altered Dpp activity acts as a driver of morphogenesis [Ambrosini et al., 2019; Manjón et al., 2007; Monier et al., 2015]. In this tissue context, apoptosis of a few cells triggers a tissue-wide folding of the epithelial sheet, due to the pulling forces orthogonal to the tissue plane exerted by the dying cells during their extrusion from the epithelium and the tight cell-cell coupling within this tissue [Ambrosini et al., 2019]. Tissue-scale phenomena can thus emerge from cell behaviors in non-trivial ways and cell interactions take central stage in the causality axis. To investigate these aspects, it is important to use an appropriate 'magnification lens' both in term of perturbation strategies and in term of detection of tissue responses, combining spatiotemporally precise manipulation methods with analysis of single cell dynamics.

In this study, we investigated the emergent behaviors arising from the interaction of activated cells with neighboring cells *in vivo* during organogenesis. To this aim, we generated a mosaic of differently fated cells in the lateral line system, by cell-autonomously activating in a subset of cells a genetic program driving mesenchymal to epithelial transition (MET). We then addressed how activated cells and their neighbors affect each other behaviors, investigating cellular dynamics at single cell level through live imaging.

4.1.2 A new tool for cell-autonomous activation of FGF signaling

FGF signaling is a central player of MET in developmental contexts such as Kupffer's vesicle and chick hindgut formation [Matsui et al., 2015; Nerurkar et al., 2019]. In addition, previous studies established FGF signaling as the main driver of epithelialization and organogenesis in the lateral line primordium [Durdu et al., 2014; Hava et al., 2009; Nechiporuk & Raible, 2008; Revenu et al., 2014]. A MET-like transition has been described to occur during pLLP migration when leader cells convert into follower cells, which are then packaged in rosette-shaped structures and deposited [Durdu et al., 2014; Revenu et al., 2014].

With the goal of driving MET in lateral line chain cells, we developed a cell-autonomous approach to induce FGF signaling in a temporally and spatially resolved manner, taking advantage of Fibroblast growth factor receptor 1a (FGFR). We hoped to gain optogenetic control over FGFR activity by adapting a fluorescently labeled FGFR version insensitive to the FGF ligand and fused with a LOV photosensitive domain, that was shown to successfully drive light-mediated dimerization and downstream signaling activation in a cell culture study [Grusch et al., 2014]. In addition, we gained control over its expression timing, level and mosaicism using a chemically inducible expression system (LexPR/LexOP) with a lateral line-specific promoter [Durdu et al., 2014; Emelyanov & Parinov, 2008]. Unfortunately, we found that the optogenetic control of the chimeric construct activity was unreliable, displaying a high dark state activity that prevented us from using it for a clean on-off optogenetic switch. Several studies suggest that, even at physiological concentration, FGFR spontaneously dimerizes in absence of ligands

[Ahmed et al., 2010; M. R. Bryant et al., 2009; Lin et al., 2012; Sarabipour & Hristova, 2016], making tight control over its signaling activity challenging. The reason for the constitutive activity of the chimeric FGFR construct could lie in the fact that its overexpression might further amplify the tendency to spontaneous activation, as suggested in other studies [Kirchgeorg et al., 2018], a likely consequence of the construct crowding at the plasma membrane. Nevertheless, we found that the chemically inducible expression system could provide both sufficient spatiotemporal control over FGF signaling and the mosaic pattern of expression necessary for disentangling cell-autonomous from non-cell autonomous effects of our manipulation. We therefore exploited the construct as an inducible constitutively active FGFR, that we termed chemoFGFR, to investigate the response of the lateral line tissue to this cell-autonomous perturbation. We found that chemoFGFR has a remarkable impact on the lateral line organization and patterning, leading to the emergence of several *de novo* clusters of cells of various dimensions in ectopic positions. Live imaging and cell tracking confirmed that these clusters were not resulting from aberrant fragmentation of primordium during migration, as observed upon sever loss of Notch signaling [Matsuda & Chitnis, 2010], but were instead assembled from chain cells that were deposited normally and converted into 3D clusters upon chemoFGFR induction.

4.1.3 MET underlies *de novo* cluster formation

An obvious question is whether the change induced in lateral line chain cells is a *bona fide* MET transition. Cell clustering alone does not necessarily indicate epithelialization, as chain cells might simply clump in a disorganized manner without losing their mesenchymal character, as observed for mesenchymal aggregates such as skeletogenic and chondrogenic condensates and dermal condensates of hair and feather buds [Giffin et al., 2019].

MET is a fundamental program involved in the assembly and organization of multicellular structures during organogenesis. It refers to the phenotypic transition of a cell from a mesenchymal to an epithelial state, which involves a switch of cell polarity towards an apical-basal polarity, acquisition of a columnar shape and of stable intercellular junctions and loss of the high motility typical of mesenchymal cells [Pei et al., 2019]. However, a large body of evidences demonstrated that this transition does not operate as a binary switch in most of the biological contexts. Cells normally display combinations of epithelial and mesenchymal features and the extent of MET transition, dependent on the progressive gain and loss of epithelial features, can vary, giving rise to a spectrum of several intermediate states. Collectively migrating tissues, like the pLLP, provide tractable models to study MET transitions as they display across the leading-trailing axis of the tissue a spectrum of different phenotypes, with a more mesenchymal leading edge and a more epithelial trailing edge. However, the 'dynamic range' of mesenchymal and epithelial character displayed across migrating collectives is not so great, as leader cells do not meet key defining features of mesenchymal cells. Several observations support the idea that the interneuromast chain cells present a higher degree of 'mesenchymal-ness' than the cells of the migrating primordium. Nevertheless, as these cells still maintain some degree of cell contact, we will continue to use the term mesenchymal-like to describe them.

First of all, we gained insights on the initial 'ground state' of the chain cells. While it is clear that these represent a multipotent population deposited by the migrating pLLP, many basic features had been defined. First, chain cells are characterized by a flat and elongated morphology. Second, chain cells display randomized polarity, as defined by their nuclear-centrosomal axis, and have their centrosome mostly located in proximity of the nucleus instead of being at the contact interfaces with neighboring cells, features that have been associated with the mesenchymal state [Burute et al., 2017]. Third, despite being connected in a continuous chain, chain cells have the capacity to move and rearrange within it. Moreover, in terms of gene expression pattern, previous studies found that chain cells express Wnt pathway genes such as Lef1 and β-catenin 2, like leader cells of the migrating pLLP [Lush & Piotrowski, 2014b; McGraw et al., 2011; Valdivia et al., 2011; Venero Galanternik et al., 2015].

Having characterized the chain cell ground state, we next defined the changes occurring during *de novo* cluster assembly. We demonstrated that during this process, chain cells adopt a series of epithelial features, such as morphological and polarity changes, intracellular rearrangements and gene expression patterns typical of wild type neuromasts. During *de novo* cluster assembly, indeed, chain cells lose their typical flat shape and adopt an 'upright' columnar morphology with a nuclear-centrosomal orientation typical of epithelia and tight junction formation. An accumulation of Cdh2 at the apical center of clusters analogous to wild type neuromasts was also observed [Revenu et al., 2014]. At the gene expression level, chemoFGFR induction drives expression of the neuromast-specific marker Krt1c5 from early stages of *de novo* cluster formation. Thus, a number of lines of evidence support the hypothesis that chemoFGFR drives *bona fide* MET of chain cells. It provides a clearer example of MET than the conversion of leader into follower cells in the migrating primordium, as chain cells do not exhibit apical-basal polarity or other classical features of epithelia prior to manipulation. We conclude that the cell-autonomous activation of FGF signaling is sufficient to trigger a user-defined epithelialization program *in vivo*.

4.1.4 *In vivo* induction of organ(-oid) formation

The finding that pluripotent stem cells can form complex organ-like structures in culture, referred to as organoids, represented a major breakthrough in biology. On one side, the possibility of generating organs 'in a dish', that recapitulate several aspects of patterning and functionality of original organs, such as optic cup, intestinal and gut organoids, had opened a new era for regenerative medicine, disease modelling and drug developments [Lancaster & Knoblich, 2014]. On the other side, organoid studies have changed in many aspects our understanding of organ formation, revealing the incredible self-assembly capability of cells. Pluripotent stem cells indeed show a remarkable ability to undergo symmetry breaking and sophisticated patterning *in vitro* in absence of overarching long-range patterning cues, unveiling a complex feedback between morphogenesis and genetic patterning [Turner et al., 2015].

What underlies the stunning self-assembly potential of progenitor cells? Addressing this question motivates an alternative approach for the study of organogenesis, where we stimulate progenitor cells to reconstitute organs from scratch by applying principles of synthetic biology and we investigate

minimal requirements for organ emergence. In the last decade, the design of synthetic effector modules providing control over various cell behaviors or entire signaling pathways, such as the Synthetic Notch system, and the development of a wide range of optogenetic tools capable of perturbing and triggering morphogenetic processes on demand, has put solid foundations for such a reverse engineering approach [Cachat et al., 2014; Krueger et al., 2019; Morsut et al., 2016]. Another avenue opened by organoid studies is the investigation of how this self-assembly capability of cells is funneled, harnessed or tuned during development, in order for robust and reproducible patterns to arise. What is the impact of signaling molecules, boundary conditions, mechanics and other extrinsic cues in the self-assembly process? Addressing this question will pave the way toward a deeper and more integrative understanding of organ formation *in vivo*.

In this study, we present an experimental approach inspired by synthetic biology methods and organoid studies, that provides the opportunity to study the assembly and differentiation of functional organs emerging from naïve mesenchymal-like cells directly *in vivo.* By inducing chemoFGFR expression in lateral line chain cells indeed, we triggered the formation of *de novo* clusters that displayed a pattern of differentiation alike the one of wild type organs, with hair cell and mantle cell differentiation. As we continue to explore principles of organogenesis, we hope that these findings will contribute to our ability to design effective strategies for tissue regeneration and engineering of transplantable organs.

4.1.5 Other mechanisms driving organ formation from lateral line chain cells

Previous studies have investigated the multipotency of chain cells, discovering that organogenesis can be triggered from them in various ways. During late larval development, chain cells physiologically give rise to a stereotyped set of intercalary neuromasts by undergoing extensive proliferation and differentiation [Grant et al., 2005; Lopez-Schier & Hudspeth, 2005; Lush & Piotrowski, 2014b; Nuñez et al., 2009; Sapède et al., 2002]. Conversion of chain cells into intercalary neuromasts can be also induced precociously at embryonic stages by employing pharmacological treatments, such as ErbB/Neuregulin1 signaling inhibitors, genetic methods, such as Sox10, ErbB and Neuregulin1 mutants, or through complete ablation of neuromasts, of lateral line segments or of lateral line nerve [Grant et al., 2005; Lopez-Schier & Hudspeth, 2005; Perlin et al., 2011; Rojas-Muñoz et al., 2009; Sánchez et al., 2016]. As little as two chain cells were shown to be sufficient to regenerate an entire neuromast upon its complete ablation [Sánchez et al., 2016]. Interestingly, these studies found that organogenesis from chain cells solely occurs when the perturbation method employed affects or damages the adjacent glial cells, tightly associated with the lateral line nerve. Glial cells indeed provide a quiescent niche for chain cells by locally preventing the activation of Wnt/β-catenin signaling. Thus, absence or damage of glia releases chain cells from this inhibition, enabling chain proliferation and differentiation. It has been proposed that, analogously, physiological formation of post-embryonic intercalary neuromasts is enabled by ventral migration of chain cells (induced by secondary neuromast deposition), that causes physical separation from the inhibitory signal released by glia [Lush & Piotrowski, 2014b].

As described in our results, during *de novo* cluster formation, glial cells are not depleted, neither show any obvious morphological alteration or a detectable chemoFGFR expression, suggesting that chemoFGFR-dependent organ formation is not the result of a glial phenotype but is lateral line autonomous. ChemoFGFR induction therefore appears as a novel approach to unlock the multipotent potential of chain cells. However, one possibility could be that chemoFGFR activity affects chain-glia interactions. As the mechanism employed by glial cells to inhibit Wnt/β-catenin signaling in chain cells is so far unknown, further studies are required to test whether FGF signaling has an impact at that level. In any case, as the chemoFGFR approach allows tight spatiotemporal control over *de novo* cluster assembly, it likely represents a more insightful route to investigate physiological cell behaviors during organogenesis. One interesting avenue of this study indeed would be to compare chemoFGFR-dependent organogenesis with physiological post-embryonic and injury-dependent organogenesis and to identify the minimal set of requirements for organ formation. A study of Lush and Piotrowski for example showed that upon abrogation of the ErbB signaling, Wnt/β-catenin activation is sufficient for organogenesis [Lush & Piotrowski, 2014b]. In this context, FGF signaling appears to be involved solely at later stages of the process, when an increase of FGF activity (likely induced downstream of chain cell proliferation) appears required for cluster differentiation and acquisition of a rosette shape, as inhibition of the pathway prevents both [Lush & Piotrowski, 2014b]. Our results instead suggest that direct activation of FGF signaling via chemoFGFR is sufficient to trigger organ formation. Specific perturbation experiments are however required to frame the relationship between FGF and Wnt/β-catenin signaling during *de novo* cluster formation. Complementarily, a side-by-side comparison of cell dynamics during chemoFGFR-dependent organogenesis and the other described modes of organ formation would shed light on other conserved aspects of the process. For example, it is possible that in physiological conditions, FGF, Wnt/β-catenin signaling levels or cell sensitivity to ligands are spontaneously heterogeneous in the chain population and this might be at the basis of the selection of chain cells initiating the assembly of intercalary neuromasts. In this eventuality, the physiological formation of intercalary neuromasts would mirror the condition that we artificially generated by imposing mosaic expression of chemoFGFR. Amplification of cell-to-cell heterogeneity is indeed at the basis of several symmetry-breaking events, such as the differentiation of Paneth cells in intestinal organoids [Serra et al., 2019] and the early development of the mammalian embryo [Q. Chen et al., 2018; Korotkevich et al., 2017].

4.2 Dissecting mechanisms of *de novo* cluster formation

The establishment of a tool that reliably drives organogenesis on demand provides an ideal entry point to dissect how epithelialization emerges from a mesenchymal cell population and spreads across the tissue. The combination of a precise control over the perturbation together with the acquisition of tissue responses and single cell dynamics in real time through high-resolution imaging allowed us to investigate mechanistic principles of *de novo* organ formation.

4.2.1 Polyclonal aggregation of chain cells drives organogenesis

Having identified chain cells as the origin of clusters, we next addressed whether clusters resulted from monoclonal proliferation of individual chain cells or from polyclonal aggregation.

Serial monoclonal expansion of a single clone is indeed a classical modality of cluster formation, that have been shown to associate with MET in several systems, from MDCK and Caco-2 cyst formation to assembly of insect sensory bristles, human embryonic stem cells cysts and intestinal organoids [Cubas et al., 1991; Datta et al., 2011; Serra et al., 2019; Taniguchi et al., 2015]. Aggregation of mesenchymal cells has been instead reported to drive cluster assembly during Kupffer's vesicle, taste bud and renal vesicle formation [Matsui et al., 2015; Schlüter & Margolis, 2009; Soulika et al., 2016].

Our results from live imaging and manual tracking during clustering reveal that polyclonal aggregation is the main driver of *de novo* cluster formation, as most of the cells within forming clusters are acquired through aggregation. While cell division was occasionally observed, we could not detect examples where single clones generated monoclonal clusters by proliferation in the time range we monitored. However, considering that some doublets are monoclonal, we cannot rule out the possibility that monoclonal clusters could originate from them at later time points. Long-term time lapse imaging is required to test this eventuality.

4.2.2 Models of emergence of apical-basal and radial polarity in organogenesis

While proliferation does not appear to be the main driver of *de novo* cluster assembly, it might serve other functions during the process, for example to direct apical-basal polarization and radial organization of clusters. Proliferation is indeed associated with the emergence of centralized lumina in multiple contexts, for instance during MDCK cyst formation, in hepatocyte and human intestinal cell polarization [Datta et al., 2011; Lujan et al., 2017; Taniguchi et al., 2015; T. Wang et al., 2014]. In these systems, apical-basal polarity is initiated at the end of the first cell division, following the formation of a midbody region at the site of the cytokinetic event. Here, a pre-apical patch is assembled and enriched of apical domain components via polarized intracellular trafficking, leading to maturation of a lumen at the interface between daughter cells. However, we find unlikely that, during *de novo* cluster formation, proliferation is required for polarity establishment. We observed, indeed, that rosette-shaped clusters assemble regardless of proliferation occurring or not, suggesting that proliferation might be dispensable. However, further experiments combining chemoFGFR induction with inhibition of proliferation and imaging of polarity reporters such as centrin are required to address this point more clearly.

An alternative model for the establishment of apical-basal and cluster polarity is that the aggregative process triggers it. Despite the mechanisms involved in the process are mostly unexplored, studies on early nephrogenesis [Z. Yang et al., 2013] and on cyst formation from human pluripotent stem cells [Taniguchi et al., 2017] shed some light on potential contributors. At early stages of renal vesicle formation, prior to polarization, mesenchymal aggregates display sparsely located plasma membrane domains enriched in the polarity protein Par3, that progressively segregate into a focal point at the center of the cluster, from which a central lumen emerges [Z. Yang et al., 2013]. Human pluripotent

stem cells instead cell-autonomously assemble their own apical domain, packaging apical components like primary cilium and microvilli into an intracellular compartment, named 'apicosome'. Following cell aggregation, apicosomes derived from individual cells fuse and give rise to the multicellular apical domain of a polarized cyst, enclosing a shared lumen. Apicosome-like vesicles have been observed in a number of other developing tissues, suggesting that this mechanism of polarity establishment might be widespread [Taniguchi et al., 2017]. Targeted experiments investigating localization and dynamics of apical membrane components in real time during *de novo* cluster formation will be required to investigate these aspects.

4.2.3 Does epithelialization propagate across collectives?

The results presented in this thesis suggest that MET of chain cells induced by FGF signaling is a collective process, resulting from cell aggregation. Two hypothetical modes of collective MET have been proposed in the literature. In the 'all-at-once-MET,' cells that receive a certain epithelialization input undergo MET simultaneously, as suggested for the MET occurring in 8-cell stage mouse embryos [Maître et al., 2015]. In the 'propagated MET' instead, MET propagates across the tissue from 'initiator' cells that receive the epithelialization input at first, leading to the progressive recruitment of neighboring cells into the forming epithelium, as suggested during Wolffian duct morphogenesis [Atsuta & Takahashi, 2015; Attia et al., 2015].

ChemoFGFR represents the ideal tool to study MET propagation, as it provides a cell-autonomous activation of FGF signaling, a key epithelialization input, in a salt and pepper pattern. Moreover, the possibility of identifying chemoFGFR expressing cells, thanks to the fluorescent tag fused with the construct, enables tracking and inspection of the behaviors of the two cellular populations of the mosaic, referred to as chemoFGFR positive cells and chemoFGFR negative cells, in time lapse experiments. We thus asked whether in lateral line chain cells, epithelialization would propagate from cells activated by high levels of FGF signaling to uninduced cells. We found that cluster formation is initiated by homotypic aggregation of chemoFGFR positive cells into a cluster 'seed', followed by the assembly of an outer cluster 'rim', to which chemoFGFR negative cells also contribute. Therefore, during assembly of the cluster seed, epithelialization does not propagate from activated to neighboring cells, while it is still unclear whether the association of negative cells around the seed might result from a propagation of the epithelial character of the central core (discussed in 4.2.6).

4.2.4 Cell-autonomous activation of FGF signaling triggers genetically encoded self-assembly

Taken together, the data of this study are consistent with a scenario where chemoFGFR triggers a multistep process where cell sorting and dynamic cell rearrangements, epithelialization and cell fate choices are tightly interconnected.

In this proposed scenario (Figure 4.1), an increased FGF activity mediated by chemoFGFR provides cells with an 'epithelial toolset' by shifting their gene expression cell-autonomously, which enables them to undergo full MET upon homotypic aggregation. Indeed, it is not until chemoFGFR positive cells interact

with homotypic partners that they epithelialize into a cluster seed. The aggregation of a cluster seed is achieved through extensive cell rearrangement and sorting of chemoFGFR positive and negative cells. During the process, cells transiently increase their motility and dynamically exchange position by crawling on top of each other in a slithering-like motion, even converging from distal sites. Homotypic cell contacts and their dynamic changes also appear to be involved in driving or reinforcing cell sorting and 'selective' aggregation of chemoFGFR positive cells. Following formation of this epithelial seed, the cluster can then expand through the association of chemoFGFR negative cells that, however, remain segregated to the periphery, constituting an outer cluster rim. The resulting inside-outside pattern of seed and rim within clusters appears to be exploited for cell differentiation, as hair cells differentiate from the inner chemoFGFR positive seed while mantle cells from the outside rim of negative cells.

Overall, the proposed scenario suggests that chain cells undergo a genetically encoded self-assembly process, that is built upon the pattern of chemoFGFR induction [Turner et al., 2015]. Cell-autonomous chemoFGFR activity is the genetic input triggering emergent behaviors in the system, such as cell reorganization, sorting and state transitions, that eventually lead to the assembly of *de novo* organs. This process is reminiscent of the formation of ectopic compound eyes and wings in *Drosophila*, triggered respectively by misexpression of Eyeless/Pax6 or Vestigial [Halder et al., 1995; Klein & Arias, 1999] and of the *in vitro* assembly of optic cups from embryonic stem cell aggregates, following Rx expression [Eiraku et al., 2011]. Genetically encoded self-assembly appears to take place also in human ESC cell cultures upon induction of mesenchymalization by mean of an optoWnt construct [Repina et al., 2019]. In this context, activation of Wnt activity in a salt and pepper pattern induces EMT in optoWnt expressing cells and, on the other side, formation of epithelial clusters from neighboring wild type cells, resulting in a spatial pattern that mirrors the primitive streak organization during gastrulation. Similar to the chemoFGFR-induced cluster formation process, here as well the introduction of a genetic trigger provides the system with emergent properties and elicits tissue reorganization and morphogenesis [Repina et al., 2019].

In the next paragraphs, we will discuss more in depth the emergent behaviors of the system at different phases of *de novo* cluster formation.

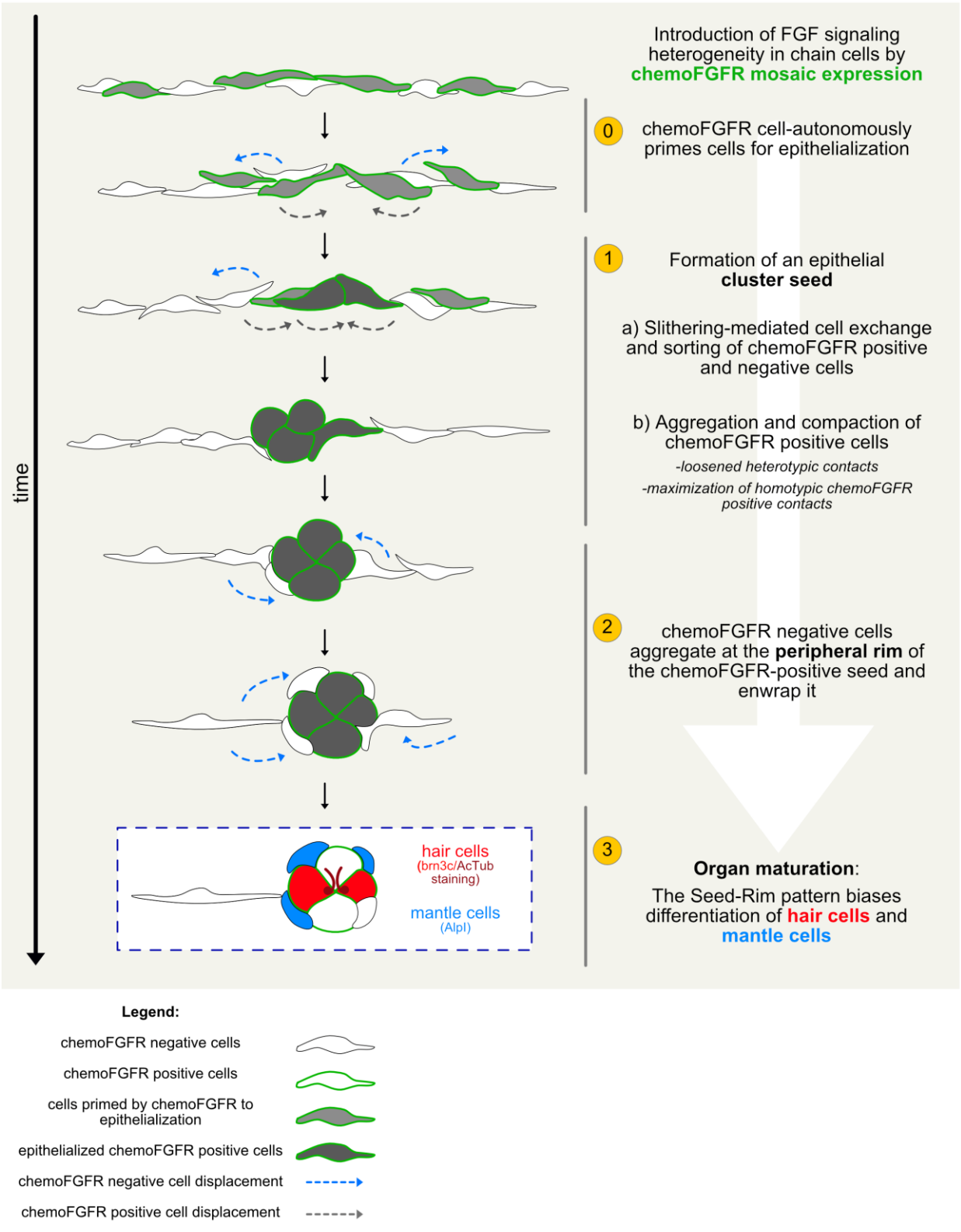

Figure 4.1: A model for* de novo *cluster formation

Schematic representing the proposed scenario for *de novo* organ formation.

4.2.5 The emergence of *de novo* clusters

4.2.5.1 How are cells rearranging during homotypic sorting?

Cell sorting refers to the process of segregation of mixed populations of cells into homotypic domains. During *de novo* cluster formation, considerable cell motility and cell rearrangements are associated with cell sorting, prior to cell clustering. The mode of cell exchange and the migratory shape repertoire described for chemoFGFR positive cells bear clear similarities to the 'slithering' migration described for neuroendocrine cells (NE) during formation of neuroepithelial bodies (NEB) in mouse and for taste bud assembly in zebrafish [Kapsimali, 2017; Kuo & Krasnow, 2015; Noguchi et al., 2015; Soulika et al., 2016]. The slithering mode of cell rearrangement is distinguished from the classical modality of cell exchange in epithelia, mediolateral intercalation, which involves a concerted shrinkage and expansion of lateral junctions between apical-basal polarized cells [Guillot & Lecuit, 2013]. In our system as well as in the NEB and the taste bud models, cells are in a mesenchymal-like state while sorting, which might enable cells to converge even from distal sites. We propose that a slithering-based rearrangement constitutes an earlier step of the sorting process during *de novo* cluster formation.

An interesting observation we made is that, prior to aggregation, chemoFGFR positive cells engage into several transient contacts with neighboring cells. It is currently unclear why some homotypic contacts persist ad result in cell aggregation while others are only transient 'touch and go' interactions. One option would be that, by engaging into dynamic contacts, cells 'scan' each other to identify potential interacting partners, as observed during cell matching in *Drosophila* dorsal closure [Millard & Martin, 2008]. It has been proposed that transient cellular 'kisses' mediated by long cellular protrusions are involved in cell homotypic recognition during NEB formation [Kapsimali, 2017; Kuo & Krasnow, 2015]. Taste bud cells, similarly, make transient contacts with cells belonging to several taste buds in their vicinity prior to integration in one of them, as if they sample which one to join [Soulika, 2015]. Endocrine cells assembling Langerhans islets instead employ filopodia-like cytoplasmic processes to scan neighbors before initiating coalescence [Freudenblum et al., 2018].

Another explanation for the dynamicity of cell-cell contacts would be the presence of inter-cellular tensile forces within the tissue. It has been suggested that cell-cell contacts can transmit mechanical pulling forces able to drag cells together, such as the zippering process preceding epithelial fusion during *Drosophila* dorsal closure [Millard & Martin, 2008] or during would closure [Davidson et al., 2002; Wood et al., 2002]. Analogously, it has been proposed that, during frog convergent extension, protrusions at the mediolateral tips of chordamesoderm cells provide the contractile forces required for cell intercalation [Shih & Keller, 1992; Walck-Shannon & Hardin, 2014]. In line with these examples, it is conceivable that during *de novo* cluster assembly chemoFGFR positive cells exert pulling forces on contacting homotypic neighbors. We observed indeed that chemoFGFR positive cells display a more persistent directionality toward a homophilic partner following cell contact with it, while they move randomly when solitary or before the contact.

What lies at the basis of the transient increase in cell motility preceding epithelialization?

One possibility could be that it is a cell-autonomous effect of chemoFGFR. It is possible that, during the process of *de novo* cluster assembly, a certain cumulative load of FGF signaling needs to be reached before a chemoFGFR positive cell encountering a homotypic partner can undergo MET, while, below this threshold, motile behaviors are instead induced. McAvoy and Chamberlain showed that the FGF concentration dictates whether progenitors of lens epithelial cells undergo differentiation, migration or proliferation and the same has been proposed to underlie mesoderm spreading onto ectoderm during *Drosophila* gastrulation and, later in development, caudal visceral mesoderm migration [Bae et al., 2012; McAvoy & Chamberlain, 1989]. In the future, it will be important to establish to what extent and for how long FGF signaling is active in cells expressing chemoFGFR during *de novo* cluster formation and which pathways are activated downstream of it at different stages of the process. Moreover, a more extensive analysis of motility of chemoFGFR positive and negative cells will be required.

Another explanation could be that the increase in cell motility is not a direct consequence of increased FGF signaling, but it is instead a byproduct of the sorting of chemoFGFR positive and negative cells. The loosening of heterotypic cell-cell interactions might enable cells to move more freely compared to cells in a typical connected chain configuration. An example of a process where a regulated disconnection promotes an extensive cell rearrangement is the so called 'mitosis-associated cell dispersal', observed in the developing neural keel and in the ureteric bud [Ciruna et al., 2006; Packard et al., 2013]. During this process, cells migrate to the apical side of the epithelium to divide but keep a cytoplasmic process basally connected. While the daughter cell inheriting the basal connection reintegrates in the original site, the other one reinserts in a non-contiguous site of the epithelium, such as on the opposite side of the forming neural tube.

Another intriguing possibility could be that, during *de novo* cluster assembly, FGF signaling has a chemotactic function. Indeed, it has been suggested that in the lateral line primordium FGF secreted by leader cells can act as a chemoattractant for follower cells, coordinating collective migration [Nogare et al., 2014]. It is thus conceivable that a constitutive activity of FGF signaling might promote cell motility. A role of FGF signaling in chemotaxis has been observed in several contexts, such as during the formation of the *Drosophila* tracheal system, the mouse lung branching, in chick and *Drosophila* gastrulation and in axon guidance [Dos Santos et al., 2019; Gabay et al., 1997; A. S. Ghabrial & Krasnow, 2006; Gisselbrecht et al., 1996; Irving et al., 2002; Min et al., 1998; Sekine et al., 1999; Shirasaki et al., 2006; Sutherland et al., 1996]. For instance, during the branching of *Drosophila* trachea, FGFR/Breathless signaling in leader tracheal cells is required for cell migration toward FGF/Branchless sources and the expression of a constitutive active form of the receptor leads to sprouting of ectopic and misguided secondary branches [Gabay et al., 1997; A. S. Ghabrial & Krasnow, 2006; T. Lee et al., 1996; Reichman-Fried et al., 1994; Sato & Kornberg, 2002; Sutherland et al., 1996]. However, in this process, a polarized activation of FGF signaling at the tip of leader cells rather than an increase in absolute FGF signaling levels appears important to drive cell migration [Lebreton & Casanova, 2016]. Moreover, FGF signaling has been shown to promote random cell motility in chick presomitic mesoderm cells during somite formation [Bénazéraf et al., 2010].

Another scenario could be that activation of FGF signaling mediated by chemoFGFR influences cellular behaviors in a non-cell autonomous manner, for instance affecting the expression of chemokine binding receptors. Previous work in our lab showed that the Sdf1a sinking receptor Cxcr7a is a positive target of FGF signaling whose expression is high in neuromasts [Durdu, 2015]. It is possible that chemoFGFR expression leads to a cell-autonomous increase of Cxcr7a levels, that might in turns locally shape the chemokine Sdf1a in the environment into a short-range Sdf1a gradient. The sensing of the local gradient through the Cxcr4b receptor might then promotes migratory behaviors in chain cells. Self-generation of a functional Sdf1a gradient has been shown to be required for pLLP and for the primordial germ cell migration in zebrafish [Boldajipour et al., 2008; Donà et al., 2013; Raz & Mahabaleshwar, 2009; Venkiteswaran et al., 2013]. To address this hypothesis during cluster formation, targeted experiments combining Sdf1a manipulation and Cxcr7 mutants together with chemoFGFR expression are required.

Are chemoattractant cues involved in cell clustering?

One fundamental question arising is whether a secreted attractive cue is required for *de novo* cluster assembly. Indeed, the presence of discrete signal-producing foci seems to direct cell migration and aggregation during formation of several periodic organs. During NEB formation, for instance, Slit ligand secreted from NEBs seems to attract NE to the forming organs and to retain them within. Consistently, perturbations of the ligand or of the relative receptor Robo lead to smaller NEBs and to a higher frequency of solitary NE cells in the epithelium [Branchfield et al., 2017]. During taste bud formation, similarly, migration of FGF8 expressing progenitor cells to the forming taste buds is directed by Type III cells already present in the buds through an unknown attractive mechanism [Soulika, 2015].

The lateral line primordium is a collectively migrating tissue that self-generates its own migration gradient [Donà et al., 2013; Venkiteswaran et al., 2013] and expresses its own differentiation cue, FGF3 and 10 ligands. Remarkably, the system not only pattern FGF ligand synthesis, that get secreted from leader cells and central rosette cells, but also regulates FGF range of action, by the establishment of closed extracellular cavities at the apical side of cells within forming pro-neuromasts where FGF is trapped and concentrated, called microlumina [Durdu et al., 2014]. Given the proposed role of FGF as chemoattractant for follower cells [Nogare et al., 2014], one obvious possibility would be than FGF might be involved in the assembly of *de novo* clusters. However, we found that FGF ligands are not required for cluster formation, as depletion of FGF3 and FGF10 with morpholino did not abrogate the chemoFGFR-dependent phenotype. On the other side, we confirmed that FGF signaling is required for the phenotype. This result is reminiscent of what observed during hair bud formation in mouse skin explants [Glover et al., 2017]. Here, epidermal foci of FGF secretion locally recruit dermal mesenchymal cells into aggregates, but these cells are still able to aggregate in the absence of FGF foci, when homogeneously exposed to FGF in the culture medium. Despite dispensable for mesenchymal condensation *per se*, focused sources of FGF might have evolved as a strategy to ensure the organization of a robust global pattern of hair follicles. In the lateral line system, FGF ligands and their

luminal accumulation might serve a similar function, ensuring the establishment of a stereotyped periodicity in organ distribution by regulating deposition timing.

While FGF ligand may not direct *de novo* cluster assembly, it is still possible that other ligands function as guiding cues during the process. However, we find unlikely that a long-range attractive cue governs *de novo* cluster assembly. The wide degree of heterogeneity in the number of cells per cluster and of clusters per embryo and their non-stereotypic positions across the lateral line, together with the observation that cells do not display a persistent directionality while rearranging, suggest that *de novo* clustering mostly relies on short-range local influences. Consistent with this idea, the initial number of chemoFGFR positive cells, their expression levels and cell-cell interactions might have an impact on the extent of *de novo* clustering.

How are adhesions remodeled during cell clustering?

De novo cluster formation is a highly dynamic process that involves cell exchanges and remodeling of cell-cell contacts. Cadherins and CAMs are the two main classes of adhesion molecules and are at the very core of a plethora of processes involving cell dynamic interactions, such as cell sorting, migration, epithelial condensation and cellular rearrangements. To mention just few examples, specific expression of cadherin subtypes or differential levels have been shown to contribute to cell packing of ommatidia [Hayashi & Carthew, 2004] and of wing epithelial cells in *Drosophila* [Classen et al., 2005], in sharpening compartment boundaries in mouse telencephalon [Inoue et al., 2001] and in the segregation of distinct populations of neurons into the spinal cord of chick embryos [Price et al., 2002]. E-cadherin is moreover involved in convergence and extension movements, for example by mediating radial intercalation of epiblasts during zebrafish epiboly [Babb & Marrs, 2004] and mediolateral intercalation during fly germband extension [Rauzi et al., 2010]. On the CAMs front, the N-CAM-like protein fasciclin 2 enriched at lateral membranes of *Drosophila* follicle cells is necessary for reintegration into the epithelium of cells that end up apically extruded upon misaligned cell division [Bergstralh et al., 2015], while fasciclin 3 instructs cell matching of cardioblast subtypes during *Drosophila* cardiogenesis [Zhang et al., 2018]. In addition, N-CAM has been implicated in the formation and maintenance of skeletogenic condensates [Giffin et al., 2019; Hall & Miyake, 2000]. Previous work in the lab, moreover, showed that FGF signaling is a key modulator of adhesive properties of cells in the lateral line system [Durdu, 2015; Durdu et al., 2014; Revenu et al., 2014].

During *de novo* cluster formation, we found that chemoFGFR cell-autonomously induces an increased Cdh2 expression and a Cdh2 enrichment at homotypic interfaces between interacting chemoFGFR positive cells. In more mature clusters, Cdh2 accumulation is shifted apically, resembling the pattern of wild type neuromasts described in previous studies [Revenu et al., 2014]. On the other side, enrichments of NCAM1b-GFP marks cell-cell contact points between NCAM1b-GFP misexpressing cells, independently of whether they are chemoFGFR positives or negatives, disclosing its potential as a tool for dynamic monitoring of cell-cell interactions in time lapses. Antibody staining of the endogenous NCAM1b protein would be required to visualize changes in expression and localization during cluster formation.

It is conceivable that Cdh2 enrichment at chemoFGFR homotypic contacts might have a role in chemoFGFR-dependent cell sorting and cell-cell 'recognition'. A large body of evidences established that cadherins regulate cell-cell contact formation by decreasing interfacial tension at contact surfaces, playing an antagonistic role to cortical contractility [Maître et al., 2012; Maître & Heisenberg, 2011]. Moreover, cadherins are involved in the stabilization of cell-cell contacts by mechanically coupling cellular cortices. It is thus possible that a cadherin mediated 'contact-zippering' could be involved in the contact expansion observed during compaction of chemoFGFR positive cells.

To address whether Cdh2 or NCAM1b are necessary for cluster formation, we performed Crispr-cas9 knockout experiments, exploiting a newly published strategy based on redundant targeting of individual genes and on direct evaluation of injected F0 embryos for null phenotypes [Jin et al., 2019]. We found that knockout of either Cdh2 or a combination of NCAM1a and b did not affect *de novo* cluster formation in chemoFGFR expressing lateral lines. There are several possible explanations for this result. It could be that Cdh2 and NCAM1b are simply not required for cluster formation. Alternatively, the lack of effect might be due to technical shortcomings or biological limitations. Other adhesion proteins might compensate for Cdh2 or NCAM1 loss. It has been recently found that genetic compensation occurs upon Crispr-mediated knockout mutations, leading to expression of genes that are paralogue or functionally related to the ablated one, a mechanism termed transcriptional adaptation [El-Brolosy et al., 2019]. Various mechanisms have been proposed to be at the basis of it, for instance chromatin remodeling mediated by DNA damage [El-Brolosy & Stainier, 2017] or mutant mRNA-dependent recruitment of nonsense-mediated decay RNA surveillance pathway [El-Brolosy et al., 2019]. This phenomenon, that is at the basis of discrepancies observed between Knockdown and Knockout phenotypes, might mitigate the effect of the loss-of-function. Another possibility would be that our Crispr-mediated gene targeting is not completely penetrant, for example due to chimerism and Crispr monoallelic cuts. In this scenario, the remaining protein might still be sufficient to mediate *de novo* cluster formation. This potential explanation only applies to F0 experiments, as such mosaicism would not be expected following germline transmission of the respective Crispr generated alleles.

4.2.5.2 How does a cluster aggregate and compact during homotypic sorting?

Cell sorting is thought to rely on differences in cellular properties between cell populations constituting the heterotypic mix, such as differential or specific adhesion [Foty & Steinberg, 2005; Moscona, 1962; Steinberg, 2007; Townes & Holtfreter, 1955], differential contractility [Harris, 1976] and differential motility [B. M. Jones et al., 1989]. The differential interfacial tension hypothesis (DITH) [Brodland, 2002] integrates elements of the differential adhesion and differential contractility hypothesis, postulating that a balance of adhesive and cortical forces governs cell sorting. Tendency to spreading of cell-cell contact area, mediated by adhesion, antagonistically opposes to the tendency to minimization of it, mediated by cell cortical tension [Brodland, 2002]. This modality of sorting is thought to be involved in a wide range of patterning processes during development such as *Drosophila* retina and lineage segregation in the mouse blastocyst [Fagotto, 2014; Käfer et al., 2007; Maître et al., 2016]. We propose that differences in mechano-adhesive properties of chemoFGFR positive and

negative cells contribute to the sorting process during *de novo* cluster formation. Our analyses of contact angles, cell-cell interface lengths and cell morphologies provide indications that interacting chemoFGFR positive cells tend to minimize heterotypic contacts and to maximize homotypic ones. The rounded morphology assumed by solitary chemoFGFR positive cells interspersed with negative cells is analogous to what observed for solitary NE cells that are prevented from clustering into NEBs [Branchfield et al., 2017]. A paper from Krieg and co-workers showed that zebrafish germ-layer progenitor cells *in vitro* present differences in cellular mechano-adhesive properties and that adhesive forces between cell pairs composed of different progenitor types (heterotypic contacts) are weaker than between cell pairs composed of the same progenitor type (homotypic contacts) [Krieg et al., 2008]. The observed sorting of mesoderm cells that, upon transplantation into ectoderm cell fields in embryos, compact into cell clusters, is consistent with the tendency of cells to minimize their heterotypic surfaces and maximize homotypic ones [Krieg et al., 2008]. Aggregating chemoFGFR positive cells, as well, spread homotypic contact interfaces in a way reminiscent to compaction, the morphogenetic process that tighten an aggregate of cells into a more packed and cohesive structure. Compaction is the result of a 'tug of war' of forces at the contact and at contact-free surfaces [Maître et al., 2015; Turlier & Maître, 2015] and it has been described in a number of contexts, such as in the mammalian 8-cell stage embryo and in the *Drosophila* ommatidium [Ducibella et al., 1977; Hayashi & Carthew, 2004; Turlier & Maître, 2015]. The establishment of the impact of actomyosin contractility and adhesion and the identification of other players of cell sorting during *de novo* cluster formation will be the subject of future investigations.

4.2.6 The establishment of an inside-outside pattern

It is plausible that differences in mechano-adhesive properties between chemoFGFR positive and negative cells not only contribute to the homotypic sorting during early stages of *de novo* cluster assembly, but also to the maintenance of the inside-outside segregation between chemoFGFR positive and negative cells within the cluster. In mouse blastocyst at the 8 to 16 cell-stage transition, blastomeres segregate depending on their cortical contractility in an inner core of highly contractile cells and an outer coat of 'softer' cells [Maître et al., 2016]. An intriguing possibility would be that within *de novo* clusters, analogously, chemoFGFR positive cells constitute a highly contractile cluster core and negative cells establish a softer outer rim. Given the established role of FGF signaling as a driver of actomyosin contractility in several contexts, including the lateral line system [Harding & Nechiporuk, 2012; Nerurkar et al., 2019; Sai & Ladher, 2008], it is plausible that chemoFGFR activity might cell-autonomously increases cortical tension. In line with this idea, analysis of the 3D shape of cells within clusters showed that chemoFGFR positive cells display a more rounded morphology compared to negative ones, an observation that in several systems is indicative of high cortical tension [Zaidel-Bar et al., 2015].

One fascinating aspect of *de novo* cluster formation concerns the association between the chemoFGFR negative cells forming the outer rim and the chemoFGR positive cells constituting the cluster seed.

First, what drives the engagement of chemoFGFR negative cells into a *de novo* cluster? Second, is the fate of negative cells altered when joining the epithelial cluster seed?

One possible scenario would be that chemoFGFR negative cells are actively recruited from the cluster seed and undergo MET while joining. This would imply that MET can indeed propagate, but only from an assembled 'epithelial core' that acts as catalyzer. Our observation that chemoFGFR negative cells composing the cluster rim adopt a columnar morphology and establish a radial polarization analogous to chemoFGFR positive cells seems to support this scenario. Another scenario would be that chemoFGFR negative cells are not actively recruited from the cluster seed but instead spontaneously associate and wrap around it when located in its proximity, while maintaining a mesenchymal-like state. Because mesenchymal cells are softer and more deformable, they might conform to the shape of the epithelial core while enveloping it. This scenario would be in line with the previously discussed idea of a contractile cluster core enclosed by a softer rim of negative cells. The presence of a mesenchymal pool in close proximity to an epithelial structure is indeed a common theme during organogenesis. In several contexts, mesenchymal cells provide signaling cues to regulate morphogenesis of the adjacent epithelium, for example during formation of villi in the embryonic intestine [Shyer et al., 2015], and often serve as progenitor pools. An example of the latter is during 'daughter somite' formation in chick, where, upon tissue deformation induced by mechanical stretching, mesenchymal cells located in the somitocoeal core of somites undergo MET and integrate into the epithelium, to provide additional cells for the splitting of the somite in two [Jackson et al., 2017; Nelemans et al., 2020]. An in-depth analysis of the gene expression patterns of chemoFGFR negative and positive cells and a clearer understanding of the sorting mechanism will shed light on the modality of association of the two cell populations and on their phenotypic states.

4.2.6.1 Examples of self-assembly feeding back on cell fate

We found that the inside-outside pattern established through cell sorting has an impact on cell differentiation. The association of FGF signaling with hair cell fate is in line with a study reporting that FGFR1a expression marks the subpopulation of supporting cells responsible for hair cell regeneration upon drug-induced hair depletion [Lee et al., 2016]. Moreover, knockout of FGFR1a leads to a severe reduction in the number of hair cells in the mouse cochlea [Pirvola et al., 2002]. However, in our system, presence or absence of chemoFGFR is not *per se* sufficient to drive cells towards hair or mantle fate.

Different scenarios might explain how cell differentiation within *de novo* clusters is patterned. Differences in actomyosin contractility of cells in the cluster seed and rim, for example, might have an impact on cell fate choices. It has been recently shown in *Drosophila* bristle patterning that high cortical tension facilitates Delta/Notch signaling, a pathway mediating lateral inhibition that is also crucial for specification of hair cells in lateral line neuromasts [G. L. Hunter et al., 2019]. Tissue mechanics can influence fate choice through various mechanotransduction strategies. Human mesenchymal stem cells differentiate into neurons or osteoclasts depending on the stiffness of the culture substrate, in a process that requires actomyosin cortex and nuclear lamin A [Engler et al., 2006; McBeath et al., 2004; Swift et al., 2013]. During feather bud formation in the avian skin instead, mechanical compression of

the epidermal layer (triggered by dermal condensation) induces epidermal activation of β-catenin, that translocates to the nucleus and induces a follicle-specific gene expression program [Shyer et al., 2017]. The mechanosensitive translocation of β-catenin is also involved in the induction of mesodermal identity in the zebrafish epiboly and in *Drosophila* [Brunet et al., 2013]. In addition, in several systems, the extent of cortical tension is proportional to the activity of YAP and TAZ, two transcription factors of the Hippo signaling pathway. These affect cell fate decisions in contexts such as *Xenopus* mesenchymal aggregates [Kim et al., 2020], mouse blastocyst [Cockburn et al., 2013; C. Y. Leung & Zernicka-Goetz, 2013] and retinal pigment epithelium of zebrafish [Miesfeld et al., 2015]. At the surface of *Xenopus* mesenchymal aggregates indeed, an increase of cellular stiffness and a concurrent increase in YAP1 activity accompany the regeneration of a mucociliated epithelium and tuning of actomyosin contractility via drugs or genetic methods controls both [Kim et al., 2020]. In addition, a recent study of zebrafish oogenesis reported a mechanism of lateral inhibition triggered by mechanical compression where nuclear TAZ levels are involved in the specification of the micropyle precursor cell within the granulosa cell layer [Xia et al., 2019].

Another way actomyosin contractility could affect cell specification during *de novo* cluster assembly is through induction of 'jamming', the transition from a fluid-like to solid-like state observed in the presomitic mesoderm during body axis extension [Mongera et al., 2019]. While an unjammed state promotes fluid cellular rearrangements, the transition to a jammed state increases tissue stiffness and stabilizes cell-cell contacts, that might in turn promote specific differentiation programs. The duration of cell-cell contacts, indeed, has been suggested to act as a 'kinetic proofreading' mechanism for the activation of signaling pathways involved in fate choices [Barone et al., 2017]. For example, during zebrafish gastrulation, a positive feedback loop emerges between cell-cell contact duration and Nodal signaling. Long-lasting contacts promote an enhanced Nodal signaling activity, driving differentiation of mesendoderm progenitors toward a prechordal plate fate, while unstable contacts lead to the acquisition of endoderm fate [Barone et al., 2017]. Similarly, during early *Drosophila* development, the induction of gut endoderm fate or neurogenic ectoderm fate depends on the time-integrated dose of ERK activity [Johnson & Toettcher, 2019]. An alternative scenario would be that, rather than contact duration, the number of cell-cell contacts and contact distribution, and thus cell size and position within the tissue, affect cell fate. Indeed, within *de novo* clusters, cells in the seed are tightly packed, while cells in the outer rim present a surface unconstrained from other lateral line cells. Which strategies can be used to convert positional information into fate choices? In the chick inner ear, cell-cell contact area is proportional to Delta/Notch signaling activation that in turns promotes hair fate specification [Shaya et al., 2017], while in the 8-cell stage mouse embryo, blastomeres in the outer rim display an enrichment of apical domain components at contact-free surfaces, that leads these cells to commit to the trophectoderm fate [Korotkevich et al., 2017; Stephenson et al., 2010].

Another aspect that might lead to a patterned differentiation of *de novo* clusters is the mesenchymal to epithelial transition. Hu and Corwin proposed that enforcement of MET through appropriate cell culture conditions is crucial for hair and supporting cell differentiation *in vitro* [Hu & Corwin, 2007]. Moreover, other studies suggested that EMT-MET cycles are important for *in vitro* reprogramming and differentiation [Di Stefano et al., 2014; Li et al., 2017; X. Liu et al., 2013] and that MET is associated

with pluripotency exit of embryonic epiblast and cultured hiPSCs [Hamidi et al., 2020]. However, whether MET in these contexts is causal or simply accompanying fate conversion is still a subject of debate [Li et al., 2014]. The exploration of mechanisms involved in cell fate establishment during *de novo* cluster formation will be the goal of future investigations.

4.3 Concluding remarks

In conclusion, in this study, we developed a cell-autonomous approach to drive MET *in vivo* and, by employing it in the lateral line chain cells, we provided insights into the process that leads to assembly of *de novo* epithelial organs from a population of naïve mesenchymal-like cells. We found that organs emerge via the aggregation of cells whose FGF signaling activity is artificially induced (chemoFGFR positive cells), that sort away from chemoFGFR negative cells and coalesce via dynamic cell rearrangements mediated by cell slithering. The aggregation and compaction into 3D clusters are accompanied by *bona fide* MET transition and remarkable remodeling of cell-cell contacts, cell morphologies and adhesive interactions. We observed that the assembled epithelial cluster can serve as a seed that catalyzes the association of adjacent chemoFGFR negative cells, forming a rim at the cluster periphery. Furthermore, we found that the inside-outside pattern of clusters emerged from the FGF signaling activity-dependent sorting, feedbacks on cell differentiation as *de novo* clusters mature into *bona fide* lateral line organs. Overall, our results suggest that chemoFGFR induction leads to a genetically encoded self-assembly process, that appears to mainly rely on homotypic cell sorting and concerted epithelialization of chemoFGFR positive cells. These insights are generally relevant for the understanding of how individual cells contribute to collective behaviors during organogenesis in physiological conditions and of mechanisms at the basis of the self-assembly potential of cells.

References

Abu-Issa, R., & Kirby, M. L. (2007). Heart field: From mesoderm to heart tube. In *Annual Review of Cell and Developmental Biology*.

Acharya, B. R., Nestor-Bergmann, A., Liang, X., Gupta, S., Duszyc, K., Gauquelin, E., Gomez, G. A., Budnar, S., Marcq, P., Jensen, O. E., Bryant, Z., & Yap, A. S. (2018). A Mechanosensitive RhoA Pathway that Protects Epithelia against Acute Tensile Stress. *Developmental Cell*.

Ahlstrom, J. D., & Erickson, C. A. (2009). The neural crest epithelial-mesenchymal transition in 4D: A "tail" of multiple non-obligatory cellular mechanisms. *Development*.

Ahmed, Z., George, R., Lin, C. C., Suen, K. M., Levitt, J. A., Suhling, K., & Ladbury, J. E. (2010). Direct binding of Grb2 SH3 domain to FGFR2 regulates SHP2 function. *Cellular Signalling*.

Amack, J. D., Wang, X., & Yost, H. J. (2007). Two T-box genes play independent and cooperative roles to regulate morphogenesis of ciliated Kupffer's vesicle in zebrafish. *Developmental Biology*.

Aman, A., & Piotrowski, T. (2008). Wnt/β-Catenin and Fgf Signaling Control Collective Cell Migration by Restricting Chemokine Receptor Expression. *Developmental Cell*, *15*(5), 749–761.

Ambrosini, A., Rayer, M., Monier, B., & Suzanne, M. (2019). Mechanical Function of the Nucleus in Force Generation during Epithelial Morphogenesis. *Developmental Cell*, *50*(2), 197-211.e5.

An, J., Zheng, Y., & Dann, C. T. (2017). Mesenchymal to Epithelial Transition Mediated by CDH1 Promotes Spontaneous Reprogramming of Male Germline Stem Cells to Pluripotency. *Stem Cell Reports*.

Atsuta, Y., & Takahashi, Y. (2015). FGF8 coordinates tissue elongation and cell epithelialization during early kidney tubulogenesis. *Development*, *142*(13), 2329–2337.

Attia, L., Schneider, J., Yelin, R., & Schultheiss, T. M. (2015). Collective cell migration of the nephric duct requires FGF signaling. *Developmental Dynamics*.

Aue, A., Hinze, C., Walentin, K., Ruffert, J., Yurtdas, Y., Werth, M., Chen, W., Rabien, A., Kilic, E., Schulzke, J. D., Schumann, M., & Schmidt-Ott, K. M. (2015). A grainyhead-like 2/Ovo-like 2 pathway regulates renal epithelial barrier function and lumen expansion. *Journal of the American Society of Nephrology*.

Aulehla, A., & Pourquié, O. (2010). Signaling gradients during paraxial mesoderm development. In *Cold Spring Harbor perspectives in biology*.

Babb, S. G., & Marrs, J. A. (2004). E-cadherin regulates cell movements and tissue formation in early zebrafish embryos. *Developmental Dynamics*.

Bacallao, R., Antony, C., Dotti, C., Karsenti, E., Stelzer, E. H. K., & Simons, K. (1989). The subcellular organization of Madin-Darby canine kidney cells during the formation of a polarized epithelium. *Journal of Cell Biology*.

Bae, Y. K., Trisnadi, N., Kadam, S., & Stathopoulos, A. (2012). The role of FGF signaling in guiding coordinate movement of cell groups guidance cue and cell adhesion regulator? *Cell Adhesion and Migration*.

Balak, K. J., Corwin, J. T., & Jones, J. E. (1990). Regenerated hair cells can originate from supporting cell progeny: Evidence from phototoxicity and laser ablation experiments in the lateral line system. *Journal of Neuroscience*.

Barone, V., Lang, M., Krens, S. F. G., Pradhan, S. J., Shamipour, S., Sako, K., Sikora, M., Guet, C. C., &

Heisenberg, C. P. (2017). An Effective Feedback Loop between Cell-Cell Contact Duration and Morphogen Signaling Determines Cell Fate. *Developmental Cell*, *43*(2), 198-211.e12.

Bedi, U., Mishra, V. K., Wasilewski, D., Scheel, C., & Johnsen, S. A. (2014). Epigenetic plasticity: A central regulator of epithelial-tomesenchymal transition in cancer. *Oncotarget*.

Bedzhov, I., & Zernicka-Goetz, M. (2014). Self-organizing properties of mouse pluripotent cells initiate morphogenesis upon implantation. *Cell*.

Bellusci, S., Grindley, J., Emoto, H., Itoh, N., & Hogan, B. L. M. (1997). Fibroblast Growth Factor 10 (FGF10) and branching morphogenesis in the embryonic mouse lung. *Development*.

Bénazéraf, B., Francois, P., Baker, R. E., Denans, N., Little, C. D., & Pourquié, O. (2010). A random cell motility gradient downstream of FGF controls elongation of an amniote embryo. *Nature*.

Berg, S., Kutra, D., Kroeger, T., Straehle, C. N., Kausler, B. X., Haubold, C., Schiegg, M., Ales, J., Beier, T., Rudy, M., Eren, K., Cervantes, J. I., Xu, B., Beuttenmueller, F., Wolny, A., Zhang, C., Koethe, U., Hamprecht, F. A., & Kreshuk, A. (2019). ilastik: interactive machine learning for (bio) image analysis. *Nature Methods*, *16*(December).

Bergstralh, D. T., Lovegrove, H. E., & St Johnston, D. (2015). Lateral adhesion drives reintegration of misplaced cells into epithelial monolayers. *Nature Cell Biology*, *17*(11), 1497–1503.

Bielmeier, C., Alt, S., Weichselberger, V., Jü, F., Salbreux, G., Classen Correspondence, A.-K., Fortezza, M. La, Harz, H., & Classen, A.-K. (2016). Interface Contractility between Differently Fated Cells Drives Cell Elimination and Cyst Formation. *Current Biology*, *26*, 563–574.

Bilder, D., Schober, M., & Perrimon, N. (2003). Integrated activity of PDZ protein complexes regulates epithelial polarity. *Nature Cell Biology*.

Bloch, R. J. (1992). Clusters of neural cell adhesion molecule at sites of cell-cell contact. *Journal of Cell Biology*, *116*(2), 449–463.

Boldajipour, B., Mahabaleshwar, H., Kardash, E., Reichman-Fried, M., Blaser, H., Minina, S., Wilson, D., Xu, Q., & Raz, E. (2008). Control of Chemokine-Guided Cell Migration by Ligand Sequestration. *Cell*.

Bolte, S., & Cordelières, F. P. (2006). A guided tour into subcellular colocalization analysis in light microscopy. *Journal of Microscopy*, *224*(June), 213–232.

Branchfield, K., Nantie, L., Verheyden, J. M., Sui, P., Wienhold, M. D., & Sun, X. (2017). Pulmonary neuroendocrine cells function as airway sensors to control lung immune response. *Science*, *351*(6274), 707–710.

Brodland, G. W. (2002). The Differential Interfacial Tension Hypothesis (DITH): A comprehensive theory for the self-rearrangement of embryonic cells and tissues. *Journal of Biomechanical Engineering*.

Brunet, T., Bouclet, A., Ahmadi, P., Mitrossilis, D., Driquez, B., Brunet, A. C., Henry, L., Serman, F., Béalle, G., Ménager, C., Dumas-Bouchiat, F., Givord, D., Yanicostas, C., Le-Roy, D., Dempsey, N. M., Plessis, A., & Farge, E. (2013). Evolutionary conservation of early mesoderm specification by mechanotransduction in Bilateria. *Nature Communications*.

Bryant, D. M., Datta, A., Rodríguez-Fraticelli, A. E., PeräCurrency Signnen, J., Martín-Belmonte, F., & Mostov, K. E. (2010). A molecular network for de novo generation of the apical surface and lumen. *Nature Cell Biology*.

Bryant, D. M., Roignot, J., Datta, A., Overeem, A. W., Kim, M., Yu, W., Peng, X., Eastburn, D. J., Ewald, A. J., Werb, Z., & Mostov, K. E. (2014). A Molecular Switch for the Orientation of Epithelial Cell Polarization.

Developmental Cell, *31*, 171–187.

Bryant, Huettner, Held, L. I., Ryerse, J., & Szidonya, J. (1988). Mutations at the fat locus interfere with cell proliferation control and epithelial morphogenesis in Drosophila. *Developmental Biology*.

Bryant, M. R., Marta, C. B., Kim, F. S., & Bansal, R. (2009). Phosphorylation and lipid raft association of fibroblast growth factor receptor-2 in oligodendrocytes. *GLIA*.

Burute, M., Prioux, M., Blin, G., Truchet, S., Letort, G., Tseng, Q., Bessy, T., Lowell, S., Young, J., Filhol, O., & Théry, M. (2017). Polarity Reversal by Centrosome Repositioning Primes Cell Scattering during Epithelial-to-Mesenchymal Transition. *Developmental Cell*, *40*(2), 168–184.

Cachat, E., Liu, W., Hohenstein, P., & Davies, J. A. (2014). A library of mammalian effector modules for synthetic morphology. *Journal of Biological Engineering*.

Cai, D., Chen, S. C., Prasad, M., He, L., Wang, X., Choesmel-Cadamuro, V., Sawyer, J. K., Danuser, G., & Montell, D. J. (2014). Mechanical feedback through E-cadherin promotes direction sensing during collective cell migration. *Cell*.

Campbell, K., & Casanova, J. (2015). A role for E-cadherin in ensuring cohesive migration of a heterogeneous population of non-epithelial cells. *Nature Communications*.

Campbell, K., & Casanova, J. (2016). A common framework for EMT and collective cell migration. *Development*, *143*(23), 4291–4300.

Campbell, K., Casanova, J., & Skaer, H. (2010). Mesenchymal-to-epithelial transition of intercalating cells in Drosophila renal tubules depends on polarity cues from epithelial neighbours. *Mechanisms of Development*, *127*(7–8), 345–357.

Campbell, K., Whissell, G., Franch-Marro, X., Batlle, E., & Casanova, J. (2011). Specific GATA Factors Act as Conserved Inducers of an Endodermal-EMT. *Developmental Cell*.

Camps, M., Nichols, A., Gillieron, C., Antonsson, B., Muda, M., Chabert, C., Boschert, U., & Arkinstall, S. (1998). Catalytic activation of the phosphatase MKP-3 by ERK2 mitogen-activated protein kinase. *Science*.

Canty, L., Zarour, E., Kashkooli, L., François, P., & Fagotto, F. (2017). Sorting at embryonic boundaries requires high heterotypic interfacial tension. *Nature Communications*, *8*(1).

Carroll, T. J., Park, J. S., Hayashi, S., Majumdar, A., & McMahon, A. P. (2005). Wnt9b plays a central role in the regulation of mesenchymal to epithelial transitions underlying organogenesis of the mammalian urogenital system. *Developmental Cell*, *9*(2), 283–292.

Cavallaro, U., & Christofori, G. (2004). Cell adhesion and signalling by cadherins and Ig-CAMs in cancer. In *Nature Reviews Cancer*.

Chakrabarti, R., Hwang, J., Andres Blanco, M., Wei, Y., Lukačišin, M., Romano, R. A., Smalley, K., Liu, S., Yang, Q., Ibrahim, T., Mercatali, L., Amadori, D., Haffty, B. G., Sinha, S., & Kang, Y. (2012). Elf5 inhibits the epithelial-mesenchymal transition in mammary gland development and breast cancer metastasis by transcriptionally repressing Snail2. *Nature Cell Biology*.

Chan, C. J., Costanzo, M., Ruiz-Herrero, T., Mönke, G., Petrie, R. J., Bergert, M., Diz-Muñoz, A., Mahadevan, L., & Hiiragi, T. (2019). Hydraulic control of mammalian embryo size and cell fate. *Nature*.

Chang, C. J., Chao, C. H., Xia, W., Yang, J. Y., Xiong, Y., Li, C. W., Yu, W. H., Rehman, S. K., Hsu, J. L., Lee, H. H., Liu, M., Chen, C. Te, Yu, D., & Hung, M. C. (2011). P53 regulates epithelial-mesenchymal transition and stem cell properties through modulating miRNAs. *Nature Cell Biology*.

Chellaiah, A. T., McEwen, D. G., Werner, S., Xu, J., & Ornitz, D. M. (1994). Fibroblast growth factor receptor (FGFR) 3. Alternative splicing in immunoglobulin-like domain III creates a receptor highly specific for acidic FGF/FGF-1. *Journal of Biological Chemistry*.

Chen, G., Gulbranson, D. R., Hou, Z., Bolin, J. M., Ruotti, V., Probasco, M. D., Smuga-Otto, K., Howden, S. E., Diol, N. R., Propson, N. E., Wagner, R., Lee, G. O., Antosiewicz-Bourget, J., Teng, J. M. C., & Thomson, J. A. (2011). Chemically defined conditions for human iPSC derivation and culture. *Nature Methods*.

Chen, Q., Shi, J., Tao, Y., & Zernicka-Goetz, M. (2018). Tracing the origin of heterogeneity and symmetry breaking in the early mammalian embryo. *Nature Communications*, *9*(1), 1–11.

Chitnis, A. B., Nogare, D. D., & Matsuda, M. (2012). Building the posterior lateral line system in zebrafish. *Developmental Neurobiology*, *72*(3), 234–255.

Choi, S. S., & Diehl, A. M. (2009). Epithelial-to-mesenchymal transitions in the liver. In *Hepatology*.

Chuai, M., & Weijer, C. J. (2009). Regulation of cell migration during chick gastrulation. In *Current Opinion in Genetics and Development*.

Chung, V. Y., Tan, T. Z., Tan, M., Wong, M. K., Kuay, K. T., Yang, Z., Ye, J., Muller, J., Koh, C. M., Guccione, E., Thiery, J. P., & Huang, R. Y. J. (2016). GRHL2-miR-200-ZEB1 maintains the epithelial status of ovarian cancer through transcriptional regulation and histone modification. *Scientific Reports*.

Cirulli, V., Baetens, D., Rutishauser, U., Halban, P. A., Orci, L., & Rouiller, D. G. (1994). *Expression of neural cell adhesion molecule (N-CAM) in rat islets and its role in islet cell type segregation*. *1436*, 1429–1436.

Ciruna, B., Jenny, A., Lee, D., Mlodzik, M., & Schier, A. F. (2006). Planar cell polarity signalling couples cell division and morphogenesis during neurulation. *Nature*.

Ciruna, B., & Rossant, J. (2001). FGF Signaling Regulates Mesoderm Cell Fate Specification and Morphogenetic Movement at the Primitive Streak. *Developmental Cell*.

Clark, I. B. N., Muha, V., Klingseisen, A., Leptin, M., & Müller, H. A. J. (2011). Fibroblast growth factor signalling controls successive cell behaviours during mesoderm layer formation in Drosophila. *Development*.

Classen, A. K., Anderson, K. I., Marois, E., & Eaton, S. (2005). Hexagonal packing of Drosophila wing epithelial cells by the planar cell polarity pathway. *Developmental Cell*.

Cockburn, K., Biechele, S., Garner, J., & Rossant, J. (2013). The hippo pathway member nf2 is required for inner cell mass specification. *Current Biology*.

Cohen, J. (1988). Statistical power for the social sciences. *Hillsdale, NJ: Laurence Erlbaum and Associates*.

Cooke, J., & Zeeman, E. C. (1976). A clock and wavefront model for control of the number of repeated structures during animal morphogenesis. *Journal of Theoretical Biology*.

Cordelires, F. (2017). Manual Tracking Fiji plugin. *Imagej.Net/Manual_Tracking*.

Cronan, M. R., Beerman, R. W., Rosenberg, A. F., Saelens, J. W., Johnson, M. G., Oehlers, S. H., Sisk, D. M., Jurcic Smith, K. L., Medvitz, N. A., Miller, S. E., Trinh, L. A., Fraser, S. E., Madden, J. F., Turner, J., Stout, J. E., Lee, S., & Tobin, D. M. (2016). Macrophage Epithelial Reprogramming Underlies Mycobacterial Granuloma Formation and Promotes Infection. *Immunity*, *45*(4), 861–876.

Cruz, I. A., Kappedal, R., Mackenzie, S. M., Hailey, D. W., Hoffman, T. L., Schilling, T. F., & Raible, D. W. (2015). Robust regeneration of adult zebrafish lateral line hair cells reflects continued precursor pool

maintenance. *Developmental Biology*.

Cubas, P., De Celis, J. F., Campuzano, S., & Modolell, J. (1991). Proneural clusters of achaete-scute expression and the generation of sensory organs in the Drosophila imaginal wing disc. *Genes and Development*.

Czubayko, F., Liaudet-Coopman, E. D. E., Aigner, A., Tuveson, A. T., Berchem, G. J., & Wellstein, A. (1997). A secreted FGF-binding protein can serve as the angiogenic switch in human cancer. *Nature Medicine*.

Dai, S., Zhou, Z., Chen, Z., Xu, G., & Chen, Y. (2019). Fibroblast Growth Factor Receptors (FGFRs): Structures and Small Molecule Inhibitors. *Cells*.

Dale, J. K., Malapert, P., Chal, J., Vilhais-Neto, G., Maroto, M., Johnson, T., Jayasinghe, S., Trainor, P., Herrmann, B., & Pourquié, O. (2006). Oscillations of the snail genes in the presomitic mesoderm coordinate segmental patterning and morphogenesis in vertebrate somitogenesis. *Developmental Cell*.

Das, T., Safferling, K., Rausch, S., Grabe, N., Boehm, H., & Spatz, J. P. (2015). A molecular mechanotransduction pathway regulates collective migration of epithelial cells. *Nature Cell Biology*.

Datta, A., Bryant, D. M., & Mostov, K. E. (2011). Molecular regulation of lumen morphogenesis. In *Current Biology*.

David, N. B., Sapède, D., Saint-Etienne, L., Thisse, C., Thisse, B., Dambly-Chaudière, C., Rosa, F. M., & Ghysen, A. (2002). Molecular basis of cell migration in the fish lateral line: Role of the chemokine receptor CXCR4 and of its ligand, SDF1. *Proceedings of the National Academy of Sciences of the United States of America*.

Davidson, L. A., Ezin, A. M., & Keller, R. (2002). Embryonic wound healing by apical contraction and ingression in Xenopus laevis. *Cell Motility and the Cytoskeleton*.

Davis, G. S., Phillips, H. M., & Steinberg, M. S. (1997). Germ-layer surface tensions and "tissue affinities" in Rana pipiens gastrulae: Quantitative measurements. *Developmental Biology*.

de Vries, W. N., Evsikov, A. V., Haac, B. E., Fancher, K. S., Holbrook, A. E., Kemler, R., Solter, D., & Knowles, B. B. (2004). Maternal β-catenin and E-cadherin in mouse development. *Development*.

Debnath, J., & Brugge, J. S. (2005). Modelling glandular epithelial cancers in three-dimensional cultures. In *Nature Reviews Cancer*.

Di Stefano, B., Collombet, S., & Graf, T. (2014). Time-resolved gene expression profiling during reprogramming of C/EBPα-pulsed B cells into iPS cells. *Scientific Data*.

Distel, M., Wullimann, M. F., & Köster, R. W. (2009). Optimized Gal4 genetics for permanent gene expression mapping in zebrafish. *Proceedings of the National Academy of Sciences of the United States of America*.

Donà, E., Barry, J. D., Valentin, G., Quirin, C., Khmelinskii, A., Kunze, A., Durdu, S., Newton, L. R., Fernandez-Minan, A., Huber, W., Knop, M., & Gilmour, D. (2013). Directional tissue migration through a self-generated chemokine gradient. *Nature*.

Dos Santos, J. V., Yu, R. Y., Terceros, A., & Chen, B. E. (2019). FGF receptors are required for proper axonal branch targeting in Drosophila. *Molecular Brain*.

Duan, D. S. R., Werner, S., & Williams, L. T. (1992). A naturally occurring secreted form of fibroblast growth factor (FGF) receptor 1 binds basic FGF in preference over acidic FGF. *Journal of Biological Chemistry*.

Dubaissi, E., Rousseau, K., Lea, R., Soto, X., Nardeosingh, S., Schweickert, A., Amaya, E., Thornton, D. J., & Papalopulu, N. (2014). A secretory cell type develops alongside multiciliated cells, ionocytes and goblet cells, and provides a protective, antiinfective function in the frog embryonic mucociliary epidermis. *Development (Cambridge)*.

Ducibella, T., Ukena, T., Karnovsky, M., & Anderson, E. (1977). Changes in cell surface and cortical cytoplasmic organization during early embryogenesis in the preimplantation mouse embryo. *Journal of Cell Biology*.

Dudka, A. A., Sweet, S. M. M., & Heath, J. K. (2010). Signal transducers and activators of transcription-3 binding to the fibroblast growth factor receptor is activated by receptor amplification. *Cancer Research*.

Dufourcq, P., Roussigné, M., Blader, P., Rosa, F., Peyrieras, N., & Vriz, S. (2006). Mechano-sensory organ regeneration in adults: The zebrafish lateral line as a model. *Molecular and Cellular Neuroscience*, *33*(2), 180–187.

Durdu, S. (2015). *Connecting cell communication and multicellular architecture during morphogenesis* (Vol. 151).

Durdu, S., Iskar, M., Revenu, C., Schieber, N., Kunze, A., Bork, P., Schwab, Y., & Gilmour, D. (2014). Luminal signalling links cell communication to tissue architecture during organogenesis. *Nature*, *515*(7525), 120–124.

Eiraku, M., Takata, N., Ishibashi, H., Kawada, M., Sakakura, E., Okuda, S., Sekiguchi, K., Adachi, T., & Sasai, Y. (2011). Self-organizing optic-cup morphogenesis in three-dimensional culture. *Nature*, *472*(7341), 51–58.

El-Brolosy, M. A., Kontarakis, Z., Rossi, A., Kuenne, C., Günther, S., Fukuda, N., Kikhi, K., Boezio, G. L. M., Takacs, C. M., Lai, S. L., Fukuda, R., Gerri, C., Giraldez, A. J., & Stainier, D. Y. R. (2019). Genetic compensation triggered by mutant mRNA degradation. *Nature*.

El-Brolosy, M. A., & Stainier, D. Y. R. (2017). Genetic compensation: A phenomenon in search of mechanisms. In *PLoS Genetics*.

Emelyanov, A., & Parinov, S. (2008). Mifepristone-inducible LexPR system to drive and control gene expression in transgenic zebrafish. *Developmental Biology*.

Engler, A. J., Sen, S., Sweeney, H. L., & Discher, D. E. (2006). Matrix Elasticity Directs Stem Cell Lineage Specification. *Cell*.

Ernst, S., Liu, K., Agarwala, S., Moratscheck, N., Avci, M. E., Nogare, D. D., Chitnis, A. B., Ronneberger, O., & Lecaudey, V. (2012). Shroom3 is required downstream of FGF signalling to mediate proneuromast assembly in zebrafish. *Development*, *139*(24), 4571–4581.

Esni, F., Täljedal, I., Perl, A., Cremer, H., Christofori, G., & Semb, H. (1999). *Neural Cell Adhesion Molecule (N-CAM) Is Required for Cell Type Segregation and Normal Ultrastructure in Pancreatic Islets*. *144*(2), 325–337.

Evans, M. J., Van Winkle, L. S., Fanucchi, M. V., & Plopper, C. G. (2001). Cellular and molecular characteristics of basal cells in airway epithelium. In *Experimental Lung Research*.

Fagotto, F. (2014). The cellular basis of tissue separation. *Development (Cambridge)*, *141*(17), 3303–3318.

Fagotto, F., Rohani, N., Touret, A. S., & Li, R. (2013). A Molecular Base for Cell Sorting at Embryonic Boundaries: Contact Inhibition of Cadherin Adhesion by Ephrin/Eph-Dependent Contractility.

Developmental Cell, *27*(1), 72–87.

Ferrari, A., Veligodskiy, A., Berge, U., Lucas, M. S., & Kroschewski, R. (2008). ROCK-mediated contractility, tight junctions and channels contribute to the conversion of a preapical patch into apical surface during isochoric lumen initiation. *Journal of Cell Science*.

Fleming, T. P., & Johnson, M. H. (1988). From egg to epithelium. In *Annual Review of Cell Biology*.

Foty, R. A., Pfleger, C. M., Forgacs, G., & Steinberg, M. S. (1996). Surface tensions of embryonic tissues predict their mutual envelopment behavior. *Development*.

Foty, R. A., & Steinberg, M. S. (2005). The differential adhesion hypothesis: A direct evaluation. *Developmental Biology*.

Francavilla, C., Cattaneo, P., Berezin, V., Bock, E., Ami, D., De Marco, A., Christofori, G., & Cavallaro, U. (2009). The binding of NCAM to FGFR1 induces a specific cellular response mediated by receptor trafficking. *Journal of Cell Biology*.

Francavilla, C., Loeffler, S., Piccini, D., Kren, A., Christofori, G., & Cavallaro, U. (2007). Neural cell adhesion molecule regulates the cellular response to fibroblast growth factor. *Journal of Cell Science*.

Francavilla, C., Rigbolt, K. T. G., Emdal, K. B., Carraro, G., Vernet, E., Bekker-Jensen, D. B., Streicher, W., Wikström, M., Sundström, M., Bellusci, S., Cavallaro, U., Blagoev, B., & Olsen, J. V. (2013). Functional Proteomics Defines the Molecular Switch Underlying FGF Receptor Trafficking and Cellular Outputs. *Molecular Cell*.

Freudenblum, J., Iglesias, J. A., Hermann, M., Walsen, T., Wilfinger, A., Meyer, D., & Kimmel, R. A. (2018). *In vivo imaging of emerging endocrine cells reveals a requirement for PI3K-regulated motility in pancreatic islet morphogenesis*.

Frisch, S. M., Farris, J. C., & Pifer, P. M. (2017). Roles of Grainyhead-like transcription factors in cancer. In *Oncogene*.

Fürthauer, M., Lin, W., Ang, S. L., Thisse, B., & Thisse, C. (2002). Sef is a feedback-induced antagonist of RAs/MAPK-mediated FGF signalling. *Nature Cell Biology*.

Gabay, L., Seger, R., & Shilo, B. Z. (1997). MAP kinase in situ activation atlas during Drosophila embryogenesis. *Development*.

Galanternik, M. V., Kramer, K. L., & Piotrowski, T. (2015). Heparan Sulfate Proteoglycans Regulate Fgf Signaling and Cell Polarity during Collective Cell Migration. *CellReports*, *10*, 414–428.

Gao, X., Wang, X., Xiong, W., & Chen, J. (2016). In vivo reprogramming reactive glia into iPSCs to produce new neurons in the cortex following traumatic brain injury. *Scientific Reports*.

Gassama-Diagne, A., & Payrastre, B. (2009). Phosphoinositide Signaling Pathways. Promising Role as Builders of Epithelial Cell Polarity. In *International Review of Cell and Molecular Biology*.

Gassama-Diagne, A., Yu, W., ter Beest, M., Martin-Belmonte, F., Kierbel, A., Engel, J., & Mostov, K. (2006). Phosphatidylinositol-3,4,5-trisphosphate regulates the formation of the basolateral plasma membrane in epithelial cells. *Nature Cell Biology*.

Ghabrial, A., Luschnig, S., Metzstein, M. M., & Krasnow, M. A. (2003). Branching Morphogenesis of the Drosophila Tracheal System. *Annual Review of Cell and Developmental Biology*, *19*, 623–647.

Ghabrial, A. S., & Krasnow, M. A. (2006). Social interactions among epithelial cells during tracheal branching morphogenesis. *Nature*.

Ghysen, A., & Dambly-Chaudiere, C. (2007). The lateral line microcosmos. *Genes & Development*, *21*(17), 2118–2130.

Ghysen, A., & Dambly-Chaudière, C. (2007). The lateral line microcosmos. *Genes and Development*.

Giffin, J. L., Gaitor, D., & Franz-Odendaal, T. A. (2019). The forgotten skeletogenic condensations: A comparison of early skeletal development amongst vertebrates. In *Journal of Developmental Biology*.

Gilbert, T., Le Bivic, A., Quaroni, A., & Rodriguez-Boulan, E. (1991). Microtubular organization and its involvement in the biogenetic pathways of plasma membrane proteins in Caco-2 intestinal epithelial cells. *Journal of Cell Biology*.

Gilmour, D. T., Maischein, H. M., & Nüsslein-Volhard, C. (2002). Migration and function of a glial subtype in the vertebrate peripheral nervous system. *Neuron*, *34*(4), 577–588.

Gisselbrecht, S., Skeath, J. B., Doe, C. Q., & Michelson, A. M. (1996). heartless encodes a fibroblast growth factor receptor (DFR1/DFGF-R2) involved in the directional migration of early mesodermal cells in the Drosophila embryo. *Genes and Development*.

Glover, J. D., Wells, K. L., Matthäus, F., Painter, K. J., Ho, W., Riddell, J., Johansson, J. A., Ford, M. J., Jahoda, C. A. B., Klika, V., Mort, R. L., & Headon, D. J. (2017). Hierarchical patterning modes orchestrate hair follicle morphogenesis. In *PLoS Biology* (Vol. 15, Issue 7).

Godt, D., & Tepass, U. (1998). Drosophila oocyte localization is mediated by differential cadherin- based adhesion. *Nature*.

Goetz, R., Beenken, A., Ibrahimi, O. A., Kalinina, J., Olsen, S. K., Eliseenkova, A. V., Xu, C., Neubert, T. A., Zhang, F., Linhardt, R. J., Yu, X., White, K. E., Inagaki, T., Kliewer, S. A., Yamamoto, M., Kurosu, H., Ogawa, Y., Kuro-o, M., Lanske, B., … Mohammadi, M. (2007). Molecular Insights into the Klotho-Dependent, Endocrine Mode of Action of Fibroblast Growth Factor 19 Subfamily Members. *Molecular and Cellular Biology*.

Grant, K. A., Raible, D. W., & Piotrowski, T. (2005). Regulation of latent sensory hair cell precursors by glia in the zebrafish lateral line. *Neuron*.

Gros, J., & Tabin, C. J. (2014). Vertebrate limb bud formation is initiated by localized epithelial-to-mesenchymal transition. *Science*.

Grusch, M., Schelch, K., Riedler, R., Reichhart, E., Differ, C., Berger, W., Inglés-Prieto, Á., & Janovjak, H. (2014). Spatio-temporally precise activation of engineered receptor tyrosine kinases by light. *The EMBO Journal*, *33*(15), 1713–1726.

Guillot, C., & Lecuit, T. (2013). Mechanics of epithelial tissue homeostasis and morphogenesis. *Science*, *340*(6137), 1185–1189.

Gunasinghe, N. P. A. D., Wells, A., Thompson, E. W., & Hugo, H. J. (2012). Mesenchymal-epithelial transition (MET) as a mechanism for metastatic colonisation in breast cancer. *Cancer and Metastasis Reviews*.

Haas, P., & Gilmour, D. (2006). Chemokine Signaling Mediates Self-Organizing Tissue Migration in the Zebrafish Lateral Line. *Developmental Cell*.

Halbleib, J. M., & Nelson, W. J. (2006). Cadherins in development: Cell adhesion, sorting, and tissue morphogenesis. In *Genes and Development*.

Halder, G., Callaerts, P., & Gehring, W. J. (1995). Induction of ectopic eyes by targeted expression of the eyeless gene in Drosophila. *Science*, *67*(5205), 1788–1792.

Hall, B. K., & Miyake, T. (2000). All for one and one for all: Condensations and the initiation of skeletal development. *BioEssays*, *22*(2), 138–147.

Hamidi, S., Nakaya, Y., Nagai, H., Alev, C., Kasukawa, T., Chhabra, S., Lee, R., Niwa, H., Warmflash, A., Shibata, T., & Sheng, G. (2020). Mesenchymal-epithelial transition regulates initiation of pluripotency exit before gastrulation. *Development (Cambridge)*, *147*(3).

Hansson, E. M., & Chien, K. R. (2012). Reprogramming a broken heart. In *Cell Stem Cell*.

Harada, M., Murakami, H., Okawa, A., Okimoto, N., Hiraoka, S., Nakahara, T., Akasaka, R., Shiraishi, Y. I., Futatsugi, N., Mizutani-Koseki, Y., Kuroiwa, A., Shirouzu, M., Yokoyama, S., Taiji, M., Iseki, S., Ornitz, D. M., & Koseki, H. (2009). FGF9 monomer-dimer equilibrium regulates extracellular matrix affinity and tissue diffusion. *Nature Genetics*.

Harding, M. J., & Nechiporuk, A. V. (2012). Fgfr-Ras-MAPK signaling is required for apical constriction via apical positioning of Rho-associated kinase during mechanosensory organ formation. *Development*, *139*(17), 3130–3135.

Harris, A. K. (1976). Is cell sorting caused by differences in the work of intercellular adhesion? A critique of the steinberg hypothesis. *Journal of Theoretical Biology*.

Hartmann, J. (2019). Complexity in Developmental Systems: Toward an Integrated Understanding of Organ Formation. *Diss. Ruperto Carola University Heidelberg*, *March*, 151.

Hartmann, J., Wong, M., Gallo, E., & Gilmour, D. (2020). An image-based data-driven analysis of cellular architecture in a developing tissue. *ELife*.

Hava, D., Forster, U., Matsuda, M., Cui, S., Link, B. A., Eichhorst, J., Wiesner, B., Chitnis, A., & Abdelilah-Seyfried, S. (2009). Apical membrane maturation and cellular rosette formation during morphogenesis of the zebrafish lateral line. *Journal of Cell Science*, *122*(5), 687–695.

Hayashi, T., & Carthew, R. W. (2004). Surface mechanics mediate pattern formation in the developing retina. *Nature*, *431*(7009), 647–652.

Heisenberg, C. P. (2017). D'Arcy Thompson's 'on Growth and form': From soap bubbles to tissue self-organization. *Mechanisms of Development*, *145*, 32–37.

Hermitte, S., & Chazaud, C. (2014). Primitive endoderm differentiation: From specification to epithelium formation. In *Philosophical Transactions of the Royal Society B: Biological Sciences*.

Hernández, P. P., Olivari, F. A., Sarrazin, A. F., Sandoval, P. C., & Allende, M. L. (2007). Regeneration in zebrafish lateral line neuromasts: Expression of the neural progenitor cell marker Sox2 and proliferation-dependent and -independent mechanisms of hair cell renewal. *Developmental Neurobiology*.

Hinsby, A. M., Berezin, V., & Bock, E. (2004). Molecular mechanisms of NCAM function. In *Frontiers in bioscience : a journal and virtual library*.

Ho, W. K. W., Freem, L., Zhao, D., Painter, K. J., Woolley, T. E., Gaffney, E. A., McGrew, M. J., Tzika, A., Milinkovitch, M. C., Schneider, P., Drusko, A., Matthäus, F., Glover, J. D., Wells, K. L., Johansson, J. A., Davey, M. G., Sang, H. M., Clinton, M., & Headon, D. J. (2019). Feather arrays are patterned by interacting signalling and cell density waves. In *PLoS Biology* (Vol. 17, Issue 2).

Hoffman, B. D., & Yap, A. S. (2015). Towards a Dynamic Understanding of Cadherin-Based Mechanobiology. In *Trends in Cell Biology*.

Hu, Z., & Corwin, J. T. (2007). Inner ear hair cells produced in vitro by a mesenchymal-to-epithelial transition.

Proceedings of the National Academy of Sciences, *104*(42), 16675–16680.

Hubbard, S. R., & Miller, W. T. (2007). Receptor tyrosine kinases: mechanisms of activation and signaling. In *Current Opinion in Cell Biology*.

Hudson, D. L. (2002). Keratins as markers of epithelial cells. *Methods in Molecular Biology (Clifton, N.J.)*.

Huff, J. (2016). The Fast mode for ZEISS LSM 880 with Airyscan: high-speed confocal imaging with super-resolution and improved signal-to-noise ratio. *Nature Methods*.

Humphries, J. D., Byron, A., & Humphries, M. J. (2006). Integrin ligands at a glance. *Journal of Cell Science*.

Hunter, G. L., He, L., Perrimon, N., Charras, G., Giniger, E., & Baum, B. (2019). A role for actomyosin contractility in Notch signaling. *BMC Biology*.

Hunter, J. D. (2007). Matplotlib: A 2D graphics environment. *Computing in Science and Engineering*.

Iannuccelli, E., Mompart, F., Gellin, J., Yerle, M., Boudier, T., De, N., Agronomique, R., Cellulaire, L. D. G., Pierre, U., Bernard, Q. Saint, Pierre, U., & Jussieu, P. (2010). NEMO : a tool for analyzing gene and chromosome territory distributions from 3D-FISH experiments. *Bioinformatics*, *26*(5), 696–697.

Inoue, T., Tanaka, T., Takeichi, M., Chisaka, O., Nakamura, S., & Osumi, N. (2001). Role of cadherins in maintaining the compartment boundary between the cortex and striatum during development. *Development*.

Irving, C., Malhas, A., Guthrie, S., & Mason, I. (2002). Establishing the trochlear motor axon trajectory: Role of the isthmic organiser and Fgf8. *Development*.

Jackson, T. R., Kim, H. Y., Balakrishnan, U. L., Stuckenholz, C., & Davidson, L. A. (2017). Spatiotemporally Controlled Mechanical Cues Drive Progenitor Mesenchymal-to-Epithelial Transition Enabling Proper Heart Formation and Function. *Current Biology*, *27*(9), 1326–1335.

Jacques, B. E., Dabdoub, A., & Kelley, M. W. (2012). Fgf signaling regulates development and transdifferentiation of hair cells and supporting cells in the basilar papilla. *Hearing Research*.

Jaffe, A. B., & Hall, A. (2005). Rho GTPases: Biochemistry and biology. In *Annual Review of Cell and Developmental Biology*.

Jaffe, A. B., Kaji, N., Durgan, J., & Hall, A. (2008). Cdc42 controls spindle orientation to position the apical surface during epithelial morphogenesis. *Journal of Cell Biology*.

Jin, L., Wu, J., Bellusci, S., & Zhang, J. S. (2019). Fibroblast growth factor 10 and vertebrate limb development. *Frontiers in Genetics*, *10*(JAN), 1–9.

Johnson, H. E., & Toettcher, J. E. (2019). Signaling Dynamics Control Cell Fate in the Early Drosophila Embryo. *Developmental Cell*, *48*(3), 361-370.e3.

Jolly, M. K., Ware, K. E., Gilja, S., Somarelli, J. A., & Levine, H. (2017). EMT and MET: necessary or permissive for metastasis? In *Molecular Oncology*.

Jones, B. M., Evans, P. M., & Lee, D. A. (1989). Relation between the rate of cell movement under agarose and the positioning of cells in heterotypic aggregates. *Experimental Cell Research*.

Jones, & Corwin, J. T. (1996). Regeneration of sensory cells after laser ablation in the lateral line system: Hair cell lineage and macrophage behavior revealed by time-lapse video microscopy. *Journal of Neuroscience*.

Jones, E., Oliphant, T., Peterson, P., & Others. (2001). *SciPy.org*. SciPy: Open Source Scientific Tools for

Python2.

Jung, H. Y., Fattet, L., Tsai, J. H., Kajimoto, T., Chang, Q., Newton, A. C., & Yang, J. (2019). Apical–basal polarity inhibits epithelial–mesenchymal transition and tumour metastasis by PAR-complex-mediated SNAI1 degradation. *Nature Cell Biology*.

Käfer, J., Hayashi, T., Marée, A. F. M., Carthew, R. W., & Graner, F. (2007). Cell adhesion and cortex contractility determine cell patterning in the Drosophila retina. *Proceedings of the National Academy of Sciences of the United States of America*.

Kalinina, J., Dutta, K., Ilghari, D., Beenken, A., Goetz, R., Eliseenkova, A. V., Cowburn, D., & Mohammadi, M. (2012). The alternatively spliced acid box region plays a key role in FGF receptor autoinhibition. *Structure*.

Kapsimali, M. (2017). Epithelial cell behaviours during neurosensory organ formation. *Development (Cambridge)*.

Katoh, M. (2012). Function and cancer genomics of FAT family genes. In *International Journal of Oncology*.

Kemphues, K. J., Priess, J. R., Morton, D. G., & Cheng, N. (1988). Identification of genes required for cytoplasmic localization in early C. elegans embryos. *Cell*.

Kim, & Bar-Sagi, D. (2004). Modulation of signalling by Sprouty: a developing story. *Nature Reviews Molecular Cell Biology*, *5*(6), 441–450.

Kim, H. Y., Jackson, T. R., & Davidson, L. A. (2016). On the role of mechanics in driving mesenchymal-to-epithelial transitions. *Seminars in Cell and Developmental Biology*, 1–10.

Kim, H. Y., Jackson, T. R., Stuckenholz, C., & Davidson, L. A. (2020). Tissue mechanics drives regeneration of a mucociliated epidermis on the surface of Xenopus embryonic aggregates. *Nature Communications*, *11*(1), 1–10.

Kimmel, C. B., Ballard, W. W., Kimmel, S. R., Ullmann, B., & Schilling, T. F. (1995). Stages of embryonic development of the zebrafish. *Developmental Dynamics*.

Kirchgeorg, L., Felker, A., van Oostrom, M., Chiavacci, E., & Mosimann, C. (2018). Cre/lox-controlled spatiotemporal perturbation of FGF signaling in zebrafish. *Developmental Dynamics*, *247*(10), 1146–1159.

Kitazawa, K., Hikichi, T., Nakamura, T., Mitsunaga, K., Tanaka, A., Nakamura, M., Yamakawa, T., Furukawa, S., Takasaka, M., Goshima, N., Watanabe, A., Okita, K., Kawasaki, S., Ueno, M., Kinoshita, S., & Masui, S. (2016). OVOL2 Maintains the Transcriptional Program of Human Corneal Epithelium by Suppressing Epithelial-to-Mesenchymal Transition. *Cell Reports*.

Klein, T., & Arias, A. M. (1999). The Vestigial gene product provides a molecular context for the interpretation of signals during the development of the wing in Drosophila. *Development*, *126*(5), 913–925.

Kluyver, T., Ragan-kelley, B., Pérez, F., Granger, B., Bussonnier, M., Frederic, J., Kelley, K., Hamrick, J., Grout, J., Corlay, S., Ivanov, P., Avila, D., Abdalla, S., & Willing, C. (2016). Jupyter Notebooks—a publishing format for reproducible computational workflows. In *Positioning and Power in Academic Publishing: Players, Agents and Agendas*.

Kniss, J. S., Jiang, L., & Piotrowski, T. (2016). Insights into sensory hair cell regeneration from the zebrafish lateral line. In *Current Opinion in Genetics and Development*.

Knutsdottir, H., Zmurchok, C., Bhaskar, D., Palsson, E., Dalle Nogare, D., Chitnis, A. B., & Edelstein-Keshet,

L. (2017). Polarization and migration in the zebrafish posterior lateral line system. *PLoS Computational Biology*, *13*(4), 1–26.

Kon, E., Calvo-Jiménez, E., Cossard, A., Na, Y., Cooper, J. A., & Jossin, Y. (2019). N-cadherin-regulated FGFR ubiquitination and degradation control mammalian neocortical projection neuron migration. *ELife*.

Korotkevich, E., Niwayama, R., Courtois, A., Friese, S., Berger, N., Buchholz, F., & Hiiragi, T. (2017). The Apical Domain Is Required and Sufficient for the First Lineage Segregation in the Mouse Embryo. *Developmental Cell*, *40*(3), 235-247.e7.

Kouhara, H., Hadari, Y. R., Spivak-Kroizman, T., Schilling, J., Bar-Sagi, D., Lax, I., & Schlessinger, J. (1997). A lipid-anchored Grb2-binding protein that links FGF-receptor activation to the Ras/MAPK signaling pathway. *Cell*.

Krens, S. F. G., & Heisenberg, C. P. (2011). Cell Sorting in Development. In *Current Topics in Developmental Biology* (1st ed., Vol. 95). Elsevier Inc.

Krens, S. F. G., Veldhuis, J. H., Barone, V., Čapek, D., Maître, J. L., Brodland, G. W., & Heisenberg, C. P. (2017). Interstitial fluid osmolarity modulates the action of differential tissue surface tension in progenitor cell segregation during gastrulation. *Development*, *144*(10), 1798–1806.

Krieg, M., Arboleda-Estudillo, Y., Puech, P. H., Käfer, J., Graner, F., Müller, D. J., & Heisenberg, C. P. (2008). Tensile forces govern germ-layer organization in zebrafish. *Nature Cell Biology*, *10*(4), 429–436.

Krueger, D., Izquierdo, E., Viswanathan, R., Hartmann, J., Cartes, C. P., & de Renzis, S. (2019). Principles and applications of optogenetics in developmental biology. *Development (Cambridge)*.

Kuo, C. S., & Krasnow, M. A. (2015). Formation of a Neurosensory Organ by Epithelial Cell Slithering. *Cell*, *163*(2), 394–405.

Kwan, K. M., Fujimoto, E., Grabher, C., Mangum, B. D., Hardy, M. E., Campbell, D. S., Parant, J. M., Yost, H. J., Kanki, J. P., & Chien, C. (2007). *The Tol2kit : A Multisite Gateway-Based Construction Kit for Tol2 Transposon Transgenesis Constructs*. *October*, 3088–3099.

Kwon, H. J., & Riley, B. B. (2009). Mesendodermal signals required for otic induction: Bmp-antagonists cooperate with Fgf and can facilitate formation of ectopic otic tissue. *Developmental Dynamics*.

Lamouille, S., Subramanyam, D., Blelloch, R., & Derynck, R. (2013). Regulation of epithelial-mesenchymal and mesenchymal-epithelial transitions by microRNAs. In *Current Opinion in Cell Biology*.

Lancaster, M. A., & Knoblich, J. A. (2014). Organogenesis in a dish: Modeling development and disease using organoid technologies. *Science*, *345*(6194).

Laprise, P., Lau, K. M., Harris, K. P., Silva-Gagliardi, N. F., Paul, S. M., Beronja, S., Beitel, G. J., McGlade, C. J., & Tepass, U. (2009). Yurt, Coracle, Neurexin IV and the Na+, K+-ATPase form a novel group of epithelial polarity proteins. *Nature*.

Lau, S., Feitzinger, A., Venkiteswaran, G., Wang, J., Lewellis, S. W., Koplinski, C. A., Peterson, F. C., Volkman, B. F., Meier-Schellersheim, M., & Knaut, H. (2020). A negative-feedback loop maintains optimal chemokine concentrations for directional cell migration. *Nature Cell Biology*, *22*(3), 266–273.

Lawrence, P. A. (1966). Development and determination of hairs and bristles in the milkweed bug, Oncopeltus fasciatus (Lygaeidae, Hemiptera). *Journal of Cell Science*.

Lebreton, G., & Casanova, J. (2016). Ligand-binding and constitutive FGF receptors in single Drosophila tracheal cells: Implications for the role of FGF in collective migration. *Developmental Dynamics*, *245*(3), 372–378.

Lecaudey, V., Cakan-Akdogan, G., Norton, W. H. J., & Gilmour, D. (2008). Dynamic Fgf signaling couples morphogenesis and migration in the zebrafish lateral line primordium. *Development*, *2705*, 2695–2705.

Leckband, D. E., & de Rooij, J. (2014). Cadherin adhesion and mechanotransduction. In *Annual review of cell and developmental biology*.

Lee, B., Villarreal-Ponce, A., Fallahi, M., Ovadia, J., Sun, P., Yu, Q. C., Ito, S., Sinha, S., Nie, Q., & Dai, X. (2014). Transcriptional mechanisms link epithelial plasticity to adhesion and differentiation of epidermal progenitor cells. *Developmental Cell*.

Lee, Huang, M., Obholzer, N. D., Sun, S., Li, W., Petrillo, M., Dai, P., Zhou, Y., Cotanche, D. A., Megason, S. G., Li, H., & Chen, Z.-Y. (2016). Myc and Fgf Are Required for Zebrafish Neuromast Hair Cell Regeneration. *PLoS ONE*. https://www.ncbi.nlm.nih.gov/pmc/articles/PMC4924856/pdf/pone.0157768.pdf

Lee, T., Hacohen, N., Krasnow, M., & Montell, D. J. (1996). Regulated breathless receptor tyrosine kinase activity required to pattern cell migration and branching in the Drosophila tracheal system. *Genes and Development*, *10*(22), 2912–2921.

Lee, Y. S., Stott, N. S., Jiang, T. X., Widelitz, R. B., & Chuong, C. M. (1998). Early Events During Precartilage Condensation in Limb Bud Micromass Cultures (Review Paper). *ECM Journal*, *8*, 19.

Legland, D., Arganda-Carreras, I., & Andrey, P. (2016). MorphoLibJ: Integrated library and plugins for mathematical morphology with ImageJ. *Bioinformatics*, *32*(22), 3532–3534.

Leung, C. Y., & Zernicka-Goetz, M. (2013). Angiomotin prevents pluripotent lineage differentiation in mouse embryos via Hippo pathway-dependent and-independent mechanisms. *Nature Communications*.

Leung, Y. F., Ma, P., & Dowling, J. E. (2007). Gene expression profiling of zebrafish embryonic retinal pigment epithelium in vivo. *Investigative Ophthalmology and Visual Science*.

Li, Hutchins, A. P., Chen, Y., Li, S., Shan, Y., Liao, B., Zheng, D., Shi, X., Li, Y., Chan, W. Y., Pan, G., Wei, S., Shu, X., & Pei, D. (2017). A sequential EMT-MET mechanism drives the differentiation of human embryonic stem cells towards hepatocytes. *Nature Communications*, *8*(May), 1–12.

Li, Pei, D., & Zheng, H. (2014). Transitions between epithelial and mesenchymal states during cell fate conversions. *Protein and Cell*, *5*(8), 580–591.

Li, R., Liang, J., Ni, S., Zhou, T., Qing, X., Li, H., He, W., Chen, J., Li, F., Zhuang, Q., Qin, B., Xu, J., Li, W., Yang, J., Gan, Y., Qin, D., Feng, S., Song, H., Yang, D., … Pei, D. (2010). A mesenchymal-to-Epithelial transition initiates and is required for the nuclear reprogramming of mouse fibroblasts. *Cell Stem Cell*.

Lim, J., & Thiery, J. P. (2012). Epithelial-mesenchymal transitions : insights from development. *Development*, *3486*, 3471–3486.

Lin, C. C., Melo, F. A., Ghosh, R., Suen, K. M., Stagg, L. J., Kirkpatrick, J., Arold, S. T., Ahmed, Z., & Ladbury, J. E. (2012). Inhibition of basal FGF receptor signaling by dimeric Grb2. *Cell*.

Liu, Q., Ensign, R. D., & Azodi, E. (2003). Cadherin-1, -2 and -4 expression in the cranial ganglia and lateral line system of developing zebrafish. *Gene Expression Patterns*.

Liu, X., Sun, H., Qi, J., Wang, L., He, S., Liu, J., Feng, C., Chen, C., Li, W., Guo, Y., Qin, D., Pan, G., Chen, J., Pei, D., & Zheng, H. (2013). Sequential introduction of reprogramming factors reveals a time-sensitive requirement for individual factors and a sequential EMT-MET mechanism for optimal reprogramming. *Nature Cell Biology*.

Lopez-Schier, H., & Hudspeth, A. J. (2005). Supernumerary neuromasts in the posterior lateral line of zebrafish lacking peripheral glia. *Proceedings of the National Academy of Sciences of the United States of America*. https://www.ncbi.nlm.nih.gov/pmc/articles/PMC547829/pdf/pnas-0409361102.pdf

Lorentzen, A., Becker, P. F., Kosla, J., Saini, M., Weidele, K., Ronchi, P., Klein, C., Wolf, M. J., Geist, F., Seubert, B., Ringelhan, M., Mihic-Probst, D., Esser, K., Roblek, M., Kuehne, F., Bianco, G., O'Connor, T., Müller, Q., Schuck, K., … Heikenwalder, M. (2018). Single cell polarity in liquid phase facilitates tumour metastasis. *Nature Communications*.

Lujan, P., Rubio, T., Varsano, G., & Köhn, M. (2017). Keep it on the edge: The post-mitotic midbody as a polarity signal unit. *Communicative & Integrative Biology*, *10*(4), e1338990.

Lush, M. E., Diaz, D. C., Koenecke, N., Baek, S., Boldt, H., St Peter, M. K., Gaitan-Escudero, T., Romero-Carvajal, A., Busch-Nentwich, E. M., Perera, A. G., Hall, K. E., Peak, A., Haug, J. S., & Piotrowski, T. (2019). scRNA-Seq reveals distinct stem cell populations that drive hair cell regeneration after loss of Fgf and Notch signaling. *ELife*, *8*, 1–31.

Lush, M. E., & Piotrowski, T. (2014a). ErbB expressing Schwann cells control lateral line progenitor cells via non-cell-autonomous regulation of Wnt/β-catenin. *ELife*, *3*.

Lush, M. E., & Piotrowski, T. (2014b). ErbB expressing Schwann cells control lateral line progenitor cells via non-cell-autonomous regulation of Wnt/β-catenin. *ELife*, *2014*(3).

Ma, E. Y., & Raible, D. W. (2009). Signaling Pathways Regulating Zebrafish Lateral Line Development. In *Current Biology*.

Ma, E. Y., Rubel, E. W., & Raible, D. W. (2008). Notch signaling regulates the extent of hair cell regeneration in the zebrafish lateral line. *Journal of Neuroscience*.

MacArthur, C. A., Lawshe, A., Xu, J., Santos-Ocampo, S., Heikinheimo, M., Chellaiah, A. T., & Ornitz, D. M. (1995). FGF-8 isoforms activate receptor splice forms that are expressed in mesenchymal regions of mouse development. *Development*.

Mackenzie, S. M., & Raible, D. W. (2012). Proliferative Regeneration of Zebrafish Lateral Line Hair Cells after Different Ototoxic Insults. *PLoS ONE*, *7*(10), 1–8.

Mahoney, P. A., Weber, U., Onofrechuk, P., Biessmann, H., Bryant, P. J., & Goodman, C. S. (1991). The fat tumor suppressor gene in Drosophila encodes a novel member of the cadherin gene superfamily. *Cell*.

Maître, J. L., Berthoumieux, H., Krens, S. F. G., Salbreux, G., Jülicher, F., Paluch, E., & Heisenberg, C. P. (2012). Adhesion functions in cell sorting by mechanically coupling the cortices of adhering cells. *Science*, *338*(6104), 253–256.

Maître, J. L., & Heisenberg, C. P. (2011). The role of adhesion energy in controlling cell-cell contacts. In *Current Opinion in Cell Biology*.

Maître, J. L., Niwayama, R., Turlier, H., Nedelec, F., & Hiiragi, T. (2015). Pulsatile cell-autonomous contractility drives compaction in the mouse embryo. *Nature Cell Biology*.

Maître, J. L., Salbreux, G., Jülicher, F., Paluch, E., & Heisenberg, C. (2012). Adhesion Functions in Cell Sorting by of Adhering Cells. *Science*, *253*(October), 253–257.

Maître, J. L., Turlier, H., Illukkumbura, R., Eismann, B., Niwayama, R., Nédélec, F., & Hiiragi, T. (2016). Asymmetric division of contractile domains couples cell positioning and fate specification. *Nature*, *536*(7616), 344–348.

Makarenkova, H. P., Hoffman, M. P., Beenken, A., Eliseenkova, A. V., Meech, R., Tsau, C., Patel, V. N., Lang,

R. A., & Mohammadi, M. (2009). Differential interactions of FGFs with heparan sulfate control gradient formation and branching morphogenesis. *Science Signaling*.

Mammoto, T., Mammoto, A., Jiang, A., Jiang, E., Hashmi, B., & Ingber, D. E. (2015). Mesenchymal condensation-dependent accumulation of collagen VI stabilizes organ-specific cell fates during embryonic tooth formation. *Developmental Dynamics*.

Manjón, C., Sánchez-Herrero, E., & Suzanne, M. (2007). Sharp boundaries of Dpp signalling trigger local cell death required for Drosophila leg morphogenesis. *Nature Cell Biology*, *9*(1), 57–63.

Manninen, A. (2015). Epithelial polarity - Generating and integrating signals from the ECM with integrins. In *Experimental Cell Research*.

Manning, B. D., & Cantley, L. C. (2007). AKT/PKB Signaling: Navigating Downstream. In *Cell*.

Marciano, D. K. (2017). A holey pursuit: lumen formation in the developing kidney. *Pediatric Nephrology*, *32*(1), 7–20.

Margaron, Y., Nagai, T., Guyon, L., Kurzawa, L., & Théry, M. (2019). *Biophysical properties of intermediate states of EMT outperform both epithelial and mesenchymal states* .

Martin-Belmonte, F., & Mostov, K. (2007). Phosphoinositides Control Epithelial Development. *Cell Cycle*.

Mason, I. (2007). Initiation to end point: The multiple roles of fibroblast growth factors in neural development. In *Nature Reviews Neuroscience*.

Matsuda, M., & Chitnis, A. B. (2010). Atoh1a expression must be restricted by Notch signaling for effective morphogenesis of the posterior lateral line primordium in zebrafish. *Development*, *137*(20), 3477–3487.

Matsuda, M., Dalle Nogare, D., Somers, K., Martin, K., Wang, C., & Chitnis, A. B. (2012). Lef1 regulates dusp6 to influence neuromast formation and spacing in the zebrafish posterior lateral line primordium. *Development (Cambridge)*.

Matsui, T., Ishikawa, H., & Bessho, Y. (2015). Cell collectivity regulation within migrating cell cluster during Kupffer's vesicle formation in zebrafish. In *Frontiers in Cell and Developmental Biology*.

Matsui, T., Thitamadee, S., Murata, T., Kakinuma, H., Nabetani, T., Hirabayashi, Y., Hirate, Y., Okamotob, H., & Bessho, Y. (2011). Canopy1, a positive feedback regulator of FGF signaling, controls progenitor cell clustering during Kupffer's vesicle organogenesis. *Proceedings of the National Academy of Sciences of the United States of America*, *108*(24), 9881–9886.

Matsuo, I., & Kimura-Yoshida, C. (2013). Extracellular modulation of Fibroblast Growth Factor signaling through heparan sulfate proteoglycans in mammalian development. In *Current Opinion in Genetics and Development*.

McAvoy, J. W., & Chamberlain, C. G. (1989). Fibroblast growth factor (FGF) induces different responses in lens epithelial cells depending on its concentration. *Development*, *107*(2), 221–228.

McBeath, R., Pirone, D. M., Nelson, C. M., Bhadriraju, K., & Chen, C. S. (2004). Cell shape, cytoskeletal tension, and RhoA regulate stem cell lineage commitment. *Developmental Cell*.

McGraw, H. F., Drerup, C. M., Culbertson, M. D., Linbo, T., Raible, D. W., & Nechiporuk, A. V. (2011). Lef1 is required for progenitor cell identity in the zebrafish lateral line primordium. *Development*.

Meenderink, L. M., Gaeta, I. M., Postema, M. M., Cencer, C. S., Chinowsky, C. R., Krystofiak, E. S., Millis, B. A., & Tyska, M. J. (2019). Actin Dynamics Drive Microvillar Motility and Clustering during Brush Border

Assembly. *Developmental Cell*, *50*(5), 545-556.e4.

Meilhac, S. M., Adams, R. J., Morris, S. A., Danckaert, A., Le Garrec, J. F., & Zernicka-Goetz, M. (2009). Active cell movements coupled to positional induction are involved in lineage segregation in the mouse blastocyst. *Developmental Biology*.

Miesfeld, J. B., Gestri, G., Clark, B. S., Flinn, M. A., Poole, R. J., Bader, J. R., Besharse, J. C., Wilson, S. W., & Link, B. A. (2015). Yap and Taz regulate retinal pigment epithelial cell fate. *Development (Cambridge)*.

Millard, T. H., & Martin, P. (2008). Dynamic analysis of filopodial interactions during the zippering phase of Drosophila dorsal closure. *Development*.

Millimaki, B. B., Sweet, E. M., Dhason, M. S., & Riley, B. B. (2007). Zebrafish atoh1 genes: Classic proneural activity in the inner ear and regulation by Fgh and Notch. *Development*.

Min, H., Danilenko, D. M., Scully, S. A., Bolon, B., Ring, B. D., Tarpley, J. E., DeRose, M., & Simonet, W. S. (1998). Fgf-10 is required for both limb and lung development and exhibits striking functional similarity to Drosophila branchless. *Genes and Development*.

Miyatani, S., Shimamura, K., Hatta, M., Nagafuchi, A., Nose, A., Matsunaga, M., Hatta, K., & Takeichi, M. (1989). Neural cadherin: Role in selective cell-cell adhesion. *Science*.

Mongera, A., Rowghanian, P., Gustafson, H. J., Kealhofer, D. A., Carn, E. K., Serwane, F., Adam, A., Giammona, J., & Campàs, O. (2019). A fluid-to-solid jamming transition underlies vertebrate body axis Elongation. *Nature*, *561*(7723), 401–405.

Monier, B., Gettings, M., Gay, G., Mangeat, T., Schott, S., Guarner, A., & Suzanne, M. (2015). Apico-basal forces exerted by apoptotic cells drive epithelium folding. *Nature*, *518*(7538), 245–248.

Moore, R., Cai, K. Q., Escudero, D. O., & Xu, X. X. (2009). Cell adhesive affinity does not dictate primitive endoderm segregation and positioning during murine embryoid body formation. *Genesis*.

Moreno-Mateos, M. A., Vejnar, C. E., Beaudoin, J. D., Fernandez, J. P., Mis, E. K., Khokha, M. K., & Giraldez, A. J. (2015). CRISPRscan: Designing highly efficient sgRNAs for CRISPR-Cas9 targeting in vivo. *Nature Methods*.

Morsut, L., Roybal, K. T., Xiong, X., Gordley, R. M., Coyle, S. M., Thomson, M., & Lim, W. A. (2016). Engineering Customized Cell Sensing and Response Behaviors Using Synthetic Notch Receptors. *Cell*.

Moscona, A. A. (1962). Analysis of cell recombinations in experimental synthesis of tissuesin vitro. *Journal of Cellular and Comparative Physiology*.

Münster, S., Jain, A., Mietke, A., Pavlopoulos, A., Grill, S. W., & Tomancak, P. (2019). Attachment of the blastoderm to the vitelline envelope affects gastrulation of insects. *Nature*.

Naoki, H., & Matsui, T. (2020). Somite boundary determination in normal and clock-less vertebrate embryos. In *Development Growth and Differentiation*.

Nechiporuk, A., & Raible, D. W. (2008). FGF-dependent mechanosensory organ patterning in zebrafish. *Science*.

Nelemans, B. K. A., Schmitz, M., Tahir, H., Merks, R. M. H., & Smit, T. H. (2020). Somite Division and New Boundary Formation by Mechanical Strain. *IScience*, *23*(4), 100976.

Nerurkar, N. L., Lee, C. H., Mahadevan, L., & Tabin, C. J. (2019). Molecular control of macroscopic forces drives formation of the vertebrate hindgut. *Nature*, *565*(7740), 480–484.

Nguyen, T., Duchesne, L., Sankara Narayana, G. H. N., Boggetto, N., Fernig, D. D., Uttamrao Murade, C.,

Ladoux, B., & Mège, R. M. (2019). Enhanced cell–cell contact stability and decreased N-cadherin-mediated migration upon fibroblast growth factor receptor-N-cadherin cross talk. *Oncogene*, *38*(35), 6283–6300.

Nieto, M. A., Huang, R. Y., Jackson, R. A., & Thiery, J. P. (2016). *Review EMT : 2016*. 21–45.

Ninomiya, H., David, R., Damm, E. W., Fagotto, F., Niessen, C. M., & Winklbauer, R. (2012). Cadherin-dependent differential cell adhesion in xenopus causes cell sorting in vitro but not in the embryo. *Journal of Cell Science*.

Nishimura, T., & Takeichi, M. (2008). Shroom3-mediated recruitment of Rho kinases to the apical cell junctions regulates epithelial and neuroepithelial planar remodeling. *Development*.

Nobuyuki Otsu. (1979). A Threshold Selection Method from Gray-Level Histograms. *IEEE Trans. Syst. Man Cybern*.

Nogare, D. D., Somers, K., Rao, S., Matsuda, M., Reichman-Fried, M., Raz, E., & Chitnis, A. B. (2014). Leading and trailing cells cooperate in collective migration of the zebrafish posterior lateral line primordium. *Development (Cambridge)*.

Noguchi, M., Sumiyama, K., & Morimoto, M. (2015). Directed Migration of Pulmonary Neuroendocrine Cells toward Airway Branches Organizes the Stereotypic Location of Neuroepithelial Bodies. *Cell Reports*, *13*(12), 2679–2686.

Norton, W. H. J., Ledin, J., Grandel, H., & Neumann, C. J. (2005). HSPG synthesis by zebrafish Ext2 and Extl3 is required for Fgf10 signalling during limb development. *Development*.

Nose, A., Nagafuchi, A., & Takeichi, M. (1988). Expressed recombinant cadherins mediate cell sorting in model systems. *Cell*.

Nowak, M., MacHate, A., Yu, S. R., Gupta, M., & Brand, M. (2011). Interpretation of the FGF8 morphogen gradient is regulated by endocytic trafficking. *Nature Cell Biology*.

Nuñez, V. A., Sarrazin, A. F., Cubedo, N., Allende, M. L., Dambly-Chaudière, C., & Ghysen, A. (2009). Postembryonic development of the posterior lateral line in the zebrafish. *Evolution and Development*, *11*(4), 391–404.

Nüsslein-Volhard, C., & Dahm, R. (2002). *Zebrafish: A Practical Approach* (Issue 975). Oxford University Press.

O'Brien, L. E., Jou, T. S., Pollack, A. L., Zhang, Q., Hansen, S. H., Yurchenco, P., & Mostov, K. E. (2001). Rac1 orientates epithelial apical polarity through effects on basolateral laminin assembly. *Nature Cell Biology*.

Oates, A. C., Morelli, L. G., & Ares, S. (2012). Patterning embryos with oscillations: Structure, function and dynamics of the vertebrate segmentation clock. In *Development*.

Oginuma, M., Moncuquet, P., Xiong, F., Karoly, E., Chal, J., Guevorkian, K., & Pourquié, O. (2017). A Gradient of Glycolytic Activity Coordinates FGF and Wnt Signaling during Elongation of the Body Axis in Amniote Embryos. *Developmental Cell*.

Oliphant, T., & Millma, J. k. (2006). A guide to NumPy. In *Trelgol Publishing*.

Ornitz, D. M. (2000). FGFs, heparan sulfate and FGFRs: Complex interactions essential for development. *BioEssays*.

Oteíza, P., Köppen, M., Concha, M. L., & Heisenberg, C. P. (2008). Origin and shaping of the laterality organ

in zebrafish. *Development*, *135*(16), 2807–2813.

Packard, A., Georgas, K., Michos, O., Riccio, P., Cebrian, C., Combes, A. N., Ju, A., Ferrer-Vaquer, A., Hadjantonakis, A. K., Zong, H., Little, M. H., & Costantini, F. (2013). Luminal Mitosis Drives Epithelial Cell Dispersal within the Branching Ureteric Bud. *Developmental Cell*.

Parslow, A., Cardona, A., & Bryson-Richardson, R. J. (2014). Sample drift correction following 4D confocal time-lapse Imaging. *Journal of Visualized Experiments*.

Pei, D., Shu, X., Gassama-diagne, A., & Thiery, J. P. (2019). Mesenchymal–epithelial transition in development and reprogramming. *Nature Cell Biology*, *21*(January).

Peng, T., Frank, D. B., Kadzik, R. S., Morley, M. P., Rathi, K. S., Wang, T., Zhou, S., Cheng, L., Lu, M. M., & Morrisey, E. E. (2015). Hedgehog actively maintains adult lung quiescence and regulates repair and regeneration. *Nature*.

Perlin, J. R., Lush, M. E., Zac Stephens, W., Piotrowski, T., & Talbot, W. S. (2011). Neuronal neuregulin 1 type III directs schwann cell migration. *Development*.

Peters, K. G., Werner, S., Chen, G., & Williams, L. T. (1992). Two FGF receptor genes are differentially expressed in epithelial and mesenchymal tissues during limb formation and organogenesis in the mouse. *Development*.

Peterson, S. J., & Krasnow, M. A. (2015). Subcellular trafficking of FGF controls tracheal invasion of Drosophila flight muscle. *Cell*.

Petridou, N. I., Spiró, Z., & Heisenberg, C.-P. (2017). Multiscale force sensing in development. *Nature Publishing Group*, *19*.

Pinto-Teixeira, F., Viader-Llargués, O., Torres-Mejía, E., Turan, M., González-Gualda, E., Pola-Morell, L., & Lopez-Schier, H. (2015). Inexhaustible hair-cell regeneration in young and aged zebrafish. *Biology Open*.

Pirvola, U., Ylikoski, J., Trokovic, R., Hébert, J. M., McConnell, S. K., & Partanen, J. (2002). FGFR1 is required for the development of the auditory sensory epithelium. *Neuron*.

Plusa, B., Piliszek, A., Frankenberg, S., Artus, J., & Hadjantonakis, A. K. (2008). Distinct sequential cell behaviours direct primitive endoderm formation in the mouse blastocyst. *Development*.

Politi, A. Z., Cai, Y., Walther, N., Hossain, M. J., Koch, B., Wachsmuth, M., & Ellenberg, J. (2018). Quantitative mapping of fluorescently tagged cellular proteins using FCS-calibrated four-dimensional imaging. *Nature Protocols*.

Preibisch, S., Saalfeld, S., & Tomancak, P. (2009). Globally optimal stitching of tiled 3D microscopic image acquisitions. *Bioinformatics*.

Price, S. R., De Marco Garcia, N. V., Ranscht, B., & Jessell, T. M. (2002). Regulation of motor neuron pool sorting by differential expression of type II cadherins. *Cell*.

Raible, F., & Brand, M. (2001). Tight transcriptional control of the ETS domain factors Erm and Pea3 by Fgf signaling during early zebrafish development. *Mechanisms of Development*.

Raj, A., van den Bogaard, P., Rifkin, S. A., van Oudenaarden, A., & Tyagi, S. (2008). Imaging individual mRNA molecules using multiple singly labeled probes. *Nature Methods*.

Rauzi, M., Lenne, P. F., & Lecuit, T. (2010). Planar polarized actomyosin contractile flows control epithelial junction remodelling. *Nature*.

Ray, H. J., & Niswander, L. A. (2016). Grainyhead-like 2 downstream targets act to suppress epithelialto-mesenchymal transition during neural tube closure. *Development (Cambridge)*.

Raz, E., & Mahabaleshwar, H. (2009). Chemokine signaling in embryonic cell migration: A fisheye view. In *Development*.

Reichman-Fried, M., Dickson, B., Hafen, E., & Shilo, B. Z. (1994). Elucidation of the role of breathless, a Drosophila FGF receptor homolog, in tracheal cell migration. *Genes and Development*.

Repina, N. A., Bao, X., Zimmermann, J. A., Joy, D. A., Kane, R. S., & Schaffer, D. V. (2019). Optogenetic control of Wnt signaling for modeling early embryogenic patterning with human pluripotent stem cells. *BioRxiv*.

Revenu, C., Streichan, S., Donà, E., Lecaudey, V., Hufnagel, L., Gilmour, D., Aman, A., Piotrowski, T., Bacallao, R., Antony, C., Dotti, C., Karsenti, E., Stelzer, E. H., Simons, K., Borghi, N., Lowndes, M., Maruthamuthu, V., Gardel, M. L., Nelson, W. J., … Manley, S. W. (2014). Quantitative cell polarity imaging defines leader-to-follower transitions during collective migration and the key role of microtubule-dependent adherens junction formation. *Development (Cambridge, England)*, *141*(6), 1282–1291.

Rieu, J. P., Kataoka, N., & Sawada, Y. (1998). Quantitative analysis of cell motion during sorting in two-dimensional aggregates of dissociated hydra cells. *Physical Review E - Statistical Physics, Plasmas, Fluids, and Related Interdisciplinary Topics*.

Roca, H., Hernandez, J., Weidner, S., McEachin, R. C., Fuller, D., Sud, S., Schumann, T., Wilkinson, J. E., Zaslavsky, A., Li, H., Maher, C. A., Daignault-Newton, S., Healy, P. N., & Pienta, K. J. (2013). Transcription Factors OVOL1 and OVOL2 Induce the Mesenchymal to Epithelial Transition in Human Cancer. *PLoS ONE*.

Rock, J. R., Onaitis, M. W., Rawlins, E. L., Lu, Y., Clark, C. P., Xue, Y., Randell, S. H., & Hogan, B. L. M. (2009). Basal cells as stem cells of the mouse trachea and human airway epithelium. *Proceedings of the National Academy of Sciences of the United States of America*.

Rodriguez-Boulan, E., & Macara, I. G. (2014). Organization and execution of the epithelial polarity programme. In *Nature Reviews Molecular Cell Biology*.

Rohani, N., Canty, L., Luu, O., Fagotto, F., & Winklbauer, R. (2011). EphrinB/EphB signaling controls embryonic germ layer separation by contact-induced cell detachment. *PLoS Biology*, *9*(3), 1–18.

Rojas-Muñoz, A., Rajadhyksha, S., Gilmour, D., van Bebber, F., Antos, C., Rodríguez Esteban, C., Nüsslein-Volhard, C., & Izpisúa Belmonte, J. C. (2009). ErbB2 and ErbB3 regulate amputation-induced proliferation and migration during vertebrate regeneration. *Developmental Biology*.

Romero-Carvajal, A., Navajas Acedo, J., Jiang, L., Kozlovskaja-Gumbriene, A., Alexander, R., Li, H., & Piotrowski, T. (2015). Regeneration of Sensory Hair Cells Requires Localized Interactions between the Notch and Wnt Pathways. *Developmental Cell*.

Röper, K. (2013). Supracellular actomyosin assemblies during development. *BioArchitecture*.

Rorth, P. (2012). Fellow travellers: Emergent properties of collective cell migration. In *EMBO Reports*.

Rowton, M., Ramos, P., Anderson, D. M., Rhee, J. M., Cunliffe, H. E., & Rawls, A. (2013). Regulation of mesenchymal-to-epithelial transition by PARAXIS during somitogenesis. *Developmental Dynamics*, *242*(11), 1332–1344.

Ryan, A. Q., Chan, C. J., Graner, F., & Hiiragi, T. (2019). Lumen Expansion Facilitates Epiblast-Primitive Endoderm Fate Specification during Mouse Blastocyst Formation. *Developmental Cell*.

Ryding, A. D. S., Sharp, M. G. F., & Mullins, J. J. (2001). Conditional transgenic technologies. In *Journal of Endocrinology*.

Sai, X. R., & Ladher, R. K. (2008). FGF Signaling Regulates Cytoskeletal Remodeling during Epithelial Morphogenesis. *Current Biology*.

Saiz, N., Grabarek, J. B., Sabherwal, N., Papalopulu, N., & Plusa, B. (2013). Atypical protein kinase C couples cell sorting with primitive endoderm maturation in the mouse blastocyst. *Development (Cambridge)*.

Samavarchi-Tehrani, P., Golipour, A., David, L., Sung, H. K., Beyer, T. A., Datti, A., Woltjen, K., Nagy, A., & Wrana, J. L. (2010). Functional genomics reveals a BMP-Driven mesenchymal-to-Epithelial transition in the initiation of somatic cell reprogramming. *Cell Stem Cell*.

Sanchez-Heras, E., Howell, F. V., Williams, G., & Doherty, P. (2006). The fibroblast growth factor receptor acid box is essential for interactions with N-cadherin and all of the major isoforms of neural cell adhesion molecule. *Journal of Biological Chemistry*.

Sánchez, M., Ceci, M. L., Gutiérrez, D., Anguita-Salinas, C., & Allende, M. L. (2016). Mechanosensory organ regeneration in zebrafish depends on a population of multipotent progenitor cells kept latent by Schwann cells. *BMC Biology*, *14*.

Sapède, D., Gompel, N., Dambly-Chaudière, C., & Ghysen, A. (2002). Cell migration in the postembryonic development of the fish lateral line. *Development*.

Sarabipour, S., & Hristova, K. (2016). Mechanism of FGF receptor dimerization and activation. *Nature Communications*.

Sato, M., & Kornberg, T. B. (2002). FGF is an essential mitogen and chemoattractant for the air sacs of the Drosophila tracheal system. *Developmental Cell*.

Sawada, A., Shinya, M., Jiang, Y. J., Kawakami, A., Kuroiwa, A., & Takeda, H. (2001). Fgf/MAPK signalling is a crucial positional cue in somite boundary formation. *Development*.

Sawilowsky, S. S. (2009). New Effect Size Rules of Thumb. *Journal of Modern Applied Statistical Methods*.

Scarpa, E., Szabó, A., Bibonne, A., Theveneau, E., Parsons, M., & Mayor, R. (2015). Cadherin Switch during EMT in Neural Crest Cells Leads to Contact Inhibition of Locomotion via Repolarization of Forces. *Developmental Cell*, *34*(4), 421–434.

Schindelin, J., Arganda-Carreras, I., Frise, E., Kaynig, V., Longair, M., Pietzsch, T., Preibisch, S., Rueden, C., Saalfeld, S., Schmid, B., Tinevez, J. Y., White, D. J., Hartenstein, V., Eliceiri, K., Tomancak, P., & Cardona, A. (2012). Fiji: An open-source platform for biological-image analysis. In *Nature Methods*.

Schlosser, G. (2006). Induction and specification of cranial placodes. In *Developmental Biology*.

Schlüter, M. A., & Margolis, B. (2009). Apical lumen formation in renal epithelia. In *Journal of the American Society of Nephrology*.

Schmidt, C., Stoeckelhuber, M., McKinnell, I., Putz, R., Christ, B., & Patel, K. (2004). Wnt 6 regulates the epithelialisation process of the segmental plate mesoderm leading to somite formation. *Developmental Biology*.

Sedzinski, J., Hannezo, E., Tu, F., Biro, M., & Wallingford, J. B. (2016). Emergence of an Apical Epithelial Cell Surface In Vivo. *Developmental Cell*, 24–35.

Sekine, K., Ohuchi, H., Fujiwara, M., Yamasaki, M., Yoshizawa, T., Sato, T., Yagishita, N., Matsui, D., Koga, Y., Itoh, N., & Kato, S. (1999). Fgf10 is essential for limb and lung formation. *Nature Genetics*.

Seleit, A., Krämer, I., Riebesehl, B. F., Ambrosio, E. M., Stolper, J. S., Lischik, C. Q., Dross, N., & Centanin, L. (2017). Neural stem cells induce the formation of their physical niche during organogenesis. *ELife*. https://www.ncbi.nlm.nih.gov/pmc/articles/PMC5617629/pdf/elife-29173.pdf

Serra, D., Mayr, U., Boni, A., Lukonin, I., Rempfler, M., Challet Meylan, L., Stadler, M. B., Strnad, P., Papasaikas, P., Vischi, D., Waldt, A., Roma, G., & Liberali, P. (2019). Self-organization and symmetry breaking in intestinal organoid development. *Nature*, *569*(7754), 66–72.

Serrano Nájera, G., & Weijer, C. J. (2020). Cellular processes driving gastrulation in the avian embryo. In *Mechanisms of Development*.

Shahbazi, M. N., Scialdone, A., Skorupska, N., Weberling, A., Recher, G., Zhu, M., Jedrusik, A., Devito, L. G., Noli, L., MacAulay, I. C., Buecker, C., Khalaf, Y., Ilic, D., Voet, T., Marioni, J. C., & Zernicka-Goetz, M. (2017). Pluripotent state transitions coordinate morphogenesis in mouse and human embryos. *Nature*.

Shaya, O., Binshtok, U., Hersch, M., Rivkin, D., Weinreb, S., Amir-Zilberstein, L., Khamaisi, B., Oppenheim, O., Desai, R. A., Goodyear, R. J., Richardson, G. P., Chen, C. S., & Sprinzak, D. (2017). Cell-Cell Contact Area Affects Notch Signaling and Notch-Dependent Patterning. *Developmental Cell*, *40*(5), 505-511.e6.

Shewan, A., Eastburn, D. J., & Mostov, K. (2011). Phosphoinositides in cell architecture. In *Cold Spring Harbor Perspectives in Biology*.

Shi, Y., Varner, V. D., & Taber, L. A. (2015). Why is cytoskeletal contraction required for cardiac fusion before but not after looping begins? *Physical Biology*.

Shibue, T., & Weinberg, R. A. (2011). Metastatic colonization: Settlement, adaptation and propagation of tumor cells in a foreign tissue environment. In *Seminars in Cancer Biology*.

Shih, J., & Keller, R. (1992). Cell motility driving mediolateralintercalation in explants of Xenopus laevis. *Development*.

Shimokawa, K., Kimura-Yoshida, C., Nagai, N., Mukai, K., Matsubara, K., Watanabe, H., Matsuda, Y., Mochida, K., & Matsuo, I. (2011). Cell Surface Heparan Sulfate Chains Regulate Local Reception of FGF Signaling in the Mouse Embryo. *Developmental Cell*.

Shirasaki, R., Lewcock, J. W., Lettieri, K., & Pfaff, S. L. (2006). FGF as a Target-Derived Chemoattractant for Developing Motor Axons Genetically Programmed by the LIM Code. *Neuron*.

Shotwell, S. L., Jacobs, R., & Hudspeth, A. J. (1981). Directional Sensitivity of Individual Vertebrate Hair Cells To Controlled Deflection of Their Hair Bundles. *Annals of the New York Academy of Sciences*, *374*(1), 1–10.

Shu, X., & Pei, D. (2014). The function and regulation of mesenchymal-to-epithelial transition in somatic cell reprogramming. *Current Opinion in Genetics and Development*, *28*, 32–37.

Shyer, A. E., Huycke, T. R., Mahadevan, L., Tabin, C. J., Shyer, A. E., Huycke, T. R., Lee, C., Mahadevan, L., & Tabin, C. J. (2015). Bending Gradients : How the Intestinal Stem Cell Gets Its Home. *Cell*, *161*(3), 569–580.

Shyer, A. E., Rodrigues, A. R., Schroeder, G. G., Kassianidou, E., Kumar, S., & Harland, R. M. (2017). Emergent cellular self-organization and mechanosensation initiate follicle pattern in the avian skin. *Science*, *357*(6353), 811–815.

Simsek, M. F., & Özbudak, E. M. (2018). Spatial Fold Change of FGF Signaling Encodes Positional Information

for Segmental Determination in Zebrafish. *Cell Reports*.

Slepecky, N. B., Henderson, C. G., & Saha, S. (1995). Post-translational modifications of tubulin suggest that dynamic microtubules are present in sensory cells and stable microtubules are present in supporting cells of the mammalian cochlea. *Hearing Research*.

Sommer, C., Straehle, C., Kothe, U., & Hamprecht, F. A. (2011). Ilastik: Interactive learning and segmentation toolkit. *Proceedings - International Symposium on Biomedical Imaging*.

Šošić, D., Brand-Saberi, B., Schmidt, C., Christ, B., & Olson, E. N. (1997). Regulation of paraxis expression and somite formation by ectoderm- and neural tube-derived signals. *Developmental Biology*.

Soulika, M. (2015). *In vivo analysis of the cellular interactions during taste sensory organ assembly in zebrafish*.

Soulika, M., Kaushik, A. L., Mathieu, B., Lourenço, R., Komisarczuk, A. Z., Romano, S. A., Jouary, A., Lardennois, A., Tissot, N., Okada, S., Abe, K., Becker, T. S., & Kapsimali, M. (2016). Diversity in cell motility reveals the dynamic nature of the formation of zebrafish taste sensory organs. *Development (Cambridge)*, *143*(11), 2012–2024.

Srinivas, S., & Rodriguez, T. A. (2017). A Tale of Division and Polarization in the Mammalian Embryo. *Developmental Cell*, *40*(3), 215–216.

Steinberg, M. S. (1970). Does differential adhesion govern self-assembly processes in histogenesis? Equilibrium configurations and the emergence of a hierarchy among populations of embryonic cells. *Journal of Experimental Zoology*.

Steinberg, M. S. (2007). Differential adhesion in morphogenesis: a modern view. In *Current Opinion in Genetics and Development*.

Steiner, A. B., Kim, T., Cabot, V., & Hudspeth, A. J. (2014). Dynamic gene expression by putative hair-cell progenitors during regeneration in the zebrafish lateral line. *Proceedings of the National Academy of Sciences of the United States of America*, *111*(14).

Stemmler, M. P., Eccles, R. L., Brabletz, S., & Brabletz, T. (2019). *Non-redundant functions of EMT transcription factors*. *21*(January).

Stephenson, R. O., Yamanaka, Y., & Rossant, J. (2010). Disorganized epithelial polarity and excess trophectoderm cell fate in preimplantation embryos lacking E-cadherin. *Development*.

Stubbs, J. L., Davidson, L., Keller, R., & Kintner, C. (2006). Radial intercalation of ciliated cells during Xenopus skin development. *Development*.

Su, W. C. S., Kitagawa, M., Xue, N., Xie, B., Garofalo, S., Cho, J., Deng, C., Horton, W. A., & Fu, X. Y. (1997). Activation of Stat1 by mutant fibroblast growth-factor receptor in thanatophoric dysplasia type II dwarfism. *Nature*.

Subramanyam, D., Lamouille, S., Judson, R. L., Liu, J. Y., Bucay, N., Derynck, R., & Blelloch, R. (2011). Multiple targets of miR-302 and miR-372 promote reprogramming of human fibroblasts to induced pluripotent stem cells. *Nature Biotechnology*.

Sugi, Y., & Markwald, R. R. (1996). Formation and early morphogenesis of endocardial endothelial precursor cells and the role of endoderm. *Developmental Biology*.

Sun, X., Meyers, E. N., Lewandoski, M., & Martin, G. R. (1999). Targeted disruption of Fgf8 causes failure of cell migration in the gastrulating mouse embryo. *Genes and Development*.

Sutherland, D., Samakovlis, C., & Krasnow, M. A. (1996). branchless encodes a Drosophila FGF homolog that controls tracheal cell migration and the pattern of branching. *Cell*.

Swift, J., Ivanovska, I. L., Buxboim, A., Harada, T., Dingal, P. C. D. P., Pinter, J., Pajerowski, J. D., Spinler, K. R., Shin, J. W., Tewari, M., Rehfeldt, F., Speicher, D. W., & Discher, D. E. (2013). Nuclear lamin-A scales with tissue stiffness and enhances matrix-directed differentiation. *Science*.

Takahashi, K., & Yamanaka, S. (2006). Induction of Pluripotent Stem Cells from Mouse Embryonic and Adult Fibroblast Cultures by Defined Factors. *Cell*.

Takaku, M., Grimm, S. A., Shimbo, T., Perera, L., Menafra, R., Stunnenberg, H. G., Archer, T. K., Machida, S., Kurumizaka, H., & Wade, P. A. (2016). GATA3-dependent cellular reprogramming requires activation-domain dependent recruitment of a chromatin remodeler. *Genome Biology*.

Tam, W. L., & Weinberg, R. A. (2013). The epigenetics of epithelial-mesenchymal plasticity in cancer. In *Nature Medicine*.

Tanaka, E. M. (2016). The Molecular and Cellular Choreography of Appendage Regeneration. In *Cell*.

Tang, N., & Marshall, W. F. (2012). Centrosome positioning in vertebrate development. In *Journal of Cell Science*.

Taniguchi, K., Shao, Y., Townshend, R. F., Cortez, C. L., Harris, C. E., Meshinchi, S., Kalantry, S., Fu, J., O'Shea, K. S., & Gumucio, D. L. (2017). An apicosome initiates self-organizing morphogenesis of human pluripotent stem cells. *Journal of Cell Biology*, *216*(12), 3981–3990.

Taniguchi, K., Shao, Y., Townshend, R. F., Tsai, Y. H., Delong, C. J., Lopez, S. A., Gayen, S., Freddo, A. M., Chue, D. J., Thomas, D. J., Spence, J. R., Margolis, B., Kalantry, S., Fu, J., O'Shea, K. S., & Gumucio, D. L. (2015). Lumen Formation Is an Intrinsic Property of Isolated Human Pluripotent Stem Cells. *Stem Cell Reports*.

Teruel, M. N., Blanpied, T. A., Shen, K., Augustine, G. J., & Meyer, T. (1999). *A versatile microporation technique for the transfection of cultured CNS neurons*. *93*, 37–48.

Thisse, B., & Thisse, C. (2005). Functions and regulations of fibroblast growth factor signaling during embryonic development. *Developmental Biology*.

Thisse, C., & Thisse, B. (2008). High-resolution in situ hybridization to whole-mount zebrafish embryos. *Nature Protocols*.

Thomas, F. C., Sheth, B., Eckert, J. J., Bazzoni, G., Dejana, E., & Fleming, T. P. (2004). Contribution of JAM-1 to epithelial differentiation and tight-junction biogenesis in the mouse preimplantation embryo. *Journal of Cell Science*, *117*(23), 5599–5608.

Thomas, & Raible, D. W. (2019). Distinct progenitor populations mediate regeneration in the zebrafish lateral line. *ELife*, *8*, 1–27.

Tomlinson, D. C., L'Hôte, C. G., Kennedy, W., Pitt, E., & Knowles, M. A. (2005). Alternative splicing of fibroblast growth factor receptor 3 produces a secreted isoform that inhibits fibroblast growth factor-induced proliferation and is repressed in urothelial carcinoma cell lines. *Cancer Research*.

Townes, P. L., & Holtfreter, J. (1955). Directed movements and selective adhesion of embryonic amphibian cells. *Journal of Experimental Zoology*, *128*(1), 53–120.

Trinh, L. A., & Stainier, D. Y. R. (2004). Fibronectin regulates epithelial organization during myocardial migration in zebrafish. *Developmental Cell*.

Trueb, B. (2011). Biology of FGFRL1, the fifth fibroblast growth factor receptor. In *Cellular and Molecular Life Sciences*.

Tsai, T., Sikora, M., Xia, P., Colak-Champollion, T., Knaut, H., Heisenberg, C.-P., & Megason, S. (2020). An adhesion code ensures robust pattern formation during tissue morphogenesis. *Science*, *116*(October), 113–116.

Tsang, M., Friesel, R., Kudoh, T., & Dawid, I. B. (2002). Identification of sef, a novel modulator of FGF signalling. *Nature Cell Biology*.

Turlier, H., & Maître, J. L. (2015). Mechanics of tissue compaction. *Semin Cell Dev Biol.*, *18*(2), 171–185.

Turner, D. A., Baillie-Johnson, P., & Martinez Arias, A. (2015). Organoids and the genetically encoded self-assembly of embryonic stem cells. *BioEssays*, *38*(2), 181–191.

Valdivia, L. E., Young, R. M., Hawkins, T. A., Stickney, H. L., Cavodeassi, F., Schwarz, Q., Pullin, L. M., Villegas, R., Moro, E., Argenton, F., Allende, M. L., & Wilson, S. W. (2011). Lef1-dependent Wnt/β-catenin signalling drives the proliferative engine that maintains tissue homeostasis during lateral line development. *Development*.

Valentin, G., Haas, P., & Gilmour, D. (2007). The Chemokine SDF1a Coordinates Tissue Migration through the Spatially Restricted Activation of Cxcr7 and Cxcr4b. *Current Biology*.

Van Der Walt, S., Schönberger, J. L., Nunez-Iglesias, J., Boulogne, F., Warner, J. D., Yager, N., Gouillart, E., & Yu, T. (2014). Scikit-image: Image processing in python. *PeerJ*.

Varner, V. D., & Taber, L. A. (2012). Not just inductive: A crucial mechanical role for the endoderm during heart tube assembly. *Development*.

Varshney, G. K., Carrington, B., Pei, W., Bishop, K., Chen, Z., Fan, C., Xu, L., Jones, M., LaFave, M. C., Ledin, J., Sood, R., & Burgess, S. M. (2016). A high-throughput functional genomics workflow based on CRISPR/Cas9-mediated targeted mutagenesis in zebrafish. *Nature Protocols*, *11*(12), 2357–2375.

Venero Galanternik, M., Kramer, K. L., Piotrowski, T., Aman, A., Piotrowski, T., Aman, A., Piotrowski, T., Aman, A., Piotrowski, T., Aman, A., Nguyen, M., Piotrowski, T., Barash, U., Cohen-Kaplan, V., Dowek, I., Sanderson, R. D., Ilan, N., Vlodavsky, I., Barbouri, D., … Brand, M. (2015). Heparan Sulfate Proteoglycans Regulate Fgf Signaling and Cell Polarity during Collective Cell Migration. *Cell Reports*, *10*(3), 414–428.

Venero Galanternik, M., Lush, M. E., & Piotrowski, T. (2016). Glypican4 modulates lateral line collective cell migration non cell-autonomously. *Developmental Biology*, *419*(2), 321–335.

Venkiteswaran, G., Lewellis, S. W., Wang, J., Reynolds, E., Nicholson, C., & Knaut, H. (2013). Generation and dynamics of an endogenous, self-generated signaling gradient across a migrating tissue. *Cell*, *155*(3), 674.

Viader-Llargués, O., Lupperger, V., Pola-Morell, L., Marr, C., & López-Schier, H. (2018). Live cell-lineage tracing and machine learning reveal patterns of organ regeneration. *ELife*, *7*, 1–23.

Vishwakarma, M., Di Russo, J., Probst, D., Schwarz, U. S., Das, T., & Spatz, J. P. (2018). Mechanical interactions among followers determine the emergence of leaders in migrating epithelial cell collectives. *Nature Communications*.

Vogg, M. C., Galliot, B., & Tsiairis, C. D. (2019). Model systems for regeneration: Hydra. *Development (Cambridge)*.

Wada, H., Ghysen, A., Asakawa, K., Abe, G., Ishitani, T., Kawakami, K., Inserm, U., & Bataillon, P. E. (2013).

Report Wnt / Dkk Negative Feedback Regulates Sensory Organ Size in Zebrafish. *Current Biology*, *23*(16), 1559–1565.

Walck-Shannon, E., & Hardin, J. (2014). Cell intercalation from top to bottom. In *Nature Reviews Molecular Cell Biology*.

Wang, H., Ding, T., Brown, N., Yamamoto, Y., Prince, L. S., Reese, J., & Paria, B. C. (2008). Zonula occludens-1 (ZO-1) is involved in morula to blastocyst transformation in the mouse. *Developmental Biology*.

Wang, S. S., Jiang, J., Liang, X. H., & Tang, Y. L. (2015). Links between cancer stem cells and epithelial–mesenchymal transition. In *OncoTargets and Therapy*.

Wang, T., Yanger, K., Stanger, B. Z., Cassio, D., & Bi, E. (2014). Cytokinesis defines a spatial landmark for hepatocyte polarization and apical lumen formation. *Journal of Cell Science*.

Warzecha, C. C., & Carstens, R. P. (2012). Complex changes in alternative pre-mRNA splicing play a central role in the epithelial-to-mesenchymal transition (EMT). In *Seminars in Cancer Biology*.

Waskom, M. (2018). Seaborn: Statistical Data Visualization — Seaborn 0.9.0 Documentation. *Sphinx 1.7.4*.

Watanabe, K., Liu, Y., Noguchi, S., Murray, M., Chang, J. C., Kishima, M., Nishimura, H., Hashimoto, K., Minoda, A., & Suzuki, H. (2019). OVOL2 induces mesenchymal-to-epithelial transition in fibroblasts and enhances cell-state reprogramming towards epithelial lineages. *Scientific Reports*, *9*(1), 1–7.

Watanabe, K., Villarreal-Ponce, A., Sun, P., Salmans, M. L., Fallahi, M., Andersen, B., & Dai, X. (2014). Mammary morphogenesis and regeneration require the inhibition of EMT at terminal end buds by ovol2 transcriptional repressor. *Developmental Cell*.

Werner, S., Peters, K. G., Longaker, M. T., Fuller-Pace, F., Banda, M. J., & Williams, L. T. (1992). Large induction of keratinocyte growth factor expression in the dermis during wound healing. *Proceedings of the National Academy of Sciences of the United States of America*.

Westerfield, M. (2007). The Zebrafish Book. A Guide for the Laboratory Use of Zebrafish (Danio rerio), 5th Edition. *University of Oregon Press, Eugene (Book)*.

White, M. D., Zenker, J., Bissiere, S., & Plachta, N. (2018). Instructions for Assembling the Early Mammalian Embryo. *Developmental Cell*, *45*(6), 667–679.

Wibowo, I., Pinto-Teixeira, F., Satou, C., Higashijima, S. I., & López-Schier, H. (2011). Compartmentalized Notch signaling sustains epithelial mirror symmetry. *Development*, *138*(6), 1143–1152.

Widelitz, R. B., & Chuong, C. (1999). Early Events in Skin Appendage Formation: Induction of Epithelial Placodes and Condensation of Dermal Mesenchyme. *Journal of Investigative Dermatology Symposium Proceedings*, *4*(3), 302–306.

Williams, E. J., Furness, J., Walsh, F. S., & Doherty, P. (1994). Activation of the FGF receptor underlies neurite outgrowth stimulated by L1, N-CAM, and N-cadherin. *Neuron*.

Williams, & Holder, N. (2000). Cell turnover in neuromasts of zebrafish larvae. *Hearing Research*, *143*(1–2), 171–181.

Wong, Lamothe, B., Lee, A., Schlessinger, J., & Lax, I. (2002). FRS2α attenuates FGF receptor signaling by Grb2-mediated recruitment of the ubiquitin ligase Cbl. *Proceedings of the National Academy of Sciences of the United States of America*.

Wong, M., & Gilmour, D. (2020). Getting back on track: exploiting canalization to uncover the mechanisms of developmental robustness. In *Current Opinion in Genetics and Development*.

Wong, M., Newton, L. R., Hartmann, J., Hennrich, M. L., Wachsmuth, M., Ronchi, P., Guzmán-Herrera, A., Schwab, Y., Gavin, A. C., & Gilmour, D. (2020). Dynamic Buffering of Extracellular Chemokine by a Dedicated Scavenger Pathway Enables Robust Adaptation during Directed Tissue Migration. *Developmental Cell*.

Wood, W., Jacinto, A., Grose, R., Woolner, S., Gale, J., Wilson, C., & Martin, P. (2002). Wound healing recapitulates morphogenesis in Drosophila embryos. *Nature Cell Biology*.

Wu, R. S., Lam, I. I., Clay, H., Duong, D. N., Deo, R. C., & Coughlin, S. R. (2018a). A Rapid Method for Directed Gene Knockout for Screening in G0 Zebrafish. *Developmental Cell*.

Wu, R. S., Lam, I. I., Clay, H., Duong, D. N., Deo, R. C., & Coughlin, S. R. (2018b). A Rapid Method for Directed Gene Knockout for Screening in G0 Zebrafish. *Developmental Cell*, *46*(1), 112-125.e4.

Wu, X. lin, Gu, M. min, Huang, L., Liu, X. song, Zhang, H. xin, Ding, X. yi, Xu, J. qiang, Cui, B., Wang, L., Lu, S. yuan, Chen, X. yi, Zhang, H. guo, Huang, W., Yuan, W. tao, Yang, J. ming, Gu, Q., Fei, J., Chen, Z., Yuan, Z. min, & Wang, Z. gang. (2009). Multiple Synostoses Syndrome Is Due to a Missense Mutation in Exon 2 of FGF9 Gene. *American Journal of Human Genetics*.

Xia, P., Gütl, D., Zheden, V., & Heisenberg, C. P. (2019). Lateral Inhibition in Cell Specification Mediated by Mechanical Signals Modulating TAZ Activity. *Cell*.

Xiao, T., Roeser, T., Staub, W., & Baier, H. (2005). A GFP-based genetic screen reveals mutations that disrupt the architecture of the zebrafish retinotectal projection. *Development*.

Yanagida, A., Revell, C., Stirparo, G. G., Corujo-Simon, E., Aspalter, I. M., Peters, R., De Belly, H., Cassani, D. A. D., Achouri, S., Blumenfeld, R., Franze, K., Paluch, E. K., Nichols, J., & Chalut, K. J. (2020). Cell surface fluctuations regulate early embryonic lineage sorting. *BioRxiv*, 2020.08.16.250084. https://doi.org/10.1101/2020.08.16.250084

Yang, Antin, P., Berx, G., Blanpain, C., Brabletz, T., Bronner, M., Campbell, K., Cano, A., Casanova, J., Christofori, G., Dedhar, S., Derynck, R., Ford, H. L., Fuxe, J., García de Herreros, A., Goodall, G. J., Hadjantonakis, A. K., Huang, R. J. Y., Kalcheim, C., … Sheng, G. (2020). Guidelines and definitions for research on epithelial–mesenchymal transition. *Nature Reviews Molecular Cell Biology*.

Yang, H., Lu, X., Liu, Z., Chen, L., Xu, Y., Wang, Y., Wei, G., & Chen, Y. (2015). FBXW7 suppresses epithelial-mesenchymal transition, stemness and metastatic potential of cholangiocarcinoma cells. *Oncotarget*.

Yang, Z., Zimmerman, S., Brakeman, P. R., Beaudoin, G. M., Reichardt, L. F., & Marciano, D. K. (2013). De novo lumen formation and elongation in the developing nephron: A central role for afadin in apical polarity. *Development (Cambridge)*.

Yayon, A., Klagsbrun, M., Esko, J. D., Leder, P., & Ornitz, D. M. (1991). Cell surface, heparin-like molecules are required for binding of basic fibroblast growth factor to its high affinity receptor. *Cell*.

Ye, J., Coulouris, G., Zaretskaya, I., Cutcutache, I., Rozen, S., & Madden, T. L. (2012). Primer-BLAST: a tool to design target-specific primers for polymerase chain reaction. *BMC Bioinformatics*.

Yu, Burkhardt, M., Nowak, M., Ries, J., Petráek, Z., Scholpp, S., Schwille, P., & Brand, M. (2009). Fgf8 morphogen gradient forms by a source-sink mechanism with freely diffusing molecules. *Nature*.

Yu, W., Datta, A., Leroy, P., O'Brien, L. E., Mak, G., Jou, T. S., Matlin, K. S., Mostov, K. E., & Zegers, M. M. P. (2005). β1-integrin orients epithelial polarity via Rac1 and laminin. *Molecular Biology of the Cell*.

Yu, W., Shewan, A. M., Brakeman, P., Eastburn, D. J., Datta, A., Bryant, D. M., Fan, Q. W., Weiss, W. A., Zegers, M. M. P., & Mostov, K. E. (2008). Involvement of RhoA, ROCK I and myosin II in inverted

orientation of epithelial polarity. *EMBO Reports*.

Zaidel-Bar, R., Zhenhuan, G., & Luxenburg, C. (2015). The contractome - A systems view of actomyosin contractility in non-muscle cells. *Journal of Cell Science*.

Zenker, J., White, M. D., Gasnier, M., Alvarez, Y. D., Lim, H. Y. G., Bissiere, S., Biro, M., & Plachta, N. (2018). Expanding Actin Rings Zipper the Mouse Embryo for Blastocyst Formation. *Cell*, *173*(3), 776-791.e17.

Zhang, S., Amourda, C., Garfield, D., & Saunders, T. E. (2018). Selective Filopodia Adhesion Ensures Robust Cell Matching in the Drosophila Heart. *Developmental Cell*.

Acknowledgements

There are many people that I would like to thank for crucially contributing to make my PhD journey at EMBL in Heidelberg and at UZH in Zürich such a valuable and fun learning experience.

First of all, many thanks to my supervisor Darren Gilmour, for his continuous support from my very first steps in the lab, for all the stimulating and inspiring discussions and for encouraging me when facing challenges along the way towards my goals. Thanks for having given me the possibility to work on such an exciting project that led me to explore *The Fabulous World of Lateral Line Chain Cells*.

Thanks to the members of my Thesis Advisory Committee Dr. Martin Jechlinger, Prof. Dr. Jochen Wittbrodt and Dr. Takashi Hiiragi for the constructive feedback and precious suggestions on the project and I am grateful to all of them and to Prof. Dr. Nick Foulkes for kindly accepting to be part of my defense panel.

Many thanks to the former and current members of the Gilmour lab at EMBL and at UZH for the amazing 'zebrabow' atmosphere in the lab. Such a collaborative, friendly and scientifically inspiring environment made the Gilmour lab not only a fruitful hive of scientific ideas but also a second family to me. Sharing a part of my journey with you all has been truly impactful for my scientific and personal growth. Thanks to Greta, Robert, Jerome, Florian, Elisabeth, Alejandra, Allyson, Sarfi and in particular to Sevi and Mie for the great discussions inside and outside the lab and for the numerous fun moments together. Thanks to Max, which translated the summary of this thesis in German and on which I could always count for image analysis help, a sincere scientific feedback, an inspiring discussion or an amazing cheese fondue. Thanks to Jonas for inputs on the project and for support in image analysis and python emergencies. A second thanks to him for all the flooding brainstorming sessions spontaneously born over tea and canteen food and for the many engaging discussions about Science, sparkling of crazy ideas and blackboard sketching. Thanks to Maaike, that I was lucky enough to supervise during her master project, for her help and dedication.

Many thanks to Francesca Peri and to the Peri lab that were happy to welcome the Gilmour lab during the Zürich transition and not only shared their spaces and resources but also their expertise, ideas and enthusiasm. Thanks to the current members of Peri lab for keeping this connection tight in Zürich as well and for all the precious comments and interesting discussions during lab meetings. Thanks to Marv and Katrin for their passionate attitude for science, for all the helpful suggestions and for the fun moments shared.

Many thanks to the members of the Gilmour and Peri lab that ensured with their work the best conditions for research to occur, providing countless technical support. In particular, I am thankful to Andreas for help and tips in my first cloning experience and to Sabine, Rick and Conny for having taken

such a good care of the fish. An additional thanks to Sabine for bearing my music tastes on her Spotify and to Andreas for bringing me evidences that spiders can be cute (when they are colorful and in love).

I am thankful to the EMBL ALMF and the UZH microscopy facility for providing great microscopy support, in particular to Yury Belyaev, Christian Tischer, Aliaksandr Halavatyi and Stefan Terjung at EMBL and to Jana Döhner, José María Mateos Melero and Joana Raquel Delgado Martins at UZH.

Many thanks also to Monika at the EMBL Graduate Office and to Angie in Zürich for the invaluable help before\during\after my move to Zürich.

Thanks to the friends from the EMBL PhD Batch 2015 that made my PhD journey even more fun. In particular I am grateful to Ambra, Anna, Brana, Christine, Jadou and Allyson for never let me down and for sharing frustration but also many fun moments and engaging chats.
Thanks to Julia for her sincere friendship, for cheering me up with her yummy waffles and for being a great Aikido buddy.
Thanks to my long-life friends Giulia, Laura and Claudia. I know I can always count on your support via Zoom/Skype/SMS/WhatsApp/spontaneous visits and for a breath of fresh air.

Un enorme ringraziamento alla mia famiglia, in particolare ai miei genitori e a mia sorella Chiara che mi hanno sempre incoraggiato a seguire le mie passioni e i miei obiettivi. Anche quando le mie passioni li hanno constretti a gite di famiglia in cave abbandonate e polverose a cercare fossili, o a procurarmi sostanze chimiche per il mio laboratorio di cristalli e persino quando una nuova avventura mi ha portata geograficamente lontano (gia' di un paio di nazioni ormai). Grazie per essermi stati ed essermi sempre vicino ad ogni mio grande o piccolo passo.

Finally, huge thanks to Marco, for being by my side during my PhD adventure (and way before that) with immense patience, encouragement and support. I can easily write another 132 pages of acknowledgements about it, but I think this thesis is long enough. Thanks for bearing me when I speak Science and I start sketching cells with all the colored pencils around, thanks for encouraging me to step out of my comfort zone to pursue my goals and in particular, thanks for making me laugh, always, even when I think it isn't possible.